REFERENCE ONLY

UNIVERSITY OF LONDON THESIS

Degree PhD Year 2006 Name of Author PAGLIARI, P

A Novel Experimental Approach To High Temperature Particle-Particle Interactions

Paolo Pagliai

University College London
November, 2005

Thesis submitted to the University of London for the degree of
Doctor of Philosophy

ProQuest LLC
789 East Eisenhower Parkway
P.O. Box 1346
Ann Arbor, MI 48106-1346

ACKNOWLEDGEMENTS

I wish to express my gratitude to my principal supervisor, Prof Stef Simons, for granting me the opportunity to carry out this exciting research, and for his support throughout the project.

I also wish to thank my industrial supervisor, Dr Dominic Rhodes for his support, and British Nuclear Fuels plc. for sponsoring this work.

A big thank you to my family and friends for supporting me during these years. In particular: Da', Murru, Gio', Pezzaaseeno, Roberta, Sara P, Skuz and the Italian crew at UCL. Thank you Ale Barba and Paco for your true interest in my research work, few of my best ideas came out from reasoning with you guys! Thanks Nan for not having any kind of interest in my work (for real man!). Thanks to anybody who made my stay in London such an exciting experience. Who feels it knows it.

ABSTRACT

Interactions at elevated temperatures between solid particles occur in a wide range of industrial processes, for instance, in the filtering of hot gases, in the drying of pharmaceutical granules, in the curing of ceramics, in the combustion of solid fuels and regeneration of nuclear waste.

Often these interactions can cause major problems in the operation of such processes. For example, it is well established that the fluidisation behaviour of certain powders is significantly affected by the presence of strong interparticle forces that, in turn, are the cause of both agglomerate formation and possible operative problems within the reactor. On the other hand, not much is known about the mechanisms of agglomeration, other than that it is mainly due to interfacial phenomena. High temperature adhesion forces arise from the formation of material bridges, usually due to the particle surfaces changing phase through either chemical reaction or simply melting. Moreover, thin liquid layers of sticky material, which may be present on particle surfaces, such as during reactive coating or drying processes, may also enhance strong interparticle bonds leading to solidification.

It is obvious that for the reliable operation of high-temperature processes a good understanding of the fundamental mechanisms of adhesion and cohesion between particles at elevated temperatures is required. Here, adhesion is meant as the force that holds the particles together, after which they exhibit cohesive behaviour. Unfortunately, the level of understanding has been hampered by the lack of techniques available to observe and measure such interactions. However, recent developments in microscopic analysis techniques now mean that high temperature particle interactions can be studied directly, which will lead to the development of new predictive models.

The main aim of the work described in this thesis is to provide experimental evidence and justification of particle-particle interactions at high temperature and to deliver original insights of the underlying mechanisms, which play a fundamental role in particulate cohesion in relation to fluidisation process. In order to fulfill this goal, a novel device, termed a High Temperature Micro-Force Balance, has been designed and developed which combines force and direct observation measurements operated through an adapted micromanipulator technique.

The flexibility of use for the HTMFB represents its strongest design advantage, permitting experimental investigations over different types of particle interactions at a small scale (crystallization of liquid binders, reactive coating, sintering and composite materials interactions). Results reported in this work provide an original contribution towards academic and industrial understanding of the micro-scale mechanisms of agglomeration and material properties at different operative conditions.

CONTENTS

LIST OF FIGURES

LIST OF TABLES

NOMENCLATURE

$\ddot{y}, y''$	Second derivative of y	m^{-1}
$\Delta\ell$	Shrinkage or dilation due to the effect of temperature	m
ΔP_c	Calculated pressure drop in a fluid-bed	mmH_2O
ΔP_i	Pressure difference between liquid and surrounding gas, $\Delta P_i = \frac{2\gamma_{LV}}{R_i}$	Pa
ΔP_m	Measured pressure drop in a fluid-bed	mmH_2O
$\Delta P_{dry}, \Delta P_{wet}$	Dry to wet fluid bed pressure drop ratio	–
ΔV	Voltage increment	$Volts$
$\dot{y}, \dot{y}_i, y', y_i'$	First derivative of y, generic or calculated at point A,B (i=A,B)	–
ℓ	Initial length of a sample of powder	m
$\overline{d_p}$	Mean particle diameter	m
$\overline{R}$	Geometric average radius, $\overline{R} = \frac{2R_AR_B}{R_A+R_B}$	m
a, a_i	Liquid bridge separation distance, generic or between particle and liquid bridge neck (i=1,2)	m
a, b, c	Coefficients used in the parabolic approximation	–
a^*, a_i^*	Dimensionless separation distance with respect particle radius, generic or calculated between two configurations (i=1,2)	–
A_1	Coefficient, $A_1 \approx 2$	–
a_c	Rupture distance of a liquid bridge	m
a_c^*	Dimensionless critical rupture distance, $a_c^* = \frac{a_c}{R}$	–
A_H	Hamaker constant	J
A_k	Rate of attrition constant, $A_k \propto \frac{E_{xs}}{f_{coh}}$	–
A_L	Area of the liquid phase	m^2

A_{SL}	Solid-liquid interfacial area	m^2
a^*_{visc}	Dimensionless separation distance with respect particle radius in viscous regime	–
b	Liquid bridge separation distance between particle and liquid bridge neck	m
b, c	Coefficients that depend on the normalised interparticle distance $\frac{a}{d_p}$	–
c	Characteristic defect size	m
C_s	Solids concentration in the binder solution	g/cm^3
Ca	Capillary number	–
d	Length of the liquid bridge	m
D_B	Bubble diameter	m
d_b	Fluid-bed diameter	m
d_c	Diameter of a coated particle, $d_c = \delta_c + d_p$	m
D_p, d_p	Particle diameter	m
D_s	Sample diameter	m
D_{aggl}, d_{agg}	Agglomerate diameter	m
D_{drop}	Droplet diameter	m
De	Deformation number, $De = \frac{\rho_a U^2}{Y}$	–
E	Energy calculated by means of DSC	mW
e_r	Coefficient of restitution after particle impact	–
E_{xs}	Energy exchange between fluid and particles	J
F	Force between particles	N
F_b	Liquid bridge force at the particle-meniscus boundary	N
F_c	Interparticle cohesive force	N
F_{max}	Maximum liquid bridge force	N
F_n	Liquid bridge force calculated at the neck of the meniscus	N
F_p	Intergranular force	N
F_p	Liquid bridge force calculated with the parabolic approximation	N

F_v	Total viscous force in a liquid bridge	N
F_w	van der Waals attraction	N
f_{coh}	Surface cohesion force of single particles	N
F_{solid}	Maximum force caused by shrinkage of a drying liquid bridge	N
G	Adhesive surface energy	N/m
g	Gravity acceleration	$9.81\frac{m}{s^2}$
G_v	Maximum force acting on the agglomerate	N
H	Characteristic length of liquid bridge	m
H	Hysteresis of the contact angle	rad
h	Height of a cylindrical agglomerate	m
h	Height of a droplet	m
h	Overall heat transfer coefficient, $h = h_{pc} + h_{gc} + h_r$	$\frac{W}{m^2K}$
h_a	Asperity height	m
h_f	Thickness of particle coating film	m
h_i	Height of cap of sphere for the i^{th} (i=A,B) particle	m
h_r	Radiative heat transfer coefficient	$\frac{W}{m^2K}$
H_{f-m}	Heat of fusion	mW
H_{f-s}	Heat of solidification	mW
h_{gc}	Gas convective heat transfer coefficient	$\frac{W}{m^2K}$
H_{mf}	Height of a fluid-bed at minimum fluidisation	m
h_{pc}	Particle convective heat transfer coefficient	$\frac{W}{m^2K}$
K	Numerical constant used for the determination of the particle surface viscosity	$-$
K	Ratio of the true wetted area to the apparent area	$-$
K	Spring constant of the flexure strip assembly	N/m
k	Spring constant of the AFM cantilever	N/m
k_1	Coefficient	$\frac{ms^2}{kg}$

k_2	Coefficient	$\frac{kg}{ms^2}$
K_g	Geodesic curvature	m^{-1}
$K_{sh,i}$	Spring constant of a single flexure sheet (i=1,2)	N/m
L	Characteristic length of liquid bridge	m
L	Load applied to a sample of powder	N
l	Height of the agglomerate above the distributor plate	m
L_0	Fluid bed height at rest	m
M	Liquid content of a wet agglomerate	–
m	Particle mass	kg
M_k	Proportionality constant	–
Nu_{gp}	Gas to particle Nusselt number	–
P, P_i	Pressure, generic or for configuration i (i=1,2)	Pa
P_{br}	Pressure within the liquid bridge	Pa
q	Pressure distributed over the bottom of the agglomerate	Pa
q_{max}	Maximum pressure before breakage of the agglomerate	Pa
R, R_i	Particle radius, generic or for particle i^{th} (i=A,B)	m
r_i	Liquid bridge radii of curvature (i=1,2)	m
r_p	Particle radius	m
r_{dn}	Size of the dried neck	m
Re	Reynolds number, $Re = \frac{\rho v D_p}{\eta}$	–
S	Liquid saturation	–
S_p	Spreading coefficient	J
St	Stokes number, $St = \frac{2mv_0}{3\pi\eta R^2}$	–
St^*	Critical Stokes number	–
St_D^*	Critical Stokes number at the point of defluidisation	–
T	Temperature, arbitrary unit	$°C or K$

t_c	Time for a sintered neck to form	s
T_g	Glass transition temperature	$°C$
T_s	Sintering temperature	$°C or K$
t_{b0}	Particle residence time in the quiescent zone	s
U	Granule velocity	m/s
u, U	Gas velocity	m/s
U^*	Superficial gas velocity at the point of defluidisation	m/s
U_B	Bubble velocity	m/s
U_{mf}	Superficial gas velocity at minimum fluidisation	m/s
V	Applied voltage	$Volts$
V	Volume	m^3
v	Relative particle separation velocity	m/s
v	Velocity of the linear actuator	pts
V^*	Dimensionless liquid bridge volume, $V^* = \frac{V_b}{R^3}$	–
v_0	Particle approach velocity	m/s
V_b	Liquid bridge volume	m^3
V_p, V_s	Particle volume	m^3
V_{sb}	Solid bridge volume	m^3
V^*_{sb}	Solid bridge volume normalised to particle volume	–
W	Rupture energy of liquid bridge	J
W^*	Dimensionless rupture energy of liquid bridge, $W = \frac{W}{\gamma_L R^2}$	–
W_i	Weight of a sample material ($i = 0$ initial weight, $i = \infty$ residual weight) nomunitkg	
W_{ad}	Work of adhesion	J
W_{co}	Work of cohesion	J
X	Radius of the sinter neck	m

x	Cantilever deflection	m
X_b	Displacement of the flexure strips	m
X_c	Sinter neck diameter	m
X_f	Final length of a dried bridge	m
X_i	Initial length of a liquid bridge	m
X_p	Relative shrinkage of a drying liquid bridge, $X_p = \frac{X_i - X_f}{X_i}$	–
X_{b0}	Deflection of the flexure strips due to calibration	m
Y	Dynamic yield stress	kg/ms^2
y, y_i	Liquid bridge ordinate, generic or calculated at point A,B (i=A,B)	m
α	Proportionality constant	–
α_r	Extent of reaction	–
α_{sb}	Volume of solids to bubbles ratio	–
β, β_i	Half-filling angle, generic or calculated at point A,B (i=A,B)	rad
β_{ls}	Layer spacing coefficient	–
δ, δ_i	Contact angle, generic or calculated at point i (i=A,B)	rad
δ_c	Thickness of the coating layer	m
δ_W	Wenzel contact angle	rad
δ_∞	Young contact angle	rad
δ_{adv}	Advancing contact angle	rad
δ_{rec}, δ_r	Receding contact angle	rad
ϵ	Relative dielectric constant	–
ϵ_0	Vacuum dielectric constant	$8.85 \cdot 10^{-12} C^2 J^{-1} m^{-1}$
η	Dynamic viscosity	$Pa \cdot s$
η_s	Particle surface viscosity	$Pa \cdot s$
γ	Surface tension	N/m
γ_l, γ_L	Surface tension of liquid binder toward external medium (either gas or liquid)	N/m

γ_S	Surface tension of solid toward external medium (either gas or liquid)	N/m
$\gamma_{LG}, \gamma_{LV}, \gamma_{lv}$	Interfacial tension between liquid and vapour (gas)	N/m
γ_{LL}	Interfacial tension in a liquid, by definition equal to zero	N/m
γ_{SL}	Interfacial tension between solid and liquid, usually binder (either in gas or liquid bulk medium)	N/m
Ω	Angle between normal to liquidbridge profile and horizontal axis	rad
ω_0	Cantilever resonance frequency	s^{-1}
Ψ	Energy constant	J
ψ, ψ_i	Half-filling angle, generic or calculated at point A,B (i=A,B)	rad
ρ	Mass density	kg/m^3
ρ_f	Fluid density	kg/m^3
ρ_g	Gas density	kg/m^3
ρ_p	Particle density	kg/m^3
σ_t	Tensile strength of the agglomerate	N/m^2
σ_y	Yield strength of the agglomerate	N/m^2
$\sigma_{1,2}$	Surface charge density, generic or for particle i (i=1,2)	C/m^2
σ_{sb}	Solid bridge tensile strength	N/m^2
σ_{tw}	Tensile strength of a wet agglomerate	N/m^2
τ	Line tension	N
τ_y	Granule yield stress	N/m^2
θ, θ_i	Contact angle, generic or calculated at point i (i=A,B)	rad
ε	Porosity of the wet agglomerate	–
ε	Voidage	–
ε_0	Initial porosity of the agglomerate	–
ε_{max}	Maximum porosity of the wet agglomerate	–
ε_{mf}	Void fraction at minimum fluidisation	–

φ	Dimensionless liquid bridge volume, $\varphi = \frac{V_b}{2V_p}$	–
φ'	Dimensionless liquid/solid bridge volume, $\varphi' = 2\varphi = \frac{V}{V_p}$	–
ζ	Dimensionless distance between bubbles	–

1. INTRODUCTION

Interactions at elevated temperatures between solid particles occur in a wide range of industrial processes, for instance, in the filtering of hot gases, in the drying of pharmaceutical granules, in the curing of ceramics, in the combustion of solid fuels and regeneration of nuclear waste. Often these interactions can cause major problems in the operation of such processes.

The photograph in figure 1.1 is of a bed of coal-ash powder that has been solidified during gasification in a fluidised bed due to sintering between the particles at high temperature. In this example, poor design of the gasifier led to regions where particle motion was poor and, consequently, hot spots could develop. The lack of vigorous motion in these areas allowed time for permanent bonds between the particles to form through sintering. Obviously, the gasifier became inoperable once the powder bed had formed this solid clinker, with the only option being to shut down the process, dismantle the vessel and remove the obstruction.

Fig. 1.1: A solidified bed of coal-ash powder caused by sintering in a gasifier.

According to Berbner and Löffler[1], adhesion forces between particles can be characterised by whether or not a material bridge exists between them. High temperature adhesion

forces arise from the formation of material bridges, usually through the particle surfaces changing phase through either chemical reaction or simply melting. Moreover, thin liquid layers of sticky material, which may be present on particles surface, such as during reactive coating or drying processes, may also enhance strong interparticle bonds following to solidification.

It is obvious that for the reliable operation of high-temperature processes a good understanding of the fundamental mechanisms of adhesion and cohesion between particles at elevated temperatures is required. Here, adhesion is meant as the force that holds the particles together, after which they exhibit cohesive behaviour. Unfortunately, the level of understanding has been hampered by the lack of techniques available to observe and measure such interactions. However, recent developments in microscopic analysis techniques now mean that high temperature particle interactions can be studied directly, which will lead to the development of new predictive models.

The main aim of the work described in this thesis is to provide experimental evidence and justification of particle-particle interactions at high temperature and to deliver original insights regarding the underlying mechanisms which play a fundamental role in particulate cohesion in relation to fluidisation process. In order to fulfill this goal, a novel device has been designed which allows force measurement and direct observation techniques, therefore providing fundamental contributions to studying interfacial phenomena.
Because of its operative flexibility, the **High Temperature Micro-Force Balance**, permitted the experimental investigation for two particle-particle systems by employing different techniques according to each case study. The major outcome proved to be essential to achieve a basic knowledge of the dependency of particle interactions from some key operative parameters.

In this thesis, **Chapter 2** presents a literature review for long range surfacial forces that happen between pair of particles in presence of material bridges. This chapter will introduce the concept of the simulation of high temperature adhesion forces using liquid bridges and then will discuss the current understanding of particle adhesion caused by liquid binders. In such a case, changes in the strength of a liquid bond are studied as function of the main parameters (such as the contact angle and hysteresis, the liquid bridge volume, etc.) that characterise the particle-particle system. Liquid bridge forces are analysed in term of a combination of capillary, surface tension and viscous effects. The energy stored by a liquid bridge is also considered as being an important parameter during granules agglomeration and deformation. An overview on the high temperature reactive binders and sintering phenomena is also provided.

To explain and characterise the bulk flow behaviour in various industrial processes, a

great deal of research has been carried out in order to scale up the microscopic particle interactions to the macroscopic properties of granules. In **Chapter 3** the reader will find the description of off-line experimental techniques employed for the determination of actual particle interactions induced by changes of either (reactive) binder or powder physical properties. In this regard, this chapter includes additional investigations carried out during the course of this work that had direct industrial support. Using a Micro-Force Balance (MFB), designed at UCL during a previous doctorate work, the adhesiveness of different liquid binders commonly used in the pharmaceutical industry (PVP, HPMC) has been tested between paracetamol crystals. Investigation of wettability and distribution of liquid after liquid bridge rupture were also investigated. Moreover, introduction to the current micro-manipulation techniques described in literature and comparison with the modern atomic force microscopy, will highlight the need of novel instrumentation capable to carry out measurements at high temperatures.

Since the main aim of this thesis is to elucidate the role of the interparticle forces in relation to fluidisation, in **Chapter 4**, a review is presented on the changes of the fluid bed behaviour when strong interparticle forces are enhanced either by liquid addition to the bed contents or temperature. The most representative models are described, which predict the defluidisation limit by following different approaches (i.e. kinetic energy or quiescent characteristic times). Moreover, a review on the most recent non-invasive measurement techniques in fluidisation is proposed.

The Colloid and Surface Engineering Group at UCL has a leading experience in micro-manipulation techniques and has been gaining successful results, in recent years, by carrying out innovative measurements in relation to particle-particle systems in gaseous and liquid media, particle-bubble interactions and crystallization processes. Thus, a novel and unique device, termed **High Temperature Micro-Force Balance**, which allows the determination of particle interactions at elevated temperatures, was developed and it will be described in **Chapter 5**.

British Nuclear Fuels has been sponsoring this project and, therefore, the realisation of the **HTMFB**, in order to shed light on the microscopic mechanisms of agglomeration of Uranium trioxide particles during nuclear fuel re-processing operated at high temperatures by means of fluidised bed reactors. To this aim, in **Chapter 6**, a novel approach is presented, namely, the direct measurement and observation of particle interactions at high temperatures on a micro-scale. Here, the fluidisation behaviour of a particular catalyst material, termed E-cat, which was previously investigated by other researchers, found an explanation on a microscopic point of view by employing the **HTMFB**. Results from the experimental campaign, carried out on such a powder, revealed, for the first time, the causes of particle agglomeration and, therefore, of defluidisation of the bed at high

temperatures.

In light of the promising results obtained in Chapter 6, the **HTMFB** was subsequently employed to investigate the adhesion mechanisms developed between glass particles coated with Magnesium nitrate hexahydrate, here used as a simulant material for the Uranyl nitrate hexahydrate employed in the real process. The mechanism of particle agglomeration was investigated, in **Chapter 7**, by studying the possible formation of a sinter neck between pairs of coated particles placed in contact at different temperatures and at different amount of coating material. Moreover, the strength exerted by increasing volumes of coating material, initially placed between particles in order to form a bond, was measured, by rupture tests, at characteristic decomposition temperatures: such an experimental technique, permitted to ascertain whether the causes of agglomeration and defluidisation, can be addressed to over-wetting rather than to sintering of the bed material.

Finally, the main conclusions and recommendations for the direction of future work are drawn in **Chapter 8**.

The Appendix section is divided into eight parts (A-H). Appendix A contains the values of the volume of the liquid bridge calculated by numerically solving the Young-Laplace equation. These data were used for comparison with the approximations for the liquid bridge volume available in literature.

Appendix B describes the mechanical measurements carried out to calculate the flexibility of the Force Measurement Assembly (FMA). Calibration of the heating element and determination of possible thermal gradients within the interaction area are explained in Appendix C and Appendix C.1, respectively.

The Visual Basic code, compiled in order to load and process the *seq* files stored by the Sequence tool, can be found in Appendix D. Whilst, the block diagram necessary to operate the data acquisition from the HTMFB is illustrated in Appendix E.

Calibration and conversion factors required to operate the particle displacement through the Encoder Driver interface are reported in Appendix F.

Appendix G reports a description of the mechanism behind the formation of liquid necks at the particle - micro-pipette junction during liquid bridge formation between a pair of particles. Such a mechanism was employed in this thesis to both operate the coating of glass particles by using a feeding particle-pipette system and ensure solid bonds between particle and pipette, which are high temperature resistant.

The final Appendix H contains a list of publications, conferences and company reports related to the work presented in this thesis.

2. TYPES OF PARTICLE-PARTICLE INTERACTIONS

During production and processing of solid matter in disperse systems, adhesion phenomena become more and more important with decreasing particle size, causing aggregation, agglomeration, coating and caking.

As shown in Table 2.1 [2], adhesion of finely divided material takes place for all operations of mechanical process engineering and can be either desired or undesired.

Unit Operation	Process	Agglomeration	
		Undesirable	Desirable
Comminution	Dry grinding	Y	N
	Wet grinding	Y	N
Separation	Screening/Sieving	Y	N
	Classifying/Sorting	Y	~Y
	Flotation	Y	~Y
	Dust Precipitation	~N	Y
	Clarification/Thickening	~N	Y
	Particle size analysis	YY	N
Mixing	Dry mixing	Y	N
	Wet mixing	Y	Y
	Stirring	Y	~Y
	Suspending/Dispersing	Y	~Y/Y
	Fluidised bed	Y	Y
Particle size enlargement	Agglomerating Briquetting Tabletting Granulating Pelletizing Pelleting Sintering	~Y	YY
Conveying	Vibratory	Y	N
	Pneumatic	Y	N
Storage	Silos/Hoppers	Y	N
	Stockpile	Y	N
Batch Metering		Y	N
Drying		Y	Y

Tab. 2.1: Agglomeration phenomena in mechanical process engineering.[2]

At normal process conditions, the forces of gravity and inertia for larger particles ($\succ$ $100\mu m$) are large if compared to the interparticle forces, therefore those particles show an individual mobility that will result in "free flow" characterization. On the other hand, for very small particles, the enhanced forces may be large when compared with the inertial and gravitational contribution, thus resulting in poor particle mobility. The different flow characterization of such systems is typically exploited by industry in order to produce material of different structural strength [3].

However, the multitude of possible binding and attraction forces between particulates in a multiphase system can result in the formation of agglomerates, even if some individual particles do not exhibit adhesion tendencies because their size is too large.
For instance, in the pharmaceutical, fine chemical, mineral, metallurgical and food industries, powders are found whose flow properties change with atmospheric humidity. These changes can adversely affect such operations as mixing, gas-solids separation, storage, fluidisation and pneumatic conveying.

Generally, the tendency to form agglomerates is particularly high if the bulk mass consists of material with a wide particle size distribution in which large voids are filled with smaller particles. In such situations, additional attractive surface forces can develop (for example in wet masses or wetting by capillary condensation), due to the presence of liquid bridges and, if the solid is soluble, due to recrystallization during drying. Moreover, in those industrial processes carried out at high temperature, such as in the combustion of coal, regeneration of spent nuclear fuel or hot gas filtering, both the physical and chemical properties of the solids surface may be modified by changes in the process conditions, such as the development of hot spots in the reactor, thus causing more effective stickiness of the powder, poor control of the process and, eventually, loss of flowability.

As a matter of fact, despite its widespread occurrence, agglomeration[1] is poorly understood: it is, for instance, both a major problem and a major application in fluidisation. The ease of operation, the rapid mixing of solids (and subsequent isothermal conditions throughout the bed) and both the high heat and mass transfer rates between gas and particles are undoubtedly advantages in fluidisation, therefore gas-solid fluidised bed reactors are largely employed in a wide range of process conditions, as illustrated in Table 2.2; on the other hand, in more than one case, industry has to deal with non-uniformity of products and poorer performance of the reactor. The main reason can be ascribed to poor gas mixing (gas by-passing or poor gas-solid contact), over-production of fines due to attrition and non-uniform residence times of solids in the bed. The above mentioned disadvantages represent both the cause and effect of enhanced surface forces developed

[1] In order to deliver a fully comprehensive reading of this dissertation, unless specified otherwise, the term 'agglomeration' will always be referred to as the result of binding between particles.

within the bed material which, in turn, may result strong enough to dramatically affect the quality of fluidisation.

Process	Example/Products	Process Conditions
Drying of solids	Inorganic materials	60-90 °C ; 1atm
	Pharmaceuticals	60 °C ; 1 atm
Calcination	Limestone	770 °C ; 1 atm
	Alumina	550-600 °C ; 1 atm
Granulation	Soap powders	5 °C ; 1 atm
	Food, Pharmaceuticals	20-40 °C ; 2-3 atm
Coating	Food, Pharmaceuticals	20-80 °C; 2-3 atm
Roasting	Food industry products	200 °C ; 1 atm
	Sulfide ores (FeS2)	650-1100 °C ; 1atm
Synthesis Reactions	Phtalic anhydride	340-380 °C ; 2.7 atm
	Acrylonitrile	400-500 °C ; 1.5-3 atm
	Ethylene dichloride	260-310 °C ; 1-10 atm
	Maleic anydride	400-500 °C ; 4 atm
	Polyethylene (low/high density)	75-120 °C ; 15-30 atm
Thermal Cracking	Ethylene, Propylene	750 °C ; 1 atm
Other Applications		
Combustion, Incineration of waste solid		800-900 °C ; 1-10 atm
Gasification of coal and coke solid waste		800 °C ; 1-10 atm
Biofluidization, cultivation of micro-organism		30 °C ; 1 atm
Semiconductor Industries		300-1100 °C ; 1 atm

Tab. 2.2: Some Industrial Applications of Fluidised Beds. After [6].

A great deal of research [4] has been carried out with special attention being paid to evaluate the effect of physical properties of the particles (such as size and particle size distribution) on the enhancement of gas-solid contact and, as a consequence, the reactor performance. The interaction between particles and thus powders flowability has also been related to static parameters such as the angle of repose, angle of friction, as well as to dynamic parameters such as the efflux time. However, Clift [5] reported that many of these parameters are only understood at a phenomenological-empirical level and their direct application to the description or characterization of fluidisation often proves difficult. Moreover, Lettieri [6] stated that, when studying fluidisation behaviour from ambient to high temperature, overlooking possible modifications induced by temperature in the structure of the fluidised bed, and therefore in the degree of interaction of the bed material, is likely to lead to a misleading prediction of the fluid-bed performance and thus to errors in evaluating heat and mass transfer phenomena.

Whether agglomeration of solid matter is the catastrophic result of certain industrial processes, therefore something to avoid, or the ultimate target of some other size enlargement operations, consequently something to control, it is of fundamental importance to achieve

a better knowledge of the microscopic adhesion/cohesion mechanisms between solid-solid and solid-liquid interactions. The main aim of this chapter is to provide a review of the current understandings on particle-particle interactions in the presence of material bridges and to deliver a sound foundation for the comprehension of the parameters responsible for the changes in both the process conditions (i.e. fluidisation behaviour between ambient and high temperatures) and final product formulation.

2.1 High Temperature Interparticle Forces

High temperature adhesive forces arise from the formation of material bridges, usually through the particle surfaces changing phase through either chemical reaction or simply melting. Thin layers of sticky material may also develop because of the presence of reactive liquids within the bulk material. The mechanical and physic-chemical properties of both the liquids and solids, together with the liquid-solid or solid-solid interaction mechanisms, play a substantial role in the rheology of the mixture and, consequently, represent one controlling factor in the growth of agglomerates. Moreover, during operation, agglomerates may form through a combination of different binding mechanisms, which, in turn, distinguish the ultimate physical and mechanical properties of the material.

The binding mechanisms of size enlargement by agglomeration were first defined by Rumpf [7]. In Table 2.3 they are grouped according to their dependence on temperature.

I	Solid bridges	a)	Mineral bridges, sinter bridges
		b)	Chemical reaction
		c)	Partial melting
		d)	Hardening binders
		e)	(i) Crystallization of dissolved substances (ii) Deposition of suspended colloidal particles
II	Interfacial forces and capillary pressure at freely movable liquid surface		Liquid bridges

Tab. 2.3: Binding mechanisms of size enlargement by agglomeration. After [7].

Solid bonds or *material bridges* occur during the production of ceramic parts from sintered powders, the manufacture of tools from powdered metals and the production of tablets in the pharmaceutical industry. They usually form by diffusion and mechanical deformation and develop under the influence of high temperature and/or pressure. In fact, in the case of *sinter bridges*, if the temperature in a disperse system rises above approximately two-thirds of the melting temperature of the material, then diffusion of molecules from one particle to another sets in at the points of contact [1]. The initial sintering temperature is strongly dependent on particle size, whilst the sintering kinetics are determined by the lowering of the free surface energy and the viscous dissipation energy. The fact that this dependence is based on chemical composition (not only of the particles, but the sur-

rounding gases as well) and geometry makes full physical modelling of sintering processes extremely difficult. Hence, most approaches to date have been semi-empirical in nature. However, sintering is an unwanted agglomeration mechanism in fluidisation, which has been studied by a relatively large body of literature [8, 9, 10] and is reviewed in Section 2.3. Theoretical and experimental approaches to defluidisation caused by sintering are reported in **Chapter 4**

The next three mechanisms, as described hereafter, normally represent somewhat of an unwanted type of interaction which causes agglomeration. Here the solid bond starts out as a liquid bridge which subsequently solidifies, tends to harden or reacts chemically with the solid. For *chemical reactions* or *hardening binders*, the formation of solid bridges depends on both the process conditions and the participating materials, their chemical reactivity (often depending on the presence of moisture) and their capability to harden. In addition, during casual contact between particles, the superficial roughness peaks of the solids may melt due to heat caused by friction and/or pressure. In such cases, the precursor of the solid bond may be a local/*partial melt* which cools and may be the cause of caking, as can often happen for substances with low melting points during storage.
The major task, required to investigate such type of interactions, is to develop suitable instruments and experimental techniques which permit to measure increasingly high bonding forces enhanced by chemical reaction (or hardening); furthermore, to provide, through specific diagrams, trend lines which relate the measured interparticle force to some process parameters, such as temperature, initial liquid volume or particle size. Such information would be extremely useful to industrial applications. In this dissertation, a novel micromechanistic approach has been applied to an industrial case study, where the measurement of the rupture force of a solid bond between pairs of particles was obtained after inducing the chemical decomposition at different temperatures of an initially formed liquid bridge of magnesium nitrate hexahydrate.

The last subgroup encompasses the class of solid bridges generated by drying of an initial liquid bond formed between particles. In the first case, *crystallization* of dissolved substances is caused by evaporation of the solvent: the (tensile) strength of the crystal bridges depends not only on the amount of the crystallizing material but also on the velocity of crystallization and increases with the drying temperature, as shown, for example, in figure 2.1. Although little literature is available on the study of this mechanism (see Section 3.2.1), crystallization has been shown to affect the quality of high temperature fluidisation tests carried out on a particular catalyst material termed E-cat [6]: **Chapter 6** illustrates how, by the means of dedicated diagrams, it was possible to qualitatively relate the drying rate to fluidisation behaviour by taking into account the particle-particle interactions.

Similarly, but exhibiting lower strength, solid bridges formed of *colloidal particles* are gen-

erated by evaporation of the liquid. The suspension of colloidal solids concentrate in the diminishing liquid bridge and the subsequent compaction is caused by the pressure exerted by the surface tension. After complete evaporation the binding forces in the remaining solid bridge are mostly caused by molecular forces which may be enhanced by electrostatic and magnetic effects.

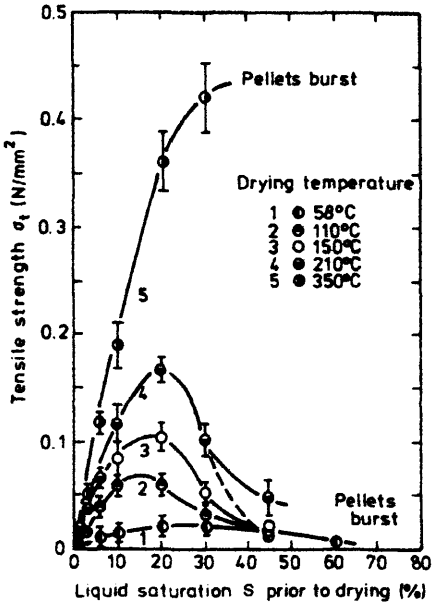

Fig. 2.1: In this example, the tensile strength of the core of agglomerates with salt bridges is plotted versus liquid saturation at various drying temperatures. After [2].

Despite the fact that the mechanism of adhesion of particles through *liquid bridging* is not temperature enhanced (except for the variation of the physical properties of the liquid and solid), the reason for which it was included in Table 2.3 and reviewed further in Section 2.2 is twofold:

1. The intentional addition of a certain amount of liquid binder, at any operative temperature, to an agitated set of particles can cause those particles to agglomerate. This type of process, known as wet or binder induced agglomeration, is of considerable technological importance, therefore a lot of interest has been dedicated to the study of the properties of pendular liquid bridges since they are often the precondition for the formation of solid bridges. For instance, pharmaceutical powders frequently exhibit poor flow and compaction behaviour making granulation necessary prior to tabletting. A granulation technique is selected to produce porous, free-flowing material that compacts at low pressures to form non-friable tablets. Although it is possible to produce binderless granules, it is usually desirable to incorporate a binding agent in the formulation to enhance granule and tablet strength. This binder is often added as a liquid, forming liquid bridges between particles that

then go on to dry to form solid bridges.

2. Achieving the required product characteristics requires process control. In fact, another important aspect, covered by experimental research in the last twenty years, is the investigation of the key role played by the interparticle forces on fluidisation behaviour. In these studies, described more in detail in **Chapter 4**, in order to determine the flow behaviour of gas fluidised beds at high temperatures, particle-particle interactions are simulated by simply adding small amounts of liquid binder of known physical properties, thus shifting the quality of fluidisation down to complete defluidisation. By observing the relevant changes of some operative variables (pressure drop across the bed, height of the bed etc), several models have been produced whose predictions are either based on the equilibrium of the forces generated within the bed or the dissipation of energy upon collision of solids and which take into account the magnitude of the enhanced interparticle forces by comparison with the hydrodynamic forces.

An extensive review of attempts to simulate high temperature interactions through the addition of liquids to the particle system being studied at room temperature, had been reviewed by Wright and Raper [11] . In fact, there are processes that require the continuous injection of liquid in a bubbling fluidised bed system. The material fed into the apparatus can be a liquid at ambient conditions or can fast become liquid at the operating temperature of the process, due to the high heat transfer rate of the fluidised system. This is, for instance, the case for various thermal processes for energy and material recovery. Agglomeration phenomena as a consequence of interactions between distinct phases have been observed in some of these processes: they rarely are a deliberate design choice and, more often, are an unplanned event that can prejudice the reactor performance and the possibility of having effective long-term stable operation.

2.2 Adhesive forces arising from liquid bridges

The study of the adhesiveness exerted by a pendular liquid bridge between particles is of fundamental importance:

- as mentioned in Section 2.1, the presence of solid-liquid (and liquid-wall) interactions during fluidisation processes can affect both process and formulation factors. At high temperatures, the presence of low melting materials, heterogeneous chemical reactions or simply the degree of humidity within the bed are all possible causes of particle adhesion through liquid bridging, which, at least if not controlled, may be the source of loss of performance of the reactor. Investigations of the underlying mechanisms of high temperature defluidisation, (see for instance McLaughlin and

Rhodes [12]), have used a model fluidised bed operating at ambient temperature; this system simplifies the problem by isolating the effects of free surface liquids and eliminates some of the complicating variables as the quantities and properties of the added liquid are known and fixed for each experiment.

- Product and formulation factors, such as the wettability of the material or binder type, can greatly influence the size enlargement process. For instance, due to the absence of strong shear forces in the fluid bed, the effect of the product properties such as wettability is expected to be larger than in a high-shear granulation device [13].

- The energy required to deform or break agglomerates is an important parameter to be correlated when investigating process control procedures. Models intended to evaluate the energy required to deform agglomerates have attempted to scale up the single particle interactions to macroscopic behaviour [14].

In the light of these considerations, liquid bridges become more interesting than non-material bridges from a practical point of view, since their magnitude (see figure 2.2 for comparison) can be adjusted by altering the amount of free liquid and its properties, such as surface tension and viscosity.

The investigation of the interparticle forces enhanced by non-material bonds in a gaseous medium, such as van der Waals, elctrostatic and magnetic forces has been covered by a large amount of literature; however, this thesis concerns the study of interaction in the presence of material bridges and, therefore, a complete review of such forces has been considered beyond the scope of this work. Nevertheless, a brief description of these types of adhesion mechanisms and the relevant changes induced on fluidisation behaviour is given in **Chapter 4**.

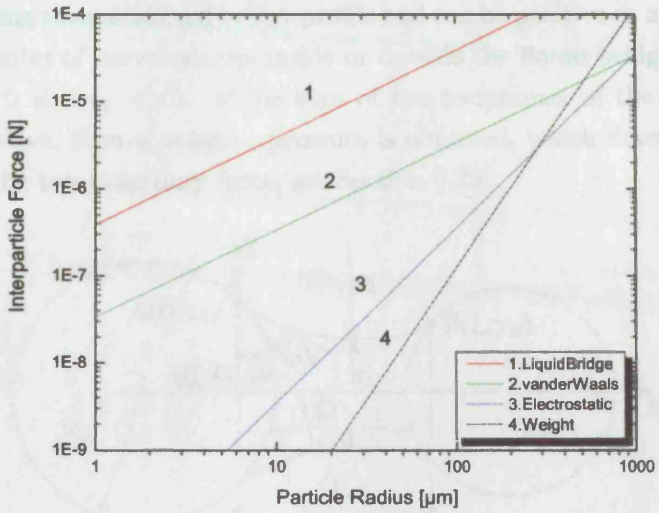

Fig. 2.2: Magnitude of theoretical interparticle forces for single-point contact between two equal smooth spheres suspended in air. Here the particle weight is plotted for comparison.

1. Liquid bridge: $F = \frac{2\pi R\gamma_L}{1+\tan\beta/2}$ [15]; $\gamma_L = 72.7\ mN/m$, half filling angle $\beta = 20°$

2. van der Waals: $F = \frac{RA_H}{12a^2}$ [16]; $A_H = 6.5\ 10^{-20}\ J$, interparticle distance $a = 4$ Å

3. Electrostatic: $F = \frac{\pi\sigma_1\sigma_2R^2}{\epsilon\epsilon_0(1+a/2R)}$ [17]; $\sigma_{1,2} = 10\ \mu C/m^2$, $\epsilon_0 = 8.9\ 10^{-12}\ C^2/Nm^2$, $\epsilon = 1$ $a = 4$ Å

4. Weight: $F = \frac{4\pi R^3\rho_p g}{3}$; particle density $\rho_p = 3000\ kg/m^3$, $g = 9.81\ m/s^2$

2.2.1 Liquid bridge configuration: the Young-Laplace equation

A schematic of a liquid bridge is shown in figure 2.3 between two spherical particles. The pressure in the liquid bridge can be obtained from the Young-Laplace relationship in Equation 2.1, which relates ΔP_{br}, the pressure difference between the liquid and the atmosphere to the curvature of the liquid-vapour interface [18, 19] provided that the volume of liquid remains constant:

$$\Delta P_{br} = \gamma_{lv}\left(\frac{1}{r_1} + \frac{1}{r_2}\right) \tag{2.1}$$

where γ_{lv} is the surface tension at the vapour-liquid interface. The radii of curvature r_1 and r_2 can be either positive or negative depending on the geometry of the bridge: conventionally, r_1 is evaluated in a direction orthogonal to the meridional profile such that its center of curvature is located along the surface normal to the bridge axis of symmetry.

Hence, the center of curvature of r_1 is always within the bridge. r_2 is evaluated in a direction containing the meridional bridge profile and can be positive or negative depending on whether its center of curvature lies inside or outside the liquid bridge, respectively (in figure 2.3, $r_1 > 0$ and $r_2 < 0$). If the sum of the reciprocals of the principal radii of curvature is negative, then a negative pressure is obtained, which develops an attractive contribution to the total capillary force, see Section 2.2.6.

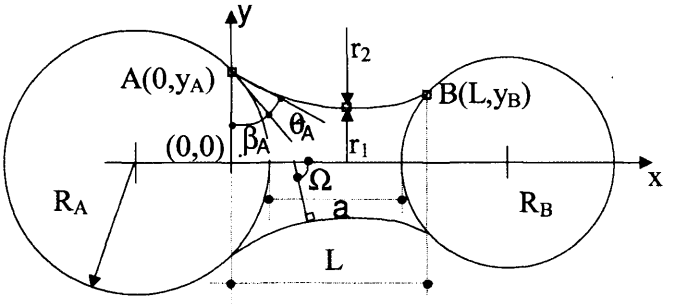

Fig. 2.3: Geometric parameters describing a liquid bridge.

When the Bond number $gL^2\Delta\rho/\gamma_{lv}$ (where g is the gravity acceleration, L some characteristic length of the bridge, $\Delta\rho$ the difference of densities between the two fluids) is sufficiently small, the effect of gravity is negligible and the mean curvature is nearly uniform; this condition is usually satisfied for the case of small particles and small liquid volumes ($\frac{gL^2\Delta\rho}{\Delta PR} \prec\prec 1$)[20].

In a Cartesian reference, Equation 2.1 can be rewritten in terms of the analytical expressions of the radii of curvature r_1 and r_2, obtaining Equation 2.2 [21]:

$$\frac{\Delta P}{\gamma_{lv}} = \frac{1}{y\sqrt{1+\dot{y}^2}} - \frac{\ddot{y}}{\sqrt{(1+\dot{y}^2)^3}} \tag{2.2}$$

In Equation 2.2, x and y are the axial and radial co-ordinates, respectively, of the liquid-vapor profile and $\dot{y}$ and $\ddot{y}$ are the first and second derivatives of y with respect to x. This equation states that the liquid bridge surface must have a constant curvature at all points. Its numerical solution is quite complex and, hence, approximations of the bridge profile are often used. The most common is the toroidal approximation. Recently, Pepin et al. [22] have developed a parabolic approximation which is much easier to use and provides predictions of bridge profile, rupture distances and post-rupture liquid distributions with reasonable accuracy.

2.2.2 The Toroidal Approximation

A schematic of the toroidal approximation for a concave geometry is shown in figure 2.4. Two unequally sized spheres of radius R_A and R_B, are separated by a distance H. The

liquid bridge has a constant radius of curvature of r_1 in the plane of the page and has a radius of r_2 perpendicular to the page at its narrowest point. The x-axis is the axis of symmetry and the origin is taken as the point where the bridge is at its narrowest. The liquid bridge contacts each sphere at a filling angle of ψ_A and ψ_B respectively, and has an apparent contact angle of θ_A and θ_B on each sphere.

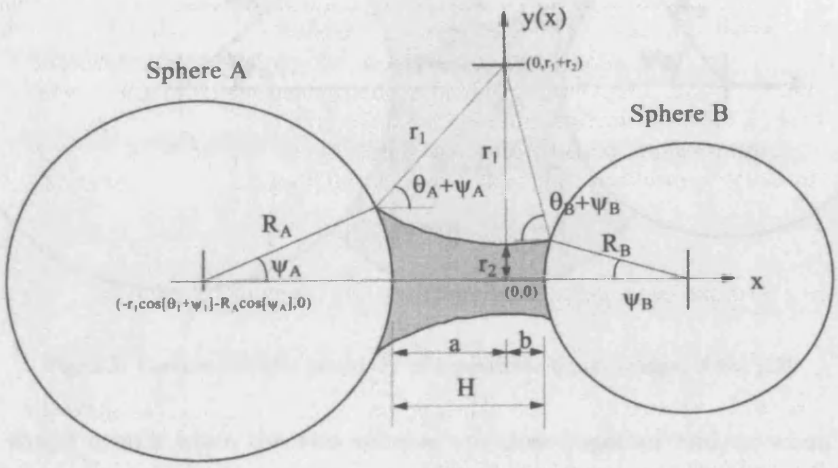

Fig. 2.4: Concave toroidal geometry of a pendular liquid bridge. After [22].

Equating the vertical (y) components of the bridge geometry gives Equations 2.3 and 2.4:

$$R_A \sin\psi_A + r_1 \sin(\psi_A + \theta_A) = r_1 + r_2 \quad (2.3)$$

$$R_B \sin\psi_B + r_1 \sin(\psi_B + \theta_B) = r_1 + r_2 \quad (2.4)$$

Likewise, equating the horizontal (x) components gives Equation 2.5:

$$H = a + b = R_A(\cos\psi_A - 1) + r_1 \cos(\psi_A + \theta_A) + R_B(\cos\psi_B - 1) + r_1 \cos(\psi_B + \theta_B) \quad (2.5)$$

where H is the interparticle distance. The equation for the upper toroidal bridge profile is given by 2.6 for a concave bridge which occurs when $(\psi_A + \psi_B + \theta_A + \theta_B) < 2\pi$, and by 2.7 for a convex bridge which occurs when $(\psi_A + \psi_B + \theta_A + \theta_B) > 2\pi$.[†]

$$y = r_2 + r_1 - \sqrt{r_1^2 - x^2} \quad (2.6)$$

$$y = r_2 - r_1 - \sqrt{r_1^2 - x^2} \quad (2.7)$$

[†] It is also possible to have a conically shaped bridge (when $\psi_A + \psi_B + \theta_A + \theta_B = 2\pi$) or a cylindrical bridge (when $\psi_A + \theta_A = \psi_B + \theta_B = \pi$).

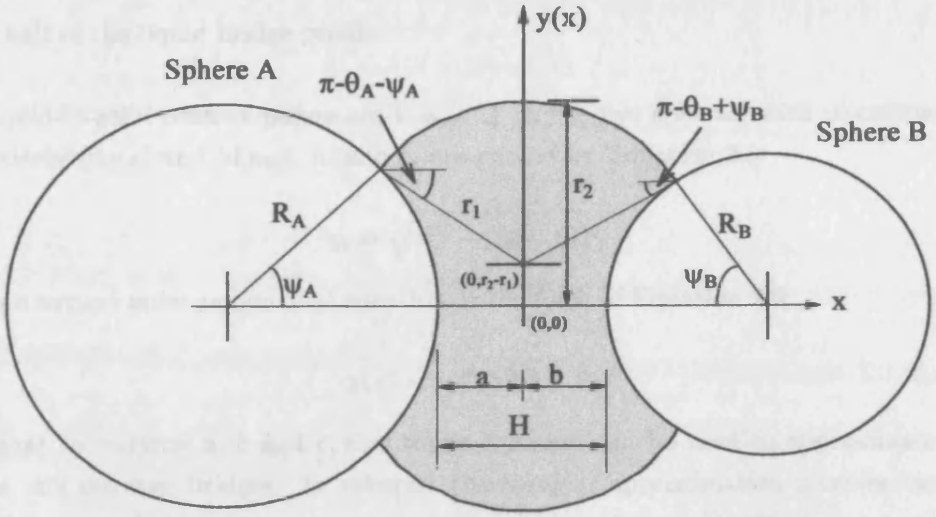

Fig. 2.5: Convex toroidal geometry of a pendular liquid bridge. After [22].

A convex shape occurs when the two spheres are close together and/or when there is a relatively large volume of liquid. A schematic of the toroidal approximation with a convex geometry is given in figure 2.5.

2.2.3 The Parabolic Approximation

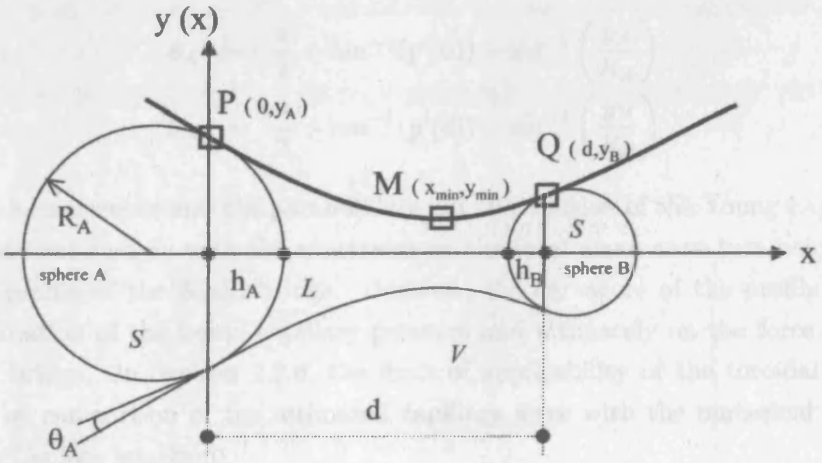

Fig. 2.6: Parabolic bridge profile approximation. After [22].

Figure 2.6 is a schematic of the parabolic bridge profile approximation. The solid-liquid interface is a spherical cap, which has a maximum height of h_i, d is the length of the liquid bridge and y_{min} is the minimum liquid neck radius of the pendular bridge. The x-axis is defined as the symmetry axis of the system and y(x) is a Cartesian function outlining the

upper half of the liquid bridge profile.

The liquid-to-solid contact points are P and Q on the two spheres, with co-ordinates of respectively (0,y_A) and (d,y_B). h_i and y_i are related by Equation 2.8:

$$y_i = \sqrt{R_i^2 - (R_i - h_i)^2} \tag{2.8}$$

y(x) is a second order polynomial equation in the form of Equation 2.9:

$$y(x) = ax^2 + bx + c \tag{2.9}$$

Note that by varying a, b and c, this single equation can be used to approximate both convex and concave bridges. In contrast the toroidal approximation involves two sets of equations, and there is also no smooth transition between the two since $r_1 \rightarrow \infty$ as the bridge approaches a conical or cylindrical shape. Hence the parabolic profile is more robust and easier to use. It should also be noted that both profile approximations are three-parameters curves. The toroidal profile is defined by r_1, r_2 and H and the parabolic profile is defined by the three parameters a, b and c.

The apparent solid-liquid contact angles can be calculated from the other parameters by Equations 2.10 and 2.11:

$$\theta_A = \frac{\pi}{2} + \tan^{-1}(y'(0)) - \sin^{-1}\left(\frac{y_A}{R_A}\right) \tag{2.10}$$

$$\theta_B = \frac{\pi}{2} + \tan^{-1}(y'(d)) - \sin^{-1}\left(\frac{y_B}{R_B}\right) \tag{2.11}$$

Since the circumference and the parabola are not the solution of the Young Laplace equation they do not comply with the constraint on the total mean curvature being constant along the profile of the liquid bridge. However, the curvature of the profile has a role in the evaluation of the liquid capillary pressure and ultimately on the force exerted by the liquid bridge. In Section 2.2.6, the limit of applicability of the toroidal method is discussed by comparison of the estimated capillary force with the numerical solution of the Young-Laplace equation.

2.2.4 The role of the liquid volume in particle adhesion

If a liquid is sprayed on a solid, different mechanisms of adhesion in the liquid-solid system can be distinguished [23], as illustrated in figure 2.7:

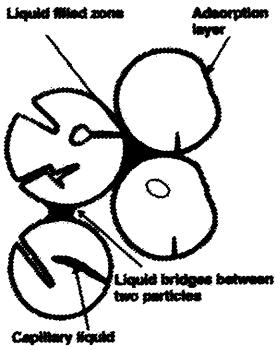

Fig. 2.7: Possible binding mechanisms in a liquid-solid system: *adsorption layers* on the surface of particles;*capillary* liquid inside the porous system of a particle;*liquid bridges* between two particles or *liquid* which fills zones between solid particles, after [23].

Clearly, the amount of liquid that is present in the pore volume of the agglomerate influences its structure and ultimately the tensile strength, σ_t, to a great degree, as indicated by Rumpf [24] in the following equation:

$$\sigma_t = \frac{1-\varepsilon}{\varepsilon^2}\frac{F}{d_p^2} \tag{2.12}$$

where the value for the tensile strength of the bulk can be determined, provided that expressions for the porosity ε and F, the interparticle bonding force, are known functions of the particle diameter d_p and both the liquid content and physical properties.
Porosity ε, the specific void volume between the particles forming an agglomerate, plays an important role in agglomerate hardness. Figure 2.8 shows the general relationship between ε and a certain liquid content M, defined as the weight percentage of liquid added to solid [25]:

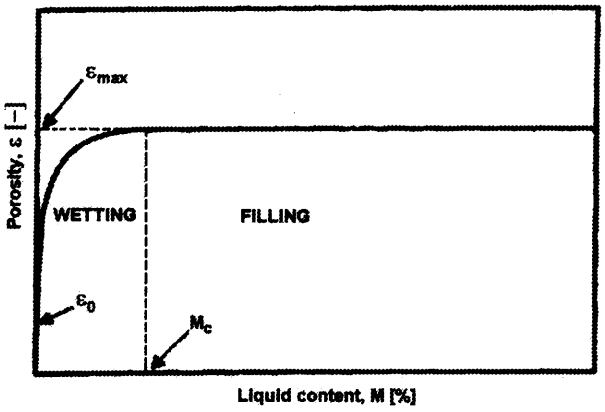

Fig. 2.8: General relationship between dry based porosity ε and liquid content M, after [25].

As argued by Feng and Yu [25], interparticle forces play a dominant role in governing the $\varepsilon - M$ relationship. The *wetting* region, shown in figure 2.8, represents the enhancement

of a capillary force when adding liquid to a set of packing particles: the relative motion between solids is hampered by the formation of liquid bridges and hence returns a higher porosity of the bulk with respect to the initial value ε_0. By increasing the amount of liquid within the system, the porosity increases until a certain value, ε_{max}, which remains relatively constant during further addition of liquid. Thus, the so-called *filling* region corresponds to an almost constant porosity, which suggests a sort of non-dependence from the capillary force after a critical liquid volume (M_c). However, recent works by Iveson et al. [26, 27] have reported that porosity does not remain constant, by taking into account the enhanced dissipative mechanisms due to viscosity of the binder and of the friction caused by the non-homogeneity of particle shape and size.

Although it is not so straightforward to quantify the relationship between porosity and interparticle force, Rumpf [24] and Schubert [28] computed through Equation 2.13 the static tensile strength of a wet agglomerate, σ_{tw}, by substituting the force term F in Equation 2.12 with the product between the surface tension of the liquid γ_l and F^*, which is a complicated function of many variables:

$$\sigma_{tw} = \frac{(1-\varepsilon)\gamma_l}{\varepsilon d_p} F^* \left(\varepsilon, S, \delta, \frac{f_1}{d_p}\right) \tag{2.13}$$

In this expression, which was derived for a bulk of homogeneously distributed monosized particles whose geometry does not necessarily have to be spherical, the authors introduced the liquid saturation S as a measurable variable.

If the liquid is distributed homogeneously at all contacts in the bulk and wets perfectly the particles, then S represents the ratio of liquid volume to void volume (liquid and gas) within the system and is defined as:

$$S = \pi \frac{1-\epsilon}{\epsilon} \varphi \tag{2.14}$$

where $\varphi = \dfrac{V_b}{2V_p} = \dfrac{V_b}{2\frac{\pi}{6}d_p^3}$ is the dimensionless liquid bridge volume which forms between particles.

According to different levels of saturation, several stages of agglomeration can be identified [28], as shown in figure 2.9.

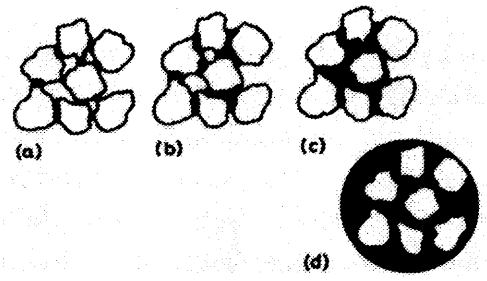

Fig. 2.9: States of a bulk as a function of the amount of added liquid: a)pendular state ($S \prec 0.3$), b)funicular state ($0.3 \prec S \prec 0.9$), c)capillary state ($S \succ 0.9$), d)droplet, after [2].

In the *pendular* state (fig.2.9(a)), only minor amounts of liquid are present, and the particles are held together by liquid bridges present only at the contact points of individual primary particles. In the *funicular* state (fig.2.9(b)), the amount of liquid is increased, so that some of the liquid bridges can coalescence and form links between more than two primary particles. The voids between the liquid bridges are partly saturated with liquid, whereas, in the *capillary* state (fig.2.9(c)), the voids are fully saturated with liquid: concave menisci develop at the surface of the agglomerate while the liquid is drawn back into the pores under capillary action, and inside the granules, the particles are completely surrounded with liquid. If more liquid is added,the granule will be converted into a system with particles suspended into the liquid. This is the so-called *droplet* state (fig.2.9(d)).

The characteristic relationship between the liquid saturation and the tensile strength of granules, as investigated by Schubert [29], is shown schematically in figure 2.10:

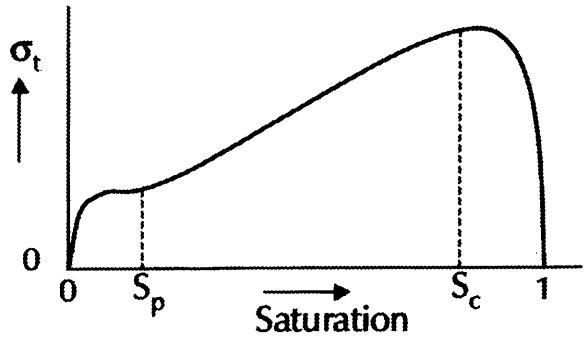

Fig. 2.10: Relationship between tensile strength of wet granules and the saturation, after . S_p denotes the end of the pendular state, and S_c the end of the capillary state. After [29].

Besides the properties of the starting material (solid and liquid), the tensile strength of a granule depends on the porosity and the liquid saturation, which ultimately depend on the amount of liquid added to the system. In order to investigate such dependence, many authors have proposed theoretical expressions for the calculation of the liquid volume, which are reviewed and discussed in the next section.

2.2.4.1 Liquid volume calculation

In order to predict the energy required to break a liquid bond through the determination of its rupture force/distance, it is essential to establish a relationship between some important parameters (such as the half-filling angle and separation distance) and liquid volume [30]. Moreover, numerical simulations of particulate flow in the presence of liquid bridges [31] or the packing behaviour of wet particles require quantification of the interparticle forces and the porosity of the bulk through the calculation of each volume of liquid formed between particles [32, 33]. In the literature, for each case studied, the computation of liquid bridge volume was provided through different expressions on the basis of geometric simplification: these are summarised in Tab.2.4. All the equations are presented in terms of the same parameters, as indicated in figure 2.11, and numerically adjusted in respect to the case of complete wetting ($\delta = 0$): such an assumption is proposed here in order to provide some direct comparison by considering the simplest possible case. Furthermore, Weigert and Ripperger [34] observed that, under this condition, different expressions for the calculation of the two radii of curvature r_1 and r_2 yield the same result.

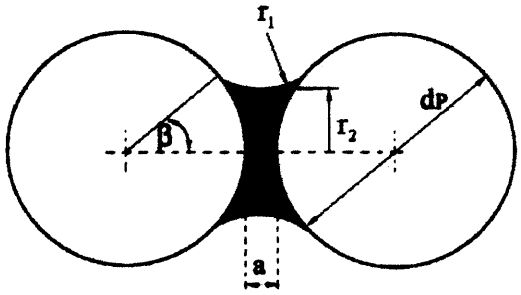

Fig. 2.11: Parameters employed for the calculation of a pendular liquid bridge volume between two mono-sized spheres: $r_{i=1,2}$ radius of curvature, β half-filling angle, a separation distance, d_p particle diameter, after [34].

By plotting values for the dimensionless liquid bridge volume φ, computed from the equations listed in Table 2.4, it is possible to ascertain the degree of approximation for each expression as a function of the half filling angle β and the dimensionless separation distance a/d_p, as illustrated in figures 2.12 and 2.13. A simple Fortran code was written in order to solve the Young-Laplace equation and, by following the computational approach described by Lian et al. [18], the correct evaluation of the liquid bridge volume was achieved. The exact numerical solution, calculated at pre-fixed half-filling angles (i.e. 5, 10, 15 and so on up to 50°), was obtained by an iterative method and results for the liquid bridge volume were reported in figures 2.12 and 2.13 for comparison with the suggested approximations (see also Table A.1 in Appendix A for a complete list of results).

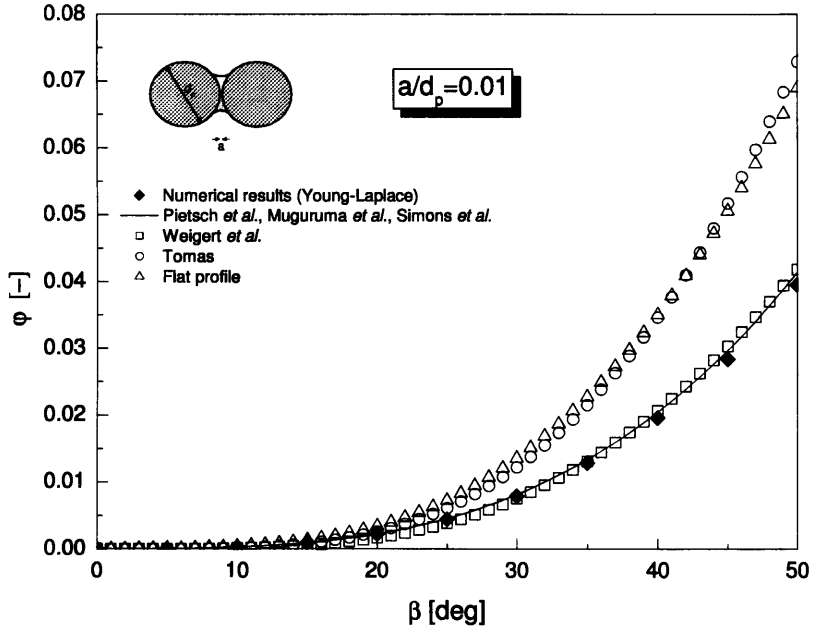

Fig. 2.12: Dimensionless bridge volume φ versus half-filling angle β for $a/d_p = 0.01$.

Values of φ were considered for β ranging between 0 and 50 degrees, which is usually taken as the limit value for the pendular stage before coalescence of the liquid bridges takes place [35]. Figure 2.12 shows good agreement for all the equations at small amounts of liquid ($\beta \prec 20°$). However, a further increase in β leads to φ being over-predicted by Equations 2.19 and 2.20: in fact, the wetted radius $\frac{d_p}{2}\sin\beta$ is comparable with the particle radius $\frac{d_p}{2}$ and the curvature of the profile cannot be considered negligible anymore.
On the other hand, Equations 2.15, 2.16 and 2.17 show the same results over the whole range of volumes, thus indicating the good consistency of the toroidal approach[2]: it should also be noted that no over-prediction or scattering of values is observed for the equation provided by Simons et al., as erroneously pointed out by Weigert and Ripperger [34]. The empirical expression proposed by Weigert and Ripperger is in good accordance with the results obtained from the numerical solution of the Young-Laplace equation and, on a practical point of view, becomes much easier to handle whether extrapolation of β or S are required. Its validity is confirmed for non-zero separation distances, as can be deduced from figures 2.12 and 2.13 ($\beta \prec 40°$).

[2] The toroidal (circular) approximation has been largely employed alternatively to the numerical solution of the Young-Laplace equation, as a simpler method for the estimation of the critical rupture distance and the strength of a pendular liquid bridge, see Sections 2.2.5 and 2.2.6, once the liquid volume is known. Moreover, it has been demonstrated that the use of the circular geometry for the calculation of the liquid volume, under the condition of null interparticle distance, involves errors of the order of only 1% [36].

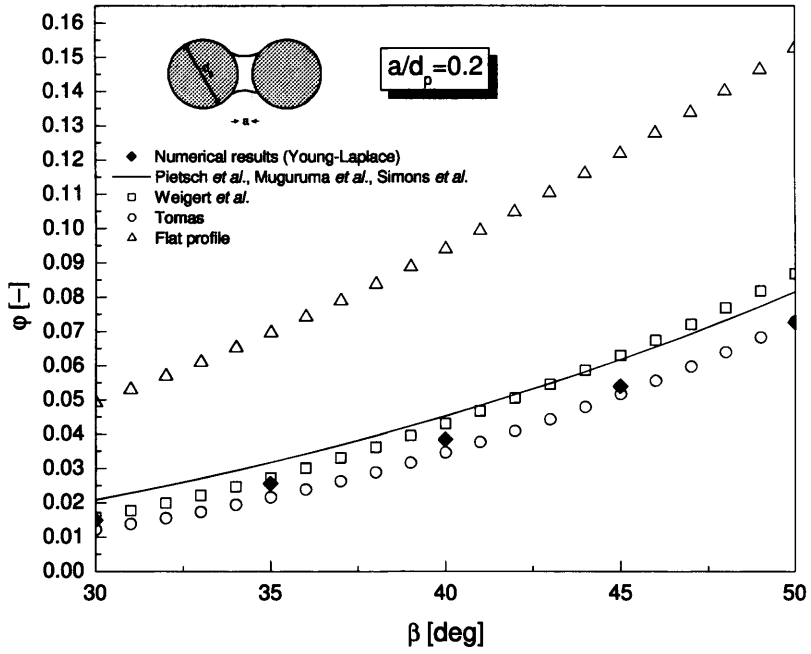

Fig. 2.13: Dimensionless bridge volume φ versus half-filling angle β for $a/d_p = 0.2$.

As the separation distance is increased by one order of magnitude, the approximation provided by the toroidal approach (i.e. Equations 2.15, 2.16 and 2.17) over-predicts the numerical results with a scatter as high as 40%; in the limit of the pendular state (i.e. $30° \prec \beta \prec 50°$), Equation 2.19 provides the better approximation at high interparticle distances, whereas, by observing the trend of data computed from Equation 2.20, one conclusion is its overprediction of the liquid volume at all separation distances.

REFERENCE	EQUATION	PARAMETERS
1] Pietsch et al. [37]	$\begin{aligned}\frac{V_b}{2\pi} &= \left(r_1^2+b^2\right) r_1 \cos\beta - \frac{r_1^3\cos^3\beta}{3} + \\ &- -b\left[r_1^2\cos\beta\sin\beta + r_1^2\left(\frac{\pi}{2}-\beta\right)\right] + \\ &- \frac{1}{24}d_p^3\left(2+\cos\beta\right)\left(1-\cos\beta\right)^2 \end{aligned}$ (2.15)	$\begin{aligned} r_1 &= \frac{d_p\left(1-\cos\beta\right)+a}{2\cos\beta} \\ r_2 &= \frac{d_p}{2}\sin\beta + \\ &+ r_1\left(\sin\beta-1\right) \\ b &= r_1+r_2 \end{aligned}$
2] Muguruma et al. [31]	$V_b = \frac{3}{2}\left\{r_1^{*2}\left[\left(1+\frac{a}{d_p}\right)-\left(r_1^*+r_2^*\right)\left(\frac{\pi}{2}-\beta\right)\right]-\frac{\left(\frac{a}{d_p}\right)^2\left(\frac{a}{d_p}+3\right)}{3}\right\}V_p$ (2.16)	$r_i^* = \frac{r_i}{d_p/2}\ ;i=1,2$
3] Simons et al. [30]	$\begin{aligned}\frac{V_b}{2\pi} &= \left[\frac{a}{2}+\frac{d_p}{2}\left(1-\cos\beta\right)\right]\left\{\frac{d_p}{2}\sin\beta+\left[\frac{a}{2}+\frac{d_p}{2}\left(1-\cos\beta\right)\right]\tan\beta\right\}^2 + \\ &- \left[\frac{a}{2}+\frac{d_p}{2}\left(1-\cos\beta\right)\right]^2\left\{\frac{d_p}{2}\sin\beta+\left[\frac{a}{2}+\frac{d_p}{2}\left(1-\cos\beta\right)\right]\tan\beta\right\}\tan\beta + \\ &- \left\{\frac{d_p}{2}\sin\beta+\left[\frac{a}{2}+\frac{d_p}{2}\left(1-\cos\beta\right)\right]\tan\beta\right\}\left[\frac{a+d_p\left(1-\cos\beta\right)}{2\cos\beta}\right]^2\left(\frac{\pi}{2}-\beta\right) + \\ &+ \left[\frac{a}{2}+\frac{d_p}{2}\left(1-\cos\beta\right)\right]\left[\frac{a+d_p\left(1-\cos\beta\right)}{2\cos\beta}\right]^2 + \\ &- \frac{1}{3}\left[\frac{a}{2}+\frac{d_p}{2}\left(1-cos\beta\right)\right]^3 - \frac{d_p}{2}\left[\frac{d_p}{2}\left(1-\cos\beta\right)\right]^2 + \\ &+ \frac{1}{3}\left[\frac{d_p}{2}\left(1-\cos\beta\right)\right]^3 \end{aligned}$ (2.17)	

4] Weigert et al. [34]	$V_b = 0.12 d_p^3 C_a \sin^4 \beta$	(2.18)	$C_a = \left(1 + 6\frac{a}{d_p}\right)$
5] Tomas [38]	$V_b = \frac{\pi}{4} d_p^3 (1 - \cos\beta) \sin^2\beta - \frac{\pi}{12} d_p^3 (1 - \cos\beta)^2 (2 + \cos\beta)$	(2.19)	
6] Flat profile [39]	$V_b = \int_0^{\frac{d_p}{2}\sin\beta} 2\pi r H(r)\, dr = \frac{\pi d_p}{4}\left[H^2\left(\frac{d_p}{2}\sin\beta\right) - a^2\right]$	(2.20)	$H(r) = a + \frac{2r^2}{d_p}$

Tab. 2.4: Expressions available in literature for the calculation of V_b.

Equations 2.15, 2.16 and 2.17 were obtained taking the toroidal approximation, illustrated in Section 2.2.2, as geometric simplification for the liquid bridge profile.

Equation 2.18 is an empirical expression and its validity is limited to monospheres (where the bridge volume depends only on the particle diameter and the half filling angle). C_a is a correction function for the separation distance between the two particles.

Equation 2.19 represents the volume of the bridge V_b calculated as a cylinder reduced for the volume of the two spherical caps that are immersed in the liquid, at null particle distance.

Equation 2.20 was firstly proposed by Matthewson [40] in order to calculate the bridge volume of a liquid interface formed between a sphere and a flat surface. By posing the condition $1 \succ\succ \sin\beta \succ\succ \frac{a}{d_p}$ the edge effects of the profile may be ignored as well as the curvature of the meniscus, therefore the geometric shape is considered right-sided. $H(r)$ is defined as the distance between the surfaces corresponding to each wetted radius value $r = \frac{d_p}{2}\sin\beta$. Recently Pitois [39] assumed the volume between two spheres separated by a distance a as double the volume calculated by Matthewson and hence obtained the expression cited above.

2.2.5 Liquid bridge rupture and critical rupture distance

As introduced in Section 2.2.4 the agglomerate hardness, and thus its resistance to breakage forces during processing, is clearly linked to the inner porosity, which in turn depends on the amount and distribution of liquid bridges formed between particles. The close relationship between the separation distance of a liquid meniscus held between two particles and its volume has been investigated by many authors and particular attention has been paid to the study of the critical rupture distance: in fact, upon elongation, the profile of the meniscus changes according to Equation 2.2 until a critical bridge separation is attained, at which point the bridge becomes unstable and ruptures. Hence, the determination of the critical rupture distance is of fundamental importance in the evaluation of the properties of the bulk, such as porosity and size, as well as the resistance opposed by the agglomerate to breakage or deformation.

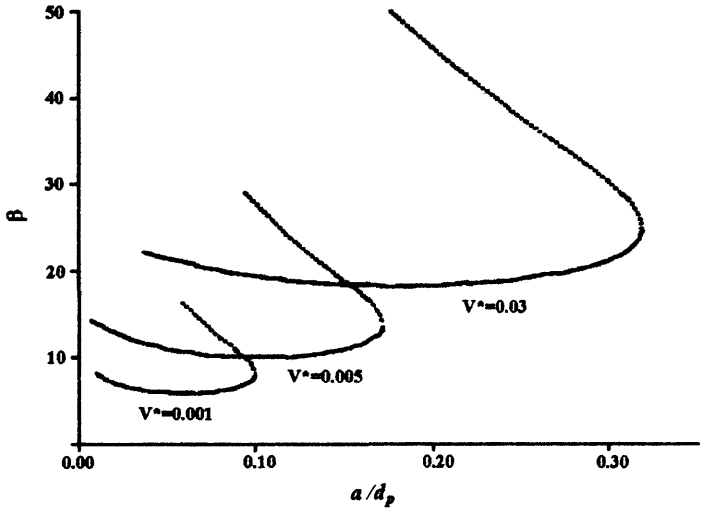

Fig. 2.14: Numerical solutions (— stable, ··· unstable) of Young-Laplace equation at different dimensionless separation distances $\frac{a}{d_p}$ versus half-filling angle β for various dimensionless liquid bridge volumes $V^* = \frac{V_b}{(d_p/2)^3}$, after [18]. All the indicated parameters are the same as illustrated in figure 2.11.

A rigorous approach permitted Lian et al. [18] to plot the numerical solution of the Young-Laplace equation as a function of the dimensionless liquid bridge volume[3]. The shape of static individual liquid bridges, and hence the determination of the critical rupture distances, can be solved from the Young-Laplace equation, which calculates the pressure difference across a curved liquid-vapour interface. The liquid bridge should have a constant curvature and the problem is solved through iterative calculations, assuming a constant volume condition for the bridge liquid, which means diminishing half-filling angle values

[3] In order to readily obtain a direct comparison between figures 2.12-2.13 and 2.14, one should apply the following conversion: $\varphi = \frac{3}{8\pi} V^*$.

as the separation distance between the particles increase. Figure 2.14 shows that rupture of the meniscus is obtained for critical separations which provide unstable solution. The authors concluded that the system is uniquely specified by knowledge of the liquid bridge volume, contact angle and separation distance and using, without distinction, one among the following criteria, which are the half-filling angle, the meniscus neck diameter, the mean curvature, the total force and total free energy of the system.
Furthermore, in order to establish a simple and practical relationship which links the critical rupture distance a_c^* to the dimensionless volume V^*, Lian et al. [18] extrapolated the expression reported below:

$$a_c^* = (1 + 0.5\delta)\sqrt[3]{V^*} \tag{2.21}$$

where δ is the contact angle in radians between the liquid and the solid. This relationship can be used with good approximation for relatively low contact angles ($\delta \prec 40°$).

However, the determination of the liquid meniscus shape through resolution of the Young-Laplace equation is still questionable, in particular with regard to the wetting hysteresis (see also Section 2.2.9.1) and the liquid volume delimited by the pendular liquid bridge. It was shown by Pepin et al.[22] that the rupture of liquid bridges would occur spontaneously at a certain interparticle distance. Two cases exist: one where the volume of liquid is fixed, that is when the three-phase contact line is observable on the particle surfaces during elongation, the second where there is no observable three-phase contact line and liquid covers the entire particle surfaces and the surrounding objects, creating liquid reservoirs outside the particles. Depending on the bridge elongation speed and viscosity of liquid binder, some liquid can move from the liquid reservoirs to the inter-particle gap and the liquid volume of the bridge can increase.

In the former case, the shape the bridge adopts depends on the wetting behaviour and the value of the three-phase contact angles [41].

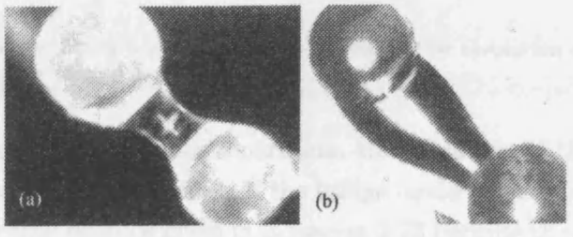

Fig. 2.15: Glycerol liquid bridges showing three-phase contact lines with glass spheres; (a) two non-silanised spheres (left, 126μm; right, 111μm), (b) left, unsilanised (118μm), right, silanised (125μm). After [22].

In figure 2.15, two examples are shown. In figure 2.15(a), the liquid does not de-wet the particle surfaces, the three-phase contact line is fixed. The shape then adjusts as the

contact angles change with separation (in order for the constant volume condition to be met). In figure 2.15(b), the liquid de-wets the silanised particle and the contact angle on this particle remains relatively constant during separation, whereas the contact angle on the unsilanised particle, which has a fixed three-phase contact line, does change. In the case where there is no observable three-phase contact line, the liquid perfectly wets the solid and the bridge shape remains toroidal throughout separation.

If the liquid bridge volume V_b is known, the variables a, b and c in Equation 2.9 are obtained from the resolution of Equation 2.22:

$$\begin{cases} y(0) = y_A \\ \pi \int_{x=0}^{x=d} y^2(x)\,dx = V_b + \sum_{i=A,B} \frac{\pi h_i}{6} \left(3y_i^2 + h_i^2\right) \\ y(d) = y_B \end{cases} \tag{2.22}$$

Equation 2.22 assumes that the pendular liquid bridges considered are axially symmetric bodies, the volumes of which can be obtained by revolution of $y(x)$ around the bridge symmetry axis, see figure 2.16.

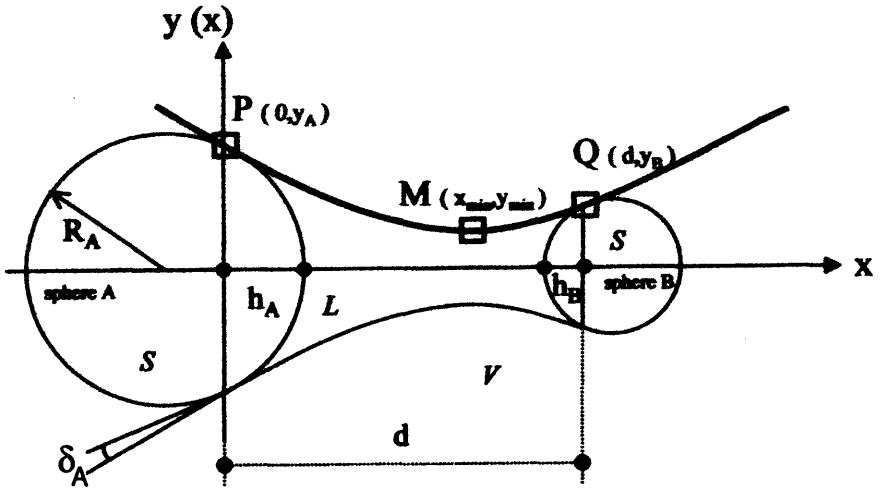

Fig. 2.16: Calculation of the liquid bridge volume V_b is obtained by revolution of $y(x)$, the curve PMQ, around the bridge symmetry axis. After [22].

If V_b, y_A and y_B are constant during separation, the evolution of the liquid bridge with interparticle distance is easily predicted. If the bridge liquid recedes from the solid particle i surface, a simple energy balance given in Equation 2.23 permits the calculation of y_i [42]:

$$2\pi\gamma_{LV}\left[R_i h_i\left(\cos\delta_r + 1\right) + \int_{x=0}^{x=d} y(x)\sqrt{1+\dot{y}^2(x)}dx\right] = \Psi \tag{2.23}$$

In Equation 2.23, Ψ is a constant which depends on the experimental conditions and can

be calculated from the knowledge of the initial liquid bridge shape. R_i is the particle i radius and δ_r is the receding contact angle of the bridge liquid on the particle i. Whether y_A and y_B are fixed or varying, apparent liquid-to-solid contact angles are calculated from Equation 2.10 and 2.11.

The separation distance where rupture occurs can be predicted using the parabolic approximation in Section 2.2.3, assuming that this occurs through the liquid's thinnest neck, y_{min}. For perfectly wetting liquids, liquid bridge volumes can be related to y_{min} by an empirical relationship [43]:

$$V_b \approx 1.673 y_{min}^3 \tag{2.24}$$

Models intended to describe the process of liquid bridge separation always assume the contact angle between the particle and the binder to be fixed and equal to zero throughout separation [21]. However, this assumption is reasonable only for perfectly wettable particles and therefore is not a general case. Predicting the behaviour of real cases is not an easy problem due to the difficulty of modelling the phenomena at the 3-phase contact line. In this regard, Pepin et al. [22] compared their experimental results with both the toroidal and parabolic approach by studying the postrupture liquid distribution on two spheres previously bonded by a liquid bridge.
The authors found that both the approximations are adequate, with the parabolic profile being slightly more accurate, but not greatly so. However, the fitting of the boundary conditions, obtained through the toroidal profile, returned, in certain cases, negative values of the contact angle; furthermore, the toroidal approximation was often more difficult to use because one of the radii of curvature goes to infinity as the bridge passes from convex to concave in shape, thus creating numerical difficulties in some cases [22]. Therefore, Pepin et al. concluded that, in situations where the evolution of the bridge shape needs to be modeled for predicting the normalized rupture distance and contact angles, the parabolic approximation is recommended.

2.2.6. Total force exerted by a pendular liquid bridge: Static capillary contribution

Fisher [15] was the first to recognize that the static capillary force, which is exerted by a pendular liquid bridge held between two spheres, can be split up into the contribution of three terms: the axial component of the surface tension force at the solid-liquid-gas interface, the force arising from the pressure deficit in the liquid bridge, which is calculated through the Young-Laplace equation, and the buoyancy force resulting from the partial immersion of each particle. However, Princen [44] demonstrated the latter to be negligible when considering particles smaller than 1 mm in diameter.

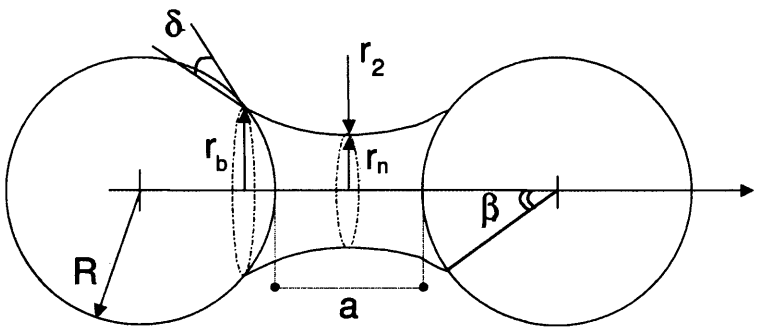

Fig. 2.17: Liquid bridge between two equal spheres.

As introduced in the previous sections, the study of the influence of certain parameters which better describe the pendular liquid-solid configuration (see figure 2.17 for details) has been extensively covered in literature since they affect the total capillary force to a great degree: in fact, it has been shown that the static force depends on the separation distance, the particle-to-particle and binder-to-particles volume ratios, the surface tension of the liquid and the contact angles that the liquid makes with the particles [17].
If gravitational distortion can be neglected (i.e. small amount of liquid), two different approaches have been commonly employed in the calculation of the static capillary force: the *first* method of evaluation, also named the "gorge" method, which was adopted by Fisher and more comprehensively investigated by Hotta [45], determines the resulting effect of the capillary force at the 'neck' of the liquid bridge, r_n:

$$F_n = 2\pi r_n \gamma_L - \pi r_n^2 \Delta P \tag{2.25}$$

where γ_L is the liquid surface tension.
In order to avoid the calculation of the exact geometric profile, which requires the resolution of Equation 2.1 through complex numerical procedures, Fisher used the toroidal approach (see Section 2.2.2), thus obtaining:

$$F_n = \frac{2\pi R \gamma_L}{1 + \tan\frac{\beta}{2}} \tag{2.26}$$

where R can be replaced by the geometric average radius in the case of two different spheres A,B: $\overline{R} = \dfrac{2R_A R_B}{R_A + R_B}$.
Although perfect wetting ($\delta = 0$) is assumed here, Lian et al. [18] extended the validity of Equation 2.26, and thus the non-explicit dependence from the wetting behaviour of the liquid, to larger contact angles (up to 40°) on the basis of the self-similarity of liquid bridges. Furthermore, the authors demonstrated that the 'gorge' method leads to errors evaluated within 10% of the exact numerical solution of the Young-Laplace equation.

The *second* method, which was adopted by Orr et al. [46] and subsequently employed by Adams et al. [47], considers the interfaces between the particles and the liquid bridge (here the replacement of the geometric average radius as per Equation 2.26 can be applied), thus obtaining the so-called "boundary" method [45]:

$$F_b = 2\pi R\gamma_L \sin\beta \sin(\beta + \delta) - \pi R^2 \Delta P \sin^2\beta \tag{2.27}$$

By treating the meridian curvature of the meniscus as an arc of a circle, the following equation is obtained for the perfect wetting condition [30]:

$$F_b = 2\pi R\gamma_l \left[\frac{2t^2 - t + 1}{(1+t^2)^2}\right] \tag{2.28}$$

where $t = \tan\dfrac{\beta}{2}$.

It should be noted that, besides the toroidal approach, the parabolic approximation proposed by Pepin et al. [22] can be applied to Equation 2.25 by substituting the "neck" value with y_{min} (see figure 2.6 for reference) therefore obtaining Equation 2.29:

$$F_p = 2\pi\gamma_L y_{min} + \Delta P \pi y_{min}^2 \tag{2.29}$$

The first two methods differ by a few percent, and the dependency of the total force on the separation distance is, in both Equations 2.26 and 2.28, implicitly accounted for by the variation of the half-filling angle, provided that the condition of constant volume during separation is respected.

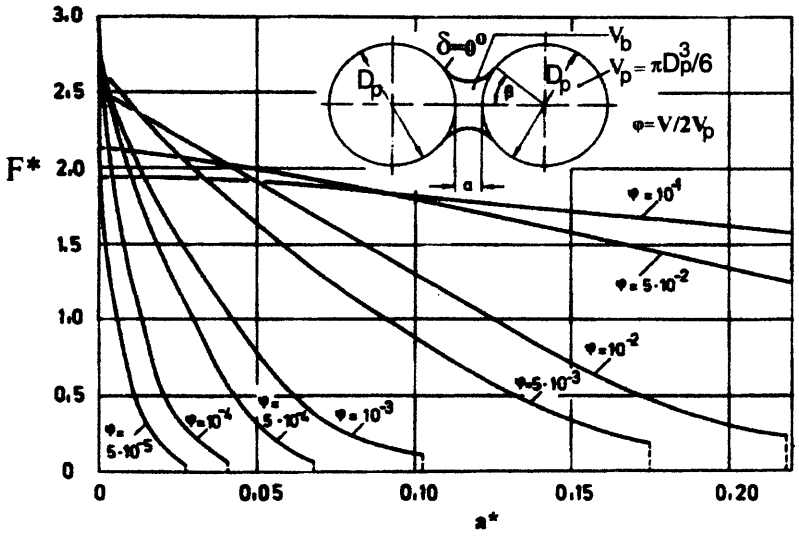

Fig. 2.18: Theoretical dimensionless adhesion force F^* $(= 2F/\gamma D_p)$ of a liquid bridge between two equal spheres against the dimensionless separation a^* $(= 2a/D_p)$, after [48].

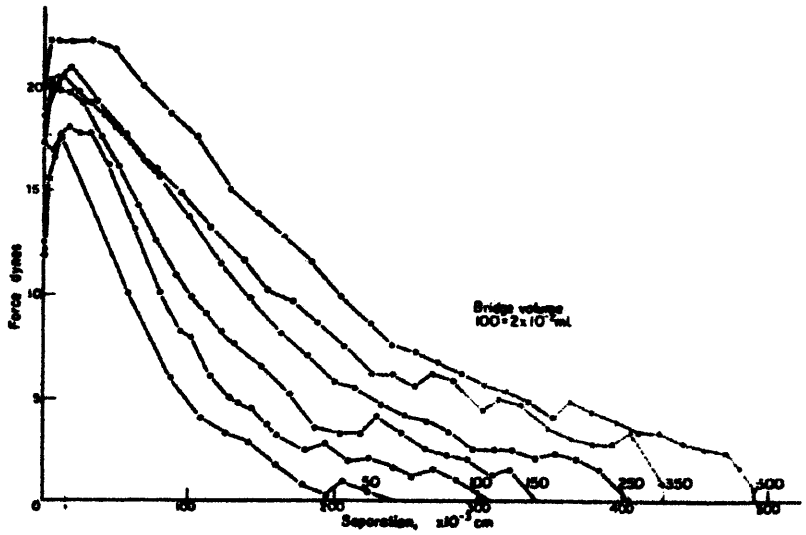

Fig. 2.19: Force versus separation curves for bridge volumes between two equal polythene spheres of 15mm radius suspended in water, after [49].

Theoretical trend lines plotted by Schubert [48], which are illustrated in figure 2.18, show good agreement in the prediction of the force versus separation with the numerical results proposed by Lian et al. [18] (not shown here): particularly, it is shown that for quasi-static separations and perfect wetting conditions the theoretical maximum value of the bridge strength is assigned for null separation distances. However, experimental results provided by different authors [20, 49, 50] show similar trends but a maximum force clearly appearing at non-zero distances, as shown in figure 2.19. As a possible explanation, Mason and Clark [49] assumed that the increasing of the force is due to a finite contact angle greater than zero formed at particle-particle contact, which is related to the volume of liquid administered and, through changes in the curvature during separation, leads to the formation of a maximum.

On the other hand, recent investigations on the experimental determination of the capillary force show results in close agreement with theory for relatively small liquid bridge systems [51, 39], provided that the viscous contribution to the total force can be considered negligible (see next section). However, the limited experimental studies reflect the difficulties in measuring the small capillary forces and length scales (i.e. the determination of particle contact) associated with sufficiently small bridges(where gravitational distortion is insignificant).

2.2.7 *Total force exerted by a pendular liquid bridge: Dynamic viscous contribution*

In a process vessel in which liquid bridges exist between particles, the liquid bridges will experience strain and shear forces as well as squeezing due to particle-particle and particle-wall collisions at varying velocities. During dynamic liquid bridge elongations or

compressions, the shear stress inside the liquid gives rise to an additional force, which is opposed to the direction of deformation and is, in fact, dependent on the viscosity of the liquid binder. This viscous term is very important for highly viscous liquids, or liquids whose viscosity changes because of the operative conditions (such as evaporation of the solvent component during hardening processes), but it also can dominate for liquids of modest viscosity at high shear rates. A full understanding of the viscous force exerted between particles is therefore required, since it may play a crucial role in the successful operation of fluidised bed reactors.

The most recognized expression for the viscous force exerted by a liquid meniscus between a pair of particles is given by Equation 2.30 [47]:

$$F_v = \frac{3}{2}\pi\eta R^2 \frac{1}{a}\frac{da}{dt} \tag{2.30}$$

where η is the liquid viscosity and da/dt is the separation velocity between two spheres of radius R (in case of particles of different size the geometric average radius can be used). Equation 2.30 represents a particular case where the particles are considered immersed in the liquid, and has been derived by Adams and Perchard [47] from the Reynold's lubrication approximation: when the particle radius is larger than the distance of closest approach between the particles, then, at low Reynolds numbers, locally and instantaneously the flow can be assumed similar to flow between parallel boundaries, where the velocity field is large in the direction orthogonal to that of separation, whilst derivatives in the direction of separation are dominant [52].

The limit of applicability of Equation 2.30 has been investigated by Mazzone et al. [41] who compared, by varying both liquid viscosity and separation velocity, the measured dynamic force with the theoretical prediction for different systems, which are uniquely defined by the values of the capillary number Ca:

$$Ca = \frac{v\eta}{\gamma_L} \tag{2.31}$$

where v is the particle separation speed.
Results were seen to be predicted by Equation 2.30 within one order of magnitude, the over-prediction of theory being addressed to the Stoke's assumption of particles submerged in an infinite fluid. To this regard, Matthewson [40] proposed a correction coefficient, shown in Equation 2.32, in the case of finite volume of liquid (i.e. cylindrical profile, see also Section 2.2.4.1), which was recently employed by Pitois et al. [39] in a similar experimental investigation on the viscosity effects:

$$F_v = \frac{3}{2}\pi\eta R^2 \left[1 - \frac{a}{H(R\sin\beta)}\right]\frac{1}{a}\frac{da}{dt} \tag{2.32}$$

where $R\sin\beta$ is the radius of the wetted area and $H(R\sin\beta)$ is the separation between the particles taken at $R\sin\beta$ distance from the horizontal axis of symmetry of the bridge.

Experimental data obtained by Mazzone et al. [41] and Pitois et al. [39] were plotted in the form of trend curves, such as those shown in figure 2.20 [41], which indicate that increasing the separation (or approach) velocity has the same effect as increasing the viscosity of the fluid: in fact, by increasing vicosity at a given separation speed the dimensionless dynamic force, defined as the ratio of the maximum total measured force to the maximum force of the relevant static bridge, can be dramatically raised up by 200 times [41].
Although for liquid bridges of finite volume such an analysis of the viscous contribution ignores the existence and the influence of the bridge meniscus on the region of the particles closest approach, the use of 2.30 remains commonly employed in the limits of low capillary numbers ($Ca \prec 10^{-3}$), small separation distances ($a/R \approx 0.01$) and sufficient bridge volumes ($V_b/R^3 \approx 0.05$). The last two conditions being necessary to justify a lubrication analysis for the viscous contribution.

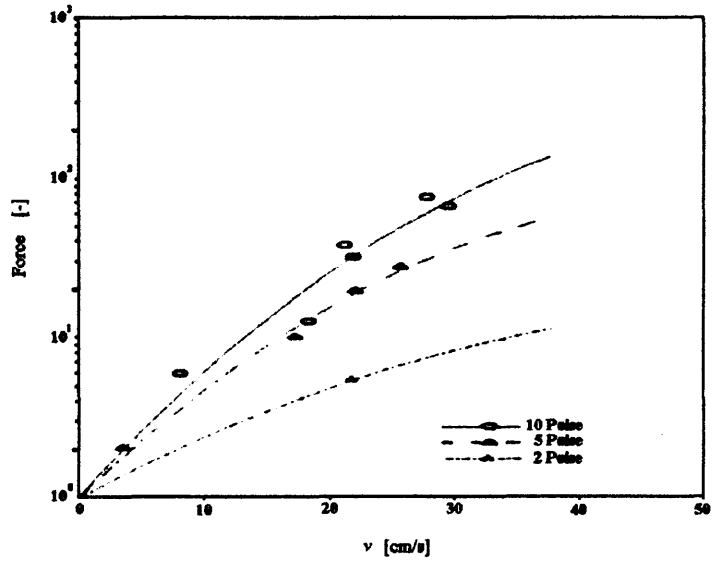

Fig. 2.20: Dimensionless maximum force *vs.* particle separation velocity with viscosity as a parameter. Properties of the solid-liquid-solid system: Dow Corning silicone fluid, $V_b = 1\mu l$;particle radius R=0.1985 cm. Figure adapted from [41].

Under the conditions and simplifications proposed for both types of forces, a general expression for the total strength exerted by a liquid bridge can be written as in Equation 2.33:

$$F = 2\pi r_1 \gamma_L - \pi r_1^2 \Delta P + \frac{3}{2}\pi\eta R^2 \frac{1}{a}\frac{da}{dt} \tag{2.33}$$

Since the total force between two bridged particles is given by summing the contributions

from the capillary and viscous forces, several authors have investigated different systems in order to ascertain whether one type of force prevails over the other. Such a non-trivial task brought Adams and Perchard [47] to state that capillary forces usually dominate in cases where the liquid exists as discrete bridges, but viscous forces can become significant when the liquid viscosity is very high or at high interparticle velocities.
The most common approach to examining interparticle forces is to scale up forces between pairs of particles to multi-body systems such as those found in fluidised beds (see Section 3.2): in fact, the rate of growth of agglomerates in a fluidised bed depends both on the successful collision between particles (figure 2.21) and the strength of the bonding, being related to both the physical and thermodynamic properties of the particle and the liquid.

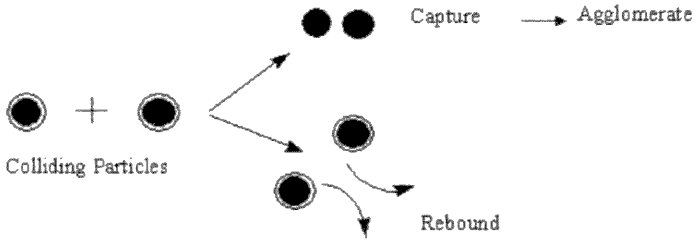

Fig. 2.21: Whether particles agglomerate or rebound depends on the strength of liquid bridges, which is conferred by the thermodynamic and physical properties of both the liquid and particles.

However this is very difficult and there is often disagreement [41, 39] on the nature of the forces at play. For example, Ennis et al. [53] compared their results to those of Mason and Clark [49], neglecting capillary forces as they considered viscous dissipation between colliding particles to be predominant, although Simons et al. [30] argued that capillary forces cannot be ignored since they are central to bridge formation. In terms of product quality, Ennis et al. [54] and Iveson et al. [26] concluded that the strength of wet agglomerates is mainly explained by viscous dissipation in the liquid binder and interparticle friction forces; however, capillary forces control the rate of agglomerate consolidation, modifying the interparticle friction forces by acting on the effective contact surfaces: for low saturation levels , they increase the friction forces as the interparticle contact area increases; for high saturation, they act as lubricants of the interparticle contact [55].

Ennis [54] and Tardos et al. [56] developed the critical Stokes number theory in order to predict whether particle collisions give rise to capture or rebound. In the case of systems of multi-particles (such as for fluidised beds), it was concluded that agglomerates formation would occur when the particles no longer had enough kinetic energy to escape capture on impact with their neighbours (see section below).
Focusing on the reverse approach and stating that viscous forces do not always dominate, Simons et al. [30] derived a predicting model based on the rupture energy of a pendular liquid bridge, see Section 2.2.8 for details. They argued that if the relative kinetic energy

of the colliding paricles was below that required to break the liquid bond then the particles would adhere together. The experimental approach followed by Simons and Fairbrother [50] found its basis on the critical rupture distance theory reported in Section 2.2.5. The authors found good agreement between experimental results and values calculated with Equation 2.21; however Pitois et al. [39] noted that in the regime where viscous forces are dominant Equation 2.21 underestimates the bridge rupture distance. They also provided a correction formula, which quantifies the variation between the viscous regime rupture distance, a^*_{visc} and Lian et al. expression 2.21 as being proportional to the square root of the separation velocity:

$$a^*_{visc} - a^* \propto \sqrt{v} \tag{2.34}$$

2.2.8 Rupture energy of a liquid bridge

The energy required to deform or break agglomerates is an important parameter which can be related to the power consumed by the process [14, 57]. Agglomerates are composed of discrete primary particles which are held together by a number of interparticle forces: models intended to evaluate the energy required to deform agglomerates have attempted to scale up the single particle interaction (i.e. particle-wall and particle-particle) to macroscopic behaviour [14] (see also Section 3.2).
Recent analytical and numerical works have aimed to model the deformation and fracture of particulate materials. It has been shown by Adams et al. [58] and Abdel-Ghani et al. [59] that the release of stored energy during crack formation is an important fracture mechanism of compacts and agglomerates, since it provides the energy to extend the crack. Moreover, in a wet bulk solid, crack extensions occur by rupture of liquid bridges: it is therefore necessary to have a simple expression to calculate the energy involved in this process. The basic terms considered in the models are the energy stored by capillary forces and the energy dissipated by friction and viscous effects.

The rupture energy, W, of a pendular liquid bridge between spherical particles in air has been modelled by Simons et al. [30] and Pitois et al. [39]. In the former, the bridge geometry was modelled with a toroidal curve (Sections 2.2.2 and 2.2.4.1) and, for the case of perfect wetting conditions, the integral of the quasi-static capillary force was calculated with respect to the separation distance. From the approximated solution of the non-trivial integral a simple expression was derived in terms of dimensionless parameters:

$$W^* = \frac{W}{\gamma_l R^2} \approx 3.6\sqrt{V^*} \tag{2.35}$$

In Equation 2.35, R is the radius of the equi-sized spheres, V is the volume of liquid in the bridge, whilst $V^* = V/R^3$ and W^* are the dimensionless volume and rupture energy of the bridge, respectively.

Pitois et al. [39] used a cylindrical (flat) approximation for the bridge profile (Section 2.2.4.1) and obtained a simplified expression, (2.36), of the capillary force:

$$F = 2\pi\gamma_l R\cos\delta\left(1-\sqrt{1+\frac{2V}{\pi a^2 R}}\right) \tag{2.36}$$

where a is the separation distance between particles and δ is the contact angle.
By integrating Equation 2.36 throughout separation distance, and using the approximation that δ stays constant, the authors found the expression, (2.37), of the dimensionless rupture energy without restrictions to the wettability exhibited by the particles:

$$W^* = 2\pi\cos\delta\left[\left(1+\frac{\delta}{2}\right)(1-A)\sqrt[3]{V^*}+\sqrt{\frac{2V^*}{\pi}}\right] \tag{2.37}$$

where $A = \sqrt{\frac{(1+2V^*)^{1/3}}{\pi\left(1+\delta/2\right)^2}}$, δ is the apparent contact angle expressed in radians, whilst W^* and V^* are defined as above.

The usefulness of Equations 2.35 and 2.37 lies in their dependency on global parameters, such as volume and contact angles, therefore these formulae represent a quantitative method of comparison between the energy dissipated on a micro-scale (i.e. how much single interactions contribute to the rupture energy of agglomerates) and the energy consumed by the process on a macro-scale. In this regard, Simons et al. [60] went on to compare the rupture energy calculated using Equation 2.35 with the kinetic energy of particles in a fluidised bed of glass ballotini doped with silicon oil. The liquid was added to simulate, at room temperatures, the increase in interparticle forces that occur at high temperatures due to sintering (see Section 2.3). The kinetic energy of the powder bed was expressed as:

$$m\frac{\left(U^*-U_{mf}\right)^2}{\gamma_l R^2} \tag{2.38}$$

where m is the particle mass, U^* is the superficial gas velocity at the point of defluidisation and U_{mf} is the minimum fluidising velocity of the dry powder bed. Hence, ΔU is the excess gas velocity required to maintain fluidisation. By plotting (2.38) versus $\sqrt{V^*}$, Simons et al. [60] found a linear relationship, indicating the importance of the liquid bridges at the particle contact points in the defluidisation process.

A second, different, approach was taken by Ennis et al. [54]. In their work on granulation phenomena between wet particles, the authors neglect static, and consider that the energy loss during collision of two particles is due to the viscous dissipation in the liquid layer. The authors introduced a viscous Stokes number to predict the minimum velocity required for two coated particles to rebound.

When two spherical particles of equal radius R and mass m, coated with liquid of viscosity η, approach from opposite directions with speed v_0 along the center-to-center axis (figure 2.22), the operating Stokes number, St, is defined as

$$St = \frac{2mv_0}{3\pi\eta R^2} = \frac{8\rho v_0 R}{9\eta} \tag{2.39}$$

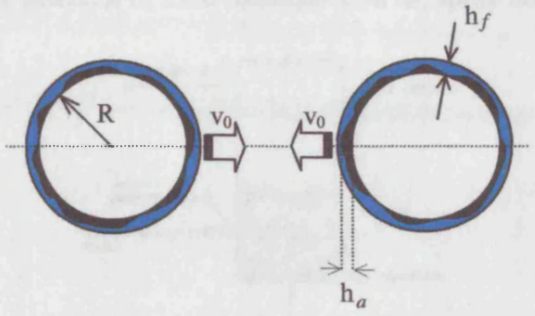

Fig. 2.22: Schematic of two colliding particles. A liquid of viscosity η is coating both particles with a layer of thickness equal to h_f, adapted from [54].

For "capture" to occur (i.e. particles stick together) the Stokes number must be below a critical value St^*:

$$St^* = 2\left(1 + \frac{1}{e_r}\right) ln\left(\frac{h_f}{h_a}\right) \tag{2.40}$$

where h_f is the thickness of the coating film, h_a is the height of the surface asperities and e_r is the coefficient of restitution of the impact.

To obtain the granule growth kinetics, one might apply traditional population balance techniques with physically realistic coalescence kernels, but such a deterministic approach must be considered an unrealistic idealization at present [54]. Therefore, it is more appropriate to examine the limiting scenarios characterized by the ratio St/St^*, shown in Table 2.5, which controls the coalescence phenomenon:

GRANULATION REGIME

$\frac{St}{St^*} \prec\prec 1$	non-inertial (all collisions successful)
$\frac{St}{St^*} \approx 1$	inertial (some collisions successful)
$\frac{St}{St^*} \succ\succ 1$	coating (no collisions successful)

Tab. 2.5: Granulation regimes according to the relative magnitude of the Stokes numbers.

On the basis of this classification, Ennis et al. [54] proposed a criterion for defluidisation of a fluid-bed resulting from the presence of viscous liquid layers on the individual particles. The non trivial task of the proposed model is to assign the correct relative particle velocity: in fact, most of the difficulties that are met in industrial practice when modelling the powder flow field arise from the presence of different internals within the process vessel. In fact, in fluidised beds, the particle movement is extremely complex due to both the bubble motion and the presence of fixed internals such as, spray nozzles, see figure 2.23.[4]

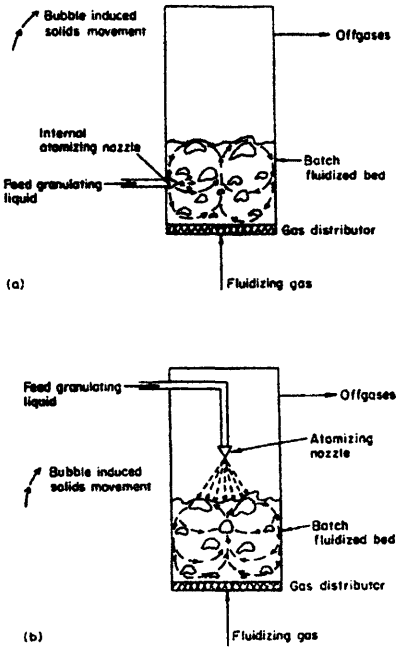

Fig. 2.23: Schematic of two batch fluidised bed granulators: particle motion depends on the bubbles velocity and whether the position of internals, such as the spray nozzle, is located within (a) or above (b) the bed material. From [2].

As a rough estimate, Tardos et al. [56] used expression (2.41) to evaluate the relative particle velocity:

$$v_0 = \frac{18 U_B R}{D_B \zeta^2} \tag{2.41}$$

where U_B and D_B are the bubble velocity and diameter respectively, ζ is the dimensionless distance, in respect to the bubble radius, between two consecutive bubbles. R is the particle, or granule, radius. Furthermore, by using such an approach, Ennis et al. [54] defined the critical defluidisation Stokes number, Equation 2.42, which represents (on the left-hand side) the minimum particle velocity for collisions to be successful (i.e. the interparticle kinetic energy prior to defluidisation):

[4] In this regard, a great deal of research has been carried out in order to develop new non-invasive measurement techniques, and an updated review is given in **Chapter 4**.

$$St_D^* = \frac{8\rho\alpha\left(U_{mf}^* - U_{mf}\right)R}{9\eta} = \left(1 + \frac{1}{e_r}\right)[ln(h_f) - ln(h_x)] \tag{2.42}$$

In Equation 2.42, U_{mf}^* is the modified minimum fluidisation velocity due to the presence of a liquid layer of thickness h_f, and α is a proportionality constant which is calculated from the regression analysis of the experimental data. By re-arranging the experimental results obtained from Gluckman et al. [61] on a St_D^* vs $ln(h_f)$ plot, the authors found a linear relationship, which clearly confirmed that defluidisation of a fluid-bed due to viscous particle layers can be considered one sort of idealized limit of granulation.

Both the approaches presented in this section introduced, in a simplistic manner, one possible theoretical way to explain defluidisation by considering the dissipation of energy between particle-particle interactions in the presence of liquid layers, therefore on the basis of the *cohesion* energy of the liquid. Whether dissipation is better described by the capillary rupture energy approach rather than the viscous coalescence model should be addressed to a different type of dissertation, which is beyond the scope and purpose of the present work. Nonetheless, changes may occur (either wanted or unwanted) in the physic-chemical properties of both the solids and liquids within a fluidised bed due, for instance, to high temperatures; here the modifications induced by the operative conditions of the process on both the binder and the solid may affect their interaction and, subsequently, the quality of the process itself, as well as of the final product. Hence, changes in the adhesive properties of a liquid and a solid are usually investigated through the determination of the wetting behaviour of the liquid/substrate system and the quantification of the relevant *adhesion* energy.

2.2.9 *Wettability and equilibrium at a line of contact. The Young's equation*

The wettability of a liquid on a solid is a thermodynamic property at equilibrium that defines the ability of the liquid to interact with the surface of the solid and therefore the structure and properties of the final material. Zisman [62] noted that the concept of contact angle and its equilibrium was valuable because it gave a definition to the notion of wettability and indicated the surface parameters needing measurement. A droplet of liquid on a solid has a tendency to spread on to the surface: when we say that a liquid is non-spreading, we simply mean that the contact angle (measured through the liquid droplet resting on a solid surface and in the environment of its vapour, as shown in figure 2.24) is non-zero; and when the liquid wets the solid completely and spreads freely over the surface at a rate depending on the liquid viscosity and solid surface roughness, we say that the contact angle is zero. Obviously, since the tendency for the liquid to spread increases as the contact angle decreases, the contact angle is a useful inverse measure of spreadability or wettability, whereas the balance of the attraction of the liquid for the

surface (adhesion) and the attraction for itself (cohesion) governs whether and how far the liquid spreads.

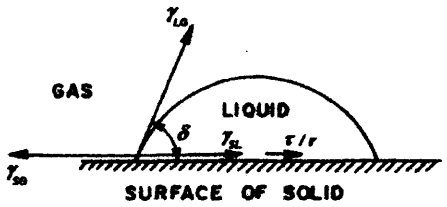

Fig. 2.24: Sessile drop system: equilibrium at a line of contact between a liquid droplet of finite volume and an ideal solid surface.

Capillary systems in porous media always involve a solid phase and at least two fluid phases: to describe thermodynamically a multiphase, multicomponent system, e.g. a sessile drop on a solid surface surrounded by a gas (figure 2.24), the fundamental equations for all phases should be considered collectively. Hence, in determining the equilibrium state for the above composite system, the equilibrium principle should be applied to the collection of the fundamental equations, i.e. bulk, surface and line. Gibbs' approach, the minimum energy principle, is the most widely used method to determine the equilibrium state for capillary systems. It can be shown, see Boruvka and Neumann [63] and Neumann [64] for the mathematical details of the derivation, that minimizing the total energy for the sessile drop system meets the mechanical equilibrium condition at the three-phase line, which is described by Equation 2.43:

$$\gamma_{LG}\cos\delta = \gamma_{SG} - \gamma_{SL} - \tau K_g \tag{2.43}$$

where δ is the intrinsic contact angle formed by the liquid on the solid surface, γ refers to the interfacial tension and subscripts L/S and G refer to liquid, solid and gas phases, respectively; τ is the line tension force (N), or more appropriately an energy per unit length (J/m), that depends on the geodesic curvature K_g of the three-phase line, which in the present case is the curvature in the plane of the solid surface[5].
In the above equation there are still too many unknowns to make it suitable as a working relationship. It should be noted that (2.43) is a particular case derived from the classical Young's equation, (2.44), which describes the relationship between contact angle and interfacial tensions of a large droplet, i.e. when $r \to \infty$:

$$\cos\delta_\infty = \frac{\gamma_{SG} - \gamma_{SL}}{\gamma_{LG}} \tag{2.44}$$

here, the solid surface is ideally considered as a smooth, chemically homogeneous, rigid

[5] In the ideal case, the sessile drop configuration, figure 2.24, would assume an axisymmetric shape, which means the three-phase line is circular. As a result, the geodesic curvature will be equal to the reciprocal of the radius of the three-phase circle, $\frac{1}{r}$.

and non reactive solid phase.
By combining Equations 2.43 and 2.44, it is possible to relate the line tension to the difference between the Young (δ_∞) and the intrinsic (δ) contact angle as per (2.45):

$$\cos\delta_\infty - \cos\delta = \frac{1}{\gamma_{LG}}\frac{\tau}{r} \tag{2.45}$$

Furthermore, a modified expression is proposed in the case of a droplet formed on a spherical particle, illustrated in figure 2.25, where β is the half-filling angle and (2.46) is the modified formula for the line tension [65]:

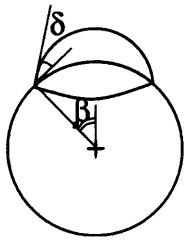

Fig. 2.25: Droplet formed on a spherical particle.

$$\cos\delta_\infty - \cos\delta = \frac{1}{\gamma_{LG}}\frac{\tau}{r}\cos\beta \tag{2.46}$$

In literature the theoretical and experimental analysis of the line tension effects is contentious and controversy exists over the magnitude and sign [66]. However, results obtained from recent experimental works carried out on three phase systems show line tension magnitudes ranging between 10^{-12} and 10^{-10} N [67].

Despite its wide use as a foundation for interfacial studies in a variety of fields (i.e. high temperature metal and ceramic coatings, wet-granulation), Young's equation has been the subject of considerable controversy and debate:

1. *Gravitational effects*: Young's equation predicts a unique value of the equilibrium angle, δ_∞, in terms of thermodynamic quantities (γ_{ii}) without regard to the presence of external fields. This is in contrast to the common observations of shape distortion of droplets on an inclined plane in the earth's gravity [68, 69].

2. *Substrate deformation*: Young's equation applies only to one-dimensional spreading and becomes invalid if the substrate is not rigid and the contact line motion takes place in both horizontal and vertical directions. The force equilibrium of figure 2.24 ignores the vertical component of the surface tension, $\gamma_{LG}\sin\delta$, which acts along the line of contact (this force is not countered by the weight that acts at the centre of mass). As the capillary forces are not balanced, external forces must be applied to the solid to achieve equilibrium [70, 71]; these forces can produce deformation in highly

deformable solids, such as gels and rubber, destroying the coplanarity of interfacial tensions assumed in Young's equation and causing ridge formation at the interfacial region. Ridge formation at the wetting front also occurs in high-temperature systems because of interfacial chemical reactions and diffusion processes (see below *Chemical inhomogeneity*).

3. *Vapour adsorption*: if the liquid vapor is adsorbed on the solid's surface, the surface tension of the solid, γ_{SG}, decreases. The concept of a spreading pressure P (defined from $P = \gamma_S - \gamma_{SG}$) is related to the need to maintain a saturated vapour of the liquid around the solid [72]. Here, γ_S is the surface tension of the solid in equilibrium with its own vapour or in vacuum, and γ_{SG} is the surface tension of the solid in equilibrium with the saturated vapour of the liquid. If the spreading pressure can be neglected (which is true for $\delta \succ 10°$) then it is possible to write the Young's equation in terms of the true or intrinsic surface tension of the solid. Techniques have been devised to test whether the spreading pressure in a given system is negligible and the measured contact angle is indeed the equilibrium angle [72].

4. *Surface roughness*: Young's equation applies to ideal surfaces that are perfectly smooth and devoid of all chemical and structural inhomogeneities. The contact angle measured on a rough surface (called the Wenzel angle, δ_W) does not obey the Young's equation; however, it is related to the equilibrium (Young) angle δ_∞ through the following expression [73]:

$$\cos \delta_W = K \cos \delta_\infty \tag{2.47}$$

where K is the ratio of the true wetted area to the apparent area.
Wenzel's equation, (2.47), applies to equilibrium angles on rough surfaces and not to advancing and receding angles of a droplet on a rough solid surface that give rise to contact angle hysteresis (see Section 2.2.9.1).

5. *Chemical inhomogeneity*: most solid surfaces (with the exception, perhaps, of single crystals) are seldom consistent and clean, with different surface domains possessing different chemistries and wetting properties. Such chemical inhomogeneity could result from oxidation, corrosion, coatings, multiple phases, adsorbed films, ledges, kinks, dislocations and grain-boundary intersections with the surface. Wettability and spreading are sensitive to such chemical and structural inhomogeneity [72]. Carefully prepared single crystals are closest to idealized surfaces and several studies have focused on the wetting behaviour of single crystals by liquid binders or metallic melts [74]. Note also that chemical reactions are often accompanied by reconstruction of the solid's surface, which could promote the chemical inhomogeneity and roughness. In the investigation of the dehydration reaction of magnesium nitrate hexahydrate,

reported in **Chapter 7**, the reaction mechanism leads to a strong weight reduction, which causes cavities to develop ahead of the contact line, thereby enhancing the surface roughness and hampering the spreading of the liquid interface.

All these important aspects may affect the quality of interaction between the liquid and the solid; however, in the next sections, much attention will be addressed to contact angle hysteresis, because of its contribution to the adhesiveness developed in the process of particle agglomeration.

2.2.9.1 Wetting hysteresis

The contact angle, being a thermodynamic quantity, should be expected to be a unique value for any particular system, but it is often found that when an interface advances along a surface the *advancing* contact angle, δ_{adv}, is larger than the *receding* angle, δ_{rec} (figure 2.26):

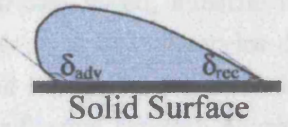

Fig. 2.26: Advancing and receding contact angle.

This is known as contact angle *hysteresis*, which is defined as the difference of the advancing and receding angles (i.e. $H = \delta_{adv} - \delta_{rec}$) and arises because the liquid-vapour interface does not retrace its original path when it recedes on the solid, so that spreading is thermodynamically irreversible. The existence of hysteresis and irreversibility usually means that a system is trapped in a metastable, non-equilibrium state. In the case of the contact angle of a liquid droplet on a solid surface, this can be due to the absence of *mechanical*, *chemical* or a combination of these including *thermal* equilibrium (note that while the droplet is moving the temperature may not be uniform across the system: therefore, the occurence of dynamic effects, such as slow adsorption and desorption of solute molecules dissolved in the liquid, may lead to hysteresis). In this regard, despite there being an ongoing debate as to its origin [75], many authors explain contact angle hysteresis as the resulting effect of the roughness and heterogeneity of the surface [76].

Generally, in the experimental observation of such phenomenon, a given system produces different contact angles depending on how the experiment is performed and the angle measured on a real surface is referred to as the apparent contact angle [77]. In particular, when careful experiments show two relatively reproducible values of the contact angle, it is not immediately obvious which, if any, of the two angles represent the truly equilibrium value. The matter has not been easy to resolve experimentally, for example, by allowing very long times, since advancing and receding angles can be stable for very long times.

However, the advancing angle is considered less sensitive to roughness than is the receding angle, the latter being usually the one measured and reported.

Contact angle hysteresis is really a manifestation of much more important effects: the hysteresis in the *adhesion* energy of two phases, where at least one is usually a solid, and the subsequent wetting and spreading behaviour of the liquid onto the solid surface. Section 2.2.9.2 therefore addresses the definition of the effect of wettability on the interfacial adhesion.

2.2.9.2 Work of adhesion, cohesion and hysteresis energy. Spreading coefficient

Wettability is manifested in numerous forms in a variety of processes. For instance, in industrial coating processes, the substrate is immersed in a liquid coating material, then withdrawn to leave a liquid film on the substrate. The film (coating) thickness depends upon the surface tension, withdrawal speed, substrate geometry, roughness, and melt viscosity. The performance of a coating during service depends not only on the inherent characteristics of the coating (and substrate) materials but also on the coating-substrate adhesion. Wettability promotes adhesion through physical, chemical, and/or mechanical bonds acting across the coating-substrate interface.
The effect of wettability on interface adhesion can be quantified by the adhesion energy W_{ad}. Adamson [78] defined the *adhesion* energy as the energy required to separate two distinct phases. The author provided Equation 2.48, which applies to systems composed of liquid adhered onto a solid substrate suspended in a liquid/gaseous medium:

$$W_{ad} = (\gamma_S + \gamma_L - \gamma_{SL})\, A_{SL} \tag{2.48}$$

here the same convention for the subscripts has been employed as in (2.43). Hence, during separation two new interfaces are created of energy equal to γ_S and γ_L respectively, both of area A_{SL}, whilst the existing solid-liquid interface is lost. By substituting Equation 2.44 in (2.48) the expression below, (2.49), is obtained, which establishes a direct relationship between the adhesion energy and the equilibrium (Young) contact angle:

$$W_{ad} = \gamma_L\,(1 + \cos\delta_\infty)\, A_{SL} \tag{2.49}$$

Similarly, Adamson [78] defined the *cohesion* energy as the energy required to separate a single phase of area A, which is expressed, in the case of liquid phase where no interface exists (i.e. $\gamma_{LL} = 0$), by (2.50):

$$W_{co} = (\gamma_L + \gamma_L - \gamma_{LL})\, A = 2\gamma_L A_L \tag{2.50}$$

Adhesion and cohesion energies assume an important role in the phenomena related to the spreading of a liquid onto a substrate. Rowe [79, 80], for instance, studied the application

of surface energy data in the field of wet granulation: in principle, the more a liquid spreads across the surface of the particles, the larger the surface area of contact within the granules, which leads to a greater strength of adhesion. The ability of the binder to spread across the particles is determined by the spreading coefficient, S_p, (2.51), defined as the difference of the adhesion and cohesion energies:

$$S_p = W_{ad} - W_{co} \tag{2.51}$$

Thus, the interaction between substrates and liquid binders can be used to guide binder selection in the process of wet granulation by considering cohesion and adhesion, and spreading coefficients [81, 82]: in fact, the more the binder is able to adhere to the substrate (favoured by a high work of adhesion, W_{ad}) compared to its tendency to self-associate (favoured by a low work of cohesion, W_{co}), the better the spreading and subsequent binding. Although Buckton [83] argued that the limitation of such approach is to consider the spreading as the major, if not the sole, mechanism in determining the behaviour of the system, the author nonetheless concluded that the approach to binder prediction does seem to be successful.

The effect of the binder on the wet spreading coefficient is usually measured through the consequential decrease in the contact angle of the liquid on the material. Hence, the approach is usually to select the binder giving the smallest contact angle. This can be measured in many ways. The most common techniques (contact angle tensiometry and goniometry [84]) involve powders or compacts and suffer from many artifacts associated with the structure of the sample, e.g. solvent penetration between the particles [83]. Moreover, they may not quantify the interface adhesiveness in the presence of hysteresis. In fact, in trying to quantitatively analyse the results of contact angle hysteresis it appears that the best criterion to use is not the hysteresis in the contact angle itself, but rather that of the adhesion energy that gives rise to it. Thus, the *hysteresis* energy is defined in (2.52) as the difference of work of adhesion between any two liquid configurations that characterize an advancing and a receding phase [85]:

$$W_{hys} = \gamma_L \left(\cos \delta_{adv} - \cos \delta_{rec}\right) A_{SL} \tag{2.52}$$

Possibly the most direct approach to measuring the relevant interactions between the liquid and solid is to measure the forces experienced between two sample particles separated by a liquid bridge using a micro-manipulator. This approach has been employed for studying drug materials production and is described in Section 3.1.1.

2.2.9.3 High temperature spreading and wetting dynamics

Wettability is a thermodynamic property which can be defined at the equilibrium and that is of special relevance in industrial processes where solid-liquid operations are involved; however, during processing, the ability of a liquid-solid system to reach the (thermal, chemical) equilibrium could be hampered by sudden changes in the process conditions, which in turn generate process unbalance, figure 2.27. In fact, high temperature wettability is influenced by a large number of variables that include temperature, contact time, atmosphere, roughness, crystal structure, composition, surface pretreatments and interfacial segregation, adsorption and reactions.

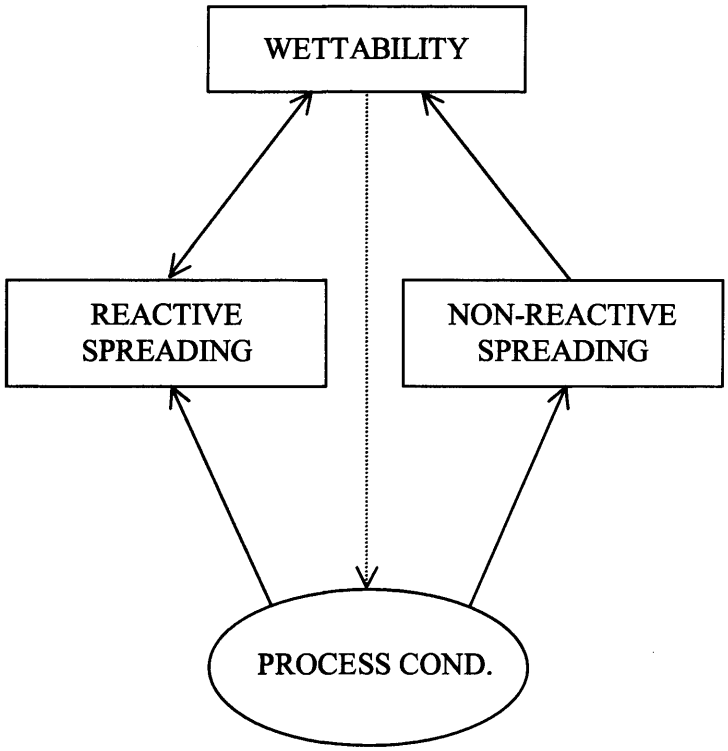

Fig. 2.27: Changes in the process conditions may affect the extent of interaction between the liquid and solid substrate by shifting the wetting(either reactive or non-reactive) equilibrium. Conversely, variations in the wetting behaviour may affect both the process conditions and, locally, the reactive spreading through a number of variables.

Depending on the type of wetting, one may distinguish several spreading dynamics, which can be studied by using different experimental approaches. In *non-reactive* systems, during its motion toward an equilibrium shape, a liquid droplet scans a range of apparent (dynamic) contact angles, which depend on the rate of spreading. In such cases, wetting behaviour of a liquid onto a solid substrate can be directly investigated by varying some process parameters, such as temperature, pressure or substrate porosity. In *reactive* systems, however, the wetting dynamics are interactively coupled with the reaction kinetics, and the spreading behaviour becomes complex and less clear. Whereas equilibrium wetting

is achieved rapidly (at times in the order of $10^{-4}/0.1$ seconds) in inert systems, equilibrium could take from 100 seconds to more than 10^4 seconds in reactive systems. Since reactive spreading strongly depends on the liquid-solid couple, high temperature wettability data have been presented in numerous systems and several authors attempted to model the complex interfacial phenomena that occur during reactive spreading [62, 86, 87].

2.2.9.4 Measuring the high temperature wetting dynamics: non-reactive spreading

In non-reactive systems the spreading rate is controlled by the liquid viscous resistance. In literature, several methods have been standardized for estimating the ability of a liquid binder or a molten material to flow onto/into a solid substrate. Although some of these are of practical help, they usually fail to separate the contribution of wetting and flow properties, which are entirely different from the view point of physical chemistry: wetting is a thermodynamic property at equilibrium, and wettability is promoted at high temperatures by a decrease of the liquid-surface tension ($\gamma_{LV}/dT \prec 0$); flow is a rheological property (dissipative property) [88] and is enhanced because of diminishing liquid viscosity at high temperatures.

Lahaye and Ehrburger [88] have investigated the coke-pitch penetration, which is a typical example where both wetting and flow should be taken into account. Coal-tar pitches and petroleum pitches are widely used in carbon technology processes, such as the production of carbon anodes for the aluminum industry and graphite electrodes for electric arc furnaces [89]; indeed, if pitch does not wet coke, there will be no penetration even if viscosity is very low. Conversely, if wettability is good but viscosity very high, penetration may become impractical. The authors concluded their experimental work stating that, working with a constant droplet size and with a given granular coke, it is possible to relate the flow behaviour of a pitch to its surface tension, viscosity and contact angle.

Rocha et al. [90] examined the pitch-coke wettability by employing the spreading drop technique; a moulded pellet of pitch was placed on a flat bed of petroleum coke and inside a furnace, as illustrated in figure 2.28a; after heating up the system, wettability curves are produced in a special diagram, such as those shown in 2.29, where the variation of the initial sample height with temperature indicates both the wetting (2.28b) and penetration stages (2.28c).

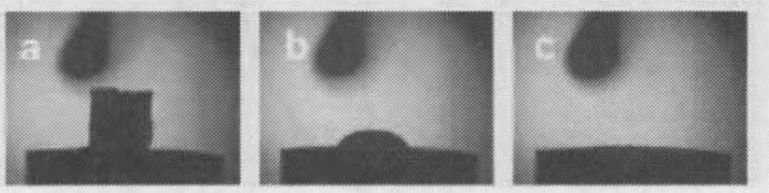

Fig. 2.28: Sequence of images of the pitch-coke system at different temperatures [90].

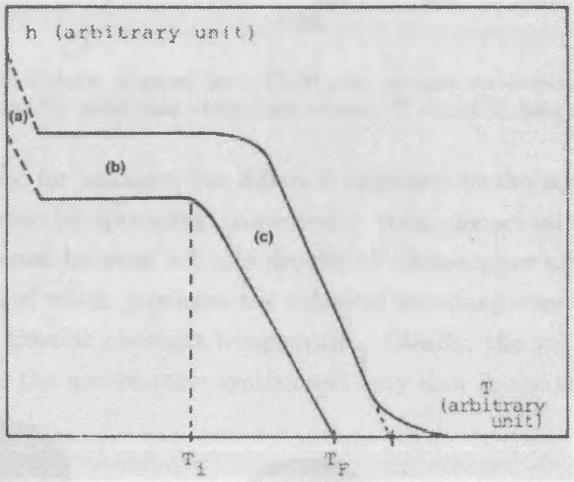

Fig. 2.29: Tests of pitch penetration through a coke bed. Height of droplet, h, versus temperature, T. T_i and T_f are the initial and final penetration stages. Adapted from [88].

The wettability curves reveal that there is a critical temperature range, figure 2.29b, at which the increase in temperature does not produce any change in pitch height. At this stage, the pitch has already softened but the cohesive forces are still stronger than the adhesive forces and so the pitch does not penetrate the coke. When adhesion prevails over cohesion in the balance of forces, the pitch flows into the coke. Consequently, the pitch height decreases sharply with temperature until complete penetration is reached, figure 2.29c.

2.2.9.5 Measuring the high temperature wetting dynamics: reactive spreading

At high temperatures, spreading to an equilibrium shape becomes difficult when a solid reaction product (e.g. an oxide) on the liquid opposes the spreading, resulting in a large value of the contact angle. However, the spreading rate toward equilibrium is nonetheless enhanced because of diminishing liquid viscosity. Hence, reactive spreading is not controlled by viscous resistance, but by the interfacial reaction itself [87].

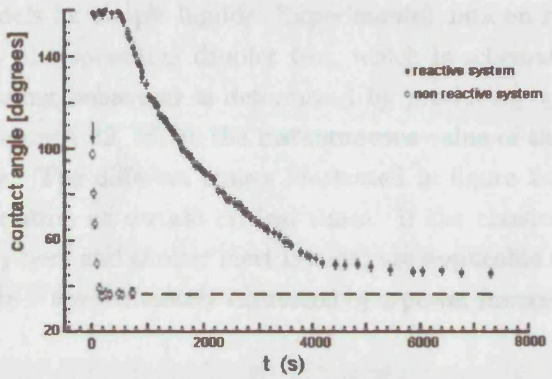

Fig. 2.30: Contact angle kinetics obtained for a Cu-Si alloy droplet on vitreous carbon (reactive) and α-silicon carbide (non-reactive) substrates under high vacuum. T=1423 K. Adapted from [87].

Figure 2.30 illustrates, for instance, the different approach to the equilibrium in the case of reactive and non-reactive spreading, respectively: here, the actual values of the contact angle, as initially formed between a liquid droplet of silica-copper alloy and two different solid substrates (one of which promotes the chemical reaction) were calculated and plotted as a function of time at constant temperature. Clearly, the wetting kinetics is very different: very fast in the non-reactive system and very slow in the reactive one.

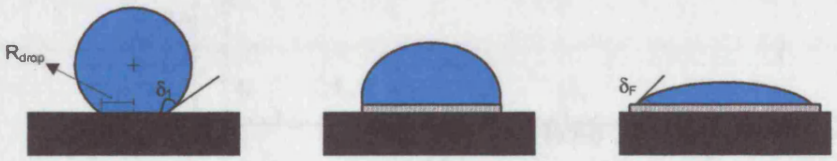

Fig. 2.31: Schematic of reactive spreading drop:(left) wetting is driven by the balance of surface energies of the relevant phases (from the initial contact angle δ_0 up to δ_1) and spreading is controlled by viscous resistance; (middle) formation of a new interface (reaction product), which becomes the controlling spreading mechanism up to attainment of the equilibrium configuration(δ_F),(right). From [87].

In complex reactive systems, such as those involving the study of reaction kinetics of metal/ceramic alloys or coating materials, chemical reaction, solute segregation, wetting, and spreading are interactively coupled. Conceptually, spreading can be divided into distinct stages. The first stage is the very rapid wetting that is due to the driving force generated by the balance of interfacial tensions and which is characteristic of inert liquids, figure 2.31(left). In the second stage, the substrate dissolves in the liquid and forms compounds, depicted by figure 2.31(middle), which later grow to form a continuous layer of the reaction product(s), shown in figure 2.31(right). Such reactions may yield one or more interfaces in place of a single solid-liquid interface. Here, wetting and spreading are controlled by the reaction kinetics.

As a first step toward understanding the complex spreading behaviour of reactive systems, a presentational approach can be used to identify different flow regimes that are consistent

with the classical models for simple liquids. Experimental data on reactive spreading are generally obtained by the spreading droplet test, which is schematically represented in figure 2.31: the spreading behaviour is determined by producing special diagrams, such as the one shown in figure 2.32, where the instantaneous value of the droplet base radius is plotted versus time. The different stages illustrated in figure 2.31 can be recognized through the slope variation at certain critical times. If the classical models (developed chiefly for viscous polymers and similar inert liquids) are applicable to reactive spreading, then the spreading rate is approximately expressed by a power function of drop base radius R_{drop} as per (2.53):

$$R_{drop}^{n} \approx t \tag{2.53}$$

where n is equal to 10 [91].

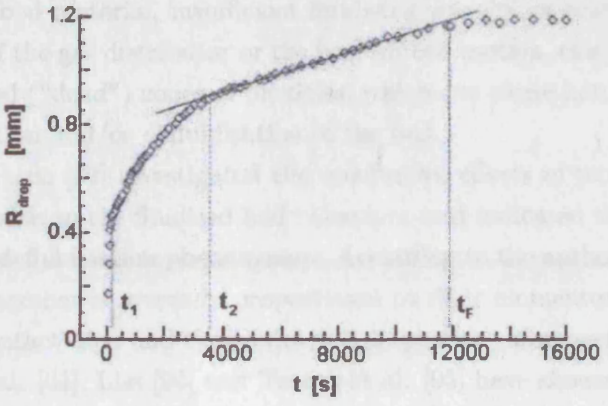

Fig. 2.32: Variation with time of the drop base radius during reactive spreading. Adapted from [87].

However, each reactive couple (liquid/substrate) may show a much more complex behaviour, exhibiting several flow patterns. Some of these patterns appear to be broadly consistent with the behaviour predicted by the classical models, (2.53); whereas others seem to follow different power laws ($n = 1 - 4$) which is characteristic of reaction and diffusion controlled spreading mechanisms, respectively [87]. Still other flow regimes appear to be inconsistent with all previous models.
Moreover, the spreading kinetics in a given system is strongly affected by the experimental/process conditions, and very different values can be measured for the same system depending upon the experimental technique (composition of the surrounding environment, temperature, surface preparation). Thus, while the presentational approach leading to (2.53) illustrates the complexity of reactive spreading phenomena vis-à-vis inert liquids, it does not shed light upon the underlying mechanisms.

In both the non-reactive and reactive systems, the effect of temperature on wetting and

spreading has been distinguished by simply running experiments based on a direct observation technique; however, in order to investigate agglomeration through liquid bridging mechanisms (e.g., non reactive and hardening binders, crystallization and reactive melts), it is necessary to couple direct observation with force measurement techniques, which permit, through the use of dedicated novel devices, the experimental quantification of particle interactions at process conditions. In this regard, a review of modern and novel off-line techniques is provided in **Chapter 3.**

2.3 Thermally induced surface cohesiveness

High temperature fluidised bed reactors are largely employed in a wide range of thermal processes, such as pyrolysis, gasification, combustion and also granulation. As described in the **Introduction** of this thesis, a number of operating and design characteristics, like the size and nature of bed material, insufficient fluidising velocity or scarcely aerated zones, inaccurate design of the gas distributor or the bottom bed section, can lead to the presence of local non-fluidised ("dead") zones of particles, which can cause hot spots and therefore agglomerate formation and/or defluidisation of the bed.
Langston and Stephens [92] investigated the qualitative effects of temperature, fluid velocity and particle size on the fluidised bed behaviour and indicated the main parameters responsible for the defluidisation phenomenon. According to the authors, the tendency for particles to stick together is inversely proportional to their momentum and directly proportional to the contact area and their adhesive properties. Moreover, studies by Siegell [93], Gluckman et al. [61], Liss [94] and Tardos et al. [95] have shown that defluidisation due to thermally induced surface cohesiveness depends on the particle physical and chemical surface properties, the heating rate of the fluidised material and the hydrodynamics of the gas and solids in the fluidised system.

The crucial point in investigating and modelling high temperature defluidisation is to elucidate the mechanisms of particle agglomeration involved in the process. Results from coal ash sintering obtained by Skrifvars et al. [96, 97] show, for instance, two main categories: in the first mechanism the stickiness of the colliding particles may be an inherent property of the bed particles themselves, which is caused by the *viscous* flow of material at the point of contact, forming a sinter neck, as in the case of low-melting ashes. The type of bond is of visco-plastic nature and usually is limited by the ability of the material to flow. The strength of the neck is proportional to the temperature and the interparticle contact time in that the higher the first and the longer the second, the greater the size of the neck itself.
In the second mechanism, defluidisation may be a consequence of the formation of either an adhesive layer on the bed particle external surface or induced by the presence of a liquid phase formed by a phase change and/or chemical reaction (this also occurs in plastic

waste thermal treatment [98]). In the latter case, the viscosity of the liquid is usually low so that, in order to prevent defluidisation, it is necessary to define the relevant critical volume as a limiting condition under which the process operates.

In industrial practice it has been found that changes in the performance of a fluid-bed reactor can occur at very different time scales, which strongly depend on the history and evolution of particle-particle interactions. In a recent work on the fluidised bed combustion of plastic fuels, Arena et al. [99] indicated the different stages that a polymer particle (PE and PET) undergoes just after its injection in a fluid-bed reactor. Figure 2.33 shows the different interactions that may occur between the injected particle and the inert (sand) bed material; all the possible routes can lead to different phenomena, which strongly affect the process quality. In fact, agglomeration of the bed material is initially enhanced by softening and subsequent adhesiveness of the polymer surface. As temperature is further increased over the melting point of the plastic core, the mechanism of agglomeration is controlled by the melt flow over the surrounding sand particles. The resulting aggregate is made of several layers of sand kept together by the polymer not yet devolatilized. At this stage, depending on the nature of the polymer material and the magnitude of the enhanced adhesive force, the process could evolve either toward a faster crumbling of the aggregates or their size enlargement by further adhesion of several layers of inert material, until the polymeric mass completely flowed throughout the sand [98].
It can be seen from figure 2.33 that both the phenomena may lead to poor performance of the reactor. In the first case, the elutration of fines, generated from the polymer-sand aggregate by abrasion with other bed materials or during crumbling, may lead to reduction of the conversion efficiency. In the second event, the size enlargement of the agglomerates, formed by rapid sintering of the inert material, is the principal cause of operative difficulties, which leads to the worsening of the fluidisation quality and subsequent risk of bed defluidisation.

In order to be able to intervene in the fluidisation at the right moment, it is crucial that one can detect at an early stage if the quality of the gas-solid fluidised state is changing. Modelling the sintering problem in fluidised beds has been attempted by several theoretical approaches, reviewed in **Chapter 4**, in an effort to provide a relationship between the physical properties of the material, its sintering behaviour and the hydrodynamics of the fluidised bed. On the other hand, investigating high temperature defluidisation from a microscopic view requires new tools that are able to provide insights into the physical mechanisms governing the particle-particle interactions. Of the existing techniques, dilatometry (Section 2.3.1.2) has been largely employed in the evaluation of the softening temperature of a wide range of materials.

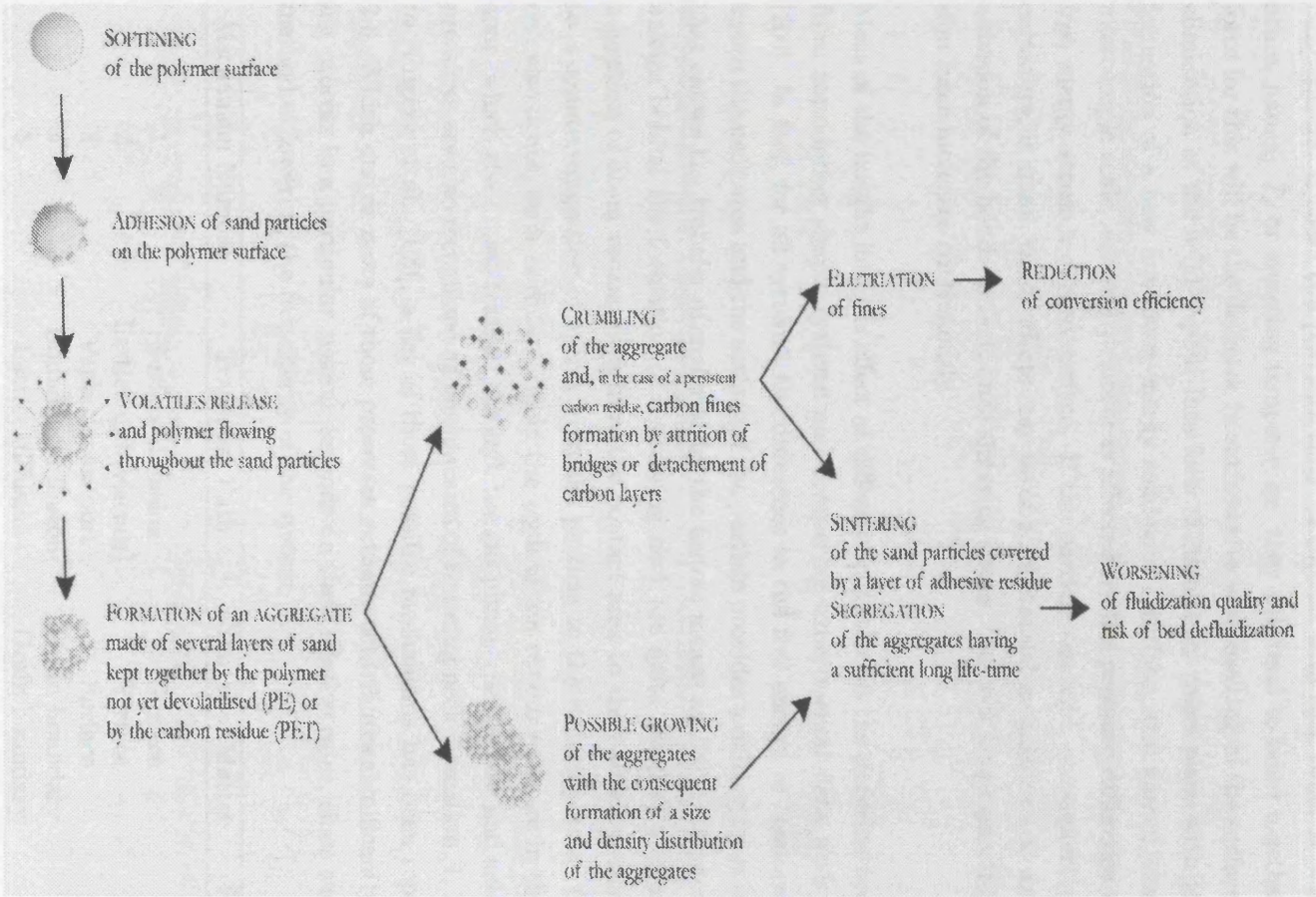

Fig. 2.33: Evolution of the phenomena that a polymer particle undergoes just after its injection into a fluidised bed reactor. After [99].

2.3.1 Sintering mechanisms

In order to explain the effects of sintering on high temperature fluidisation, it is necessary to consider the microscopic sintering rate between two particles in contact as a function of temperature. If these two particles come in contact with each other at a certain temperature, namely T_s or sintering temperature, they will tend to bond together. The driving force for this will be the decrease in surface area and lowering of the surface energy by the elimination of the solid-vapour interface. This usually takes place with the coincidental formation of a new but lower-energy solid-solid interface, also named *sinter neck*. On a microscopic scale, material transfer is affected by the pressure difference and changes in free energy across a curved surface. If the particle size and, consequently, the radius of curvature, is small, these effects may be of a substantial magnitude and so is the relevant adhesion of the bond: in fact, once sintering starts, the neck keeps growing and the cohesion force increases continuously.

Most of the insight into the effect of different variables on the sintering process has come from considering simple systems and comparing experimental data with simple models [100]. In fact, for all systems, the difference in the free energy or chemical potential between the neck area and the surface of the particle provides a driving force (surface energy) that causes the transfer of material by the fastest means available; in general, the mechanisms behind the formation of a sintering neck are quite complex and involve diffusive migration of atom vacant sites from the contact area to the particle surface, which leads to a counter-migration of atoms from the particle to the sintering neck. Other phenomena also occur, such as differences in the equilibrium vapour pressure in the particle-neck zone, which gives mass transfer through the gas phase; viscous flow and externally applied pressures are also recognized as mechanisms of sintering neck formation [1, 101]; according to Kingery et al. [100], a list of these possible mechanisms has been reported in Table 2.6. Which one or more of these processes actually contributes significantly to the sintering process in a particular system depends on their relative rates, since each is a parallel method of lowering the free energy of the system.

Mechanism Number	Transport Path	Source of Matter	Sink of Matter
1	Surface diffusion	Surface	Neck
2	Lattice diff.(viscous)	Surface	Neck
3	Vapour transport	Surface	Neck
4	Boundary diffusion	Grain boundary	Neck
5	Lattice diffusion	Grain boundary	Neck
6	Lattice diffusion	Dislocations	Neck

Tab. 2.6: Alternate paths for matter transport during the initial stages of sintering. From [100]

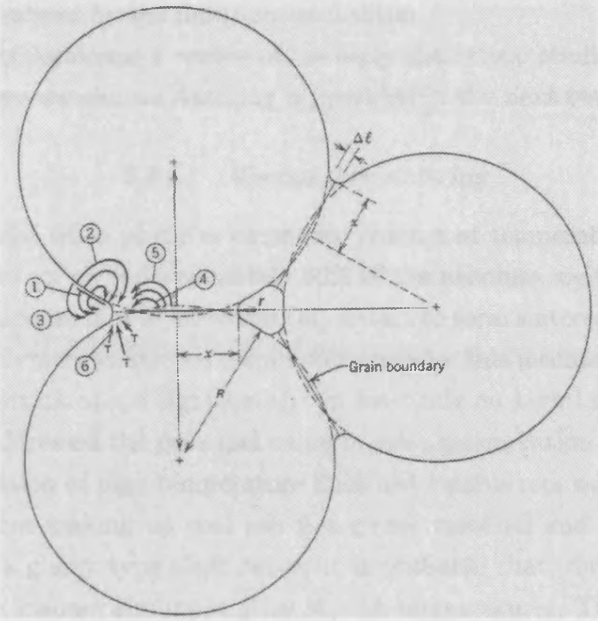

Fig. 2.34: Alternate paths for matter transport during the initial stages of sintering. Adapted from [100]

By considering different industrial technologies, Siegell [93] rated the most important sintering mechanisms that play a fundamental role in defluidisation. The author stated that the sinter neck formation by vapour transport is probably the least important in defluidisation, whereas, depending on the physical properties of the bed-solids, diffusional mechanisms of sintering, an example of which is shown in figure 2.35(left), may be of first importance in comparison to viscous transport [102]. Nonetheless, the sinter neck and bond area growth is much more rapid if the sintering takes place by viscous flow, figure 2.35(right); here the mass transfer mechanism is due to the movement of entire planes of lattice, as opposed to the movement of single atoms which occurs in the diffusion mechanism.

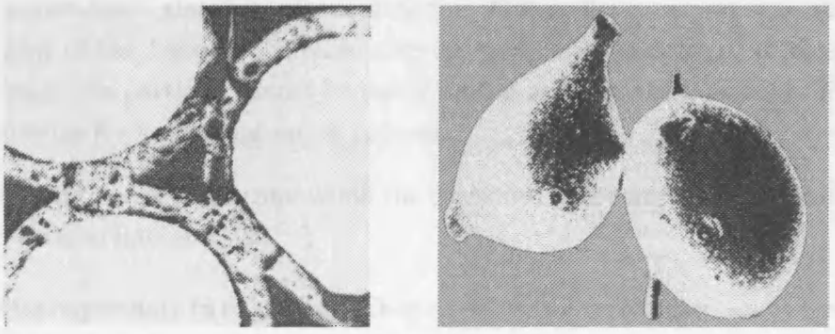

Fig. 2.35: Micrographs of diffusional sintering of copper shots (left) and viscous flow sintering of glass particles (right) [93].

Moreover, agglomerates formed due to viscous flow sintering tend to be much more strongly

bonded than those caused by the diffusion mechanism.
In light of these considerations, a review of the early theoretical studies and recent experimental investigations on *viscous* sintering is provided in the next two sections.

2.3.1.1 Viscous flow sintering

Solid bridges can arise when particles come into contact at temperatures high enough to cause the surfaces to soften (approximately 60% of the absolute melting point [103]), resulting in viscous material flow at the points of contact to form sintered bridges. Typically, glasses and most polymeric materials form bond zones by this mechanism, which tends to alter the original particle shape significantly. In his study on high temperature defluidisation, Siegell [93] addressed the principal cause of ash agglomeration to viscous sintering. In fact, in the operation of high temperature fluid-bed combustors with high ash content, the major constituent making up coal ash is a glassy material and the final product of coal gasification is a glassy type slag; hence, it is probable that, during the process the ash will behave in a manner similar to glass at high temperatures. The author concluded that, in order to understand defluidisation, further theoretical and experimental studies on the ash sintering mechanism are mandatory.

From theory, three distinct steps have been identified for viscous sintering at particle contact, namely:

1. *zipping* contact growth that is driven by adhesive intersurface forces and accommodated by visco-elastic deformation. This is an initial stage that is caused by the occurrence of stresses generated by the contact of particles along a boundary. These forces cause the particles to adhere and some early neck growth begins; however, the weak nature of such bond means that the particles can be easily broken apart.

2. *stretching* contact growth, which is driven by surface tension and accommodated by viscous flow - classical viscous sintering. Material is transported to this zone as the area of the bonding increases and the particle centres begin to approach. At this stage the particles cannot be easily broken apart at the boundary. This step is responsible for the defluidisation process.

3. *coalescence* stage, which represents the continued and complete densification of the two particles into one.

Because of its importance in enhancing adhesiveness between particles, a number of studies have been focused on the second stage of sintering in order to achieve a better understanding of the defluidisation process. Here the main findings are summarized.
When two particles are initially in contact, as shown in figure 2.34, there is a negative pressure at the small negative radius of curvature r compared with the surface of the

particles. At a certain sintering temperature T_s, this causes a viscous flow of material into the pore region. By neglecting all other forces, including gravity, and equating the rate of work done by surface tension γ to the rate of energy dissipation due to viscous flow (calculated as for a Newtonian fluid), Frenkel [103] predicted that the neck radius x, formed between two spheres, increases as a simple power law of sintering time t (2.54):

$$\frac{x}{R} = \left(\frac{\gamma t}{\eta_s R}\right)^{\frac{1}{2}} \tag{2.54}$$

where R is the constant radius of spheres ($R(t) = R(t = 0)$) and η_s is the fluid viscosity. An important consequence of Equation 2.54 is that normalized neck growth depends only on the geometric scaling R, as pointed out by Herring [104]. Moreover, experimental evidence on the sintering of glasses supporting Equation 2.54 can be found in Kuczynski [105]. Factors of most importance in determining the rate of such a process are the surface tension, viscosity and particle size, while the shrinkage ($\Delta\ell$), which indicates the beginning of surface softening, is measured with the approach of the two particles centres ($\ell_0 = 2R$ is the initial length of the sample) by using Equation 2.55:

$$\frac{\Delta V}{V_0} = \frac{3\Delta\ell}{\ell_0} = \frac{9\gamma}{4\eta R}t \tag{2.55}$$

where V is the volume of material transferred in respect to the initial particle volume. The initial rate of shrinkage is therefore directly proportional to the surface tension, and inversely proportional to the viscosity and particle size, respectively.
Softening and contraction of certain material surfaces are important properties that have been investigated by several researchers in order to calculate the surface viscosity at characteristic sintering temperatures. It will be shown, in Section 4.2.3, that the capability of measuring such important parameter (see Section 2.3.1.3), is of fundamental importance in developing models of prediction for the high temperature defluidisation due to viscous sintering.

2.3.1.2 Experimental determination of the sintering temperature

Following the early works of Gluckman et al.[61], Siegell [106] and Basu [107] who investigated the high temperature fluidisation behaviour of different materials according to their physical properties, a number of authors have employed a dilatometry method (see also Section 3.3.2.4) to measure the onset temperature (i.e. sintering temperature, T_s) for particle agglomeration, Table 2.7.

Reference	Material	Size	$T_s[°C]$
Gluckman et al. [61]	Copper shot	-16+20 US mesh	-
	Polyethylene beads	3x3.6 mm	-
	Polypropylene beads	2.2x3.4 mm	-
	Dacron (PET)	1.4x3.3 mm	-
	Glass ballotini	-14+16 US mesh	-
Siegell [106]	Copper shot	-16+20 US mesh	898
	Dacron (PET)	1.984 mm	83.3
	Polyethylene beads	2.440 mm	118.3
	Polyethylene beads	3.175 mm	127.2
	Coal ash	-40+50 US mesh	874
	Glass spheres	1.3 mm	655
	Glass spheres	1.095 mm	649
Basu [107]	Coal ash	-40+50 US mesh	-
Tardos et al. [108]	Polyethylene granules	0.712 mm	112
	Polypropylene granules	3.2 mm	140
Compo et al. [109]	Polyester	4.350 mm	260
	Glass powder	0.195 mm	577
	Coal	T_s depends on type of coal	
	Calcium chloride	0.5 mm (irregular)	440
Compo et al. [109]	Sodium chloride	0.359 mm (cubic)	463
	Sodium bromide	0.359 mm (cubic)	480
	Titanium dioxide ore	irregular size distr.	1035
Seville et al. [110]	LDPE	2x1.5 mm	108
Lettieri et al. [111]	FCC catalyst Type 1	71 μm	757
	FCC catalyst Type 2	57 μm	800
	FCC catalyst Type 3	49 μm	800
	FCC catalyst Type E-cat	54 μm	134

Tab. 2.7: Previous studies on high temperature fluidisation carried out through dilatometry technique.

In the dilatometry test, a small amount of loosely packed particles is introduced in a cylindrical sample holder and a shaft with a piston at its end is placed against the sample in the cylinder. A load is applied to the rod and the sample is heated to a desired temperature at a programmed rate of temperature rise. During sample heating, the change in sample length is monitored and plotted as a function of temperature. A typical plot of data is shown in figure 2.36. Initially the sample increases its length linearly with temperature, due to thermal expansion. As higher temperatures are reached, the rate of expansion

decreases. This is attributed to the onset of a separate phenomenon competing with the thermal expansion, i.e. sintering or densification. As the temperature is further increased, a point is reached where the slope of the expansion curve becomes zero. At that point, the expansion due to thermal effects is just balanced by the contraction due to sintering. This characteristic temperature is the *initial sintering temperature*, or T_s. After this critical point , sample contraction dominates until the end of the experiment.

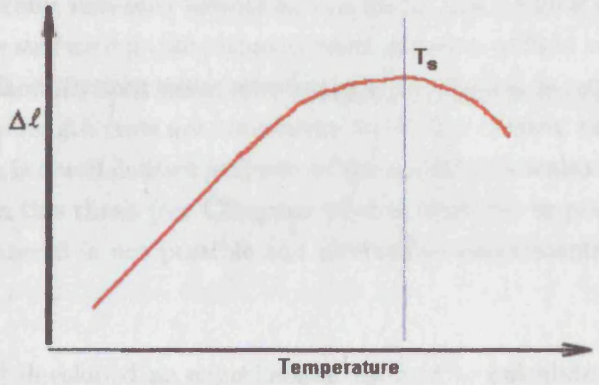

Fig. 2.36: Typical result of dilatometry. Adapted from [106].

Table 2.7 reports the experimental evidence that the initial sintering temperature, as measured through dilatometry, is strongly particle size dependent. For instance, Berbner and Loffler [1] reported an exponential decrease of T_s with diameter of titanium nitride (TiN) particles. To establish a formal relationship among the different results obtained for the same material, Compo et al. [10] argued that dilatometry tests should be carried out at constant intergranular force F_p (2.56), defined by Rumpf [24] as the actual surface force between two contacting granules in the sample:

$$F_p = \frac{4\varepsilon D_p^2 L}{\pi (1-\varepsilon) D_s^2} \tag{2.56}$$

where D_p is the particle diameter, D_s is the sample diameter, ε is the voidage, and L is the total load on the sample.

Nonetheless, there are still two indipendent variables, the magnitude of the load and sample heating rate, in the measurement of the initial sintering temperature, where conflicting information can appear [10, 61, 107]. With regard to whether, and how great, a force should be applied to the sample, Siegell [93, 106] suggested that, in order to duplicate the physical conditions in a fluidised bed, the actual load should be kept low (actual values are not given). However, since the instrument (dilatometer) is susceptible to vibration and frictional forces, Compo et al. [10] found reproducible results only by applying moderate loads.

Sample heating rate was also reported to have a certain influence on the outcome of the

measurement, [10, 108, 109]; however, little studies have been so far dedicated to this effect.

As has emerged from recent works of Compo et al. [10, 109] and Lettieri et al. [111], the shrinkage experienced by a sample of powder during dilatometry is not always indicative of viscous sintering through partial melting of the sample surface; in the case of inorganic salts or, more generally, non-pure materials, it is rather the manifestation of structural re-arrangement at the surface due, for instance, to evaporation of light compounds or shifting of a reaction interface. In such cases, pre-drying of the sample is required before analysis and a set of yield strength tests are mandatory to further confirm that the minimum sintering temperature is a well defined property of the material (see also Section 4.2.2). It will be further shown in this thesis (see **Chapter 6**) that often pre or post treatment/analysis of the sampled material is not possible and alternative experimental techniques have to be developed.

Tardos et al. [108] developed an experimental method to calculate the surface viscosity of pure materials at their sintering temperature; the importance of this technique is due to its later employment by Tardos et al. [112] and Seville et al. [110] in the modelling of high temperature defluidisation due to viscous sintering (see **Chapter 4** Section 4.2.3). For completeness, the experimental method has been summarized in the following section.

2.3.1.3 Experimental evaluation of the surface viscosity through dilatometry

As explained in the previous section and illustrated by Equation 2.55, contraction of a material sample at a characteristic temperature is addressed to viscous sintering, where the surface viscosity and sinter neck size are evaluated through simple geometric considerations.

According to the relevant size of the test material and its spatial distribution within the sample holder, a unique relationship can be derived between the contraction of the sample $\Delta\ell/\ell_0$ and the radius of the sinter neck X. In the case of large chain-like arranged particles, as shown by figure 2.37, the geometric properties of the particle-particle system yield Equation 2.57.

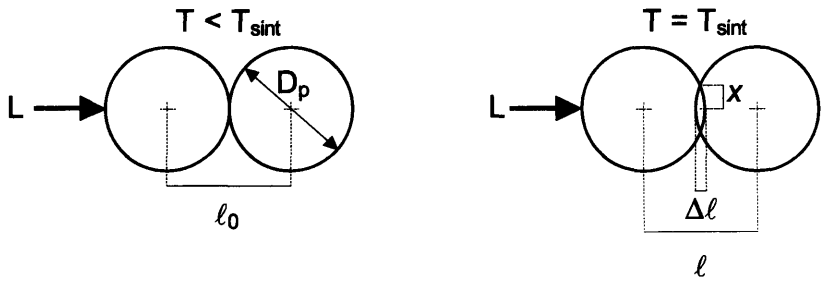

Fig. 2.37: Chain-like arrangement of coarse particles. Adapted from [108].

$$\frac{\Delta\ell}{\ell_0} = \frac{\Delta\ell}{D_p} = 1 - \sqrt{1 - \left(\frac{2X}{D_p}\right)^2} \tag{2.57}$$

where D_p is the granule diameter and X is the distance over which flattening has occurred.

If a set of smaller particles is otherwise placed with random spatial distribution within the sample holder, then a corrected expression is provided, as in (2.58) [108]:

$$\frac{\Delta\ell}{\ell_0} = \frac{2}{3\beta_{ls}}\left[1 - \sqrt{1 - \left(\frac{2X}{D_p}\right)^2}\right] \tag{2.58}$$

where β_{ls} is the so-called layer spacing coefficient that was defined by Dullien [113] by considering a rhombohedral unit cell in which the spheres are moved equally apart to give a mean porosity ε corresponding to the random packing:

$$\beta_{ls} = \sqrt{\frac{2}{3}}\left[\frac{\pi}{3\sqrt{2}\,(1-\varepsilon)}\right]^{1/3} \tag{2.59}$$

The concept behind using such a coefficient is explained by Dullien [113] as follow: every regular packing can be thought of as consisting of parallel layers of identical structure. For any orientation, two successive layers of spheres will lie a fixed distance apart, the distance between sphere centres being termed the *layer spacing* $\beta_{ls}D_p$, where D_p is the sphere diameter. For common packings, β_{ls} will lie in the range $0.707 \leq \beta_{ls} \leq 1.00$, the limits being at rhombohedral and cubic, respectively.

In order to obtain a single expression that can be employed in the calculation of the sinter neck size from dilatometry readings, Tardos et al. [108] assumed the contraction of the sample $\Delta\ell$ small as compared to its initial length ℓ_0 and therefore obtained:

$$\frac{X}{D_p} \cong \left(\frac{f\Delta\ell}{2\ell_0}\right)^{1/2} \tag{2.60}$$

where f is equal to 1 or $3\beta_{ls}/2$ in the case of coarse particles in linear (chain-like) arrangement and small particles randomly arranged, respectively.

Rumpf [7] assumed that if the radius of the contact area X is small compared to the granule diameter D_p, the following relationships can be employed:

$$\left(\frac{X}{D_p}\right)^2 = \left[\frac{4\gamma_s}{5D_p} + \frac{2}{5\pi}\frac{(F_w + F_p)}{D_p^2}\right]\left(\frac{t}{\eta_s}\right) \tag{2.61}$$

$$\left(\frac{X}{D_p}\right)^3 = \left[\frac{3\,(F_w + F_p)}{32D_p^2}\right]\left(\frac{t}{\eta_s}\right) \tag{2.62}$$

where γ_s is the material's surface tension, t is the time of contact during which intergranular force[6], F_p, occurs and η_s is the viscosity of the granule surface. The force F_w is the van der Waals attraction. The choice of a suitable expression is demanded on the type of shrinkage mechanism involved: in Equation 2.61 the contribution to shrinkage is associated with the material's surface tension, whereas in Equation 2.62 the governing mechanism is the viscoelastic flattening.

However, by neglecting the contribution of the van der Waals force in both expressions, Tardos et al. [108] produced a single general relationship between the size of the sinter neck X, the compression force F_p, the time t and the viscosity η_s:

$$\frac{X}{D_p} = \left(\frac{KF_p t}{D_p^2 \eta_s}\right)^n \tag{2.63}$$

where K is a numerical constant and the coefficient n is expected to take values between 1/3 and 1/2.

Furthermore, by taking the derivative with respect to t^n and combining with (2.60) the following expression for the surface viscosity was obtained:

$$\eta_s = \frac{KF_p}{D_p^2\left[\frac{\partial(f\Delta\ell/2\ell_0)^{0.5}}{\partial t^n}\right]^{1/n}} \tag{2.64}$$

Hence, by obtaining dilatometer data, where a porous sample of initial length ℓ_0 and granule size D_p is heated at a certain rate and compressed by a known force F_p (or L) while the contraction $\Delta\ell$ is measured as function of time, it is possible to measure the surface viscosity at any operative temperature, as illustrated for example in figure 2.38 .

[6] It should be noted that if coarse particles in chain-like arrangement are used, then the programmed operative load L has to be substituted by the intergranular force F_p in Equations 2.61 and 2.62 respectively.

In fact, the deformation $\Delta\ell$ versus time will yield, on a log plot, the coefficient n as the slope of the obtained curve; while the slope of the deformation $\Delta\ell$ versus time raised to the power n will lead, through Equation 2.64, to the value of the surface viscosity.

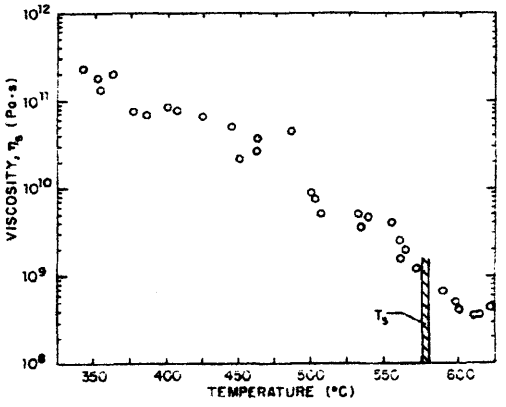

Fig. 2.38: Surface viscosity vs. temperature for glass particles 20-30 US mesh. From [108].

Although dilatometry tests are time consuming and, in some cases, of difficult interpretation, such an experimental technique is nonetheless a simpler and more direct method to measuring minimum sintering temperatures than performing fluidisation-defluidisation tests on the granules. This is achieved on the basis that at the point of sintering the granule's solid surface deforms, the surface viscosity drops and/or contraction of the sample is measured.

2.4 *Understanding interparticle forces to avoid defluidisation*

The tendency of agglomeration in a fluidised bed is the direct result of stickiness of the bed material. In order to understand the phenomena, many aspects need to be addressed: Which compounds are responsible for the particles in the bed becoming adhesive? How are these compounds transferred to the particle surfaces? How do the adhesive particles affect the fluidisation behaviour and the formation of agglomerates? And what are the important process parameters affecting defluidisation?

The focus of the work that will be reported in this thesis is to provide a sound foundation to the understanding of the factors governing the stability of high temperature fluidisation processes at a microscopic point of view. The importance and extent of particle adhesiveness and liquid-solid wettability will be highlighted, in the next chapters, by investigating different types of interaction between solids. This is also a fundamental aspect necessary to arrive at appropriate scale up design procedures and product formulation.

3. OFF-LINE MEASUREMENT TECHNIQUES AND INSTRUMENTATION

Much data on the agglomeration process in a full-scale fluid bed, such as the effects of operating variables, material parameters and agglomerate growth rate curves, have been collected in the past with the "experimental" (*trial* and *error*) method. This method highly depends on the experiences and creativity of the scientist and the technician. With this procedure, the influence of different processing variables as well as their mutual interactions can be investigated, and the sensitivity of a number of different processing variables can be studied at the same time.

However, as already mentioned, the description and control of the growth of agglomerates in a fluidisation process is complicated, because many mechanisms, such as wetting, drying, sintering and coalescence of the powder granules are involved. Moreover, these mechanisms determine the properties of the granule. These mechanisms can be studied in detail for a single granule [114]. When the conditions applied to the single granule resemble the conditions of the full-scale process, one can use small-scale experiments to describe the full-scale process conditions.

Other requirements for small-scale experiments are:

1. rapid and reproducible experiments;
2. cheap experiments, which allow enough data collection to achieve a good reproducibility of the measurements.
3. similar formulation;
4. geometric similarity with the large scale process is not necessary, provided that dynamic similarity of the particles exists (equal forces on the particles as a function of time). In fact this means that the experiments are representative for the full scale.

Some remarks regarding these requirements can be made:

1. Not all aspects are always important. For instance, some authors have used the scaling-down approach to study the initial wetting of powder during granulation processes; for instance, large droplets (up to one order of magnitude greater than droplets sprayed in large processes) have been used to study agglomeration in a

low shear environment (fluid-bed) [115], with drying not taken into account. Such experiments do not simulate the full-scale process as a whole, but only the wetting behaviour.

2. A typical scale-down experiment is often limited to one or two aspects (e.g. the influence of temperature on minimum fluidisation velocity, or on growth and breakage of agglomerates). However, this is often also true for classical (scale-up) experiments of complicated processes (due to the impossibility of keeping all relevant dimensionless numbers at a constant value during scale-up).

3. The advantage of scale-down is two fold. First, it gives more experimental room for manoeuvre (no geometric similarity needed). Second, it provides rapid insight in the relative importance of the different mechanisms that are potentially involved.

4. It is not always necessary to realise exactly the same value of the aspects at different scales of operation. The same order of magnitude is often sufficient (e.g. to find the most important mechanisms involved).

Although the effect of the processing variables can be described using small-scale experiments, these effects are often not (mechanistically) understood and extrapolation of the results is therefore not often possible. Therefore, in order to achieve a better understanding of the changes to the bed material with process conditions (e.g. temperature), micro-mechanistic approaches must be developed through the design of novel devices dedicated to the off-line investigation of particle-particle interactions under process conditions.

The main aim of this chapter is to shed light on the importance of coupling off-line measurement techniques to scale-down instrumentation and its crucial role in research, whether product formulation or process control variables are being investigated.

3.1 Wettability and adhesion in the liquid binder-particle interaction

In the previous chapter, it was pointed out that agglomeration of a fluid-bed mixture may occur at high temperatures through liquid bridging between particles. This can be achieved through sudden physical change of low melting components (e.g. hot-melt granulation, coal-ash gasification) or by addition of suitable liquid binders (either reactive or non-reactive) that solidify during operation.

Whether modelling of the process is required in order to control its performance, or final product properties represent the main goal of the experimental investigation, analytical methods have been developed to study the liquid-particle interactions at a microscopic level. In fact, the understanding of the type and extent of these interactions would certainly help with taking scaling-up decisions as well as process control procedures.

In this regard, Pietsch [2] stated the following:

In reality, one binding mechanism seldom occurs alone. In most cases several binding mechanisms participate in agglomerate bonding. Therefore, selection of the model substance for experimentation is of the utmost importance. In this context a suitable model substance is a particulate matter which, due to its chemical or physical characteristics and under the normal conditions of a specific process, allows the development of only one binding mechanism. This opens up the possibility to attempt a comparison of experimentally obtained data with theory.

A large number of systems, which fulfill the above conditions, have been employed in the past to modelling agglomeration: for example, in the case of agglomerates with liquid bridges or other wet agglomerates, distilled water and/or alcohol have been employed to agglomerate pure limestone or quartz powders [2].In such cases, simulated macro-scale effects of micro-scale phenomena are being studied. However, the development of micro-mechanistic approaches, which employ the actual process material, to determining the granule (product) properties and process performance have gained favour over recent years, since many believe that is the interfacial properties that are the governing parameters and that only by having a full understanding of the effects of these properties can macro-scale behaviour be accurately predicted.

For instance, in the pharmaceutical industry, powders frequently exhibit poor flow and compaction behaviour, making granulation necessary prior to tabletting. Pharmaceutical granules offer a further complexity to full understanding of formation and breakage under complex and different shear conditions (e.g. high-shear and fluid-bed granulators), since they are usually made up of mixtures of solid species (e.g. drug and excipient) that can exhibit very different interfacial behaviour when in contact with the liquid binder (which then is dried to a solid, often polymeric, bond). During pharmaceutical granulation, the objective is to produce granules that have, on average, a uniform (and repeatable) distribution of drug particles within the bulk carrier (excipient) solid. This can be difficult to achieve and both drug depletion and enrichment in granules can occur. Hapgood et al. [116] have proposed the following mechanisms for the causes of uneven drug distribution:

- Low extent of granulation, leaving behind significant amounts of un-granulated drug.
- Attrition of the granules during processing and handling, dislodging weakly held drug particles.
- Wetting differences between the components (e.g. a hydrophobic drug mixed with hydrophilic excipients).
- Particle size differences between the drug and excipients, causing one component to preferentially granulate over another.

- Solute migration during drying, causing transport of soluble drugs to the granule surface and recrystallization as the solutes evaporates.

Most of the reported studies in the literature tend to focus on the effects on drug/excipient distrbution as a function of differences in primary particle size (see, for instance, Refs. [117, 118]). Drug particles are usually very much smaller than excipient particles, which may be as large as 100 μm in diameter and be comparable to the median final target granule size of approximately 200 μm in diameter. Hapgood et al. [116] conclude that coarse granules tend to always be drug-enriched since the drug particles are the finest component and preferentially granulate, provided that the particles are capable of sustaining liquid bridges. This latter point is very important and is, in part, due to the wetting behaviour exhibited by the liquid binder on the solid particles (it can also be dependent on the amount of liquid required to saturate the excipient and, possibly, hydrate the binder before liquid is present on the particle surfaces). Hence, it would appear that a crucial step in optimising granulation performance would be to select the most appropriate drug/excipient/binder system to enhance the formation of liquid bridges between both solid species.

A case study will be hereafter presented in order to develop an analytical technique which minimises the amount of material required, based on micro-scale observation and measurement, to provide sufficient information to enable this selection. This work was carried out by the author in order to develop the use of off-line micro-scale measurement techniques for large-scale process optimisation.

3.1.1 Binder selection criteria: a case study

To minimise formulation development time, it is desirable to make an early decision on the type of binder for a drug, based on the binder's intrinsic ability to adhere the drug into granules. Two types of approach for selecting binder are considered here, both of which rely on optimising the ability of the binder to spread across the surface of the drug. In principle, the more the polymeric substance spreads across the surface of the particles, the larger the surface area of contact within the granules, and the greater the strength of adhesion. The ability for the binder to distribute between particles can be seen as the result of the competitive effect between the adhesion of the binder with the particle and the cohesion for itself. Such property is determined by the spreading coefficient S_p, which was previously defined in Equation 2.51 and whose expression is included here for clarity:

$$S_p = W_{ad} - W_{co}$$

In the first approach to binder selection, the thermodynamics of the final, dry product is considered; in the second, spreading in solution is considered. The more the binder

is able to adhere to the drug compared to its tendency to self-associate, the better the spreading and subsequent binding, which ultimately favors the mechanical properties of the agglomerate resulting from the formation of more uniformly distributed solid bridges during the drying phase.

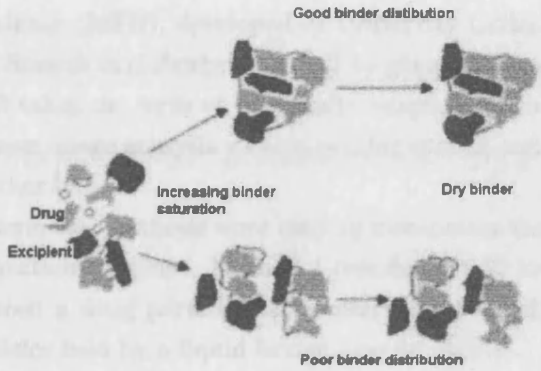

Fig. 3.1: Schematic representation of binder distribution during the process of granulation and drying.

The result of drying is that the binder forms bonds between particles (figure 3.1). If one assumes that the amount of bonding after drying is entirely determined by the thermodynamics of the dry materials, the binder can be selected on the basis of the dry polymer having a high spreading coefficient S_p (Equation 2.51). The dry spreading coefficient can be predicted from the surface free energies of the dry binder and drug, usually derived from contact angle measurements of probe liquids such as water and diiodomethane. Examples of such predictions are those of Rowe [81], where the spreading coefficient on paracetamol was predicted to increase in the order:

Starch $\prec$ PVP (polyvinylpyrrolidone) $\prec$ Acacia $\prec$ HPMC (hydroxypropyl methylcellulose)

Measurements of the granule friability, tablet strength and capping index of paracetamol wet granulated with these binders were found to be in line with this ranking. Rowe [80] showed that selection between binder systems for a drug can be gauged simply from the surface polarity of the drug concerned. A disadvantage of this approach is that it does not consider the effect of the solvent. During granulation, the binder solutions form wet bridges between the particles, allowing wet granules to be formed. If it is assumed that the amount of bonding after drying is entirely determined by the contacts set up during wet granulation, the binder can be selected on the basis of it giving a high spreading coefficient of the liquid across the surface. The effect of the binder on the wet spreading coefficient is usually determined by measuring the consequential decrease in the contact angle formed by the liquid on the solid surface. The binder selection is therefore addressed to the binder

giving the smallest contact angle value. An alternative technique, which is described hereafter, is to measure the forces experienced between two drug particles separated by a liquid bridge using a micromanipulator.

3.1.2 A novel experimental technique: The Micro-Force Balance (MFB)

A novel micro-force balance (MFB), developed at University College London, has previously been applied by Simons and Fairbrother [50] to glass ballotini in the study of wet granulation. The MFB takes the form of a specially adapted microscope stage, coupled, via a digital camera, to an image analysis video recording system and is described in detail in Simons and Fairbrother [50].
In the work reported here, two methods were used to manipulate the particles and to obtain images of the separation sequence. Method 1 (see figure 3.2) involved measurements on liquid bridges between a drug particle and a reservoir of solution binder, Method 2 between two drug particles held by a liquid bridge (see figure 3.3).

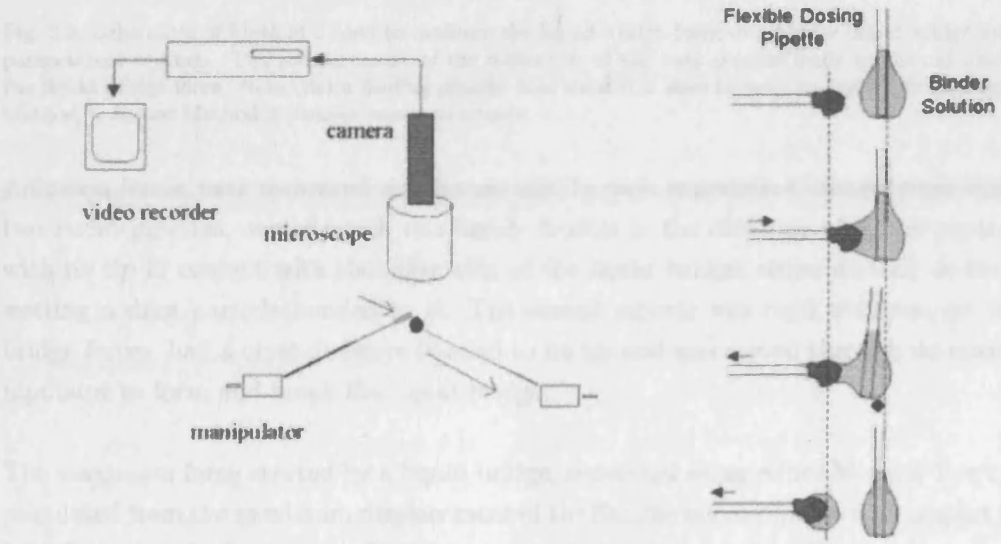

Fig. 3.2: Schematic of Method 1 used to measure the liquid bridge force between a reservoir of liquid binder and a single paracetamol crystal. The measurement of the deflection of the feeding pipette leads to the calculation of the liquid bridge force.

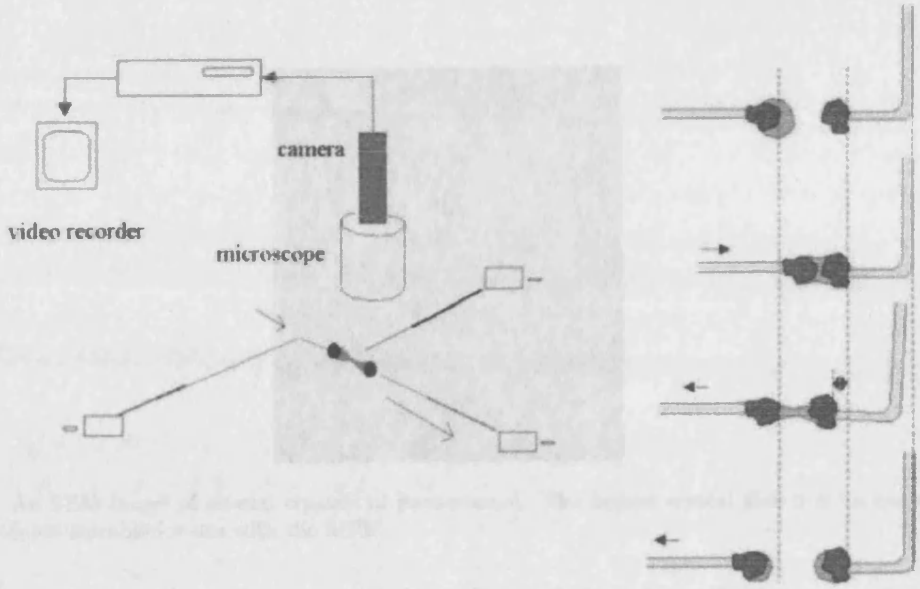

Fig. 3.3: Schematic of Method 2 used to measure the liquid bridge force of a binder liquid bridge and two paracetamol crystals. The measurement of the deflection of the bent pipette leads to the calculation of the liquid bridge force. Note that a feeding pipette (not shown) is used to wet the crystal, in analogy with Method 1, before Method 2 measurements are made.

Adhesion forces were measured simultaneously. In each experiment, images were taken of two micro-pipettes, one of which was highly flexible in the direction of bridge separation with its tip in contact with the other side of the liquid bridge, either directly or through wetting a drug particle bonded to it. The second pipette was rigid with respect to the bridge forces, had a crystal always bonded to its tip and was moved through its micromanipulator to form and break the liquid bridge.

The maximum force exerted by a liquid bridge, separated using either Method 1 or 2, was calculated from the maximum displacement of the flexible micro-pipette with respect to its initial, undisturbed, position. This micro-pipette was previously calibrated by attaching known weights to determine its spring constant, generally in the range between 0.1 and 0.3 N/m.

It was acknowledged that the force measurements taken using either of Methods 1 and 2 are affected by geometric factors such as particle orientation or the extent of the wetting area. Due to the extreme irregularity of the particles, (see figure 3.4), no attempt was made to measure the area of the crystal wetted by the binder in order to normalise the binder force. Due to the difficulty of attaching a crystal to the tip of the pipette, the orientation at which the crystals were bonded to the pipette was only coarsely controlled in terms of whether the crystal was attached as a prolongation of the tip or orthogonal to

it.

Fig. 3.4: An SEM image of several crystals of paracetamol. The largest crystal shown is an example of one considered suitable for use with the MFB.

Receding contact angles were measured through detailed analysis of the images of the liquid bridge stretching. The baseline of the particle surface was taken before liquid contact and the tangents to the liquid profile were taken at the points of liquid contact. The contact angle was then measured from the angle between the baseline and the tangent. The values obtained in this way were only indicative of the crystal-to-binder wetting behaviour since this method does not account for the asperities and irregularities of the crystal surface.

Other parameters, such as the bridge volume or the residual film of binder deposited onto a crystal, can be calculated directly from the images. For the experiment carried out using Method 1, the volume of the binder reservoir can be calculated as the solid of revolution generated by a parabola (the approximation of the binder meniscus) around the axis of the feeding pipette. For the experiments conducted using Method 2, the volume of the liquid bridge was calculated from the difference in the shape of the droplet on the dosing pipette before and after bridge formation. The profile of the liquid bridge on the feeding micro-pipette was approximated by a segment of a parabola and volumes were calculated through geometric revolution. The residual film of binder was observed after contacting the crystal and the liquid binder through Method 1. After each contact the crystal was flushed with an aqueous saturated solution of paracetamol to wash out any excess of the binder and to avoid crystal dissolution. The wet crystal was then dried with fresh air blown through a capillary tube positioned near the wet crystal. By using this washing/drying technique the crystal was never removed from its micromanipulator so that the orientation, the focus length and the light intensity were kept constant to avoid misinterpretations of surface properties during image processing.

Paracetamol crystals (Sigma Aldrich) were adhered to the glass micro-pipettes using

Loctite™ Super Glue GEL. The crystal were needle-shaped, only a small percentage of which were large enough to be successfully adhered to the pipettes.
Two different types of binder were employed. PVP (Plasdone K-29/32) was obtained from ISP. HPMC (Methocel, 6 cps grade) was obtained from Dow. Liquid binder was prepared with Analar water (BDH). Several liquid bridge separations were performed for each binder concentration. Five different concentrations ($wt_{\text{binder}}/ml_{H_2O}$) were prepared: PVP1%, PVP4%, PVP10%, HPMC1% and HPMC4%. It was not possible to use higher concentrations of HPMC due to the very fast drying rate. The 1% concentrations were used to investigate the deposition of residual binder films.

Not all drug-binder-drug (Method 2) experiments were successful, primarily due to the fast drying rate of the liquid bridges at the PVP10% and HPMC4% concentrations and the difficulties of dispensing small volumes of binder on to the crystals, especially with the PVP4% concentration. In contrast, drug-binder-pipette (Method 1) measurements were less susceptible to drying effects due to the larger volumes of liquid involved.

3.1.3 Wetting behaviour and post rupture liquid distribution

Figures 3.5 and 3.6 show that, on contact with the crystals, PVP solutions rapidly spread over the crystal surfaces (figure 3.5(b) and 3.6(a)). However, on withdrawing the crystals, the liquid dewetted the surfaces (figures 3.5(c) and 3.6(b)), leaving the profile of the paracetamol surface smoother than before wetting.
On both figures 3.5 and 3.6 the low contact angle shows a good wettability between the crystal and the PVPs. The contact angles are measured during the withdrawal of the crystal from the reservoir and, therefore, correspond to a receding phase. The differences exhibited by the two menisci can be attributed to the asymmetry of the contact between the crystal and the binder. contact angles, however, were only analysed qualitatively due to the irregularity of the crystal shape, which did not allow the experimental values to be calculated exactly.

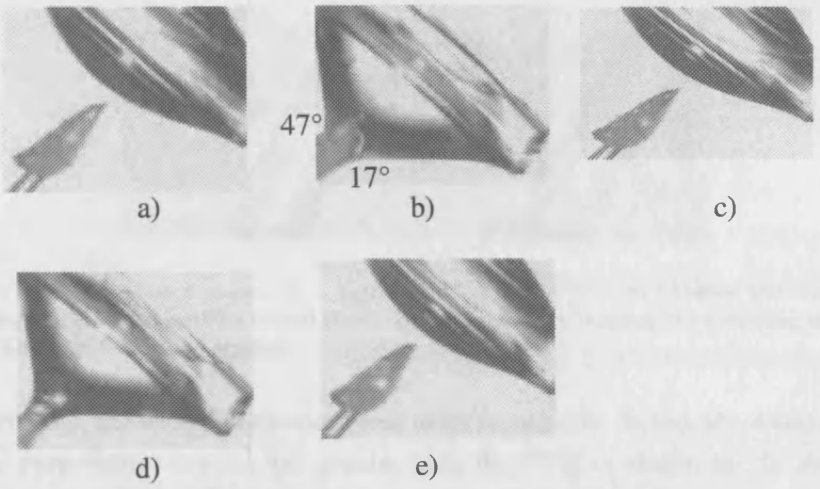

Fig. 3.5: PVP4% (a) initial approach of crystal to liquid, (b) first contact: crystal engulfed in liquid (c) removal of crystal from liquid, (d) second contact with liquid and (e) second withdrawal from liquid. The two contact angles indicated in frame b) refer to the three-phase contact lines and are calculated from an ideal smooth baseline.

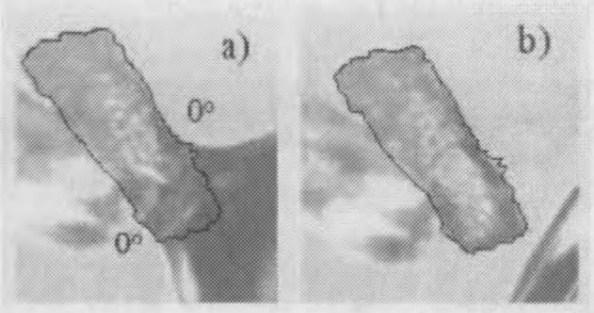

Fig. 3.6: PVP10% first contact: (a) crystal engulfed in liquid, (b) removal of crystal from liquid. The two contact angles indicated in frame a) refer to the three-phase contact lines and are calculated from an ideal smooth baseline.

On the first withdrawal of a crystal from the PVP solutions the meniscus receded from the surface of the crystal and only after the surface profile had been changed through wetting and withdrawal was it possible to deposit liquid of sufficient volume. In these repeated contacts it is plausible that some PVP may have become deposited on the surface (see figure), improving the spreading coefficient of the coated substrate. Alternatively, it cannot be excluded that in the experiment shown in figure 3.7, during the time spent to repeat the contacts between the crystals and the binder ($\approx 90s$), the concentration of the liquid binder may have increased due to partial evaporation of the water fraction. This latter effect would reduce the surface tension of the binder and therefore the cohesion energy in favour of the spreading coefficient adhesion energy.

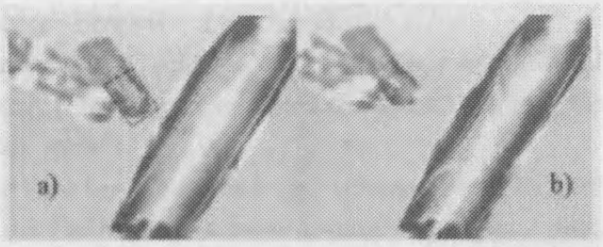

Fig. 3.7: PVP10% experiment presented in figure 3.6 after a few contacts between the crystal and the binder; a) dried binder has partially coated the crystal (black box) increasing the spreading coefficient. b) some liquid binder is left on the crystal.

With the HPMC, the wetting behaviour was more favourable. In fact the volume of binder left on the paracetamol crystal was greater than for PVP, as shown by the sequences in figure 3.8, where some liquid is captured on first contact. This effect can be explained by a lower surface tension exhibited by the HPMC4% solution if compared with those of the PVP solutions, which makes the rupture of the liquid bridge more energetically favourable than the liquid receding from the surface. Values of the surface tension, which were either calculated using a tensiometer (Kruss K12) or obtained from literature, are presented in Table 3.1.

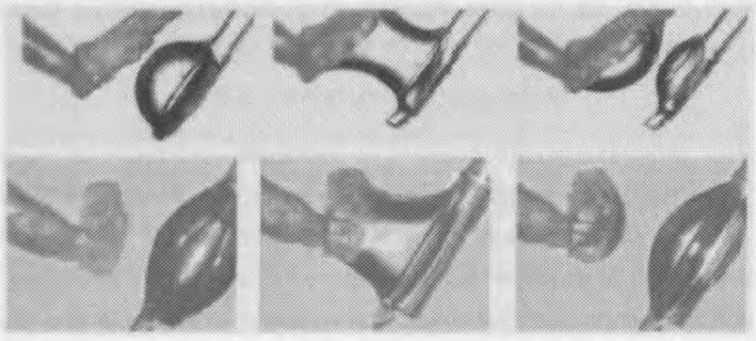

Fig. 3.8: HPMC4% and paracetamol crystal. First contact on both sequences.

Binder Solution	**Surface Tension, $\gamma_l[mN/m]$**	**Ref.**
PVP1%	67.3	
PVP4%	62	[119]
PVP10%	56.7	
HPMC1%	46.3	
HPMC4%	42.4	[120]

Tab. 3.1: Values of surface tension of the binder solutions.

For the PVP solution the cohesive energy of the binder is higher then the crystal-to-binder interfacial energy ad therefore it is thermodynamically more favourable the receding of the

interface rather than the breakage of the liquid.
On the contrary, for the HPMC solution, the complementary effects of interfacial (crystal-to-binder) and cohesive (binder) energy, favour the liquid binder breakage instead of dewetting from the crystals surface.
Questions arise as to whether or not the larger volume deposition exhibited by the HPMC solution in figure 3.8 is the result of a more favourable geometry when compared with the needle-shaped crystals used in the PVP experiments shown in figures 3.5 and 3.6. The wetting behaviour is indeed a matter of surface properties and is not largely influenced by the geometry of the crystal, as can be seen in figure 3.9, where a crystal engulfed in a PVP10% solution is withdrawn without retaining a large binder droplet.

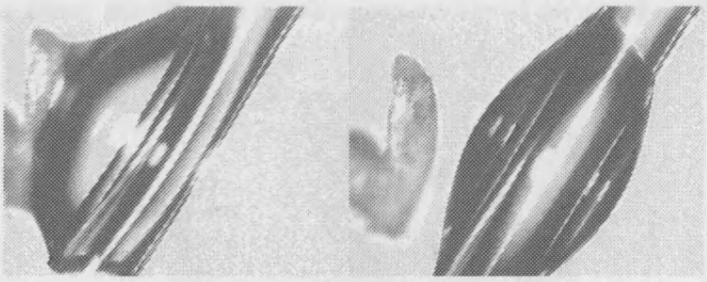

Fig. 3.9: Paracetamol crystal engulfed (left) in the PVP10% binder solution and after withdrawal (right).

3.1.4 Residual film deposition

By exploiting the methodology described as Method 1 it was possible to investigate the residue of binder left on the surface of the crystal after contact with the binder. Two crystals were used, one for the set of experiments involving PVP1% and the other for those carried out using HPMC1%. The experimental sequence of liquid bridge formation, crystal washing and drying was repeated five times for each crystal without moving the crystal from its micromanipulator.

Figures 3.10 and 3.11 show the images of the dried crystals in the five experiments and those of the virgin crystals.

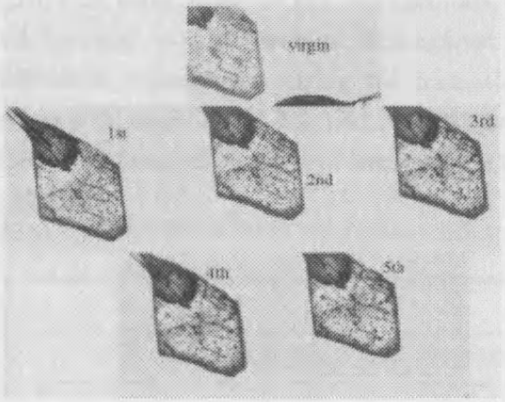

Fig. 3.10: Dried crystals after n^{th} wash for the experiments carried out using PVP1% as the binder.

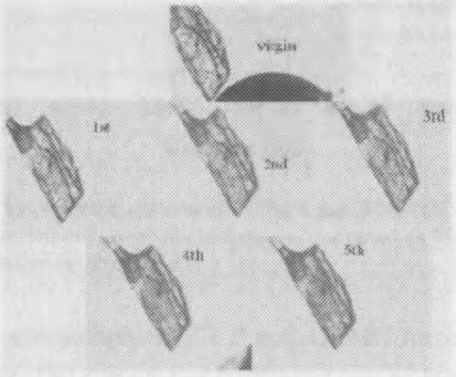

Fig. 3.11: Dried crystals after n^{th} wash for the experiments carried out using HPMC1% as the binder.

Although figure 3.10 shows that the PVP1% solution leaves some residue of binder on the surface of the crystal (indicated by the dark patches), there is a little difference between the first and the fifth wash. A different behaviour results from the HPMC1% solution (see figure 3.11), where the patches of dried binder enlarge with repeated washes to cover almost the entire crystal. The behaviour seems to confirm higher adhesion with the crystal in favour of the HPMC solutions.

3.1.5 Force measurements

The forces exerted by the liquid bridge were calculated using both Methods 1 and 2 and employing the techniques described in Section 3.1.2. The volume of the liquid bridge was often quite large with respect to the volume of the crystals and the formation of the bridge was often difficult using Method 2, especially with PVP4% which tended to leave the crystal surface unwet after contact as can be seen from the results of Method 1 in figure 3.5. In this case, the liquid bridge was successfully formed by displacing the binder droplet from the feeding pipette using the micromanipulators.

For each sequence of separation using either of the two methods, the force was evaluated at different distances and the maxima values were plotted against the volume of the liquid binder. Due to the difficulties experienced during the formation of the liquid bridge between two crystals (Method 2), results from Method 1 should be preferred especially for the PVP4% solution, where significant disagreement between the two methods is observed as indicated in figure 3.12.

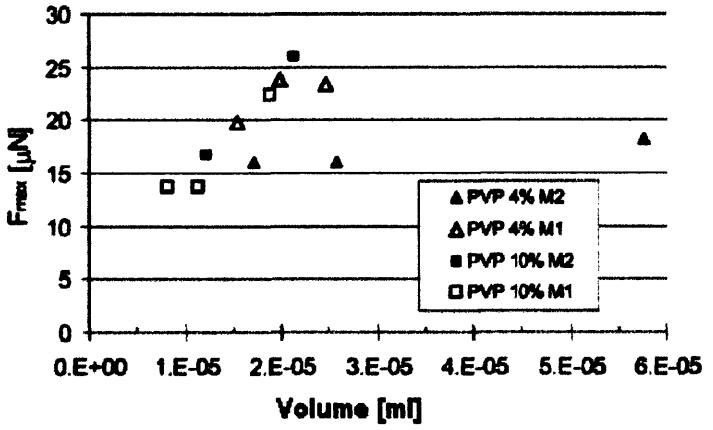

Fig. 3.12: Max. liquid bridge force versus volume of PVP4% and PVP10% solutions. The experiments of liquid bridge separations are carried out using the techniques indicated as Method1 (crystal-binder-pipette, M1) and Method 2 (crystal-binder-crystal, M2).

Figure 3.13 shows that a comparison of PVP and HPMC force data at the same binder concentration (either 1% or 4%) reveals the PVP solutions to have higher adhesion force in comparison to the HPMC, which is consistent with the higher value of the surface tension exhibited by the PVP solutions.

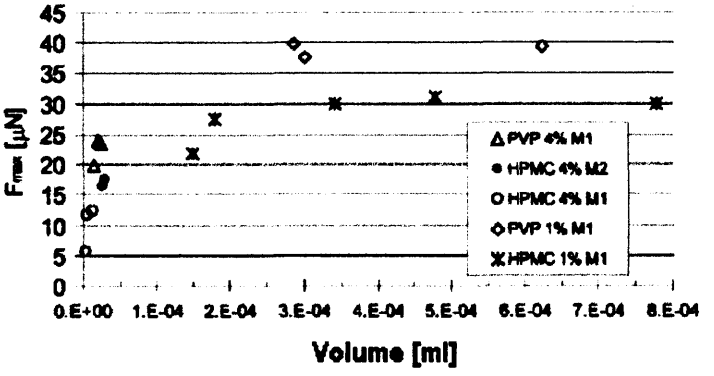

Fig. 3.13: Max. liquid bridge force versus volume of different binders for experiments of liquid bridge separation carried out using the techniques indicated as Method1 (crystal-binder-pipette, M1) and Method 2 (crystal-binder-crystal, M2).

All the force measurements were made only when the binder was in the liquid phase (i.e.

as soon as the bridges were formed). In fact, with the present set up, it was not possible to measure the change in adhesion force with time as the bridge dries to a solid[1]. This is principally due to the use of the deflection of the flexible micro-pipette in the calculation of the force. With solid bridges, this deflection is so great prior to rupture that it moves beyond the field of view of the microscope and therefore cannot be observed (see Chapter 7 in Ref. [122]). Two sets of cantilevers could be used to measure the bridge force before and after the liquid bridge solidifies; one, which is more flexible, for the experiments carried out when the binder is still liquid and a stiffer one for the case where the binder is dried. This method would imply two different experiments carried out on two different crystals and would not necessarily provide information about the evolution of the binder force with time, since the two experiments would probably involve different volumes of binder and crystal geometries.

The relative importance between the wetting behaviour and the adhesive strength of a single liquid bridge seems to lie in favour of the former parameter, which is responsible for the distribution of liquid binder during granulation. The low interfacial adhesiveness observed for the PVP solutions and the consequent tendency to dewet from the crystal surface seems to indicate that during granulation the binder would not be uniformly distributed between the paracetamol particles. Moreover, the high evaporation rate exhibited by the PVP solutions can rapidly increase the viscosity of the binder and contribute to enhanced differences in the binder distribution. These differences can lead to problems during the drying phase, since areas of fragility result within the agglomerate.

A different scenario holds for the HPMC solutions. The higher interaction at the crystal-binder interface improves the distribution of binder between particles and a more homogeneous mixture results during granulation. Since the mechanical strength of agglomerates is the result of the adhesive force of single solid bridges which are the result of binder crystallisation during the drying phase, the distribution of binder just before drying is a fundamental parameter to achieving uniform mechanical properties and controlling the process performance. This conclusion is in agreement with previous results obtained by Rowe [81], who found that paracetamol gave lower granule friability, lower tablet capping index and higher tablet strength when granulated with HPMC than with PVP. Rowe explained this in terms of the spreading coefficient of the dry binder. The results here reported suggest another possible mechanism: HPMC solutions spread better over the drug, generating stronger liquid bridges than PVP solutions.

The effects of viscosity and drying on the liquid bridge forces (as well as the dewetting behaviour and crystals geometry) require further investigation. In fact, both PVP and

[1] This kind of study has been previously undertaken by Tardos and Gupta [121] and is reviewed in Section 3.2.3 of this thesis.

HPMC solid bridges exhibit very strong adhesion that is outside the measuring capability of the MFB equipment. Moreover, the use of the MFB presents further limits: it requires lots of dexterity and skill in preparing the micropipettes and performing the experiments and a considerable amount of time is also spent in forming and calibrating micropipettes. Furthermore, another limit of the MFB used in this work is the difficulty experienced in measuring the adhesive force using the current micro-manipulator components and this limit directed most of the investigations of liquid bridge adhesion towards using image analysis [122]. As a result, improvements have now been made to the system to increase the range of movement and the displacement resolution. In addition, for the high temperature work reported in this thesis, changes were made to negate the need to manufacture the flexible pipettes (see **Chapter 5**).

Among the mechanisms that can be investigated using the MFB, the measurements of the liquid bridge strength (either axial or of shear), the post rupture liquid binder distribution, the advancing and receding contact angles (binder-to-particle), the binder drying rate and the particle shape and porosity all have an impact on the final performance of an agglomeration process. Some of these quantities can also be measured using more traditional techniques. Investigations of wettability and post rupture binder distribution can be successfully obtained on samples of larger dimensions in the cm scale. Contact angle measurements can be achieved by either using the Wilhelmy-plate technique or by direct observations of liquid binder deposited on large samples. Solid-particle adhesiveness can be measured using a processor tensiometer. These types of measurement can be integrated with the data obtained using the MFB to obtain a clear picture of the phenomena behind agglomeration, both at a macro (e.g. powder flow) and micro (particle interactions) scale.

3.2 Scaling-up from interparticle forces to multibody systems

The cohesive properties of powder materials (e.g. agglomerates) predominantly determine their flowability. Thus, parameters such as cohesion, unconfined yield strength, and tensile strength are important information for reliable design of process equipment. During the past hundred years, many methods and devices have been developed to determine the flow properties of powders [123]. In particular, shear testers are well investigated, and for some applications, such as silo design, it is well understood how shear test results can be interpreted and used [124].

However, shear testers fail if the desired range of normal loads is too small and important properties, such as the cohesion and the tensile strength can only be obtained by extrapolation. In fact, the data defining *strength* obtained from these tests cannot be theoretically described because stressing is not uniform and the specific strain leading to failure is normally not known. Theoretically, the extrapolation could be validated against the tensile

strength obtained from tensile tests with split cell testers and watch-glass testers [125], but, unfortunately, attempts to apply these techniques have not been very successful so far.

There are mainly two conceivable explanations for this apparent lack of success. First, at present no sample can be used twice, in either a shear test as well as a tensile test. Therefore, it is difficult to ensure identical micro-structural conditions. Secondly, the design and operation of shear and tensile testers are very different. In consequence, it is also difficult to confirm any theories trying to estimate cohesive properties.

One of the important advances in the study of powders was the development by Rumpf [7] of the concept that the strength of an agglomerate, σ_t, or a cake can be calculated from the strength of interparticle bonds, F, and some other powder characteristics (see Section 2.2.4):

$$\sigma_t = \frac{1-\varepsilon}{\varepsilon^2}\frac{F}{d_p^2} \tag{3.1}$$

where σ_t is the tensile strength, ε is the porosity of the granule and d_p is the initial particle size.
The expression was proposed for the determination of tensile strength of agglomerates for scientific investigations. Data from such tests can be compared with each other, approximated with physical models, and described by theories. Since, with a high degree of probability, failure always occurs at the highest tensile strain, Rumpf's proposal is justified [2].

Following Rumpf's approach, Johnson et al. [126] and Kendall et al. [127] applied the concepts of modern material science of fracture mechanics to the calculus of the tensile, σ_t, and yield, τ_y, strength of an agglomerate where the dry granules are held together by auto-adhesive forces, thus providing a mathematical extension to Rumpf's expression, as indicated by (3.2) and (3.3):

$$\sigma_t = 24.7 z(\varepsilon)\frac{\gamma_s}{d_p} \tag{3.2}$$

where z(ε) is a function of porosity (see Section 3.2.2) and γ_s is the solid surface energy, which is assumed to be equal to the interfacial fracture energy.

$$\tau_y = 0.5\frac{K_c}{\sqrt{c}} = 15.5\frac{(1-\varepsilon)^4 G}{\sqrt{c d_p}} \tag{3.3}$$

where c is a characteristic defect size (i.e., measure of cracks in the material), K_c is the fracture toughness and G is the adhesive surface energy of the interparticle bonds. These

theories predict that, in order to separate bodies in intimate contact, mechanical work must be expended to overcome the adhesive forces and that this work goes to create new surface. Moreover, the behaviour of solids differs markedly from that of liquids. The spreading or contracting of one liquid surface over another or over a solid surface to reach an equilibrium state is dominated by the minimization of surface energy. For example, when a liquid drop is brought into contact with a solid surface its final contact size at equilibrium may be predicted from surface energy considerations (see Section 2.2.9). On the other hand, when a contact is formed between two solid surfaces, the equilibrium largely depends upon the distribution of elastic forces in the contacting bodies. However, Johnson et al. [126] concluded that, under conditions of light loading between elastic solids, surface forces can make a significant contribution to the contact equilibrium.

Furthermore, there are particular cases where the consolidation of a newer solid interface between two particles can start from the initial formation of a liquid bond, which, depending to its physical properties and process conditions, undergoes a phase change to become solid. In such cases, theories on the tensile strength of an agglomerate and prediction of the solid bridge strength are mostly related to surface energy considerations.

Since agglomerates are composed of discrete primary particles which are held together by a number of interparticle forces, significant progress has been made recently in developing closed-form solutions for various interparticle forces including auto-adhesion (JKR theory [126]), friction [128] and liquid bridging [18]. However, their effect on the macroscopic behaviour of agglomerates is still not well understood. From a microscopic point of view, the mechanical behaviour of agglomerates is completely determined by the interactive forces between the primary particles as functions of their relative locations and velocities. Lian et al. [14] observed that while this is a nominally simple description of agglomerates subjected to a particular stress or velocity field, the many-body calculations, involved in determining the evolving microstructure, gross geometries and energy dissipation processes, require a numerical simulation scheme.

Lian et al. [14] have studied by computer simulations, the deformation behaviour of moist agglomerates formed in a gaseous system. The model is focused on the dissipation mechanisms of the kinetic energy upon collision of two agglomerates, which is illustrated in figure 3.14. Dissipation of kinetic energy for the moist deformed agglomerates was not solely due to the viscous resistance and breakage of the interstitial liquid bridges, but also to rearrangement (plastic deformation) of the particle structure, which involves friction dissipation according to the JKR theory [126]. By setting the viscosity of the binder at 10 mPa s and the collision velocities in a range between 0.5 and 5 m/s, the viscous force was found to account for the dissipation of about 60 % of the initial kinetic energy. Energy dissipated by friction was also very significant ($\approx$ 30%), whilst the energy dissipated as a

result of rupturing the internal liquid bridges was only a small proportion, at around 5 %. Despite the small contribution to the overall deformation energies, the authors pointed out the important implications that liquid bridge breakage has on the internal damage suffered by the agglomerates.

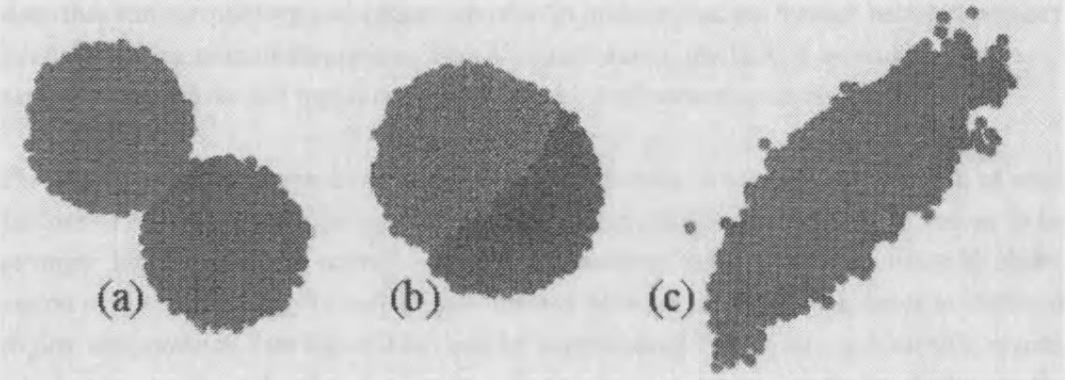

Fig. 3.14: Visualizations of computer simulated wet agglomerates for an interstitial fluid viscosity of 10 mPa s after impact at relative velocities of (a) 0.5 m/s, (b) 2.0 m/s and (c) 5.0 m/s. From [14].

3.2.1 *The effect of drying on the particle-binder-particle adhesion*

In wet granulation processes, agglomeration is usually caused by the addition of a binder solution of a rather low viscosity, typically within the range of 2-300 mPa·s. In a fluidised bed granulator, however, a marked evaporation of the solvent occurs during the process. This will increase the viscosity of the binder solution and the liquid bridges within the agglomerates might rapidly become immobile (i.e. solid), thus causing changes in both product properties (e.g. size, porosity and strength of granules) and flow behaviour (e.g. formation of large lumps,which require higher rupture energy to be broken to insure powder flow). Moreover, a similar problem occurs in the dry granulation technique (hot melt granulation), which exploits adhesion developed by the melting or softening of materials that are heated to near their melting point. In such processes the viscosities of the molten binders are normally higher than the viscosities of the binder solutions used for wet agglomeration. It has been found that the agglomerate growth rate can increase in an uncontrollable way when the viscosity exceeds an upper critical limit, which is dependent on the initial material and process variables [129].

An accepted view holds that the liquid binder wets and spreads in the interstices between primary particles, forming liquid bridges that hold them together by capillary and viscous forces. These wet or "green" granules are subsequently dried and liquid evaporates from the bridges to leave behind solid bridges or "necks" that impart mechanical strength to the dry granules.
Formation and strength of liquid bridges between fine particles has been studied exten-

sively (see **Chapter** 2). More recently, Pepin et al. [43] applied the knowledge gained from the study of these bridges to the strength of moist agglomerates, such as "green"granules, and, in the attempt to scale-up micro-data to macro properties, they assumed a certain granule structure and binder distribution. Solid bridges, on the other hand, have been studied to a much lesser extent; in fact, there is very little in the open literature that describes the morphology and properties of solid bridges that are formed between primary particles during granule formation. This is mainly due to the lack of dedicated instrumentation, which allows the measurement of such kind of particle-particle interactions.

Pietsch [2] in his monograph on agglomeration processes recognized the strength of solid bridges to have a strong influence on the tensile strength of agglomerates, as well as to be strongly dependent on the operative drying temperature: such a point was made by observation of the morphology of salt bridges formed between model glass spheres at different drying temperatures (see figure 3.15) and by experimental tensile strength measurements, which were conducted, after drying at different temperatures (see figure 3.16), on the core of agglomerated glass particles with salt bridges. Results showed that, in the case of Sodium Chloride (NaCl) crystallized between glass spheres, thinner and stronger bonds resulted at higher drying temperatures. Nonetheless, the intrinsic strength of the bridge itself was not studied.

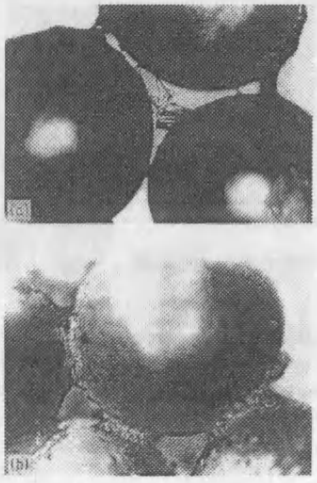

Fig. 3.15: Sodium Chloride (NaCl) crystallized between glass spheres during a model experiment. (a) Drying at room temperature, (b) drying at 110 oC. Differences in the drying rate of the solid bridges may have consequences on the tensile strength of the agglomerate. From [2].

Various drying mechanisms described in literature indicate that, in reality, to establish mechanistic relationships between agglomerate strength and the strength of a dried bridge is quite complex. Different scenarios may hold during drying, which may hinder either theoretical or experimental approaches to the problem. In fact, if one assumes some solubility of primary (solid) particles in the fluid, the liquid bridges can be multicomponent solutions

that may form solid bonds of complex microstructure when dried [130]. For instance, a schematic of a dry granule produced with granulating fluid containing a polymeric binder is presented in figure 3.17.

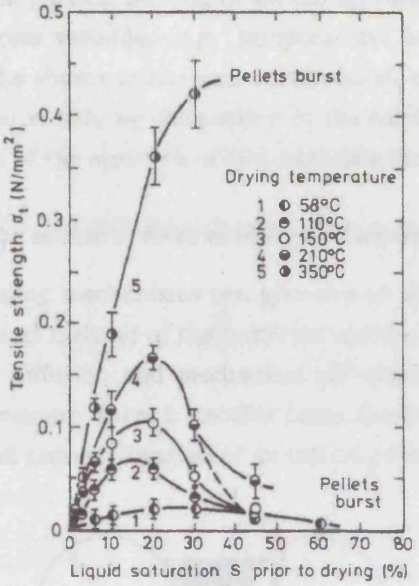

Fig. 3.16: In this example, the tensile strength of the core of agglomerates with salt bridges is plotted versus liquid saturation at various drying temperatures, after [2].

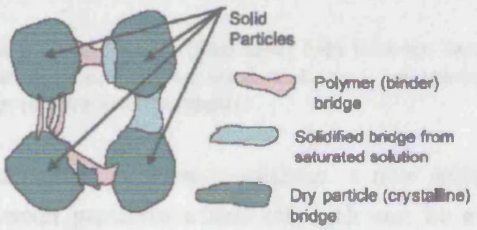

Fig. 3.17: Schematic of dry interparticle bridges formed by coprecipitation of base powder and polymer. The bridge on the left consists of filaments of polymer. The bridge on top contains both the polymer and a solidified crystalline bridge formed by recrystallization of the base powder. The bridge on the right is pure recrystallized base powder that is only partially attached to the upper particle due to poor wetting of the parent liquid bridge. The bridge on the bottom is a combination of a small primary particle embedded in recrystallized base powder, after[130].

Bika et al. [130] clearly proposed in such a schematic only some of a large variety of combinations that could exist in reality, thus leading to the following questions that must be answered to achieve a better knowledge of dry granule strength, namely:

What kind of solid bridge will actually form inside the granule as liquid evaporates? What will characterize its strength? What are the governing interfacial energies? Where will it break when subjected to a mechanical load? Will it break by fracture of the bridge body

or by adhesive failure at the interface with the primary particle?

It is evident that, depending on the type of process and bridging mechanism examined (e.g. sintering obtained from particle melting or softening) further questions can be added on the role of certain process variables (e.g. temperature, humidity) on the quality of bonding. However, it will be shown in the next section that, due to the nature of such a study, models can be validated only by comparison of the calculated bridge strength with independent measurements of the strength of the materials involved in bridge formation.

3.2.2 *Prediction of the adhesion force developed after drying of a liquid bridge*

A number of different bonding mechanisms can give rise to dry neck formation between particles. While sintering and melting of the particles surface represent the class of solid bridges that may form by diffusion and mechanical deformation under the influence of high temperature and/or pressure, there is another class of solid bridges that starts out by evaporation, dissolution and recrystallization of an initially formed liquid bond, see figure 3.18.

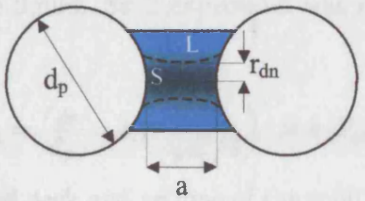

Fig. 3.18: Evolution of an initial liquid bridge (blue area) held between two equal sized particles during drying. The interparticle distance, a, and the dried neck, r_{dn}, are necessary parameters required to calculate the final solid bridge (darker area) strength.

In both cases and depending on process conditions, a new solid interface with distinct properties is formed between particles whose strength can be evaluated from Equation 3.4, provided that the bridge can be considered of cylindrical shape (with r_{dn} the base radius) and breaks at its narrowest point (and not at the interface with either particle):

$$F = \pi r_{dn}^2 \sigma_{sb} \tag{3.4}$$

where r_{dn} is the dried neck (i.e. the narrowest point) of the solid bridge and σ_{sb} is its strength. In this equation, the force and the corresponding stress can be either tensile (compression or tension) or shear.

In order to evaluate the strength of an agglomerate, σ_t, a further equation is necessary to establish a relationship between the agglomerate strength and the strength of the solid bridge, σ_{sb}. Such equation is provided by Rumpf's correlation, which has been rewritten as follows

$$\sigma_t = z(\varepsilon)\frac{F}{d_p^2} \tag{3.5}$$

where $z(\varepsilon)$ is a function of porosity that assumes different forms according to whether Rumpf's (i.e. $z(\varepsilon) = (1-\varepsilon)/\varepsilon$) or Kendall's (i.e. $z(\varepsilon) = 13.3(1-\varepsilon)^4$) expressions are employed.[2]

In order to derive a useful expression, Equation 3.6, that correlates the strength of both an agglomerate and a solid bridge, expressions 3.4 and 3.5 can be now equated, provided that the values assumed by the dry neck, r_{dn}, during drying are known.

$$\sigma_t = \pi z(\varepsilon)\frac{r_{dn}^2}{d_p^2}\sigma_{sb} \tag{3.6}$$

Simple considerations on conservation of mass led Pietsch and Rumpf [37] to derive a semi-analytical expression (not reported here), where the dried neck, r_{dn}, is a function of the initial liquid bridge volume, V_b, and the volume of the dried bridge, $C_s V_b$. Here C_s is the solid concentration in the liquid. Such expression was rewritten by Bika et al. [130] as follows

$$r_{dn}^* = \frac{r_{dn}}{d_p} = b\left(\frac{C_s V_b}{\rho_p d_p^3/8}\right)^c = b\,(V_{sb}^*)^c \tag{3.7}$$

where r_{dn}^* and V_{sb}^* are the dried neck and volume of the solid bridge normalised to particle diameter and volume, respectively, while b and c are coefficients that are functions of the normalised interparticle distance $a^* = 2a/d_p$, as indicated in Table 3.2:

$a^* = 2a/d_p$	b	c
0	0.288	0.210
0.01	0.381	0.326
0.02	0.717	0.494
0.03	1.170	0.680

Tab. 3.2: Coefficients b and c in Eq. 3.7. After [130].

The values presented in Table 3.2 were obtained by assuming that the bridge volume is

[2] It should be noted that Rumpf's equation has been derived for the tensile strength calculation of wet agglomerates and that the model is based on the following assumptions:

- All the particles are monosized spheres, statistically (on the average uniformly) distributed in the agglomerate.
- The bonds are statistically distributed across the surface and over the directions in space.
- The effective bonding forces are distributed around a mean value, F, which can be used in the calculations.

small (as would be the case for solid bridges formed by evaporation) and the meniscus of the bridge surface conserves its circular curvature as it shrinks and precipitates its dissolved solids. Other formulae can be found in literature, which provide analytical and empirical solutions of the neck size either at particles contact (Pepin et al. [43]) or as function of other parameters (Ref. [23] cited in [130]). Although Equation 3.7 is considered more precise than non analytical solutions and therefore should be preferred in the calculation of the dried neck size, it requires knowledge of the distance between particles within the agglomerate or, in other words, the coefficients b and c must be obtained through best fitting of the granule strength plotted against the dimensionless bridge volume, thus involving experimental errors related to the reproducibility of results, as explained in Section 3.2.

Hence, alternative expressions should be searched, where possible, among those independent from the interparticle distance. In this regard, Figure 3.19 shows a comparison between the semi-analytical approach of Pietsch and Rumpf [37] and the empirical extrapolation, Equation 3.8, derived at zero interparticle distance by Pepin et al. [43] and rewritten on the basis of their results by Bika et al. [130] as follows

$$r^*_{dn} = 0.42 \left(\frac{C_s V_b}{\rho_p d_p^3 / 8} \right)^{1/3} = 0.42 \sqrt[3]{V^*_{sb}} \tag{3.8}$$

It appears that, despite the fact that the empirical expression, (Eq. 3.8), was derived at zero interparticle distance ($a^* = 0$), it actually fits well with the values obtained from (3.7) at $a^* = 0.01$. Such a discrepancy can be explained by a possible error made by the authors in the determination of the zero/contact distance through image analysis[3]; however, it should be noted that, in practice, no absolutely smooth particles are found, and therefore the case $a^* = 0$ seldom occurs in a real agglomerate.

It can be seen that, for adimensional bridge volumes, V^*_{sb}, ranging between 10^{-2} and 10^{-1}, values of the dried neck size obtained from Equation 3.8 are quite similar to those calculated through the semi analytical approach, (Eq. 3.7), whereas, for smaller bridge volumes, between 10^{-2} and 10^{-4}, the interparticle distance starts to have an influence.

[3] Pepin et al. [43] employed glass spheres of average diameter equal to $100\mu m$. In this case, consider that $a^* = 0.01$ means a separation of approximately $1\mu m$ between spheres, and that the experimental error committed according to such evaluation is $\pm 1\mu m$.

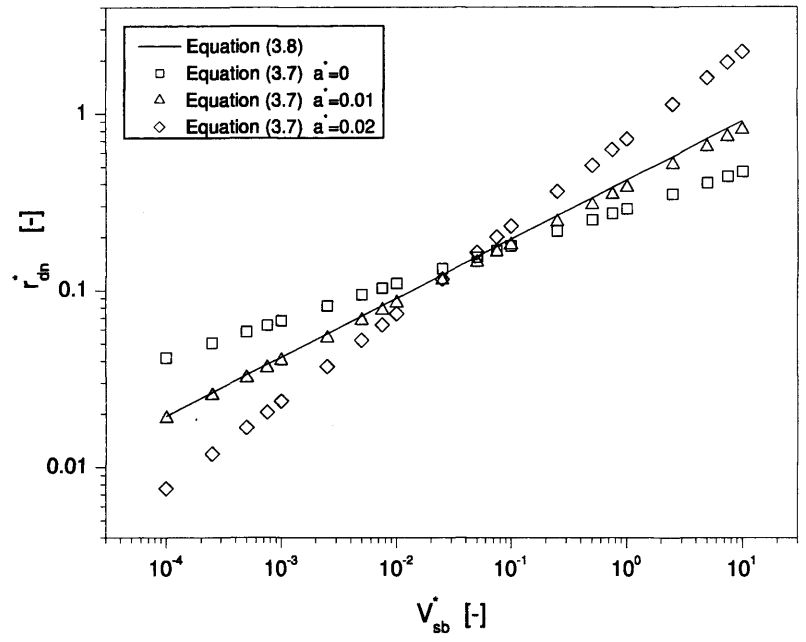

Fig. 3.19: Dimensionless dried neck radius, r_{dn} vs. solid bridge volume.

Combining Equations 3.6 and 3.7 yields a direct dependence of the granule strength on the volume of the initial liquid bridge and the solid concentration as follows:

$$\sigma_t = z(\varepsilon)\pi b^2 \left(\frac{C_s V_b}{\rho_p d_p^3/8}\right)^{2c} \sigma_{sb} \tag{3.9}$$

Equation 3.9 can be used to evaluate the tensile strength of an agglomerate σ_t if the strength of the solid bridge, σ_{sb}, is known. Alternatively, the bridge strength can be evaluated through independent measurements of the agglomerate strength. In both cases, the model presented by Bika et al. [130] can be validated with independent measurements of both parameters.

Tardos and Gupta [121] were among the first who pioneered the study of solidifying liquid bridges by investigating, at a microscopic level, the variation of solid bridge properties with composition and drying rate. In their work, presented in the next section, they observed the microstructure of individual solid bridges and its time evolution directly in an effort to understand the factors that determine interparticle bridge strength in dry granules.

3.2.3 Measurement of the adhesion force developed during drying of a liquid bridge

The experimental approach proposed by Tardos and Gupta [121] aimed to investigate the strength exerted by a liquid bridge initially formed between two particles and left drying at room temperature (T=20 °C and 55-60% RH). In particular, the forces generated by two different types of solutions were measured, namely: an aqueous solution of carbowax-PEG 350 ($C_s = 28$ wt.%), which was used to simulate the drying properties of a typical binder used in granulation, and a saturated solution of sodium carbonate that was used to elucidate the behaviour of a typical crystalline powder during a caking process.

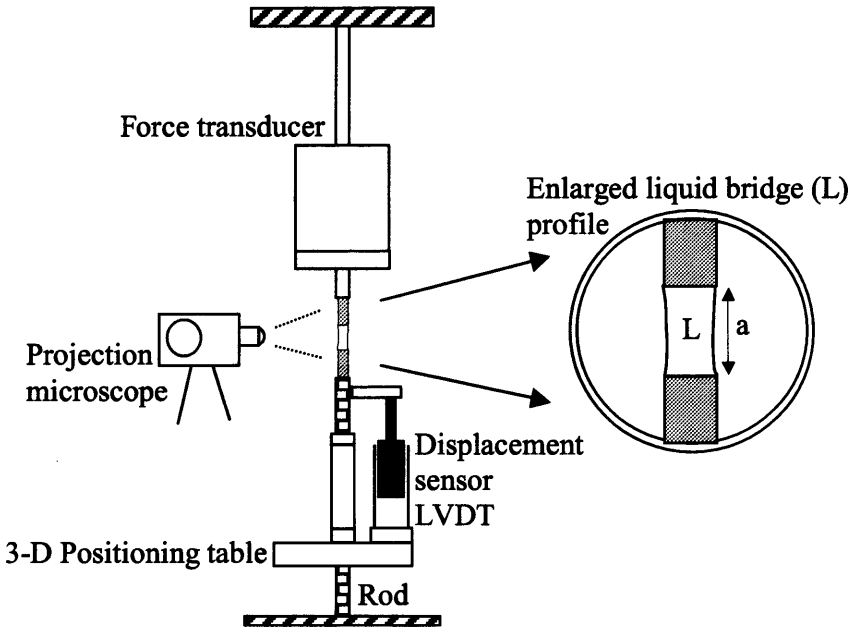

Fig. 3.20: A schematic of the experimental set up employed to study the strength of a drying liquid bridge. Adapted from[121].

In both experiments, the authors employed glass particles in the shape of small cylindrical rods (5 mm in diameter), thus focusing the objective of their research on the mechanical strength of the drying bridge by neglecting the important influence of the dissolution of primary particles into the liquid binder.

A schematic of the experimental set up employed in their investigation is depicted in figure 3.20, whereas details of the experimental method can be found in [121].

In a typical experiment, the strength exerted by the bridge during drying is measured by a force transducer (maximum load 5 g and sensitivity ± 2.5 mg) through imbalance of its magnetic reluctance, which releases a pre-calibrated electrical signal equal to 2.775 V/g. Such a signal is filtered and amplified through a carrier demodulator which gives up to 1 mV/volt sensitivity. A projection microscope ensures the coupling of force measurement

technique with direct observation of the liquid bridge profile: in fact, the evaluation of the initial liquid volume was achieved through image analysis.

Results were produced in the form of dimensionless force (the measured value has been divided by the initial weight of the bridge, that is $m_0 = \rho V_b$) plotted versus (drying) time, as shown in figures 3.21, 3.22 and 3.23.

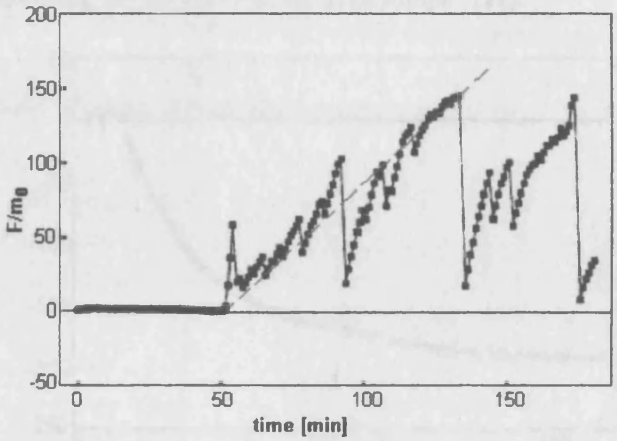

Fig. 3.21: Strengthening of a solidifying bridge of carbowax (PEG 350) solution. Large volume, $m_0 = 46$ mg, $a = 0.23$ cm. A red dashed line was drawn in order to obtain an approximate calculation of the drying rate of the liquid bridge. From [121].

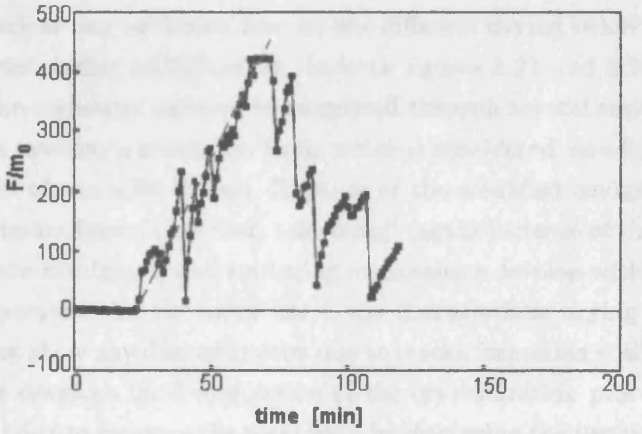

Fig. 3.22: Strengthening of a solidifying bridge of carbowax (PEG 350) solution. Small volume, $m_0 = 13.1$ mg, $a = 0.135$ cm. A red dashed line was drawn in order to obtain an approximate calculation of the drying rate of the liquid bridge. From [121].

There is evidence, from a comparison between results, of the different nature of strengthening mechanisms developed by carbowax and sodium carbonate solutions. Upon drying, the former produces a positive attractive force (see figures 3.21 and 3.22) that increases upon a certain limit during evaporation of the water solvent and further solidification of

the bridge. On the other hand, the latter develops a negative strength that pulls the particles apart during crystallization, as shown in figure 3.23. This result was used by the authors to provide a possible explanation of the caking problem on a microscopic point of view: in fact, changes in temperature and/or relative humidity can result in solvent (water) evaporation and the formation of dry bridges. Compressive forces generated at this point will compact the material until mechanical deformation of the particle surface takes place, thus resulting in the creation of large lumps [121].

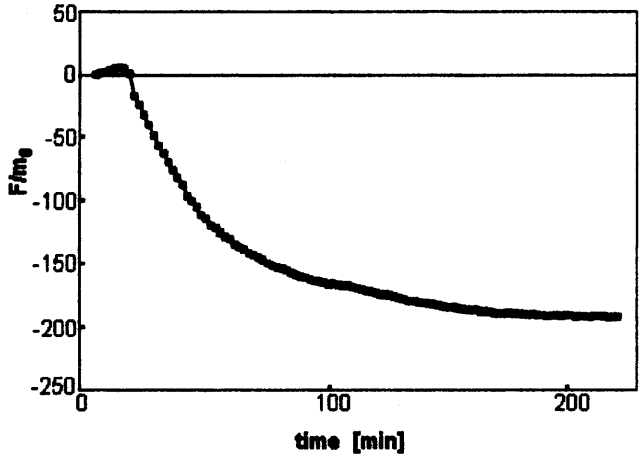

Fig. 3.23: Strengthening of a solidifying bridge of sodium carbonate solution, $m_0 = 26$ mg and $a = 0.13$ cm. From [121].

Further considerations can be drawn here on the different drying behaviour shown by the two types of binder during solidification. In both figures 3.21 and 3.22, it appears that solidification of the carbowax solution is completed through several rupture and strengthening steps before reaching a maximum force, which is considered, as a first approximation, to be the strength of the solid bridge. Rupture of the solidified bridge also occurs after reaching the maximum force; after that, reforming[4] (again increase of the total force up to values similar to the maximum) and rupturing mechanisms develop within the bridge until all solvent is evaporated. On the other hand, the characteristic drying curve reported in figure 3.23 does not show any discontinuities due to cracks formation within the bridge, and the strengthening develops until completion of the crystallization process. In this latter case, the authors tried to measure the total force by displacing the two particles in order to obtain the rupture of the solid bridge. Unfortunately, detachment of the bridge/particle interface occurred for all attempts and no experimental data are available. Obviously, the difference in the solid concentration of the two solutions (28% for the carbowax and saturation for the sodium carbonate) generates, during and after solidification, cohesion forces of different type and magnitude. Moreover, in the case of the carbowax solution,

[4] The bridge was helped to reform by re-approaching the particles through manipulation of the rod (see figure 3.20).

the presence of both large internal forces that develop during solidification and residual stresses can explain a common observation in granules produced by binder granulation namely, internal cracks [121]. Hence, the authors proposed the instrument and procedure described here to be used for optimal binder selection by using the actual solid particles in the experiment attached to the "arms" of the measuring device.

Possibly the most important aspect of this work regards the effect of the drying rate on the strengthening process. Since it was not possible to intervene on certain parameters, like temperature and relative humidity, the authors compared the drying behaviour and total force of increasingly large volumes of carbonwax solution.
As can be expected, Tardos and Gupta [121] noted substantial differences in the drying rate of large bridges in respect to the smaller ones. This can be better observed by drawing a straight line between the value of the force just before the steep increase due to solidification and the first measured value of the maximum force (red dashed line drawn in figures 3.21 and 3.22). The slope of such lines represents the rate of approach to the maximum force during time of solidification (i.e. drying rate), which inherently depends on the initial liquid volume (or weight). By approximately calculating the slopes from the published results and plotting versus the reciprocal of the initial liquid mass $1/m_0$, a trend line can obtained, as shown in figure 3.24:

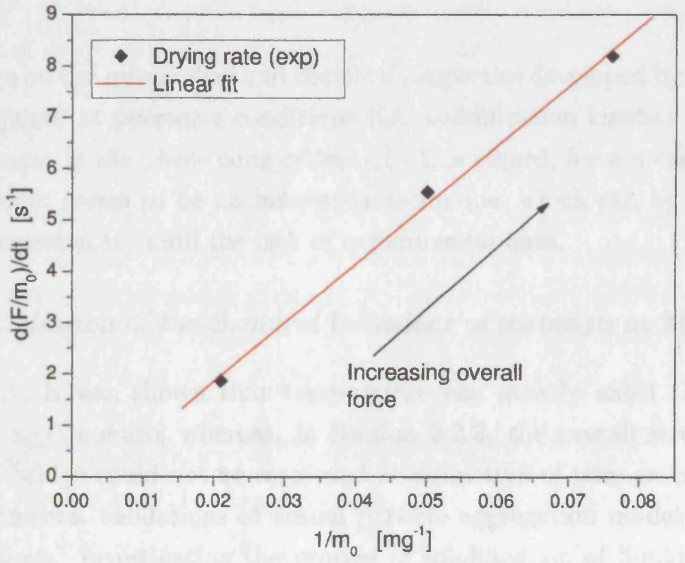

Fig. 3.24: At ambient conditions, the drying rate of a 28% solution of carbon wax appears to be inversely proportional to the initial mass of liquid bridge.

Hence, from figures 3.21, 3.22 and 3.24 it can be concluded that during solidification of a large bridge of carbonwax solution, since the material dries somewhat more slowly, it attains smaller peaks of force before breaking. On the contrary, smaller bridges develop higher strength in a shorter time. Larger bridges contain more liquid and the distribution of solid and liquid material, as the bridge dries, is less uniform with respect to smaller bridges. This can be the cause of more internal ruptures and hence smaller overall forces. Furthermore, the authors did not exclude that the initial interparticle distance would have played a role, since larger liquid bridge volumes require wider separations and therefore experiments were not conducted at the same initial condition.

These findings suggest that small liquid bridges require further investigation, since they might have an overwhelming effect on the process outcome. Moreover, appropriate measures to generate small bridges (by controlling spreading and liquid adsorption) and to control drying rates (by adjusting temperatures and gas flow rates) will thus have tremendous influence on the control of the process. Results of rupture force tests obtained through micromanipulation techniques, see for instance [131, 132], showed that real particles can be employed in order to ascertain whether the way primary particles adhered had a significant impact on the breaking force of the formed aggregate. Such a technique can be used to characterize the breaking force of a wide range of aggregates used in the chemical and bioprocessing industries, and should therefore help in the elucidation of agglomerative mechanisms.

More knowledge on the mechanical and chemical properties developed by process materials is therefore required at operative conditions (i.e. solidification kinetics and adhesion developed by changes in the phase composition); in this regard, force measurement through micromanipulation seems to be an innovative technique, which can be coupled to traditional instrumentation to fulfill the lack of experimental data.

3.3 Characterization of the chemical behaviour of materials at high temperature

In Section 3.2.1, it was shown that temperature can greatly affect the final adhesive strength of an agglomerate, whereas, in Section 3.2.3, the overall strength exerted by a drying liquid bridge could not be measured as a function of temperature, thus theoretical and experimental validations of actual particle aggregation models are bounded to ambient conditions. Investigating the process of solidification of liquid bridges and formation of dry bridges from saturated solutions at high temperature is not a trivial task, since they often occur by means of a complex multi-step process, which may involve more than one chemical reaction. Such a complication also occurs in the study of crystallization processes, where the liquid bridge starts to crystallize within several minutes but then may continue for several weeks, causing slow changes in bridge composition and microstruc-

ture.

In fact, adhesion is related to temperature in that changes in the chemical properties (composition, reaction rate) of the interacting materials cause variations of the type and extent of bonding mechanisms. For instance, solid bridges may form through chemical reaction between components within the bridge (e.g. thermal decomposition) or at the particle/bridge interface (e.g. dissolution and reaction), hence the determination of the type of reaction, reaction rate and its dependency on temperature is of fundamental importance in order to understand the adhesion developed at high temperature. This kind of investigation is nonetheless complicated by the presence of new solid interfaces, which may originate from local/partial melt followed by crystallization, sublimation or phase transformation, thus the definition of the type of such an occurrence and whether it exerts a significant influence on the kinetic characteristics and mechanism are of equal importance.

3.3.1 Determination of the reaction rate

Experimental measurements of reaction rates usually form part of a more comprehensive investigation undertaken to determine the mechanism of a chemical change. In general, the most reliable theoretical explanations of observed behaviour are based on data obtained from a variety of different, but complementary, investigative techniques. Approaches primarily concerned with rate determinations often provide evidence relating to other features of the reaction (e.g. variations in stoichiometry, or that the process proceeds to completion in more than one single step, etc.), while ancillary experimental techniques (microscopic observations, hot stage microscopy, etc.) are required to supplement conventional kinetic data in the formulation of a reaction mechanism. In principle, any parameter quantitatively related to the extent of reaction, α_r, can be used for rate studies, though in practice, product gas evolution, mass loss and enthalpy changes have found the most widespread application. Coupling such techniques with analytical measurements (mass spectrometry, gas chromatography, etc.) provides information on the stoichiometry of reaction. Concurrent or parallel microscopic observations are invaluable in establishing the interface geometry (in reactions of solids, it is often convenient to consider separately the geometry of interface development and the chemical changes which occur within that zone of locally enhanced reactivity [133]). More detailed characterization of the phases present are afforded by X-ray diffraction measurements. Examples of those diverse experimental techniques which have found profitable application in investigations of reaction kinetics are mentioned in Section 3.3.2.

Crystallization and thermal decomposition of saturated liquid solutions, as well as of phase transition of solids, are chemical processes that belong to the solid (thermal-) decomposition class of chemical reactions. Two alternative methods have been used in kinetic

investigations of thermal decomposition, and, indeed, other reactions of solids: in one, yield-time measurements are made while the reactant is maintained at a constant (known) temperature while, in the second, the sample is subjected to a controlled rising temperature. Measurements using both techniques have been widely and variously exploited in the determination of kinetic characteristics and parameters. However, in the more traditional approach, isothermal studies, the maintenance of a precisely constant temperature throughout the reaction period represents an ideal which cannot be achieved in practice, since a finite time is required to heat the material to reaction temperature.

The rate-determining step in any solid phase reaction can be either (i) diffusion, i.e. the transportation of participants to, or from, a zone of preferred reaction, or (ii) a chemical reaction, i.e. one or more bond redistribution steps, generally occurring at a reaction interface. Intermediate behaviour, and transition regions from one type to the other, are also known [133]. It is usually a preliminary part of any investigation to establish the range of conditions under which each alternative applies; moreover, preliminary work may also determine the influence on kinetic characteristics of such variables as the total mass/volume of reactant, distribution and disposition, the availability of other possible reactants and the pressure and composition of all volatile substances, including products, in the immediate vicinity of the reactant.

Figure 3.25 represents a typical α_r vs reduced time plot obtained from rate measurements of a thermal decomposition reaction. As already mentioned, α_r represents the degree of transformation during reaction time, which has been scaled to $t_{0.5} = 1.00$ when $\alpha_r = 0.5$.

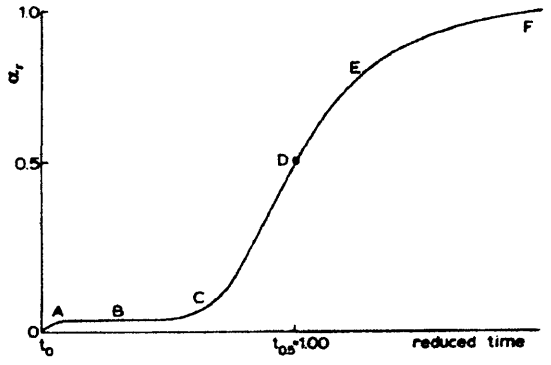

Fig. 3.25: Generalized α_r-time plot summarizing characteristic kinetic behaviour observed for isothermal decompositions. There are wide variations in the relative significance of the various stages (distinguished by letter in the diagram). Some stages may be negligible or absent, many reactions of solids are deceleratory throughout. A, initial reaction; B, induction period; C, acceleratory period; D, point of inflection at maximum rate (in some reactions there is an appreciable period of constant rate); E, deceleratory period (or decay); and F, completion of reaction. After[133].

The step A is an initial reaction, sometimes associated with the decomposition of impurities

or unstable superficial material. B is the induction period, usually regarded as being terminated by the development of stable nuclei. C is the acceleratory period of growth of such nuclei, perhaps accompanied by further nucleation, which extends to the maximum rate of reaction at D. Thereafter, the continued expansion of nuclei is no longer possible, due to impingement and consumption of reactant and this leads to the deceleratory or decay period, E, which continues until completion of reaction, F. One or more of this features (except D) may be absent or negligible; variations in their relative importance results in the appearance of a wide variety of different types of kinetic behaviour in which the maximum reaction rate, D, is achieved at different values of α_r. In the quantitative analysis of the shapes of α_r-time curves, it is usually assumed that the isothermal rate of reaction per unit area of interface is constant, so that progressive changes in rate provide a measure of the time-dependent variations in the effective areas of reactant-product contact. In the quantitative kinetic analysis, it is sometimes convenient to use data from which the influences of any initial reaction, A, have been subtracted [133].

The rate of decomposition of a solid depends upon the temperature and the amount of material. If only a single reaction is involved, it is usually assumed that these functions are separable and the equation used to describe the progress of reaction is as follows:

$$\frac{d\alpha_r}{dt} = \Theta(T)Z(\alpha_r) \tag{3.10}$$

where t is the time and T is the absolute temperature. Increases in reaction rate with temperature are often found to obey the Arrhenius equation, (3.11), from which the apparent values of the reaction frequency factor, A, and the activation energy, E, are calculated. However, the possibility that the kinetic law changes with temperature must also be considered.

$$\Theta(T) = A\exp(-\frac{E}{RT}) \tag{3.11}$$

Usually, α_r is measured through different techniques (see next section) and a suitable expression for $Z(\alpha_r)$ is searched through best fitting and extrapolation from the experimental values. The most common and widely applicable method for determining the solid-state decomposition equation is to employ the Avrami-Erofe'ev equation [134], as follows:

$$\alpha_r = 1 - \exp(-Bt^m) \tag{3.12}$$

where B is a constant and m is an intrinsic value obtained from the theoretical equation for solid-state decomposition. For α_r values ranging from 0.15 up to 0.5, Equation 3.12 can be written as:

$$\ln[-\ln(1-\alpha_r)] = \ln B + m \cdot \ln t \tag{3.13}$$

When the slope m is calculated from the plot of $\ln[-\ln(1-\alpha_r)]$ vs $\ln t$, the mechanism of solid state decomposition can be classified by referring to Table 3.3.

Magnitudes of m have been empirically established for those kinetic expressions which have found most extensive application: e.g. values of m for diffusion-limited equations are usually between 0.53 and 0.58, and for the contracting area and volume relations are 1.08 and 1.04, respectively.

$\mathbf{Z(\alpha_r)}$	**m**	**Mechanism / Observations**
1	1.24	Zero-order kinetics / one-dimensional advance of the reaction interface
$(1-\alpha_r)^{1/2}$	1.11	One-half order kinetics / two-dimensional advance of the reaction interface, phase boundary rection, cylindrical symmetry
$(1-\alpha_r)^{2/3}$	1.07	Two-thirds order kinetics / three-dimensional advance of the reaction interface, phase boundary reaction, spherical symmetry
$(1-\alpha_r)$	1.00	First order kinetics, random nucleation
$(1-\alpha_r)[-\ln(1-\alpha_r)]^{1/2}$	2	Random nucleation / two-dimensional growth of nuclei
$(1-\alpha_r)[-\ln(1-\alpha_r)]^{2/3}$	3	Random nucleation / three-dimensional growth of nuclei
$1/\alpha_r$	0.62	One-dimensional diffusion / parabolic law
$1/[-\ln(1-\alpha_r)]$	0.57	Two-dimensional diffusion
$(1-\alpha_r)^{2/3}/[1-(1-\alpha_r)^{1/3}]$	0.54	Three-dimensional diffusion / Jander equation
$(1-\alpha_r)^{1/3}/[1-(1-\alpha_r)^{1/3}]$	0.57	Three-dimensional diffusion / Ginstling-Brounshtein equation

Tab. 3.3: Kinetic expressions of $Z(\alpha_r)$ and values of m for the most common mechanisms of solid-state decomposition.

The most significant problem in the use of this approach is in making an accurate allowance for any error in the measured induction period, since variations in t (i.e. $t + t_0$) can introduce large influences upon the initial shape of the plot. Care is needed in estimating the time required for the sample to reach reaction temperature (isothermal conditions), particularly in deceleratory reactions and in considering the influences of an induction period and/or an initial preliminary reaction. The description of alternative approaches can be found in Bamford and Tipper [133].

3.3.2 Thermal analysis and instrumentation

A number of experimental techniques and applications in the kinetic analysis of processes exist in literature. Differences are equally found in the experimental method (i.e. isothermal or non isothermal conditions) and in the use of specific devices dedicated to the measurement of changes, either chemical or physical, in the material sample properties with temperature. The most known, and traditional, approaches are reviewed in this section.

3.3.2.1 Accumulatory pressure measurements of evolved gas

The kinetics of many decomposition and solid reactions are conveniently studied from measurements of the pressure of the gas evolved in a previously evacuated and sealed constant volume system. It is usually assumed that gas release is directly proportional to α_r, so that the method is most suitable for reactants which yield a single volatile product by the irreversible breakdown of a substance that does not sublime on heating in vacuum. A cold trap is normally maintained between the heated reactant and the gauge to condense non-volatile products (e.g. water vapour) and impurities.

Various methods of gas pressure measurement have been used, including manometer, glass spoon gauge and mass filter pressure gauge. Procedural methods have ranged from manual operation to the use of high speed and computer recording of responses from the electrical devices. One drawback is encountered whenever a rate process involves or is preceded by the release of a condensable product, since some error is inevitably introduced during the period of diffusion of this temporary gas from reactant to cold trap. Furthermore, reversible dissociations are not appropriately studied in a closed system, where product readsorption and diffusion effects within the product layer may control the rate of gas release.

3.3.2.2 Mass loss measurements: Thermogravimetry (TG)

The development and ready availability of reliable and accurate electronic microbalances have led to their wide application in kinetic studies of the decomposition of solids. By

employing thermogravimetry techniques, the disadvantages mentioned for pressure measurements are less important or are effectively eliminated, since reaction can proceed in a controlled environment ranging from high vacuum to a pressure of several atmospheres of gas of specified composition (mostly inert gases), which can be altered at will. The main drawbacks of thermogravimetry are thermomolecular flow effects at low pressures, accurate sample temperature calibration and the influence of volatile product on rates of reversible decomposition reactions.

Mass loss determinations refer to the total change resulting from reactant decomposition and usually include contributions from a mixture of product compounds, some of which would normally be condensed under conditions used for accumulatory pressure measurements. Generally, the degree of transformation, α_r, is related to mass loss, as in Equation 3.14:

$$\alpha_r = \frac{W_0 - W}{W_0 - W_\infty} \tag{3.14}$$

where W is the actual weight of solid sample and the subscripts 0 and ∞ refer to the initial and residual amounts, respectively.

There are two alternative experimental methods. In isothermal TG the solid reactant is kept under constant temperature condition and several experiments must be carried out at different temperatures in order to determine the temperature dependency of the reaction rate. In such a technique, it is advisable to use a furnace of low thermal capacity, unless suitable arrangements can be made to transport the sample into a preheated zone.

In non-isothermal TG the solid is submitted to a gradual increase in temperature (usually linear with time) and in this case it is possible, in principle, to obtain the kinetic parameters (activation energy, E, and pre-exponential constant, A) and the kinetic function, $Z(\alpha_r)$, with a single experiment. Usually, the furnace temperature, controlled by a sensor in the balance or a pressure gauge, is increased at such a rate as to maintain either a constant rate of mass loss or a constant low pressure of volatile products in the continuously evacuated reaction vessel. Such non-isothermal measurements have been used with success for decomposition processes, the rates of which are sensitive to the prevailing pressure of products, e.g. carbonates and hydrates [133].

Non-isothermal TG allows for a wide range of temperatures to be covered, which is not always possible in isothermal TG, particularly at high temperatures, since significant solid conversion may occur during temperature stabilization at the beginning of the experiments. On the other hand, one of the problems associated with rising temperature experiments is that the kinetic parameters obtained are frequently dependent on some

procedural factors (heating rate, initial amount of solid sample, gas phase composition, reactor geometry, particle size and solid porosity). However, it is common practice to avoid the problems associated with heat and mass resistances by using small samples of solid material (at the expense of a possible decrease in homogeneity), low particle sizes and moderate heating rates [135].

3.3.2.3 Evolved gas analysis (EGA)

As pointed out above, accumulatory pressure and weight loss measurements usually refer to the total reaction. Hence, when there are several volatile products, it is necessary to identify all components and investigate progressive changes in gas composition. Quantitative determinations of the amounts of each product should, ideally, be combined with measurements of the total extent of reaction, although caution in the interpretation of results from simultaneous measurements is usually recommended. The most widely applied techniques of EGA have been mass spectrometry (MS) and gas chromatography (GC).

Qualitative or quantitative mass spectrometric analysis can be made by one of two alternative configurations. Either the sample is decomposed in the high vacuum chamber of the mass spectrometer (MS) itself or reaction proceeds in an external system at higher pressure (e.g. a microbalance) from which samples are withdrawn and admitted to the MS through a suitable inlet. Decomposition of the reactant within the MS, where the path length to the detector is short, reduces the probability of secondary gas-phase reactions and fractionation which may arise when sampling from higher pressure. The mass spectrometer has been found to be particularly suitable for EGA in thermal analysis of polymers, minerals and many inorganic solids. Moreover, the high sensitivity of the MS makes it a particularly appropriate tool for the investigation of nucleation and growth processes, since it is possible to measure rates during the early part of the reaction using small samples or individual crystals.

The gas chromatograph (GC) resembles the MS in providing both qualitative and quantitative EGA but is significantly slower in operation. The interval between analysis is normally controlled by the retention time of the last component to be eluted from the column; such delay may permit the occurrence of secondary reactions between primary products. The sample withdrawal can be achieved without the necessity for performing the reaction in an atmosphere of carrier gas. By suitable choice of separation column or combination of columns, it is possible to resolve species which are difficult to measure in a small low-resolution MS. However, the quality of data originated by both instruments is generally judged about equal [133].

3.3.2.4 Other methods of thermal analysis: Thermo-mechanical analysis (TMA)

The techniques referred to above may be operated for a sample heated in a constant temperature environment or under conditions of programmed temperature change. Very similar equipment can often be used; differences normally reside in the temperature control of the reactant cell. Non-isothermal measurements of mass loss are generally termed DTG, absorption or evolution of heat is termed differential scanning calorimetry (DSC), and measurement of the temperature difference between the sample and an inert reference substance is termed differential thermal analysis (DTA). These techniques can be used singly or in combination and may include provision for EGA (see also **Chapter 6**). Applications of non-isothermal measurements have ranged from the rapid qualitative estimation of reaction temperature (see also **Chapter 7**) to the quantitative determination of kinetic parameters.

Other parameters which have been used to provide a measure of α_r include magnetic susceptibility, light emission, reflectance spectra (dynamic reflectance spectroscopy, DRS), dielectric properties (dynamic scanning dielectrometry, DSD) and physical dimensions (thermomechanical analysis, TMA).

A Thermo-Mechanical Analyser is usually a part of a thermal analysis group of instruments (TGA,DTA,etc.) that are aimed more toward the chemical behaviour than physical properties of materials. A thermo-mechanical analyser, as its name implies, was developed for mechanical properties determination of plastics, such as load bearing when heated, penetration, bending, etc. It uses a small sample and it usually comes with a variety of shaped tips to do the above. At some point it was an obvious extension to try measuring expansion coefficients as well, after all the device has a sensitive transducer. This was reasonably possible with plastics where the expansion coefficient is in the $100 - 300 \cdot 10^{-6}/°C$ range, and a few mm thick sample would expand quite a bit. Metal samples, for example, will expand about 1/10 of plastics, and some ceramics only 1/100: this means that a TMA that has a $\pm 1\%$ accuracy for a plastic sample can have a $\pm 100\%$ inaccuracy for a ceramic sample. Such inaccuracy can neither be calibrated out nor levelled off with higher amplification of the signal.

In the TM-Analyser, the dimensional change undergone by a sample whilst being either heated, cooled , or studied at a fixed temperature, is the primary measurement. Figure 3.26 shows a schematic diagram of a typical TMA instrument. The sample sits on a support within the furnace. Resting upon it is a probe to sense changes in length, which are measured by a sensitive position transducer, normally a Linear Variable Differential Transformer (LVDT). A TMA nearly always employs an LVDT or a capacitive transducer, both of the high sensitivity, short stroke type. These devices have a narrow range within

which they are linear to some degree. Both types are prone to drift caused by amplifiers and thermal effects, and therefore they require frequent recalibration.

The probe and support are made from a material such as quartz glass (vitreous silica), which has a low, reproducible and accurately known coefficient of thermal expansion and also has low thermal conductivity, which helps to isolate the sensitive transducer from the changing temperatures in the furnace. A thermocouple near the sample indicates its temperature. There is usually provision for establishing a flowing gas atmosphere through the instrument, to prevent oxidation for example, and also to assist in heat transfer to the sample. Helium is effective in this respect.

The load may be applied either by static weights, as shown in figure 3.26, or by a force motor. This latter method gives the advantage that the applied load can be programmed to allow a greater range of experiments. The instrument is calibrated for position measurements by heating a sample whose expansion coefficient is accurately known. When the sample carries a zero, or negligible load, the measurement follows the free expansion or contraction of the material and accurate coefficients of thermal expansion can be routinely determined.

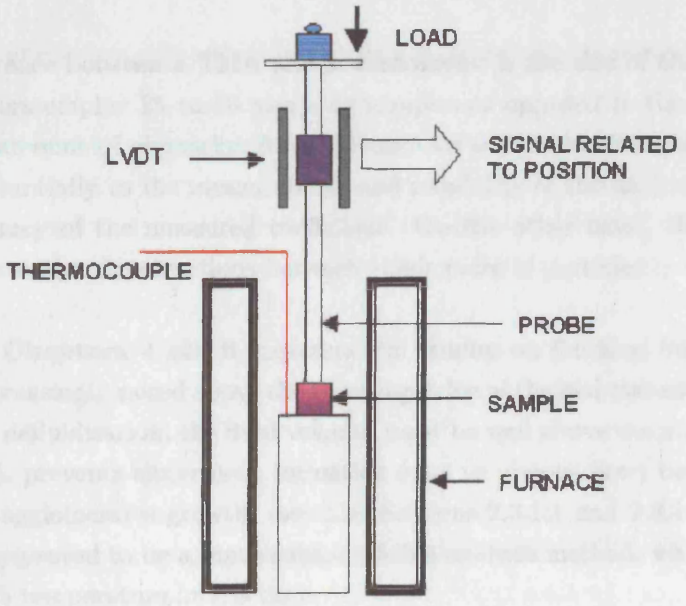

Fig. 3.26: Schematic of a dilatometer. Adapted from http://www.anasys.co.uk/library/tma1.htm

Calibration is usually done by mechanical means, such as gauge blocks, micrometer screws, etc., and these devices have their own limitations in the small displacement region. A micrometer, for example, can be read only to a certain limit, which may be 1 to 10% of the

entire displacement range of the transducer. This will produce a very high uncertainty in the numbers. Any uncertainy in calibration will carry over in direct proportion to the expansion coefficient that is measured. The scatter, due to poor resolution, will produce an identical scatter in the final coefficient values.

The materials studied are usually rigid or nearly rigid solids, as implied by most of the experimental arrangements shown in figure 3.26. Liquids can be studied in a specially designed accessory, which can also be used to measure the volume changes of irregularly shaped samples or powders that are then submerged in an inert liquid such as silicon oil. Powders can also be studied as a layer with a loosely fitting lid on top, or when pressed into a pellet. Solid-state transition can be followed in this way.

The use of a *dilatometer* is generally preferred, when reliable measurements of the coefficients of thermal expansion on materials other than polymers are required (see Section 2.3.1.2). In fact, differently from TMA instruments, dilatometers usually employ longer stroke LVDTs which are somewhat easier to calibrate and are more stable. Moreover, in some cases absolute digital displacement transducers are used which do not require periodic calibrations at all.

One major difference between a TMA and a dilatometer is the size of the sample. Normally, dilatometers employ 25 to 50 mm long samples as opposed to the 1 to 2 mm for TMA, thus the amount of expansion for a dilatometer sample is 25 times greater. This contributes substantially to the measurability and reliability of the data and therefore to the overall accuracy of the measured coefficient. On the other hand, this represents a limitation to the study of interactions between single pairs of particles.

As described in **Chapters 4** and **6**, experimental studies on fluidised bed behaviour at temperatures increasingly raised above the sintering value of the bed material show that, in order to prevent defluidisation, the fluid velocity must be well above the normal minimum fluidisation. This prevents sinter neck formation (due to viscous flow) between particles and subsequent agglomerates growth, (see also Sections 2.3.1.1 and 2.3.1.3). In this regard, dilatometry proved to be a fundamental off-line analysis method, which permits the modelling of high temperature interactions.

3.4 The Atomic Force Microscope (AFM)

The properties of bulk solids are of great importance, since many processes are rendered difficult due to poor flow properties of the bulk. These flow properties are determined by the forces acting between individual powder particles, whose magnitude, compared to the particle weight, may vary from lower values, such as van der Waals forces, up to

higher values, such as capillary and sintering forces. It is therefore recognized that knowledge of single particle interactions is important when attempting to develop mechanistic predictions of the behaviour of bulk assemblies. Measurements on bulk samples do not elucidate the prevalent mechanisms operating at the scale of the single particle. Adhesive interparticle forces are the dominant components in bulk powder cohesion and their understanding is necessary to improve the efficiency of process operations such as powder flow, agglomeration, dispersion, fluidisation and filtration.

Developments in the microscopy field, as in control, manipulation and measurement devices on a nanoscopic scale, led to the invention of the Scanning Tunneling Microscope (STM) by Binnig and Rohrer in 1982. Shortly afterward, in 1986, Binnig et al. [136] invented the Atomic Force Microscope, which provided the sensitivity to measure forces between particles of a size that is relevant to the powder processing industries. STM relies on measurement of exponentially decaying tunneling current between a metal tip and a conducting substrate. Not being restricted to conductive materials, AFM is a much more versatile instrument than STM, and more adopted in studies applied to colloidal systems and soft matter. The number of publications related to AFM has increased constantly since its invention, and the instrument is now a fundamental tool in most research laboratories around the world.

The Atomic Force Microscope probably earned its initial popularity in virtue of its capability of providing images of samples with atomic resolution in either vacuum, air or liquid environments. The list of materials investigated is almost endless: thin and thick film coatings, ceramics, composites, synthetic and biological membranes, biological macromolecules, metals, polymers and semiconductors. The AFM is being applied in several fields of research, such as materials science and engineering, biochemistry and biology, in studies of the most varied phenomena, such as colloidal stability, characterisation of nanostructures and molecules, adhesion and delamination, surface elasticity, corrosion, etching, friction and lubrication to name but a few.

Sample imaging at sub-optical resolution is not the only function of Atomic Force Microscopy. Interaction forces up to nanoNewton scale can be measured with ease of operation and of sample preparation. AFM allowed for the first time the direct measurement of molecular and surface forces between nanometer sized surfaces (the interaction area can be as small as 10x10 nm^2). Soon after the invention of AFM, forces were measured in air and in water, thus permitting the investigation of many phenomena of scientific and industrial interest.

3.4.1 Functional principles

The atomic force microscope probes a sample surface with a sharp microfabricated tip fastened to a cantilever spring with typical lateral dimensions of 100-200 μm and a thickness of 1 μm. As the cantilever bends due to the interaction with the sample surface, its position is detected by the optical deflection of a laser beam using a Position Sensitive Detector (PSD), figure 3.27.

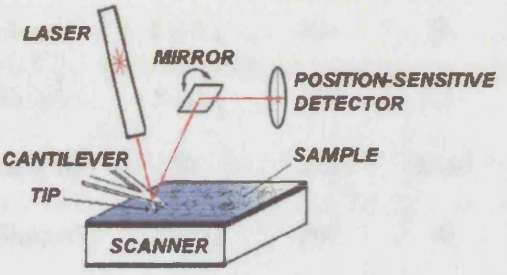

Fig. 3.27: Schematic of the main components and optical deflection technique for detecting cantilever deflection of an AFM.

The sample is mounted on top of a ceramic piezoelectric crystal and is raster scanned under the tip (or vice versa the tip is scanned above an immobile sample, depending on the design of the instrument), and the cantilever deflection is measured in order to reproduce the sample topography. A controller collects and processes the data and drives the piezo scanner. As shown in figure 3.27, a pyramidal probe tip is mounted on a sensitive cantilever spring, usually oriented at an angle of about 12° with the surface and positioned very close (or in contact) to the sample surface. Interaction forces between the sample and the tip cause the cantilever to deflect according to Hook's Law[5]:

$$F = kx \tag{3.15}$$

where k is the spring constant (N/m), a characteristic of each cantilever and x is the cantilever vertical deflection (nm).

The first AFM tip-cantilever assembly, constructed by Binnig et al. [136], was made by meticulously gluing a tiny shard of diamond at the end of a rectangular strip of gold foil. Nowadays, the typical tip-cantilever assembly is microfabricated industrially from Silicon or Silicon Nitride (Si_3N_4); cantilevers are mainly of two shapes: rectangular and V-shaped (as depicted in figure 3.27). Many nanotechnology companies sell cantilevers and tips of

[5] A recent study from Heim et al. [137] showed how effectively the spring constant of the cantilever increases according to the tilt angle of about 10-20%.

many types and dimensions and cost is usually the only limitation to choice, see Table 3.4. The choice of tip type and spring constant of the cantilever depends on the application: probes with a lower spring constant, k, are more sensitive, but at the same time are more easily trapped by capillary forces on the surface of humid samples. Stiffer probes are less sensitive, but can be pulled free from the surface more easily.

Company	**Geometry**	**Material**	**L** [μm]	**W** [μm]	**T** [μm]	k [N/m]
Topometrix	V-Shaped	Si_3N_4	200	36	0.6	0.064
	V-Shaped	Si_3N_4	100	22	0.6	0.37
	Rectangular	Si	225	30-45	6-8	24-85
Digital Instr.	V-Shaped	Si_3N_4	200	40	0.4-0.6	0.01-0.6

Tab. 3.4: Some examples of commercial cantilevers: the dimensions L (length), W (width) and T (thickness) are given as well as the cantilever spring constant,k.

The rear side of the cantilever (the one not in closest proximity with the sample) is usually coated with a thin layer of gold to enhance its reflectivity. Albrecht et al. [138] provided some criteria that the cantilever stylus used in AFM experiments should meet:

1. In order to register a measurable deflection due to a small force, the cantilever must have a relatively low spring constant, typically between 0.1 and 1 N/m.

2. A high resonance frequency reduces the sensitivity of the cantilever to mechanical vibrations of low frequency, and allows higher imaging rates. Therefore cantilevers with resonance frequencies around 10-100 kHz are ideal. The cantilever resonance frequency ω_0 is given by:

$$\omega_0 = \frac{1}{2\pi}\sqrt{\frac{k}{m}} \tag{3.16}$$

   where k is th spring constant and m the mass of the cantilever. In order to keep k small and ω_0 large, m must be very small. Modern microfabrication techniques allow the construction of cantilevers with very small masses (typical length 100 μm and thickness $\prec 1\mu m$).

3. In order to reduce the effect of lateral forces in AFM, high lateral stiffness of the cantilever is desirable. When operating in contact imaging or in force mode (see next section), frictional forces can cause appreciable lateral bending of the cantilever, leading to stick-slip motion of the lever. A V-shaped cantilever is preferable to exploit a substantial lateral stiffness.

4. To obtain a good imaging resolution, the tip must have a small effective radius of curvature (ca. 300 Å) and a small aperture angle, a pyramidal or conical geometry which makes the terminal point of the tip very sharp, and a high aspect ratio (ratio between height and width of the tip) in order to be able to penetrate in small pits of the surface.

3.4.2 Major use of the AFM

AFM studies can be broadly split in two categories: topography (contact AFM, Tapping Mode AFM and other imaging modes) and probe-to-surface interactions.

Topographic measurements allow for the determination of friction coefficients, elastic moduli, roughness, normal and shear stresses of sampled surfaces at both room and high temperature. The monitored property in AFM, the interaction force with the sample, can be kept constant (equiforce mode) or varied (variable deflection mode) during the scanning motion. In the equiforce mode, the force is controlled by keeping the deflection of the cantilever constant by means of a feedback loop. In the variable deflection mode, during the scan process the feedback control is turned off and deflections of the cantilever are measured from the current of the photodetector (PSD). This mode is normally applied to samples with limited range in the vertical direction.

The AFM can operate both in contact and non-contact regime. In the former regime, the tip is in close contact with the sample and traces the sample features like a surface profilometer. Contact imaging normally achieves the higher resolution, but often implies greater damage to soft samples. A different imaging mode that further reduces tip-sample direct contact is the non-contact imaging mode. Digital Instruments has patented the non-contact mode with the name of Tapping Mode. In the non-contact mode the cantilever is kept vibrating, by means of piezoelectric elements, above and close to the sample (within 10 nm of the sample), at a modulation frequency close to the resonance frequency of the cantilever. The signal of the detector is measured by lock-in techniques and variations in phase or amplitude of the vibration are converted into information on the surface properties and morphology.

In the probe technique, a particle (probe) is glued to the tip of the cantilever, as shown in figure 3.28, and is approached to a either a solid, liquid or fluid surface, allowing the determination of either short range (e.g. van der Waals) or adhesion forces, depending on whether the probe and the sample are put into contact or simply narrowed to very small separation distances.

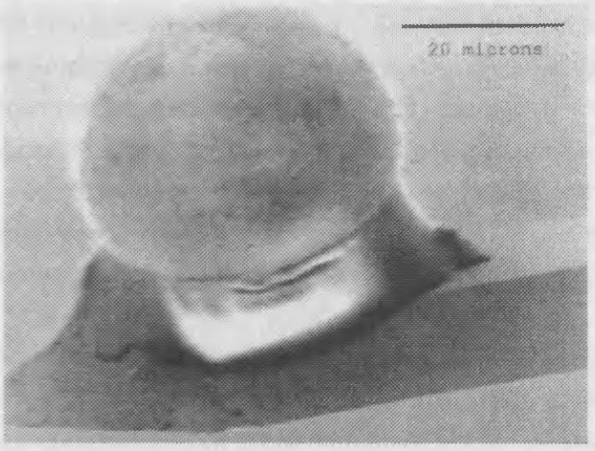

Fig. 3.28: SEM image of a glass micro-sized sphere mounted on an AFM cantilever. From [140].

The (colloid) probe technique offers a number of significant advantages for the measurement of surface forces. The force applied after the tip makes contact with the surface can provide a measurement of the stiffness or compliance of the sample, whilst the force required to pull the sample up from the surface is a measure of the adhesion between the tip and the sample. This is illustrated in figure 3.29. The radius of the probe is easily determined to a high degree of accuracy using electron microscopy (figure 3.28). A single probe can be reused multiple times in a series of experiments and a wide range of surface chemistries are available. The main limitations are that the particle should be smooth and spherical and that it should be of a size that can be easily manipulated in probe preparation ($\succ 1\mu m$). This is particularly important in developing an understanding of data collected at small separation distances where surface asperities will dominate the interaction [139].

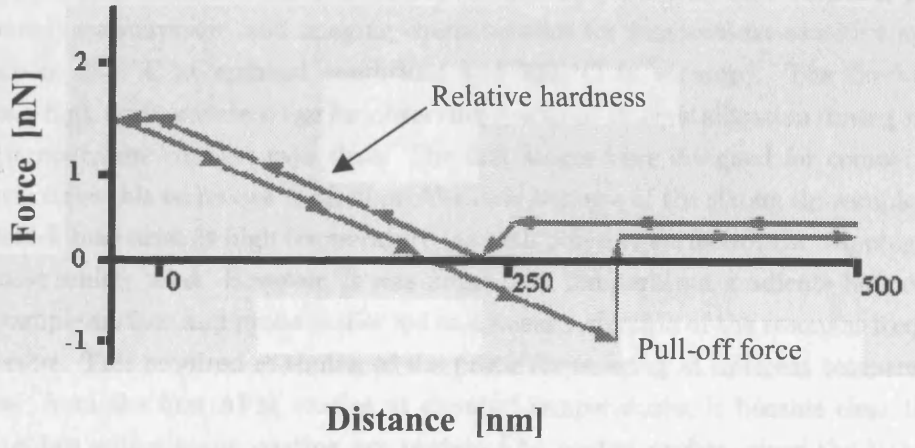

Fig. 3.29: Typical Force-Distance chart obtained by the AFM probe technique.

The crucial factor for the probe technique is the determination of the cantilever spring constant that cannot be assumed to be the same as that declared by the manufacturer. The probe that is glued on the AFM cantilever in fact changes the resonant frequency of the system (mass+cantilever) and therefore further measurements are required in order to calculate the spring constant of the cantilever. However Tyrrell and Cleaver [140] noted that, in order to minimize this effect, it is necessary to use a minimal quantity of very viscous adhesive (i.e. which will not spread over the cantilever with a resulting increase of the rigidity when it sets).

The spring constant can be calculated through different techniques: the simplest approach involves measuring the static deflection of the cantilever under the action of a known mass. However, accurate measurements of such small deflections and the need for numerous repetitions make this approach somewhat problematic [139]. Instead, the spring constant can be calculated through the investigation of the shifting of the resonant frequency of the cantilever before and after the probe is glued. In fact, the resonant frequency is related to the added mass thorough a constant of proportionality that is equal to the spring constant [141]. The need for a recalculation of the cantilever spring constant has lead to the increasing use of commercial AFM instruments (Nanoscope IIIa, Digital Instruments) that have this feature built in.

3.4.3 High temperature Atomic Force Microscopy

Atomic force microscopes cannot always meet all the requirements for a project, particularly when the thermal behaviour of the sample surface is desirable, and need to be customized for high temperature tasks. This involves the design of a proper environment in which the particle and the sample interact without limiting the movement of the cantilever. New generation AFMs, also named Enviroscopes (Digital Instruments), provide the common measurement and imaging characteristics for temperature-sensitive applications (up to 185 °C at ambient conditions and 300 °C in vacuum). The Enviroscope provides a high temperature stage for observing reactions or crystallization during mild or drastic temperature changes over time. The first stages were designed for contact mode AFM but, since this technique is often problematic because of the strong tip-sample interaction which may arise at high temperature (as with polymer surfaces), the Tapping mode is the most widely used. However, it was found that temperature gradients between the heated sample surface and probe holder led to a linear reduction of the resonant frequency of the probe. This required re-tuning of the probe for imaging at different temperatures. Moreover, from the first AFM studies at elevated temperatures, it became clear that Si etched probes without any coating are preferred to coated probes, since the latter can bend and/or twist at elevated temperatures. It has also been found that water condensation occurs when operating in Tapping mode at medium and high temperatures. In fact,

when the sample temperature approaches 100 °C and the probe is slightly colder, water condensation in the form of small droplets is typically observed on the probe's reverse side. In some cases the volatile components of the heated sample can also cause droplet formation. For these reasons heating of the probe was implemented.

By placing a heater close to the probe mount it became possible to change the probe temperature by regulating the voltage on the heater. In this case, heating of the probe and the probe holder assembly to the target temperature also induces heating of the sample from above, which can significantly improve the homogeneity of the temperature distribution throughout the sample [142]. In order to quantify and control the probe temperature and the conditions for imaging, accurate measurement of the temperature is required. The temperature of the probe itself is usually achieved through evaluation of the changes in the resonant frequency of the probe with temperature, nonetheless such calculations involve knowledge of the functional relationship of both Young's modulus and material density from temperature.

Toikka et al. [143] highlighted the limitations of AFM in the measurement of adhesion forces between a particle and a sample in a heated environment. It is very difficult with a conventional atomic force microscope to place a particle, attached to the cantilever tip, into contact with a sample surface and then to maintain that position over an extended period of time in a controlled environment. As previously explained, atomic force microscopes usually make several contacts over short time periods, which, in itself, can lead to changes in the interaction geometry and can introduce cross-contamination of the sample. Toikka et al. [143] therefore designed an apparatus based on AFM but with the capability of not only placing but maintaining a micron-sized particle in contact with a heated sample and then measuring the pull-off force.

A schematic of the rig is shown in figure 3.30. As in the probe technique, the particle is attached to the tip of the cantilever, which is placed in a holder located at the end of the displacement arm. Vertical displacement between the particle and a fixed sample, located directly below the particle, is made by using an Inchworm (Burleigh).

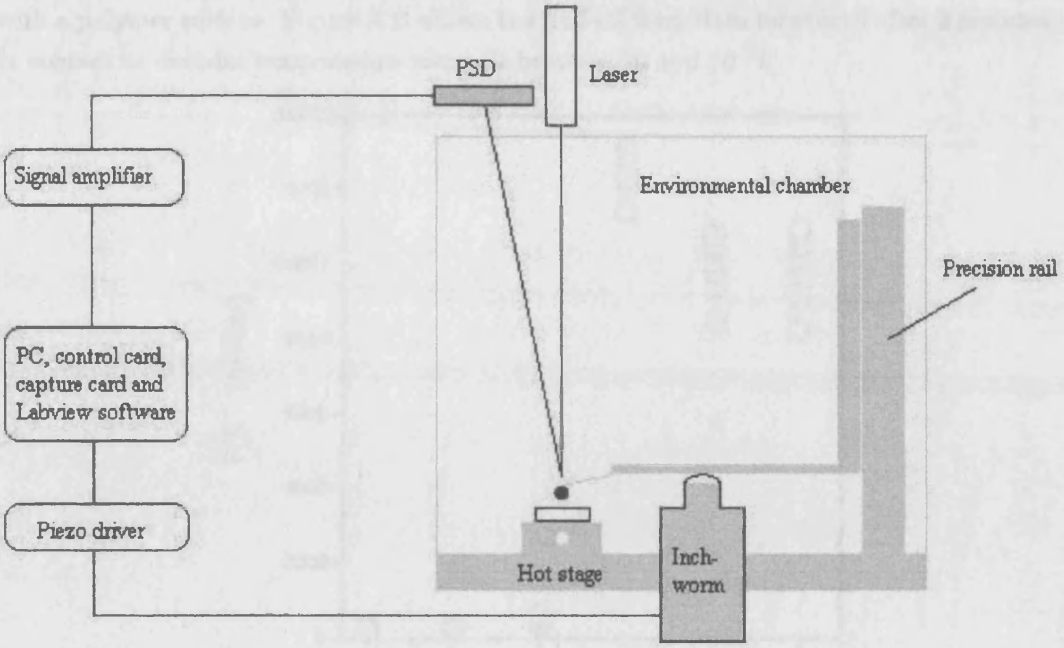

Fig. 3.30: Schematic of the force rig designed to measure fine particle adhesion via pull-off force. Redrawn from [143].

This design allows considerable movement with submicron resolution and the holding of position, when required. Movement is controlled, via a PC, by expanding and contracting a Piezo-Electric Crystal (PEC) in the vertical z-direction whilst the Inchworm is sequentially reclamped at each end (the action is described by the authors as being similar to the crawl of a caterpillar). Conventional atomic force microscopes suffer from PEC hysteresis and this is why they cannot hold position over extended time periods. However, the Inchworm technique also has its limitations. The clamping causes a vertical glitch of around $\pm 1 \mu m$, leading to occasional shear forces being detected in the measured data.

The heating device takes the form of a hot stage, which consists of a resistive wire inside a ceramic tube (rated to 800 °C). The temperature of the sample surface is measured directly using a thermocouple and voltmeter. An optical encoder ensures the accuracy of all measured displacements, whilst the cantilever deflection is detected using a laser diode and a PSD. The environmental chamber is constructed so that the laser can be directed through a glass top, whilst plastic walls made for ease of construction and include inlets for the heating device and thermocouple. During the experiments the chamber can be maintained at low pressures.

Toikka et al. [143] used their device to study the effects of temperature on the fracture adhesion energy of an inorganic particle (zirconia sphere, 10.6 μm diameter) in contact

with a polymer surface. Figure 3.31 shows the pull-off force data measured after 2 minutes in contact at decadal temperature intervals between 20 and 70 °C.

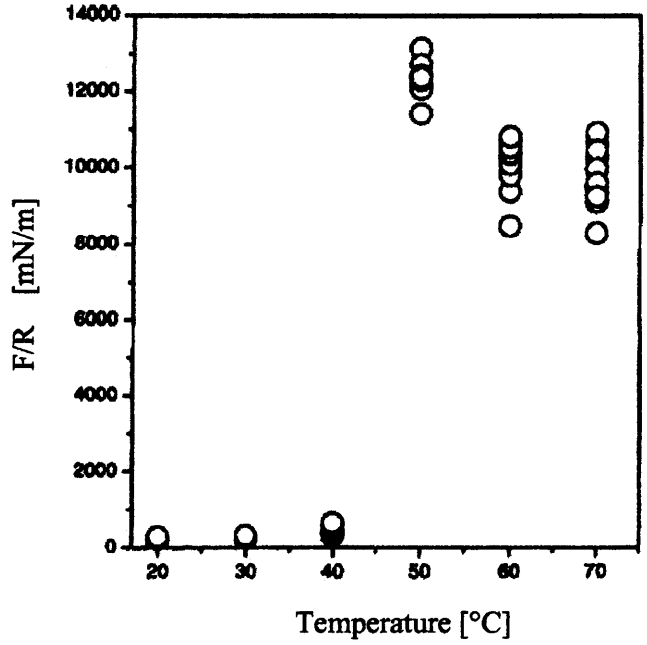

Fig. 3.31: Pull-off force between a zirconia particle and a polyester surface measured as a function of temperature. From [143].

The force can be seen to increase moderately up to 40 °C, then by almost two orders of magnitude at 50 °C, reaching a maximum before decreasing again at higher temperatures. Separate Dynamic Mechanical Analysis (DMA) shows a glass transition temperature of the polymer of approximately 40 °C (figure 3.32), giving a good correlation with the AFM device.

The maximum adhesion energy was due to the visco-elastic and plastic deformation of the polymer surface during contact and removal of the particle, whilst the subsequent decrease was due to the decrease in viscosity of the surface at higher temperatures. Toikka et al. [143] did find, however, that the measured data fell below theoretical predictions and they attributed this to the effect of surface asperities reducing the actual contact area between probe and sample.

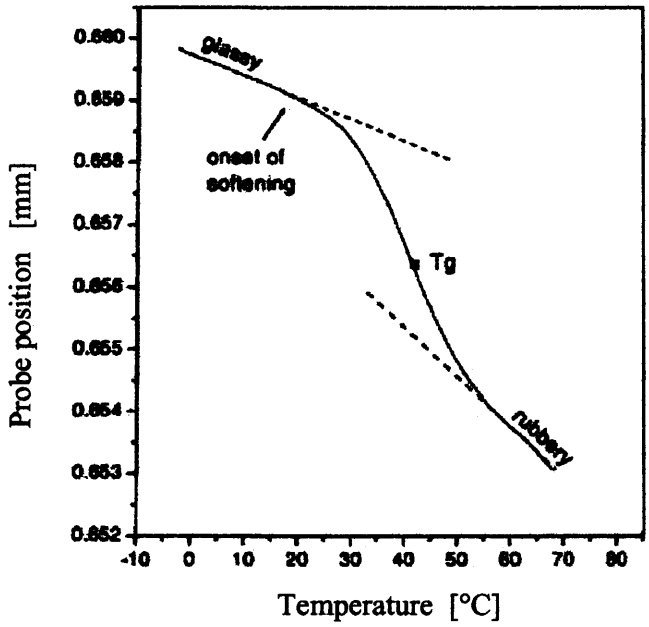

Fig. 3.32: Dynamic thermo-mechanical analysis data measured on the polyester film showing the glass transition temperature of 43 °C at the point of inflection. From [143].

3.5 *Concluding remarks*

Collisions between moist agglomerates containing many primary particles occur in a wide range of powder processing operations such as mixing, granulation, dispersion and fluidisation. Depending on process conditions, the powder flowability is affected by collisions between moist agglomerates, which may result in coalescence and/or attrition of granules (see **Chapter 4**). The phenomenological behaviour depends not only on the impact kinematics but also on the microstructure of the agglomerates and the interactions between primary particles. Moreover, in many industrial processes particles of different surface properties are agglomerated together through the addition of a liquid binder and the resultant differences in the (particle) wetting behaviour can cause problems in the final composition of the product, since some species can be agglomerated at the expense of others.

Hence, the experimental investigation of the microscopic interactions is required to develop a better understanding of the micromechanical behaviour of agglomerates and it subsequently represents a crucial step in developing (through scale-up modelling) novel technologies for the processing of granular materials. In this regard, a number of different experimental techniques have been developed to study the microscopic interactions between particles at ambient conditions. Moreover, although the fundamental mechanisms of particle interactions at elevated temperatures are still poorly understood, significant

advances have been made in recent years by combining micro-scale data (obtained for instance by TMA technique) with macro-scale observations (see **Chapter 4**), particularly in the area of defluidisation of fluidised beds due to particle sintering.

The increase in sophistication of AFM and the development of micro-mechanical devices is now leading to new possibilities in the determination of the fundamental mechanisms through direct observation and measurement of the interactions as they occur. Since its introduction more than ten years ago, the colloidal probe technique has been proved to be a valuable tool for the investigation of particle-sample interaction and adhesion. Applications range from fundamental questions of contact mechanics to the screening of material properties in industry. However, further development and improvement of routine procedures is required for measuring the spring constants of cantilevers, techniques to attach particles to cantilevers and easy to use analysis software.

On the other hand, customization of the measuring device and control of the environment are necessary to permit the investigation of particle-particle interactions. Moreover, a number of customizations have been designed in order to allow the study of a wide range of interactions (i.e. particle-particle at different relative humidity conditions, particle-bubble), which can be largely found in literature (see for instance Refs. [144, 145, 146]). In this regard, alternative techniques, such as the use of micromanipulation stages, are finding encouraging success, when applied to the study of complex interfacial phenomena at ambient conditions.

Nonetheless, the study of high temperature particle-particle interactions seems to be hindered by the lack of dedicated designs, both in relation to micromanipulation and atomic force microscopy techniques. Complications arise, for instance, from achieving high operative temperatures and temperature control by the means of heat conduction, as in hot stage microscopy, since temperature gradients can easily occur through the different materials composing the assembly. Further hindrance occurs when studying adhesion enhanced by temperature in reactive systems (including drying and phase transitions). In such systems the environmental control of temperature is of most importance as well as the capability of the device to reproduce the main experimental conditions as it happen on a macro-scale (e.g. in a fluidised bed reactor, the heat transfer between gas and solid phases mainly occurs through gas conduction and convective mechanisms) and to operate reliable measurements of adhesion. The latter can be a problem that occurs using Atomic Force Microscopy because of physical-chemical modifications to the cantilever, which can greatly influence the determination of the spring constant and ultimately affect the force evaluation.

4. THE ROLE OF ADHESION ON HIGH TEMPERATURE FLUIDISATION

In recent years many industrial processes operated at high temperatures have been developed. In particular, there has been growing interest in processes such as fluid-bed combustion, gasification and granulation. Given the importance of process conditions on the operation of fluidised beds, several researchers have studied over the past two decades how pressure and temperature influence the fluidisation quality.

The operating conditions influence the behaviour of fluid-particle systems because they affect gas density and viscosity. Increasing temperature causes gas density to decrease and gas viscosity to increase. Most predictions of fluidisation behaviour at high temperatures have been based solely on considering such changes in the gas properties. However, this approach is valid under the condition that only hydrodynamic forces control the fluidisation behaviour. In fact, as shown in the previous chapters of this thesis, temperature can have a considerable effect on particle adhesion, enhancing the role of the interparticle forces on the fluidisation quality.

The studies of high temperature agglomeration started in the early 70's in the development of coal gasification. Gluckman et al. [61] first elucidated the features of the defluidisation phenomena. They demonstrated experimentally that addition of liquid into a fluidised bed will lead to worsening of the fluidisation process until defluidisation.
In fact, by definition, a state of fluidisation exists when the force of gravity on a set of particles is balanced by the drag arising from the flow of the fluidising fluid. Since the drag force on the particles due to the fluid flow is equal to the manometric pressure drop across the bed, the point of incipient fluidisation (i.e. the minimum fluidisation velocity, U_{mf}) is therefore defined when the manometric pressure is equal to the buoyant weight of the bed, figure 4.1. It follows that small interparticle forces, which may not be noticeable in other circumstances, may have observable consequences at the point of fluidisation and beyond.

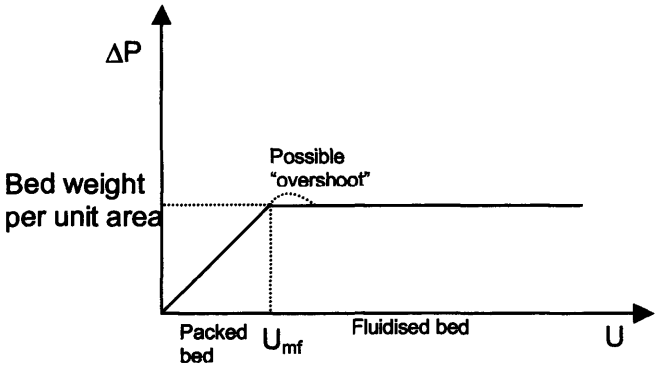

Fig. 4.1: Dependence of the pressure drop ΔP on the fluid velocity U through a packed and fluidised bed. Redrawn from [148].

Seville and Clift [147] explained this defluidisation phenomena by a changed ratio between particle gravity and interparticle forces when a small amount of liquid was added to a fluidised bed. As the amount of liquid increases, the fluidisation quality decreases and poor flow behaviour is observed.

Experimental observations of a wide range of fluid-solid systems led Seville and Clift [147] to conclude that, depending on the properties of the powder and the gas, a number of distinct flow patterns may develop:

- uniform expansion
- 'jetting', 'bubbling' or 'slugging'
- 'spouting'
- nucleation and growth of stationary cavities
- channelling ('rat holing')

As indicated by Seville et al. [148], all of these types of behaviour, with the exceptions of spouting and channelling, can be described as fluidisation, because the bed and the individual particles within it are wholly supported by the pressure drop. Spouting and channelling cannot, because in general, the pressure drop during these types of behaviour is less than that required to support the bed.
There have been several attempts to devise theoretical and empirical classifications of these behavioural types, most of which relate only to gas-solid fluidisation. The most widely used is the empirical classification of Geldart [149], see figure 4.2 and Table 4.1.

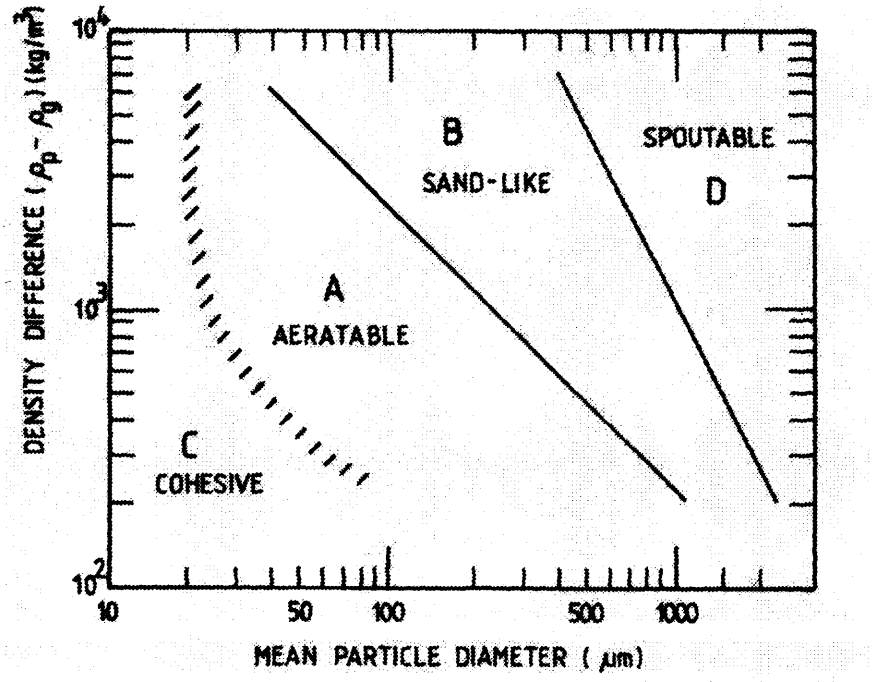

Fig. 4.2: Geldart's group classification diagram for the four types of fluidisation behaviour. **Group A** materials are small particles (typical diameter from 30 to 150 μm) with low density, exhibiting a region of non-bubbling expansion for gas velocities above the minimum fluidisation velocity, U_{mf}. **Group B** particles usually range from 40 to 500 μm with a density of 1400 to 4000 kgm^{-3}. Particles in this group are easily and smoothly fluidised. The largest ($\overline{d}_p \succ 500\mu m$) and most dense particles are defined as **Group D.** These powders show a tendency to "spout" rather than to fluidise. For those materials belonging to **Group C** a cohesive behaviour has been observed when fluidised. They are difficult to fluidise in a smooth manner, often forming channels and rising as a plug, or locking together in a packed bed or defluidised bed. After [149].

When trying to describe the fluidisation of different materials the nature of the forces acting between adjacent particles becomes of major importance. It is well-known that finely divided Group C powders are very difficult to fluidise. The commonly accepted reason for this behaviour is the dominance of surface forces. The ratio of the surface forces to body forces increases with diminishing particle size (see figure 2.2 in Section 2.2). It is well established in the literature that interparticle forces also exist in Group A powders, although their importance as compared to body forces is not yet unequivocally defined, mainly due to the difficulty in recognizing the nature of the interparticle forces involved and, therefore, to quntify their effect on the fluidisation behaviour. Molerus [150] studied the transition from one Geldart group to another, comparing the cohesion (resulting from van der Waals forces) between particles and their weight; he concluded that by taking into account interparticle cohesive forces, one can derive limiting conditions (i.e. the shifting from types A, B or D towards type C fluidisation behaviour) which result in classification of powders equivalent to the definition given by Geldart.

	Group			
	C	A	B	D
Most obvious characteristic	Cohesive, difficult to fluidise	Bubble-free range of fluidisation	Starts bubbling at minimum fluid. vel.	Coarse solids
Typical examples	Flour, cement	Cracking catalyst	Building sand, table salt	Crushed limestone, coffee beans
Property:				
1. Bed expansion	Low when bed channels; can be high when fluidised	High	Moderate	Low
2. Deaeration rate	Can be very slow	Slow	Fast	Fast
3. Bubble properties	Channels	Splitting and coalescence predominate. Limiting bubble size. Large wake fraction	Stable size large, and may not be reached	Size limited by vessel. Small wake fraction
4. Solids mixing	Very low	High	Moderate	Low
5. Gas back-mixing	Very low	High	Moderate	Low
6. Slug properties	Solid slugs	Axisymmetric; breakdown to turbulent fluidisation	Asymmetric	Horizontal voids. Solid / Wall slugs
7. Spouting	No, except in very shallow beds	Shallow beds only	Shallow beds only	Yes, even in deep beds

Tab. 4.1: Characteristic features of Geldart's classification of fluidisation behaviour, after [148].

4.1 Effect of liquid addition on fluidisation behaviour

It should be stressed that many of the most common applications of fluidised beds involve the processing of particles which exhibit substantial interparticle attractive forces. Examples include fluidised bed drying, coating and agglomeration, coal gasification and combustion. On the other hand, the "Geldart diagram" is applicable only to particles fluidised by air under ambient conditions and in the absence of long range interparticle forces (due to the presence of liquid layers on the particles, for example). However, the grouping of fluidised systems in terms of experimentally observed behaviour is of wider application, even in cases where interparticle forces are artificially enhanced [148].

In the last two decades several authors have addressed their research work to the study of the role of interparticle forces in fluidisation behaviour and, in particular, the effects of the surface properties on particle-particle interactions. Most of the experimental work has involved the observation of the behaviour of fluidised beds in which the addition of liquids of known properties is used to enhance long-range interaction forces (see for example [11, 147]). In such cases more sluggish/cohesive behaviour is observed, compared to the dry bed. This observation is consistent with the theory that fluidisation behaviour tends to shift towards Geldart C upon the addition of liquid and the corresponding increase in interparticle forces that this generates [11].

Despite the economic importance of such industrial processes, little is known about the way in which the variables involved in interparticle cohesion influence the bed hydrodynamics. These variables may include relative particle velocities and separation distances, coordination number of particles in agglomerates or distribution of liquid volumes. Moreover, in high temperature processes the ability to make visual observations, which can aid understanding, is often limited. For these reasons, the main purpose, in a number of experimental studies and models, is to achieve the capability to predict a fail point (defluidisation), rather than to describe, quantitatively, the quality of fluidisation. Hence, in order to investigate the underlying mechanisms of defluidisation, a "cold" model fluidised bed operating at ambient temperature has usually been employed, with interparticle forces being enhanced by the addition of liquid.

In principle, an increase in interparticle forces increases the settled bed void fraction and the void fraction at minimum fluidisation, ε_{mf}. The imposed pressure gradient for a given operating gas velocity is therefore reduced so that the superficial gas velocity at minimum fluidisation, U_{mf}, is increased. Here, U_{mf} is taken as the minimum fluidisation velocity measured with increasing gas flow, i.e. at the transition from a packed to a fluidised bed, as shown in figure 4.1. The distinction is important, since the defluidisation velocity (i.e. the velocity at which fluidisation ceases as the gas velocity is decreased) becomes

increasingly separated from U_{mf} as adhesion increases, see figure 4.3. Defluidisation is a transition from a mobile to a static bed and is therefore a dynamic process; in general, it is the defluidisation velocity which is of more practical importance in determining the boundaries of the operating regime.

McLaughlin and Rhodes [12] continued a previous experimental work by Seville and Clift [147] in the effort to produce a specific diagram where the transitions in Geldart group behaviour, brought about by addition of liquids to a fluidised bed, are mapped as a function of fixed ratios of interparticle force to fluid drag force (i.e. particle buoyant weight at minimum fluidisation conditions).

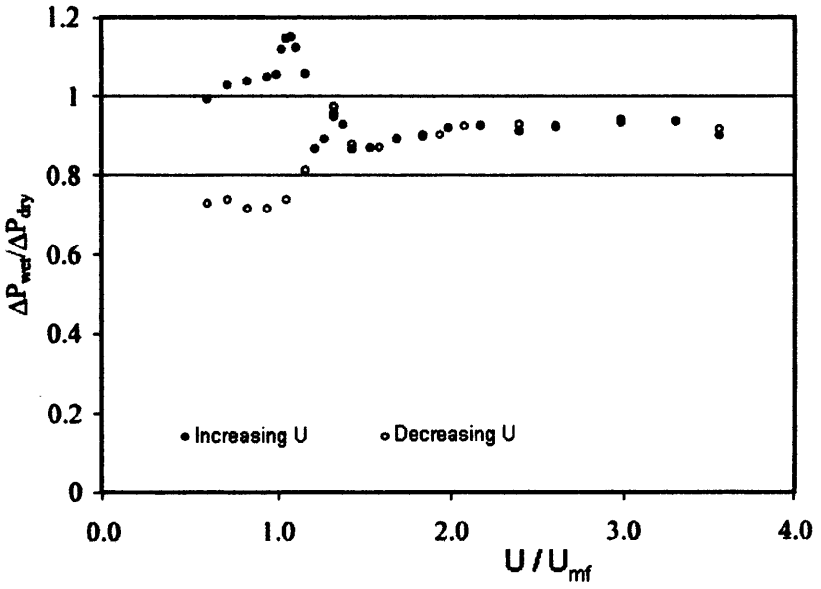

Fig. 4.3: Normalised bed pressure drop versus superficial air velocity after injecting a known amount of Dow Corning silicone fluid, DC 200/12500 (liquid volume = 0.151%; viscosity = 12.5 $Pa \cdot s$). The volume of liquid and its viscosity enhance adhesion among the bed materials, which manifests through decoupling of the fluidising and defluidising curves. The determination of the Geldart's group behaviour (rated A/C in this test) is also confirmed by visual observation of the bed characteristics during experiment. After [12].

Details of the experimental materials and method employed in their investigation can be found elsewhere (McLaughlin and Rhodes [12]), whilst, in figure 4.3, a typical result of a fluidisation-defluidisation test is shown. Upon addition of liquid, the pressure drop across the bed was recorded as a function of gas velocity for increasing and decreasing gas flow rate, and normalised in respect to the pressure drop measured across the fluidised bed of dry particles. Values of gas velocity normalised in respect to the minimum fluidisation velocity for dry particles were used as well. This permitted easier comparison between different conditions.

By increasing the amount of liquid injected into the bed and its viscosity, the authors observed the fluidising behaviour shifting from adequately fluidised bed condition (i.e. when the total bed pressure drop is approximately equal to the buoyant weight of the material[1], or, equivalently, the normalised pressure drop is close to unity), which was classified as A or B behaviour, up to poor fluidisation behaviour (i.e. lack of support of bed material and gas bypassing) that was categorised as C. Thus, according to the large amount of results collected, McLaughlin and Rhodes [12] were able to draw a behavioural map, which is illustrated in figure 4.4.

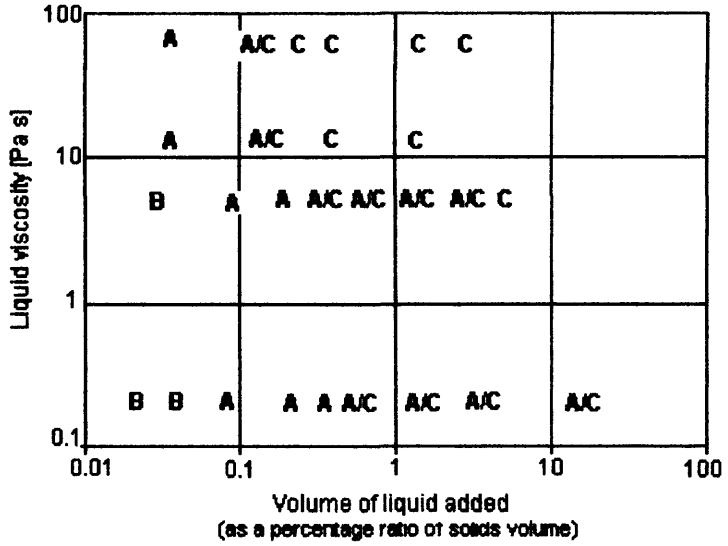

Fig. 4.4: The effect of liquid viscosity and volume of liquid added on the Geldart behaviour observed for $d_p = 1.09$ mm, $\rho_s = 2594$ kg/m^3. After [12].

Furthermore, samples of material, representative of the bed conditions, were withdrawn from the bed during each experiment and SEM micrographs were analysed. Results showed that agglomeration of particles occurred through liquid bridging and values of the filling angles were calculated via image analysis. The authors were therefore able to evaluate the average force exerted between particles (by addition of the calculated capillary and viscous terms of the liquid bridge strength); a further comparison with the buoyant weight of a single particle led McLaughlin and Rhodes [12] to draw a diagram representative of the fluidisation behaviour as function of the interparticle forces generated by the liquid bridges, thus demonstrating that changes in the flow regime occur at a fixed interparticle to buoyant weight force ratio.

Such coclusions, however, show the lack of general validity, which was conversely charac-

[1] Particle adhesion to the vessel walls occurs due to the wet conditions of the bed, hence, the value of the bed mass supported by the gas is somewhat less than the total bed mass. The authors therefore distinguished between fluidisation and defluidisation hydrodynamic regimes according to whether values of the normalised pressure drop fall within the 0.8 and 1 boundary values or below 0.8, respectively.

teristic of Geldart's classification; for instance, the authors did not take into account the influence of the solid/liquid wettability on the flow behaviour and, in their fluidisation tests, only smooth mono-sized glass particles were employed.

Nonetheless, the results of the "cold model" here reported were used in this thesis as a source of comparison, which helped to shed light onto one possible mechanism of high temperature defluidisation that is described in **Chapter 6**.

4.1.1 Process and material parameters responsible for agglomeration

Several physical, chemical and biochemical processes use a continuous injection of liquid in a gas fluidised bed system. The material fed into the apparatus can be a liquid at ambient conditions or can fast become liquid at the operating temperature of the process. Moreover, fluidised bed reactors are widely applied in the field of heterogeneous gas-phase catalysis. There, reactants can be injected into the reactor in a liquid state. Since the reactors are operated at temperatures well above the boiling point, the reactants evaporate in the interior and subsequently undergo the respective chemical reactions in the vapour phase (an example of the successful application on the industrial scale is the FCC process for the cracking of hydrocarbons).

It is not a rare event, however, that some of these processes experience defluidisation due to formation of large agglomerates within the fluidised bed. The genesis and evolution (until the complete bed defluidisation) of the phenomenon can be substantially different, depending on the physical and chemical properties of the interacting phases and on the operative conditions of the processes. In such cases, different fluidisation behaviour can be observed, depending on the value of some parameters, such as gas fluidisation velocity, reactor temperature, physical properties of liquid stream and diameter of bed material, as well as on the occurrence or not of a chemical reaction. Similar problems are also experienced in those processes where agglomeration of the bed material, obtained through drying of liquid binders, is a deliberate design choice (size enlargement processes, granulation etc). Here the prediction of the reactor performance is much more complicated, since it requires control of the size of the agglomerates generated during the process.

In these cases, avoiding or controlling agglomeration phenomena in a fluidised bed is difficult, since wetting, drying and mixing of particles all occur simultaneously in the bed. These mechanisms affect each other and are difficult to control independently. It is therefore necessary to understand the mechanisms involved and their relation to each other and to the operating variables. In this regard, much of the theory available in literature concerns studies of the size enlargement processes, whereas dedicated publications on defluidisation, occurring in other types of "liquid-injected" processes, have been found too

specific or of minor interest for the scope of this thesis.

Several *process* and *material* variables may affect the process of agglomeration in a fluidised bed. Pietsch [2] provided a classification that is shown in Table 4.2:

Process variables	
Apparatus	
Bed load	
Fluidising air:	
	Pressure
	Flow rate (velocity)
	Temperature
Binder solution:	
	Flow rate
	Atomisation (droplet size and distribution)
Nozzle:	
	Design (single or two phase)
	Position (height)
	Port size
	Spray angle
Processing time	
Material (product) variables	
Starting material(s):	
	Particle size and distribution
	Surface area
	Wettability
	Water absorption properties
	Solubility
Binder(s):	
	Type
	Concentration
	Quantity
	Media (water, inorganic or organic solvent)
Binder solution:	
	Temperature
	Viscosity

Tab. 4.2: Process and material variables which control agglomeration in a fluidised bed, after [2].

Among the process (equipment) variables, extensive research has been done to examine

the effects of nozzle type and location in the bed as well as its operation. The nozzle is an important instrument to distribute the moisture on to the fluidising particles. It can be placed above or in the bed, as shown in figure 4.5, spraying sideways, upwards or downwards. Usually, a disadvantage of spraying in the bed is the enlarged attrition of granules due to the high air velocities near the nozzle and therefore nozzles are commonly placed high above the bed (this is also to achieve a larger area of particle/liquid contact).

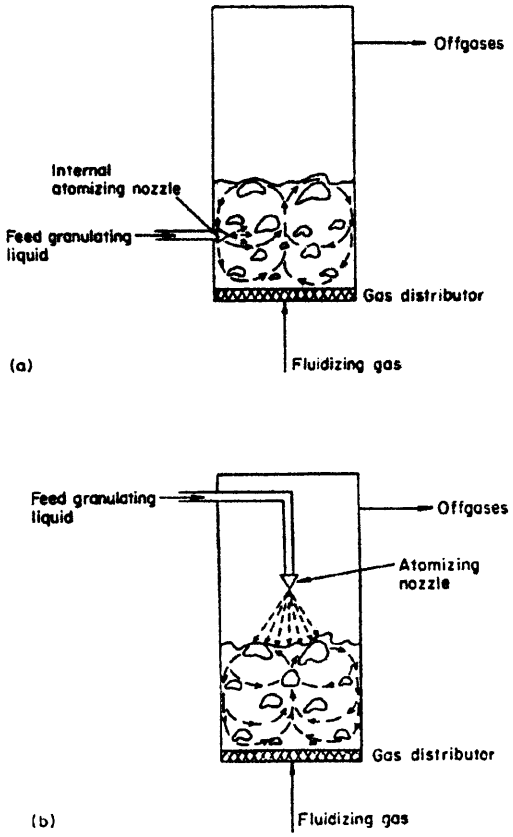

Fig. 4.5: Batch fluidised bed design with nozzle mounted (a) within and (b) above the bed material. After [2].

The major feature of the nozzle is the control of the granule size. The liquid flow rate of the nozzle should be balanced with the evaporation rate. A high liquid flow will result in overwetting of the bed, which may cause difficulties (if not defluidisation) in the flow behaviour. On the other hand, a low liquid flow rate or very small droplets may result in (partial) drying of the binder liquid, thus increasing the amount of fines generated during processing and leading to poor performance of the granulation process. Several authors (see for example [129]) found a linear relationship between the binder flow rate and the mean granule size. In fact, as indicated in **Chapter 7**, the evolution of the average granule size can depend from the amount of liquid feed deposited on a primary particle each time it

goes through the spray cone. The nozzle determines the droplet size distribution, the spray rate and spray pattern upon the spray surface and can be characterised independently of the granulation process itself, which makes it a good tool to control the process.

Other characteristic control parameters for the process are the bed humidity, moisture content and both the bed and inlet air temperature. They are all related to the liquid concentration in the fluid bed. The liquid concentration (or drying rate) determines the adhesion between particles and thus the agglomeration. In particular, humidity not only influences the granule size and growth, but also has an important role on the mixing of solids during fluidisation. In fact, the adsorption of water molecules on the particle surface will increase at higher relative humidity. The adsorbed liquid layer can enhance the interparticle forces and therefore change the bed voidage at incipient fluidisation severely by formation of liquid/solid bridges between the particles. Bonding between particles may also occur during processes involving a chemical reaction; here, hydrated compounds, which are chemically stable at high operative temperatures, can be responsible for strong interparticle forces enhanced by diffusion of water across the particle surfaces followed by formation of crystalline solid bridges (see also **Chapter 7**).

4.1.2 Mechanisms of agglomerate growth

Three mechanisms can be distinguished, which determine the properties and growth of the agglomerate formed in a full-scale fluid-bed granulator: wetting, drying and rupture.

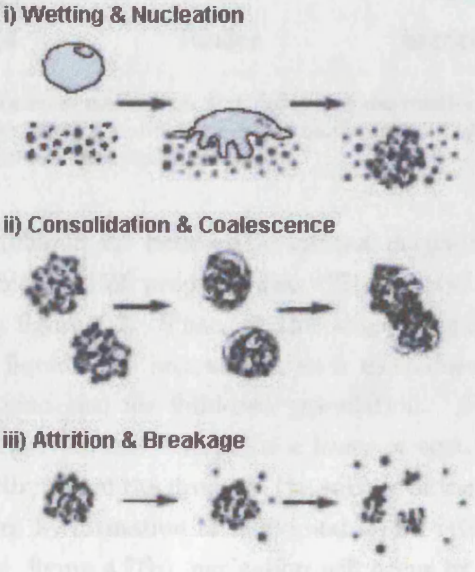

Fig. 4.6: Agglomeration growth: (i) wetting and nucleation, (ii) consolidation and coalescence, (iii)attrition and breakage. After [151].

These mechanisms are usually recognized as occurring in three different stages of agglomerate formation [151], as shown in figure 4.6:

- *Wetting and nucleation*, figure 4.6(i), where the liquid binder is brought into contact with a dry bed of primary particles and is distributed throughout the bed to give a distribution of nuclei granules. This is a crucial stage of agglomerate formation, since wetting of the powder determines the coalescence of the primary particles and thus the growth of the agglomerate. Material variables, which are central to liquid distribution and nuclei formation, are the wettability of the powder towards the binder and the ability of the liquid binder to spread across the surface of the dry powder. Both these parameters, discussed in Sections 2.2.9 and 2.2.9.2, influence the capability for a particle to form larger contact with the binder, which ultimately is beneficial to the distribution of the binder between particles and to the adhesion of liquid bridges formed between pairs of particles [122].
  In addition to such material variables, there is a process variable that can play an important role in this first stage of agglomerate growth: the initial size of the droplet.

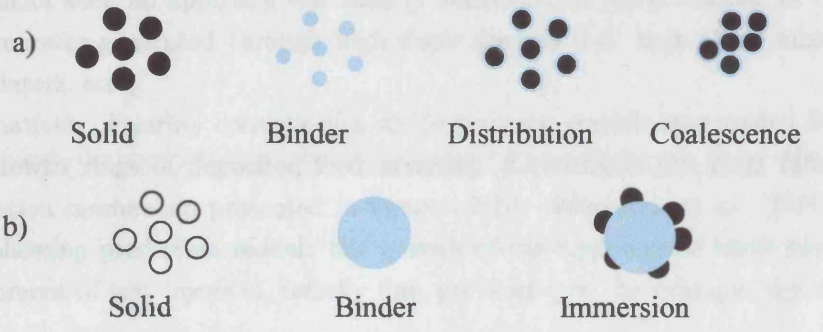

Fig. 4.7: The nucleation formation mechanism may depend of the relative sizes of the binder droplet to primary particle size. (a) Coalescence and (b) immersion nucleation mechanisms in presence of small and large binder droplets, respectively. Adapted from [151].

According to the different size between the sprayed droplets and the primary particle, Schæfer and Mathiesen [152] proposed two different mechanisms of nucleation in a high shear mixer, figure 4.7. Since, at this stage of granulation, shear forces do not influence the liquid/solid interaction, such mechanisms can be more generally considered to happen also for fluid-bed granulation. As shown in figure 4.7(a), nucleation with relatively small drops (size lower or equal to the primary particle) will occur by distribution of the drops on the surface of the particles, which will then start to coalescence by formation of individual liquid bridges. On the other hand, if the drop is large, figure 4.7(b), nucleation will occur by immersion of the smaller particles into the larger drop, which produces nuclei whose inner pores are entirely saturated by the liquid.

- *Granule consolidation and coalescence*, figure 4.6(ii), takes place throughout the process, but occurs most prominently in the early stage of the fluid-bed process where, in contrast to high shear mixers, the agglomerates are usually formed by direct interaction of the spray droplets with the solid, whilst the bed of material remains relatively free flowing. The coalescence of droplets and/or nuclei is generally observed in the spray area. Here, coalescence is expected to depend on the nucleus size, droplet size distribution over the spray area, and the spray rate. The role of mixing in distributing the liquid is thus rather small.

  Two types of granule growth are generally identified: *coalescence* refers to the successful collision and adhesion of two primary particles or granules. Particles wetted by the liquid feed successively coalesce and thus, after the liquid has dried to form solid bridges, produce agglomerates. Ennis et al. [54] proposed an approach for modelling the agglomeration growth due to coalescence of granules, whose base principles have been previously explained in Section 2.2.8 of this thesis. However, the development of such an approach was mainly addressed to the prediction of the size of agglomerates generated through high shear devices (i.e. high shear mixers, drum granulators, etc.).
  Alternatively, *layering* consists of a single primary granule surrounded by concentric growth rings of deposited feed material. Layering is the stage following the nucleation mechanism presented in figure 4.7(b). Schaafsma et al. [115] proposed the following prediction model: the growth of the agglomerate takes place by the attachment of new layers of, usually fine, particles (see, for example, figure 4.8).

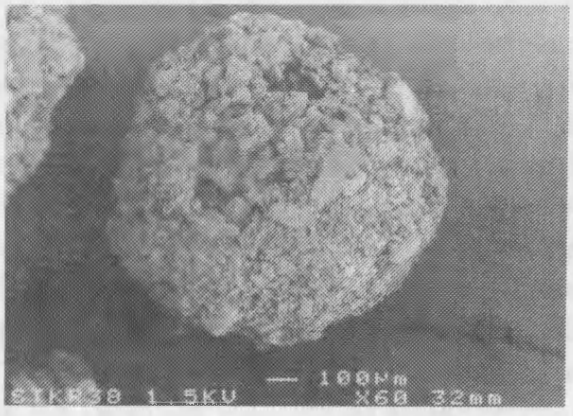

Fig. 4.8: An example of granule growth by *layering*. From [13].

If a pore at the surface of an agglomerate is sufficiently filled with binder liquid, a free particle can reach the liquid phase in the pore and a liquid bridge can be formed. During growth, the liquid is drained from the voids inside the agglomerate to the newly wetted pores formed by the attached particle at the surface of the agglomer-

ate. Due to the resistance of liquid flow this drainage is the rate-limiting process for the growth rate.

The liquid flow is induced by the capillary pressure differences between the pores inside the agglomerate and the pores with lower saturation near the surface of the agglomerate. The liquid saturation inside the granule, defined as the ratio of the binder volume to the total free volume and considered unity for the initial configuration of the agglomerate, decreases during the granule growth following the depletion of liquid, which results from drainage towards the surface. The minimum value of the saturation is reached when no further liquid can arrive at the granule surface and hence the agglomerate growth terminates. This model gave good agreement with data obtained by experiments granulating lactose with different PVP solutions [115]. By assuming that porosity is constant during the time of growth, and consequently neglecting compaction of the agglomerate, the final size of the granule was also predicted and correlated to the initial drop size of the binder. A power law correlation resulted, as indicated in 4.1:

$$D_{drop} \approx (D_{aggl})^{0.89} \tag{4.1}$$

where D_{drop} and D_{aggl} are the diameters of the droplet and agglomerate, respectively. The relation is shown to hold with little variation of the exponent coefficient (from 0.8 to 0.85) for fluidised bed granulators with varying initial binder droplet size in the range from 350 to 4000 μm.

Which of the two mechanisms presented above (*coalescence* and *layering*) may occur during fluid-bed granulation was the object of investigation by Smith and Nienow [153]. The authors findings indicate that, although the binder solutions used in their study have similar surface tensions and similar viscosities over the range of feed concentrations, some liquids showed a rapid increase in viscosity upon solvent evaporation; for such binders, the ability to flow around a bed particle and cover the solids surface is somewhat hindered and therefore coalescence of granules is likely to happen rather than layering growth. However the authors noted that, by increasing the fluidising gas velocity further than the minimum fluidisation value (e.g. increasing the excess gas velocity), the growth of agglomerates by layering takes place for all the systems analysed.

An attempt to incorporate the material properties in the growth mechanisms on a qualitative and somewhat on a quantitative manner was made by Iveson and Litster [154].They describe a shear regime, which starts from a stage of no rupture to a stage of server rupture forces. In this way, the authors covered the whole range from

low-shear to high shear devices. This is depicted by a "granule growth" map, shown in figure 4.9.

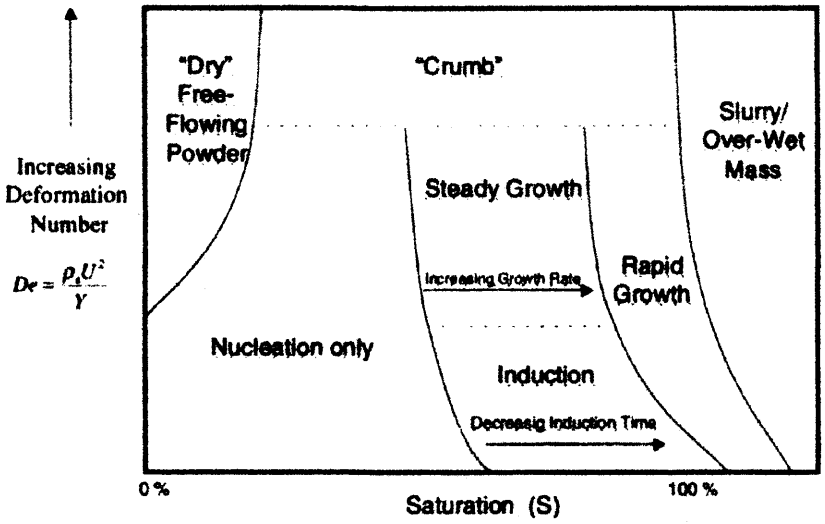

Fig. 4.9: Granule growth map. Adapted from [154].

In figure 4.9 De is the deformation number, which is a measure of the ratio of impact kinetic energy ($\rho_a U^2$, where ρ_a and U are the granule density and velocity, respectively) to plastic energy absorbed per unit strain (Y, the granule dynamic yield stress), and S the pore saturation. Since densification of granules is not an issue in fluid bed agglomeration, Schaafsma [13] concluded that, by taking into account the growth map shown in figure 4.9, growth in the fluid bed is governed by nucleation (engulfment) and layering.

- *Breakage of wet and dry granules*, figure 4.6(iii), is due to (partial) evaporation of the binder solvent, which causes solidification of liquid bridges between particles. As a result of the rupture forces in the agglomeration apparatus, bonds between particles may be broken. The equilibrium between granule formation and breakage is the condition that limits the granule size during the wet phase of agglomeration. On the other hand, breakage of dried granules generates dusty fines resulting, in general, in an impoverishment of the final characteristics.
  Experimental investigations on granulation, coating and drying processes operated by either fluidised or spouted beds, refer to the study of the amount of fines produced inside the bed during the process; this variable is considered as an indicator of the action of disruptive forces over the mechanical strength of the agglomerates. Disruptive forces, as indicated by Shamlou et al. [155], may be originated by different sources of stress inside the bed: chemical stresses, which may cause general weakening of the material strength; thermal stresses due to temperature differences

across the column and which may be the cause, in terms of absolute magnitude, of different strength that holds the generated agglomerates together; fluid-dynamic induced stresses or contact stresses generated by particle-particle or particle-wall collisions and excess fluid energy stresses induced by bubbles motion either in the bulk or near the distributor plate of the reactor.

Because of the difficulty of measuring all these sources of stress, many workers [155, 156, 157] proposed results where breakage of material within the bed is caused by purely hydrodynamic forces, i.e. due to the excess energy of the fluidising gas. This has led to the formulation of the rate of attrition constant of the material, A_k, which depends upon the efficiency of energy exchange between the fluid and the particles in the bed, E_{xs}, and on the surface cohesion force of single particles, f_{coh}:

$$A_k \propto \frac{E_{xs}}{f_{coh}} \tag{4.2}$$

Unfortunately, the development of suitable models that describe the complex mechanisms of breaking and forming of agglomerates within the bed has been hampered by the lack of information on particle interactions at the operative conditions.
In their work, Shamlou et al. [155] investigated fluidisation of non-reacting materials under essentially isothermal and ambient conditions. Moreover, the authors highlighted the need of suitable tests describing the cohesive behaviour of particles in order to better define the effect of f_{coh}, in Equation 4.2, over the attrition rate.

In this thesis (**Chapter** 7), the surface cohesive behaviour of pairs of particles is investigated, in order to provide further information, at a micro-scale level, on agglomerate formation and disruption mechanisms involved in the reactive coating of Magnesium Nitrate Hexahydrate (abbr. MgNH). The effect of temperature and volume of the coating material was studied through the calculation of its strength, thus providing precious information for further modelling work on fluidisation of reactive systems.

4.1.3 Defluidisation due to liquid injection: quenching

Quenching is a defluidisation phenomenon that can occur when liquid is introduced into the bed. If the defluidisation occurs through the formation of large wet clumps due to inadequate heat availability, it is known as "wet" quenching; if due to the formation of large dry, multi-particle agglomerates, held together by dry solute, it is known as "dry" quenching [153].
In this thesis, it has already been suggested that the initial stages of agglomeration, which is a desirable growth mechanism, and of bed quenching, which is disastrous for granulation

and is to be avoided, are exactly the same.

What was proposed in the previous section is that all modes of growth, and bed quenching, have the same initial stage: namely, the formation of liquid bonds between adjacent particles in the fluidised bed.
When spraying top-down in a fluidised bed, two different zones can be distinguished in which different stages of the agglomeration process take place, figure 4.10.

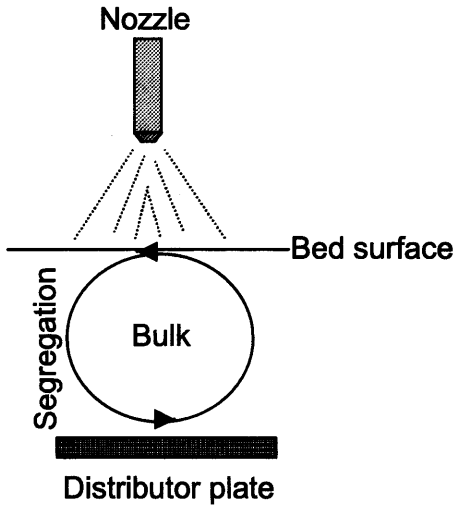

Fig. 4.10: Mechanism of rewetting agglomerates. Adapted from [13].

The first zone is at the surface, the wetting zone, where there is a high liquid concentration and the powder is wetted by the binder liquid droplets. The spray zone, also named spray "cone", is characterised by a high humidity content and a lower temperature in comparison to the rest of the bed [158]. The second zone is the bulk of the fluid bed where the liquid concentration is lower and mixing of the agglomerates and the primary powder in the bed occurs. In this zone the agglomerates are dried.

In the wetting zone, an agglomerate may be formed by one droplet or by several droplets, depending on the spray distribution and the residence time of an agglomerate at the bed surface. The droplet size distribution, the spray density distribution and the spray rate determine, together with the surface renewal rate, the agglomerate growth. In the most unfavourable situation, the spray surface will be overwetted. This results in the formation of large lumps and defluidisation of the bed.

In the bulk zone, the wet agglomerate will segregate in the bed while drying and may reappear at the bed surface after a period of time, the "turnover time". Depending on the ratio between the turnover and drying times, the agglomerate can be dry or still be

partially wet when it reappears at the spray surface. This may be important for the agglomerate growth. If the agglomerate is dry when reappearing at the spray surface, upon rewetting it will suck the binder liquid into its pores. This uptake of liquid is a very fast process if the particle surface is well wettable by the liquid. This results in less liquid available for binding other particles at the surface of the agglomerate. If the agglomerate is still wet when it reappears at the surface, less liquid is sucked into it when rewetted [13].

Smith and Nienow [153] investigated the period between the start of an experiment and the beginning of growth, which was named the "no-growth" period. In their experimental results, the start of growth is indicated by a sudden, large increase in weight-moment mean diameter (due to agglomeration), see figure 4.11, by a rise in temperature at the bottom of the bed (indicating segregation) or by visual observation of large agglomerates forming on the distributor plate. Their conclusion was that the "no-growth" period is a function of binder concentration, and therefore of the binder mass input, in that the higher the latter the shorter the first.

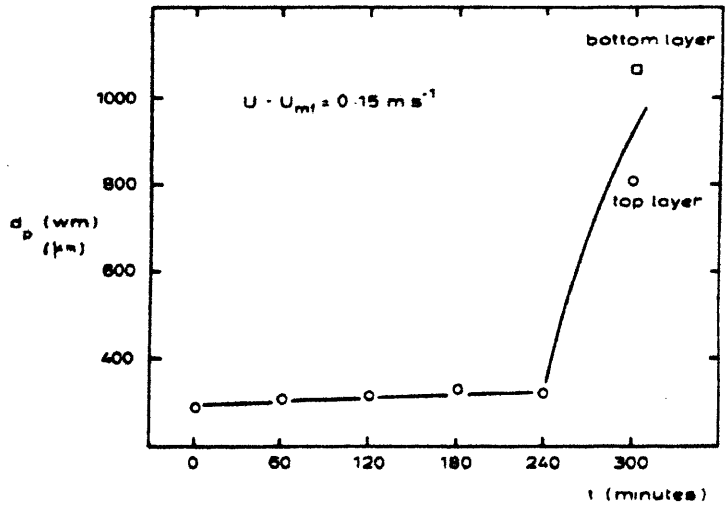

Fig. 4.11: "No-growth" period (circa 240 minutes) for porous alumina fluidised with 10% benzoic acid solution. From [153].

However, when solvent is evaporated from the feed solution, liquid bonds will give rise to solid bridges between adjacent particles, unless there is a redistribution of binder either before or after the solution dries. Whether this redistribution takes place by a breaking of either liquid bonds or solid bridges will depend on the balance between the two elements of fluidised bed granulation: first the binding mechanism which results in particles joining together to form larger ones because of the presence of liquid in the fluidised layer and, secondly, the abrasive action of the fluidised bed, which tends to break down, or prevent the formation of agglomerated particles. Smith and Nienow [153] noted that the magnitude

and relative importance of these effects will depend upon, on the one hand, the quantity and physical properties of the liquid feed and, on the other, upon the characteristics of the fluidised bed, such as the size and nature of the bed particles. In fact, smaller bed particles are more likely to form permanent bonds, and then to quench, because of their smaller inertia. The force tending to shear apart two particles is equal to the product of the particle mass and the distance between the two centres of mass. For the case of two spherical particles joined together at their surfaces, this force will be proportional to the particle diameter raised to the fourth power.

4.2 High temperature defluidisation: sintering effect

Much of the success of fluidised bed reactors in industrial applications is directly associated with their thermal properties. Accordingly, after the earliest fluidised coal gasifiers and FCC units, many of the industrial plants exploiting fluidisation technology have been designed for operations run at thermal levels well above ambient temperature. This is the case, for instance, of fluidised bed combustors for coal and biomass, of solid waste incinerators, of many catalytic reactors for organic syntheses and nuclear waste reprocessing.

Design criteria and performance predictions for fluid bed units working at medium or high temperature have been, so far, almost entirely based on fluid dynamic models elaborated from experimental results produced under room conditions.
However, extrapolating results and relationships available at ambient conditions to elevated temperature is not straight forward, and, indeed, overlooks possible modifications induced by temperature in the structure and dynamics of the fluid-bed. This is likely to lead to errors in evaluating heat (and mass) transfer phenomena which determine the reactor performance [159].

4.2.1 Heat transfer in fluidised beds

Although gas-to-particle heat transfer coefficients based on the total particle surface area are often small, a fluidised bed of particles is capable of exchanging heat very effectively with the fluidising gas because of the very large surface area exposed by the particles ($1m^3$ of $100\mu m$ diameter particles has a surface area grater than $30{,}000m^2$, which is equivalent to the surface area of the Great Pyramid of Cheops [160]). Typically, coefficients based on total area may be as low as 6 to 23 W/m^2K. It is thus apparent that only a fraction of the total particle surface can be actually accessible to the fluidising gas, but this rarely presents a limitation in achieving adequate heat transfer between the fluidising gas and the bed particles because of the very large total particle surface area involved.

In fact, it seems reasonable to suppose that the gas, with its relatively low heat capacity (e.g. the thermal capacity of air at atmospheric pressure is of the order of one thousandth

of that of the particles), will rapidly approach the temperature of the solids it is fluidising and with which it is in contact across such a large surface area. However, Botterill [160] reported marked temperature differences between them. In tests on a bed of spent cracking catalysts cooling from an initial temperature of 210°C, gas temperatures of the order of 100°C were measured when the bed had cooled to 170°C. Nevertheless, because of its high heat capacity, it is the temperature of the solids which dominates the bed thermal behaviour and it is the gas temperature that follows that of the particles rather than the other way round.

On the basis of the gas-to-particle heat transfer correlation given by Kunii and Levenspiel [161], Equation 4.3, the temperature difference between the entering gas and a well mixed bed of particles (so that it can be assumed the isothermal condition of the bed material) can be estimated to drop to half its initial value within a short distance from the gas entry.

$$Nu_{gp} = 0.03Re^{1.3} \tag{4.3}$$

Nu_{gp} and Re are the gas-to-particle Nusselt and Reynolds numbers, respectively and the correlation is valid for $Re \prec 50$.

More interesting from a practical point of view is heat transfer between the bed material and immersed surfaces (vertical bed walls or tubes) in a bubbling fluidised bed. Particle-to-particle and particle-to-surface contact areas are too small for significant heat transfer to occur through points of solid contact (solid-solid conduction). Heat has to transfer by conduction through the gas phase which constitutes the chief resistance to heat transfer in this mechanism because of its low thermal conductivity. Consequently, the increase in bed-to-surface heat transfer coefficients with operating temperature is due to the increase in gas thermal conductivity with increasing temperature.

It is generally accepted that the overall heat transfer coefficient, h, between an immersed surface and a gas fluidised bed can be expressed as the sum of three components [160], as shown in (4.4):

$$h = h_{pc} + h_{gc} + h_r \tag{4.4}$$

where h_{pc} is the particle convective heat transfer coefficient, which describes the heat transfer due to the motion of packets of solids carrying heat to and from the surface. The coefficient h_{gc} represents the gas convective heat transfer and describes the transfer of heat by motion of the gas between the particles. The third coefficient, h_r, is the radiative heat transfer.

The radiative component is of significance only above about 600°C while the gas convective term is of importance only for beds of large Group B and Group D materials, as shown

in figure 4.12. For Group A and small Group B powders, h_{gc} is usually insignificant under normal operating conditions and so, in the absence of radiation effects it is h_{pc} that dominates the heat transfer process.

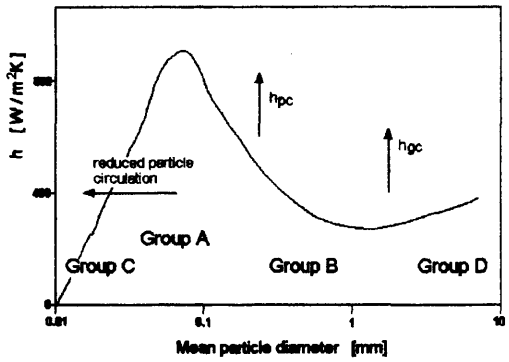

Fig. 4.12: Range of bed-surface heat transfer coefficients and the effect of particle size on the dominant heat transfer mechanism. From [162].

The strong inverse dependence of the heat transfer coefficient, h, upon particle size results from the increase in the effective proportion of the surface area through which heat can flow by *short transfer paths* between particles and surfaces as particle size reduces, until eventually interparticle forces restrict particle circulation (Group C materials) [162]. The coefficient then falls with further reduction in mean diameter. On the other hand, increasing gas velocity beyond minimum fluidisation improves particle circulation and so increases particle convective heat transfer. However, the heat transfer coefficient increases with fluidising velocity up to a broad maximum and then declines as the heat transfer surface becomes blanketed by bubbles.

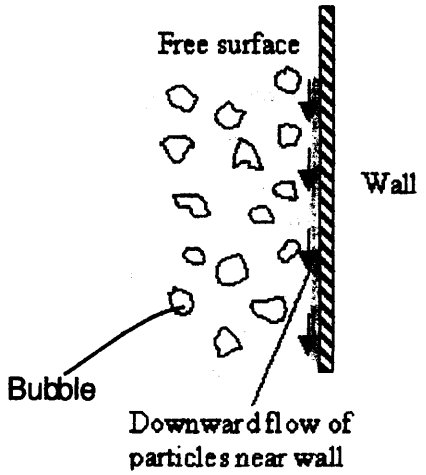

Fig. 4.13: Particle flow at a containing wall.

Different considerations should be taken in the case where the surface in the bed-to-surface heat transfer refers to the side walls of the vessel, figure 4.13.

The flow of particles at the wall surface tends to be generally downwards, the particles sticking and slipping down intermittently; the particle flow at the containing wall is only occasionally disturbed by bubbles which move to the wall. Because of comparatively little particle convection and the relatively long particle residence time at any one region on the containing wall (as can be observed by a simple laboratory experiment with particles fluidised within a transparent tube), the heat transfer coefficient, h, at the bed-to-wall interface may be expected to be lower than that to, say, a horizontal cooling tube immersed in the well fluidised region of the bed. There are practical difficulties in trying to find suitable models of such heat transfer, in that the heat transfer coefficient arising from such modelling requires knowledge of an 'effective' thermal conductivity of the emulsion sliding down the wall and the time taken to slide down (the latter can only be estimated crudely). Furthermore, knowledge of the fraction of the wall covered by bubbles and the velocity of sliding is also required.

Given the extent and the relevance of its applications, research on the influence of temperature on high temperature fluidisation has been gaining a growing interest in recent years. However, studies published so far show, as recently indicated by Yates [163], that experimental findings are somewhat controversial and that a satisfactory understanding of the phenomena responsible for differences between ambient and high temperature fluidisation has not yet been achieved. As a consequence, although experimental studies (see next section) have given good contributions to a better understanding of specific aspects of fluidisation at superambient temperature, much uncertainty still exists about the way fluidisation theory should be managed to encompass the role of this variable [159].
Similarly, the study of defluidisation at high temperature seems to be hampered by the lack of suitable experimental techniques and theoretical models, which can help in the design and control of the process. Poorly designed fluidised beds or insufficient fluidising velocity can affect the mechanism of heat transfer quite severely, thus leading to the presence of local non-fluidised ("dead") zones of particles that can cause hot spots and therefore particle sintering and agglomerate formation. This then lead to a rapid expansion of the dead zones and eventually the bed becomes completely defluidised.

4.2.2 Agglomeration induced by sintering

Currently, the most important aspect of high temperature cohesion in industrial fluid-particle systems is to avoid it. Difficulties caused by high temperature cohesion include particle deposition in high temperature cyclones, fouling of transport lines, agglomerate formation at distributor plates and other fluidised bed surfaces, poor heat transfer and

Different considerations should be taken in the case where the surface in the bed-to-surface heat transfer refers to the side walls of the vessel, figure 4.13.

The flow of particles at the wall surface tends to be generally downwards, the particles sticking and slipping down intermittently; the particle flow at the containing wall is only occasionally disturbed by bubbles which move to the wall. Because of comparatively little particle convection and the relatively long particle residence time at any one region on the containing wall (as can be observed by a simple laboratory experiment with particles fluidised within a transparent tube), the heat transfer coefficient, h, at the bed-to-wall interface may be expected to be lower than that to, say, a horizontal cooling tube immersed in the well fluidised region of the bed. There are practical difficulties in trying to find suitable models of such heat transfer, in that the heat transfer coefficient arising from such modelling requires knowledge of an 'effective' thermal conductivity of the emulsion sliding down the wall and the time taken to slide down (the latter can only be estimated crudely). Furthermore, knowledge of the fraction of the wall covered by bubbles and the velocity of sliding is also required.

Given the extent and the relevance of its applications, research on the influence of temperature on high temperature fluidisation has been gaining a growing interest in recent years. However, studies published so far show, as recently indicated by Yates [163], that experimental findings are somewhat controversial and that a satisfactory understanding of the phenomena responsible for differences between ambient and high temperature fluidisation has not yet been achieved. As a consequence, although experimental studies (see next section) have given good contributions to a better understanding of specific aspects of fluidisation at superambient temperature, much uncertainty still exists about the way fluidisation theory should be managed to encompass the role of this variable [159].
Similarly, the study of defluidisation at high temperature seems to be hampered by the lack of suitable experimental techniques and theoretical models, which can help in the design and control of the process. Poorly designed fluidised beds or insufficient fluidising velocity can affect the mechanism of heat transfer quite severely, thus leading to the presence of local non-fluidised ("dead") zones of particles that can cause hot spots and therefore particle sintering and agglomerate formation. This then lead to a rapid expansion of the dead zones and eventually the bed becomes completely defluidised.

4.2.2 Agglomeration induced by sintering

Currently, the most important aspect of high temperature cohesion in industrial fluid-particle systems is to avoid it. Difficulties caused by high temperature cohesion include particle deposition in high temperature cyclones, fouling of transport lines, agglomerate formation at distributor plates and other fluidised bed surfaces, poor heat transfer and

fluidisation quality and catastrophic defluidisation. Tardos et al. [112] stated that "basic knowledge in the area is so limited that industry relies mostly on empiricism to avoid defluidisation of beds containing sticky particles" and, despite the number of works increasingly published on the subject, so far there is still no mechanistic model available that can reliably predict under what conditions defluidisation will occur. However, a number of attempts at modelling the defluidisation process caused by sintering of particles have been made and are reviewed here after.

Whether or not beds defluidise would seem to depend on a balance between the cohesiveness or "stickiness" of the particle surfaces and the kinetic energy of the particles due to the fluid forces acting on them (similar to the agglomeration mechanism explained in Section 4.1.2) [163]. In fact, Gluckman et al. [61] showed that, above a certain temperature, the minimum fluidisation velocity will not follow the theoretical value calculated by Ergun's equation [164] by simply accounting for the variations of the gas properties, but increase sharply with temperature, see figure 4.14(a). They defined this onset temperature as the 'initial sintering temperature', T_s. Thus, the minimum fluidisation velocity as a function of temperature demonstrates two hydrodynamic regimes delimited by T_s.

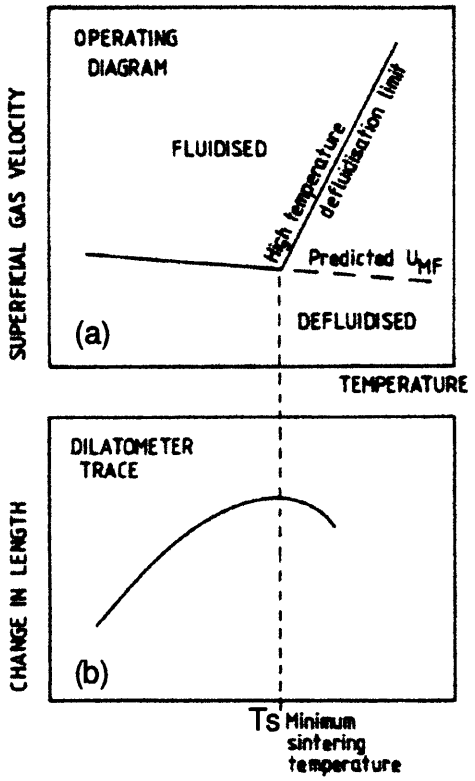

Fig. 4.14: High temperature defluidisation: (a)operating region diagram and corresponding dilatometer trace (b). After [61].

Gluckman et al. [61], Compo et al. [10] and Tardos et al. [95] noted that the temperature at which the measured defluidisation velocity departed from the predicted behaviour in the absence of interparticle forces coincided with T_s, as measured using a dilatometer (see Section 2.3.1.2), and as shown in figure 4.14(b). These authors concluded that at such temperatures fluidisation is no longer determined by a balance of gravity, buoyancy and drag forces, but that interparticle cohesiveness and particle kinetic energy must also be taken into account.

Compo et al. [109] investigated the minimum sintering temperatures for different types of fluidisable powder materials by incorporating detailed analysis of the results for the relevant thermograms obtained by dilatometry.

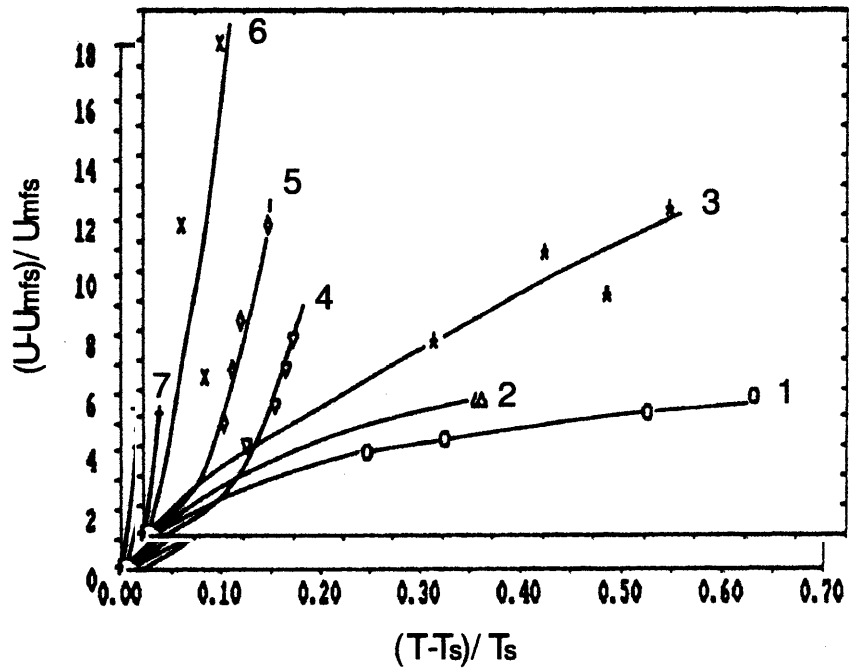

Fig. 4.15: Defluidisation curves for crystalline (solid lines: 1-Calcium chloride, 2-Sodium citrate, 3-Sodium chloride) and amorphous (solid lines: 4-Glass d_p=0.741 mm, 5-Glass d_p=0.275 mm, 6-Coal, 7-Polyethylene) materials. The lines are least square fits to the data. After [10].

Such results were combined with defluidisation experiments and summarized in figure 4.15, which shows defluidisation temperature plotted against gas velocity, both quantities being normalised by means of T_s and U_{mfs}, the latter being the minimum fluidisation velocity of the material at the defluidisation temperature calculated and corrected (through the Ergun's equation [164]) from the value at ambient conditions [10]. Since none of the materials analysed was found to defluidise below its sintering temperature, the authors distinguished two categories according to their fluidisation behaviour:

1. The first category encompasses those materials, such as glass beads, coal powder and polyolefin granules (lines marked as 4, 5, 6 and 7 in figure 4.15) that agglomerate quickly after T_s has been reached and the increase in gas velocity needed to keep the bed fluidised increases exponentially.

2. The second group behaves similarly to ionic solids (lines marked as 1, 2 and 3 in figure 4.15), which form relatively weak agglomerates and for which only a slight increase in fluidising velocity is necessary to restore fluidisation once agglomeration has begun.

However, in further work, Compo et al. [10] reported difficulties of interpretation for the elongation/contraction curves shown by different inorganic hydrated salts during dilatometry tests; in fact, some major issues were pointed out in relation to the validity of the experimental technique employed. For instance, the virgin sample could not be used in the dilatometer because otherwise the release of surface water dissolved the sample and formed a solution. Moreover, because of the release of intercrystalline water from the material, the dried sample expanded greatly upon heating and formed an agglomerate. The 'non-sintering' mechanism associated with this type of high temperature agglomeration could not be further investigated. Finally, none of the experiments were conducted under the same conditions.

In this regard, innovative and reproducible results obtained from the development of a unique experimental technique are presented, in this thesis, in **Chapter 7**.

4.2.3 Modelling viscous sintering in fluidisation

Theories of sintering mechanisms are based on the concept of a series stages, the first of which is the initial bond formation (see Section 2.3.1). In these models the particles are assumed to be in contact before heating. In a high temperature fluidised bed, the particles come into contact at sintering temperatures and so initial bonding must depend on what happens in the short duration of contact/collision. Hence, modelling the sintering problem in fluidised beds has been attempted by several theoretical approaches in an effort to provide a relationship between the physical properties of the material, its sintering behaviour and the hydrodynamics of the fluidised bed.

In order to develop a model suitable to predict/avoid the high temperature defluidisation due to viscous sintering, Tardos et al. [112] calculated the theoretical limiting gas velocity, U_s, necessary to break the largest agglomerate in the bed and thereby to keep a bed of sticky particles fluidised at temperatures above the minimum sintering temperature. Starting from the principle that the forces acting on particles in fluidised beds may be classified either as attractive (giving rise to particle bonding) or breaking forces (due to

the motion of gas bubbles in the bed), the authors looked for conditions in which the dynamics of such forces are in equilibrium. In their assumptions they considered that the largest agglomerate, cylindrical in shape for simplicity, occupied the entire cross section of the bed, but conceded that in large beds defluidisation would be likely to occur before this size was reached (in this case the predicted limiting velocity, U_s, should be considered a lower bound for the fluidising gas velocity). Further simplification was added by assuming that such an agglomerate is not freely buoyant but occupies a fixed position in the bed (above the distributor plate), and that rupture forces are addressed to the disruptive shear caused by bubble motion (thus neglecting rupture caused by the interstitial flow of the gas).

Although the forces acting on a buoyant body are smaller than those on a fixed body, and that the vertical force on a submerged body fluctuates as a function of the position of the bubble, the authors employed an equation of Livshits et al. [165] to correlate the maximum force, G_v, acting on the agglomerate to the excess velocity $(U - U_{mf})$, as shown in Equation 4.5:

$$G_v = 0.1\rho_p d_{agg}^{1.5}\left\{1.9\left(\frac{d_b}{L_0}\right)^{0.5}[g(U-U_{mf})l]^{1/3} + U - U_{mf}\right\} \tag{4.5}$$

where L_0 is the bed height at rest, d_b is the bed diameter, d_{agg} is the diameter of the agglomerate and l is the height of the cylinder (aggregate) above the distributor plate.

By assuming that the force G_v is uniformly distributed over the agglomerate's bottom surface, the corresponding pressure, q, can be obtained as in (4.6):

$$q = \frac{4G_v}{\pi d_{agg}^2} \tag{4.6}$$

This pressure will cause failure of the structure (i.e. breaking of the agglomerate) if its value exceeds q_{max} where:

$$q_{max} = \sigma_y\left(\frac{2h}{d_{agg}}\right)^2 A_1 \tag{4.7}$$

where σ_y is the yield strength of the agglomerate, h is the height of the agglomerate and A_1 is a coefficient approximately equal to 2.

Combining these equations results in a rather complicated expression, the evaluation of which requires knowledge of two fundamental physical quantities, the surface viscosity, η_s, and the strength of a sinter neck, both as functions of temperature. The surface viscosity can be found from dilatometer data (see Section 2.3.1.3), whilst the strength of the solid bridge can be estimated using adhesion theory or calculated from experimental data (see

Section 3.2.2).

A different approach was taken by Seville et al. [110] who proposed a model based on characteristic residence times by relating the dependence of the excess fluidising velocity on temperature, thus avoiding the theoretical considerations on the strength and growth behaviour of sintered agglomerates. During fluidisation particles are considered to remain in quiescent zones with relatively little movement until they are disturbed by the passage of bubbles. According to the 'two-phase' theory of fluidisation, where it is assumed that all gas flow in excess of that required for incipient fluidisation flows through the bed in the form of bubbles, Equation 4.8 relates the measure of the residence time, t_{b0}, in the quiescent zones to the excess fluidising velocity:

$$t_{b0} = \frac{H_{mf}}{\alpha_{sb}(U - U_{mf})} \tag{4.8}$$

where H_{mf} is the bed height at minimum fluidisation condition, α_{sb} is the ratio of the volume of solids moved by bubbles to the volume of bubbles and $(U - U_{mf})$ is the excess gas velocity. The equation describes the time required to turn the contents of the bed over once, which, if sufficiently long, can be compared to the characteristic time for the sinter neck to reach a critical size such that the agglomerates cannot be disrupted by the bubble motion.

By assuming that the size of a given critical neck is not dependent on the fluidising gas velocity, the following expression was derived for the time, t_c, for a sintered neck to form:

$$t_c = \left(\frac{X_c}{r_p}\right)^2 \frac{\eta_s}{k_1} \tag{4.9}$$

where X_c is the neck diameter, r_p is the particle radius, k_1 is a coefficient depending on both material properties and environmental conditions and η_s is the surface viscosity at operative conditions and whose dependence on temperature is provided by the Arrhenius law:

$$\eta = \eta_0 \exp\left(E/RT\right) \tag{4.10}$$

By equating (4.8) with (4.9) and (4.10), the authors obtained a relationship for the temperature dependence of the minimum fluidising velocity under sintering conditions:

$$ln\frac{(U - U_{mf})}{H_{mf}} = ln\left(\frac{k_2}{\alpha_{sb}\eta_0}\right) - \frac{E}{RT} \tag{4.11}$$

where k_2 characterises the effect of the critical size of the sinter neck, as it is equal to $\left[(X_c/r_p)^2\, 1/k_1\right]^{-1}$.

It should be noted that in this model it is also necessary to obtain experimental values of two important physical quantities, namely the surface viscosity and activation energy, which can be calculated, in some cases, by means of dilatometry. Equation 4.11 provides predictive capability by showing an exponential trend of the minimum fluidising velocity, required to prevent defluidisation, with temperature.
Seville et al. [110] tested Equation 4.11 by fluidising polyethylene at temperatures between 100 and 120°C, where sintering occurs. Figure 4.16(a) is a photograph of the sintered particles, whilst figure 4.16(b) shows the increase in minimum fluidising velocity required as temperature increases.

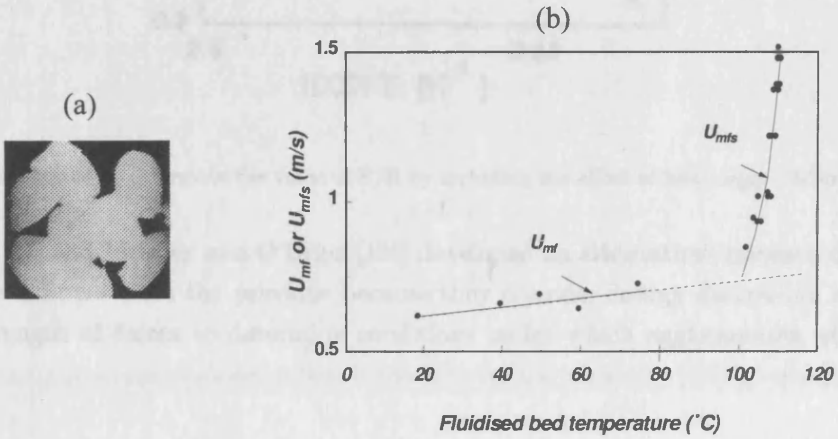

Fig. 4.16: (a) Photograph of sintered polyethylene particles, (b) effect of sintering on the minimum fluidising velocity. After [110].

Figure 4.17 shows the calculation of E/R from the slope of the log-log plot of Equation 4.11. Thus the sintering effect can be fully predicted.

The size of the sinter neck predicted by this model is approximately of two order of magnitudes smaller than theoretical values. The authors addressed this difference to the theoretical under-estimation in the contact area between the cylindrical beads employed in their experimental work, as this parameter would be larger than that estimated for spherical shaped particles. For the same reason, the particles may compress less under load than spherical particles, giving surface viscosity values which are higher than the true values (circa three orders of magnitude). Hence, the effect of particle size and shape on dilatometry measurements is a crucial step in the validation of the model presented and, in this regard, the authors commented that further dilatometry and defluidisation studies need to be undertaken.

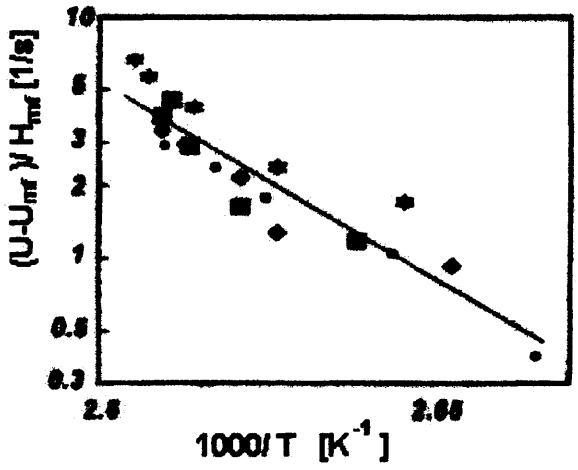

Fig. 4.17: Data plotted to determine the value of E/R by including the effect of bed height. After [110].

Ennis et al. [54] and Moseley and O'Brien [166] developed an alternative approach that is conceptually different from the previous because they consider energy dissipation rather than the strength of forces to determine conditions under which agglomerates will not form.

The theory of Ennis et al. [54], which was reviewed in Section 2.2.8 of this thesis, is based on the concept of the dissipation of the kinetic energy of particle collisions via surface viscosity and is particularly applicable to fluid bed granulation through the introduction of liquid binding agents. Altghough the theory compared favourably with results from Gluckman et al. [61], it applies better to mechanisms of defluidisation where the presence of excessive liquid layers on the particle surfaces is due to melting or reaction, rather than to viscous sintering.

On the other hand, Moseley and O'Brien [166] proposed a kinetic model more suited to viscous sintering. In their theory, the particles are considered sticky, elastic and spherical. The kinetic energy is taken to be dissipated in doing work against an adhesive force on rebound, taken to be proportional to the area of contact. They obtained a relationship between the critical collision velocity and the adhesion force. Clearly, again, a problem of the approach is the need to express the adhesion force as function of operative parameters and, possibly, not in relation to material properties.

4.3 Non-invasive measurement techniques

Fluidised beds operating at high temperature are employed in a wide variety of applications such as combustors of dirty fuels, nuclear fuel reprocessing, chemical reactors, ore roasters and coating applicators. Designers of large commercial beds are well aware that the fluid dynamics at such operative conditions can directly influence the performance of the process; on the other hand, because of the complexity of the multiphase phenomena, a theoretical solution for the bed behaviour based on first principles remains unsolved. The modern design approach is concerned with the relationship between the performance of the industrial unit and results from much smaller pilot plants, where the dynamic investigations can be carried out at ambient conditions. The understandings achieved in this way provides precious information for the optimisation of the quality of the process. For example, in a bubbling fluidised bed, the size, frequency and distribution of bubbles are directly linked to particle mixing and gas to solid interaction. A bed of uniformly distributed fine bubbles will yield higher chemical conversion than a bed containing a few large bubbles concentrated at the centre. The particle residence time in a circulating fluidised bed combustor has a strong influence on the combustion efficiency and the level of pollutant emission.

Nonetheless, a satisfactory understanding of the phenomena responsible for modifications in the structure of fluidised beds, and therefore responsible for changes in the flow behaviour, between ambient and high temperature, has not yet been achieved. The flow behaviour diagram obtained by plotting the density difference of the solids and fluidising gas against the mean particle size can be a useful guide at ambient conditions. However, at higher temperatures and pressures, the usefulness in maintaining this classification becomes doubtful and it is just these conditions that prevail in most commercial reactors. Hence, the closer the match between the 'model' of the fluidised bed and the real reacting system and physical processes, the more likely it is that the model will accurately describe the 'physics of fluidisation' and track changes in the fluid dynamics of the real system.

In this regard, Simons [167] noted, in his recent review on measurement techniques in fluidisation, that imaging techniques have proven to be ideal in providing hitherto inaccessible data on bed behaviour, since they are non-invasive, are generally unaffected by the sometimes harsh process conditions, and can produce scans in three dimensions. In the development of non-invasive methods, however, it has to be taken into account that industrial applications of fluidised beds are typically very large reactors. For example, the combustion chambers of fluidised bed boilers have cross-sectional areas of between 25 and 100 m^2 and heights of between 20 and 40 m. Fluidised bed reactors in the chemical industry commonly have diameters between 3 and 5 m with heights ranging from 5 to 15 m. These are dimensions that are a big challenge for non-invasive measurement techniques.

It is therefore not surprising that the application of such methods is currently restricted (with, perhaps, exception of the X-ray imaging technique) to academic investigations of fluidised beds with diameters between 5 and 50 *cm* [168].
In the following sections a brief review of the most commonly employed non-invasive techniques is presented; the attempt is twofold: first, to establish a link between the macro-scale investigation of the process and the off-line measurements taken at a micro-scale (e.g. AFM). Second, to deliver a wider contribution to the understanding of the topic of this thesis rather than provide a detailed review work. However, the reader will be able to find, in each section, sufficient referenced material for further in-depth analysis and information.

4.3.1 X-ray imaging technique

The majority of the work carried out on fluidised systems using X-ray attenuation has been conducted by Rowe (e.g.[169]) and Yates and co-workers (e.g.[170]) at University College London (UCL). Investigations have been centred on the behaviour of gas-bubbles in solid beds, phenomena such as bubble growth, bubble splitting, the effect of gas distribution, elevated temperatures and pressures and co-axial nozzles all being studied via X-ray images. The essential elements of the X-ray equipment are shown in figure 4.18

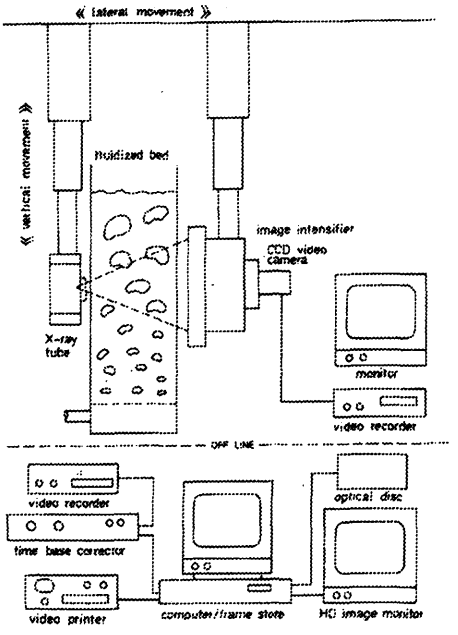

Fig. 4.18: X-ray attenuation equipment (UCL). After [171].

The technique, described in deteail elsewhere [171], provides a non-intrusive method of obtaining real time moving images of the internal flow patterns of fluids and solids inside the fluidised bed. A pulsed (50 Hz), high-energy beam (50-180 kV) is produced from

a rotating anode. The beam is passed through the test vessel, where absorption occurs depending on the amount and distribution of fluid and solids within the vessel. The pulse-rate frequency of the X-ray beam is syncronized with a video camera, thus 'freezing' internal motion and allowing the internal flow patterns to be continuously detected and recorded.

Such a technique has been employed in industry by BP to investigate and measure the nozzle jet penetration in a fluidised bed [172]. Newton et al. [172] identified the benefits of using X-ray imaging in five major points:

1. X-ray imaging provides unambiguous, real-time information.
2. It is a non-intrusive technique, therefore provides both qualitative and quantitative information. However, this technique require relatively long imaging times (minutes to days), and so is suited to off-line imaging for process development and/or quality control.
3. The technique is applicable to large-scale vessels. However, it was reported by Morton and Simons [173] that attenuation of the radiation signal restricts maximum vessel diameters to around 1 m.
4. Understanding of process fluid dynamics, which leads to improved plant design and optimization, can be achieved through X-ray imaging.
5. X-ray imaging is a diagnostic tool for assessing engineering designs and trouble shooting.

The X-ray apparatus has been recently used at UCL by Lettieri et al. [111] for the investigation of the flow behaviour of different FCC catalysts as the temperature of the fluidised bed was increased up to 650 °C. In order to elucidate the material related properties responsible for the observed changes, the authors combined the results of both thermo mechanical (TMA) and thermo gravimetric (TGA) analysis (see Sections 3.3.2.4 and 3.3.2.2) for each sample of powder with the experimental observations obtained using the X-ray imaging technique.

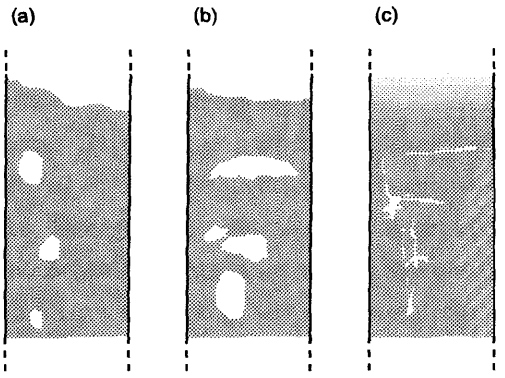

Fig. 4.19: (a) Bubbling, (b) Slugging, (c) Channelling flow behaviours when fluidising the E-cat catalyst at different temperatures.

Among the materials employed, the equilibrium (E-cat) FCC catalyst received particular attention because its physical properties and flow behaviour. Pressure drop measurements and image analysis indicated changes in bed behaviour, figure 4.19, with increasing (and decreasing) temperature. In particular, fluidisation of this powder could not be achieved at temperatures above 200 °C as irreversible defluidisation occurred. The catalyst could not be re-fluidised after the system had been cooled back to ambient temperature. The pressure drop across the bed remained at zero for all flow rates and particles were found permanently agglomerated in solid bridges at the distributor plate. Moreover, it was only possible to break up this solid material by using a strong solvent followed by sand blasting.

Clearly, the operative temperature is the controlling variable of strong particle-particle cohesive interactions. This was not investigated further by Lettieri et al. [111]. In order to shed light on the binding mechanisms occurring between E-cat particles at high temperature, a micro-mechanistic approach was undertaken and results are presented in **Chapter 6**. This is a clear example of how a combination of non-invasive imaging and particle-particle manipulation can provide a comprehensive description of defluidisation phenomena at high temperatures.

4.3.2 Positron emission particle tracking (PEPT)

Positron emission particle tracking, generally known as PEPT, is an imaging method for following the motion of a single tracer particle in a dense medium; recent improvements in this technique allowed particles smaller than 100 μm to be traced. Perhaps uniquely among measurement techniques, PEPT can provide insight into processes such as agglomeration by enabling the motion of an individual radioactively labelled particle of granular material to be followed in detail at high speed inside a fluidised bed, the accuracy of detection of the particle location and the speed of data processing being largely dependent on the quality

of the data acquisition software.

In principle, positron emission particle tracking relies on a tracer particle labelled with a radioisotope which undergoes β^+ decay, i.e. a positron is emitted. The positively charged positron is the antiparticle of the normal electron, and when the positron encounters an electron the two annihilate. Energy is then released in the form of a pair of 511 keV gamma rays which, in order to conserve momentum, are emitted back-to-back. Simultaneously detecting these two gamma rays using a 'positron camera' comprising a pair of position sensitive detectors operating in coincidence defines a line close to which the decay must have occurred. After detecting a small number of such gamma-ray pairs the position of the tracer particle can be determined by triangulation, as shown in figure 4.20.

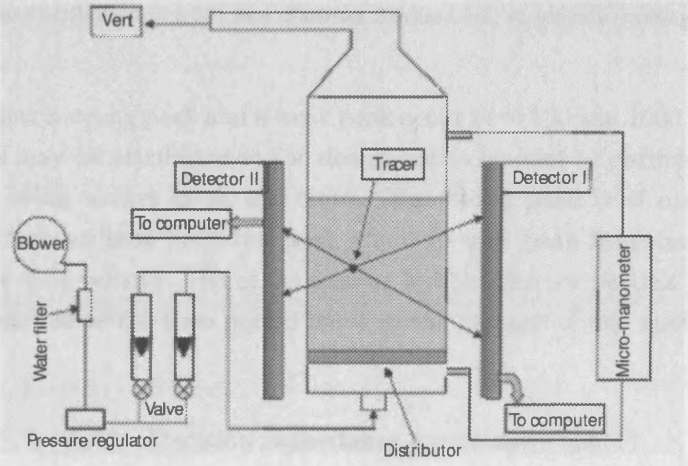

Fig. 4.20: Schematic of the experimental system composed of a fluidised bed armed with PEPT facility. Position of the tracer is re-composed by dedicated software. After [174]

PEPT can provide hitherto inaccessible real-time data on local particle motion which will prove invaluable to the development of mathematical models for design purposes. Moreover, from the wealth of information obtained with such a technique in tracking single particle motion, quantitative information on other phenomena, such as particle collision velocities and residence times, can also be determined. In particular, the characteristic idle time spent by the particle in quiescent zones during fluidisation process can be determined through PEPT and data can be used for modelling of defluidisation due to sintering (see Section 4.2.3). In this regard, figure 4.21 shows the idle time distribution that Stein et al. [174] obtained from the analysis of PEPT data for different fluidisation conditions.

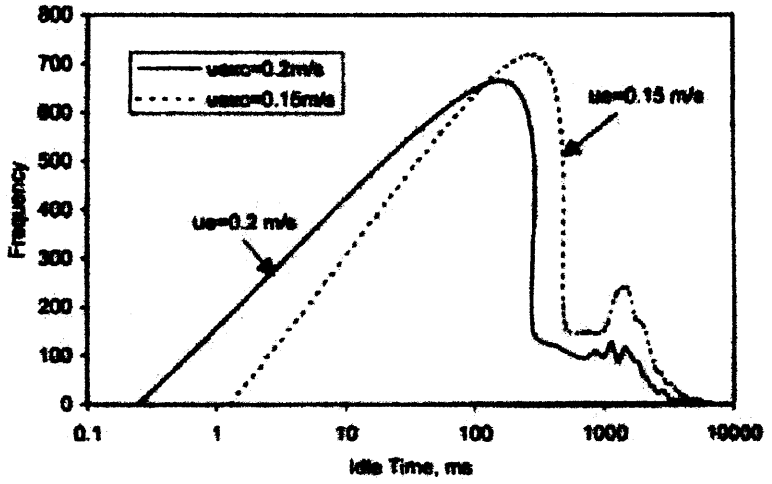

Fig. 4.21: Idle time distribution in a 141 mm diameter fluidised bed at various excess gas velocities. After [174].

It can be seen that a strong peak and a weak peak occur at $\approx$ 100 and 1000 ms, respectively. The small peak may be attributed to the downward movement of particles near the wall, these particles being always in an idle state. The strong peak is of major interest. In fact, figure 4.21 shows that both the peak idle time and peak frequency decrease with increasing gas excess velocity. Hence, as passing bubbles induce particle motion, the idle time can be regarded as the time period between the passage of two bubbles at the same bed height.

4.3.3 Electrical capacitance tomography (ECT)

Besides the non-invasive techniques based on radiation absorption methods, a relatively new and innovative technique, namely electrical capacitance tomography (ECT), is making an impact. ECT is gaining acceptance as an on-line tool to analyse multi-phase systems such as powder conveying, oil/water/gas transport, trickle-bed reactors and powder fluidisation. The use of capacitance measurement in gas-solid and solid-liquid systems is based on the principle that the change in population of solids between a pair of capacitance sensing electrodes will vary the effective permittivity, or dielectric constant, and therefore the measured capacitance can be used to give an indication of the concentration of the solid phase present [167].

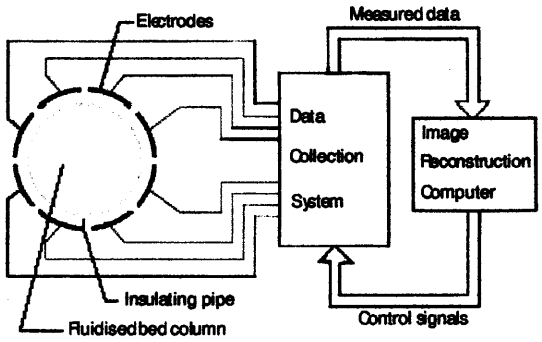

Fig. 4.22: Capacitance flow imaging system. After [168].

An ECT system consists of three basic units, as shown in figure 4.22: the sensor (electrodes), the electronic panel and the host computer. The sensor consists of a number of sensing and guard electrodes usually placed outside or embedded within an insulating pipe (fluidised bed column in figure 4.22). The resolution of the reconstructed image and speed of frame capture strongly depend on the number of electrodes. The electronic system provides fast (ca. 6600 measurements s^{-1}) and accurate measurements of the capacitances for the independent electrode connections. The host computer controls the measurement process and manipulates the captured data to obtain a reconstructed cross-sectional image using an appropriate algorithm.

As introduced at the beginning of this Section, (4.3), qualitative and quantitative information on the flow pattern during fluidisation process is necessary for optimum design of the reactor. However, the flow pattern within the fluidised bed has a random character which can be described by the fluctuations of the particle concentration. Such rapid fluctuations (over milliseconds intervals or less) of voidage in the bed normally negate the possibility of using radiation-based tomographic sensors, but such phenomena can be sensed using electrical methods.

The continued evolution of powerful computers and of instrumentation technology has led to relaxation of certain limitations of ECT (such as poor resolution, blurring of voidage boundaries and uncertainties relating to deconvolution of the current measurements [167]), and has permitted, in fact, the characterisation of different fluidisation regimes. An example is shown in figure 4.23, which illustrates a typical result of ECT measurement of solid fraction distribution obtained by Makkawi and Wright [175] for four different flow regimes (single bubble, slugging, turbulent, and fast fluidisation regime).

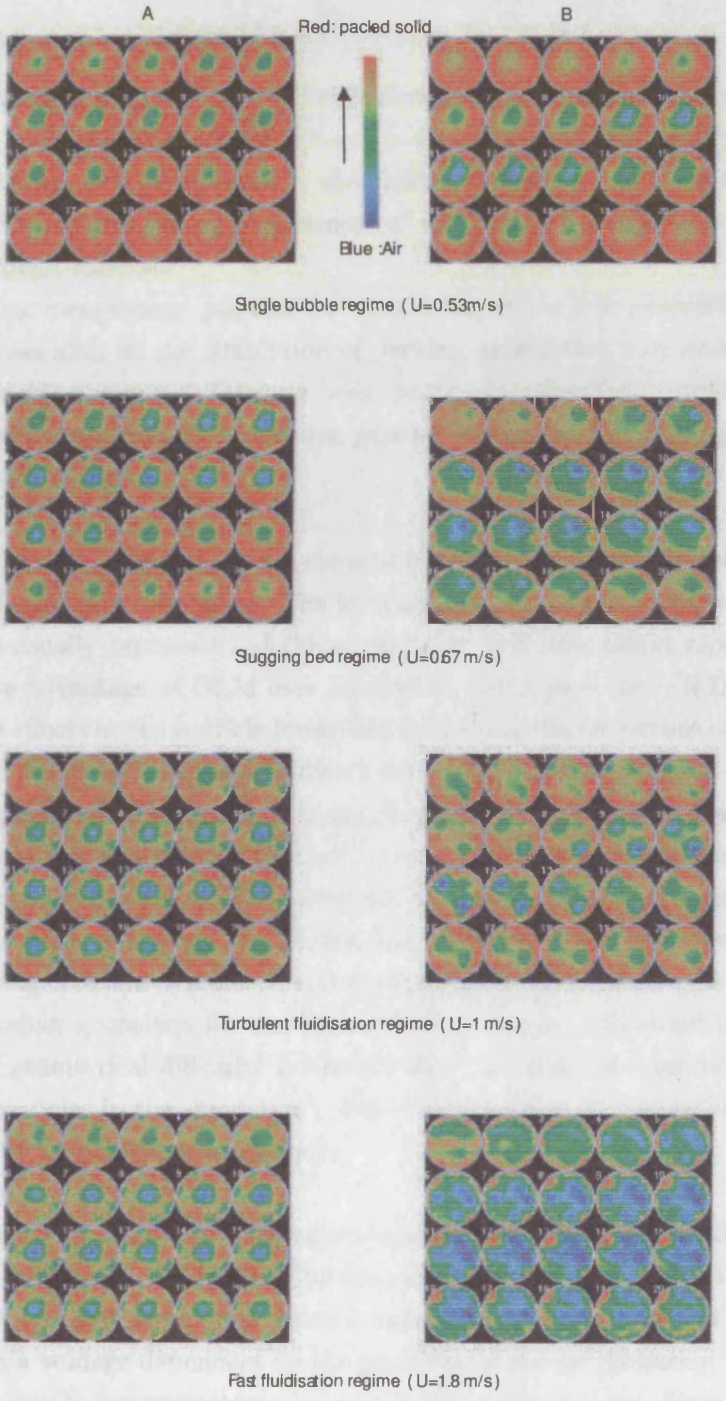

Fig. 4.23: Fluctuations of voidage concentration at different fluidisation regimes. Images shown in columns A and B are taken at two different levels above the distributor plate (A and B represent the lower and upper level, respectively). After [175].

4.3.4 The Distinct Element Method (DEM) in fluidisation

More often, nowadays, results and images produced by non-invasive measurement techniques are used to validate the numerical results obtained from the computational simulation of a defined process. For instance, the ability of PEPT to map the trajectory and velocity of individual particles is a requirement of verification for many flow codes such as the Distinct Element Method.
DEM is becoming increasingly popular for simulation of particle assemblies. It is now being used in areas such as the simulation of packing geometries, agglomerate collisions, quasi-static assembly strength, vibrating beds, pneumatic conveying, avalanches, hopper flow, mixing, trickle-bed reactors, stockpiles, powder forming and metallurgy and fluidised beds (in Ref. [148] Section 5.3).

Using this technique, the position of each element is evaluated and the interactions between the elements subsequently calculated. The interactions may then affect the element positions. Elements usually represent individual particles, but they might represent clusters of particles. One advantage of DEM over continuum techniques (i.e. CFD modelling) is that it simulates effects at the particle level. Individual particle properties can be specified directly and the assembly response is a direct output from the simulation. Forces acting on a single particle and between particles can be specified according to each case study. Hence, simulations can be extended to model those processes involving cohesive forces of different magnitude, such as those due to van der Waals up to liquid bridges, by using the appropriate interaction equations (see Section 2.2). Gravitational forces can be defined in DEM models using constant vectors. Another advantage of DEM models is that they can handle any container geometry, for example a drum mixer or a fluidised bed. These do not present any geometrical difficulty (although their size may be a problem in terms of the number of particles in the simulation). Particle-wall interactions can be handled in a manner similar to particle-particle contacts.

In modelling fluid beds, mass and momentum balances are carried out on the gas for each zone, using a finite element technique. The drag force on each particle is calculated using the Ergun equation [164], the region around each particle being modelled as a localised packed bed with a voidage dependent on the positions of the neighbouring particles. The drag force effect on the gas momentum balance is also accounted for. Since DEM models of fluidisation of non-cohesive powders have produced results (in terms of computational values of the bed pressure drop at minimum fluidisation condition), which have been validated by comparison with calculated theoretical values, as shown in Table 4.3, several authors have now developed models for cohesive fluidised beds [102, 176].

Particle density $[kg/m^3]$	DEM [Pa]	Theoretical calc. [Pa]
180	43	46
900	203	231
1590	360	408
2120	475	544
2650	600	680

Tab. 4.3: Comparisons of simulated and theoretically calculated bed pressure drops at minimum fluidisation of non-cohesive powders. After [176].

In particular, Wang and Rhodes [177] developed a numerical code that permitted the study of some process variables, such as the average quiescent time and velocity of the bed particles, as a function of excess gas velocity and an artificially imposed interparticle (cohesive) force, F_c, between the particles; the latter was expressed as a multiple (here indicated as M_k to avoid confusion in the notation taken in this thesis) of the buoyant weight of a single particle, as in 4.12:

$$F_c = M_k \pi d_p^3 g(\rho_p - \rho_f)/6 \tag{4.12}$$

where d_p is the particle diameter and ρ_p and ρ_f are the particle and fluid densities, respectively. The authors assumed the cohesive force, F_c, to be enhanced only upon particles collision, but disappearing as soon as particles detach. Hence, such a force represents a rather simple interparticle cohesion force.

Nonetheless, results obtained from the DEM simulation involving different particle sizes and excess velocities show that the drag force acting on a single particle approximately balances the buoyant weight of the particle, regardless of whether the bed is bubbling or partially defluidised, thus exposing the traditional force balance approach to some criticism. Furthermore, Wang and Rhodes [177] proposed a possible criterion for defluidisation, which is based on the ratio of the time averaged repulsive force and the time averaged cohesion force acting on the particles in contact. Figure 4.24 shows the trend of this ratio for a particular case (excess gas velocity equal to 0.3 m/s) as a function of the multiple of the buoyant weight of a single particle, M_k. As expected, the decreasing trend was observed as the interparticle force is increased. On the basis of their results, the authors concluded that, in order to maintain the free bubbling regime (and therefore avoid defluidisation), the time-averaged repulsive force due to particle-particle collisions need to be at least 20% more than the cohesive force; that is, in order to obtain free bubbling, the particles not only need to be able to overcome the bondage of other particles but also to be able to move at a reasonable speed after the collision.

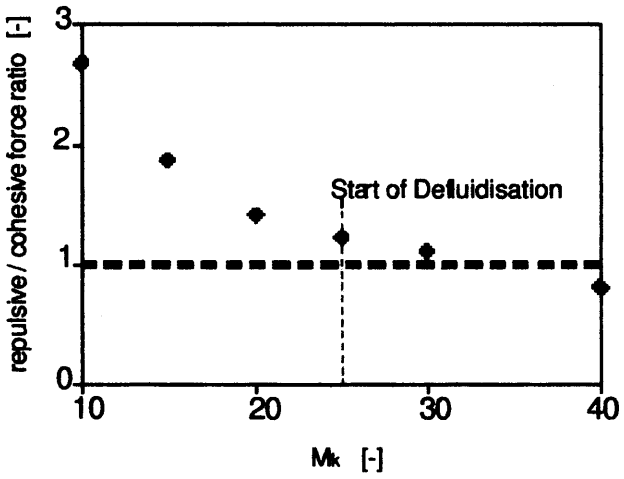

Fig. 4.24: Time averaged variation of repulsive/adhesive force ratio with M_k at $(U - U_{mf}) = 0.3$. After [177]

Clearly, the main limitation of the model is that the artificial cohesive force assumed by Wang and Rhodes [177] is not realistically defined, and perhaps too simplistic to explain complex particle-particle interactions and flow patterns that may occur at high temperatures. Therefore, experimental validation of the computational results is mandatory. Moreover, even with current computing power, simulations can usually only reasonably be undertaken with a relatively small number of particles, by comparison with the total number of particles in the real system. However, the principal use of current DEM models is to gain an insight into the physics of the system, in translating single particle properties into bulk phenomena. Hence, DEM models should be viewed as complementary to continuum models and experimentation both at the macro and micro scales [148].

5. THE HIGH TEMPERATURE MICRO-FORCE BALANCE (HTMFB)

The study of high temperature long range interparticle forces between pairs of particles is important to fluidisation processes. Measuring how the adhesion of liquid/solid bridges is affected by the operative temperature and the physiochemical properties of both particles and bridge material represents valuable information for the understanding of the early stage of agglomeration, and, therefore, of high temperature defluidisation.

In previous works, particle-particle interactions have been investigated by neglecting the common size scale and shape of agglomerated particles (see Section 3.2.3), usually sub 250 μm. On the other hand, recent developments in atomic force microscopy have allowed for measurements of micro-sized particle interactions to be taken at relatively high temperatures (see Section 3.4.3), but the reproducibility of the process conditions seems, so far, a limiting factor of such an experimental technique.

In order to fulfill such a lack of data, a micro-force balance (MFB), capable of measuring forces between micro-sized particles and recording, visually, the geometries liquid bridges attain under a range of conditions, has been designed and successfully employed at the Department of Chemical Engineering of University College London (see Section 3.1.2). The MFB apparatus, which is mounted on a microscope stage, was employed by Rossetti [122] for investigations of liquid bridges formed in gaseous and liquid media at ambient temperature. Furthermore, the MFB has attracted the attention of a large pharmaceutical company (Merck Sharp & Dohme^{TM}), which is interested in testing the adhesiveness of different binders holding paracetamol crystals in order to gain useful information on the optimal formulations required for granulation. This work is described in Section 3.1.2.

Following the significant experience accumulated and the successful results obtained through the micromanipulation technique by the Colloid Surface and Engineering Group at UCL, British Nuclear Fuels (BNFL plc) sponsored the work described in this thesis in order to develop the design, and subsequent realisation, of a novel micro-force balance, namely the High Temperature Micro-Force Balance (HTMFB), dedicated to force measurements between particles at high temperatures in relation to agglomerate formation in fluidised beds. In particular, as shown in **Chapters 6** and **7**, specific experimental techniques were developed according to each case study; results from these experimental investigations have highlighted the use of the HTMFB as a unique instrument among available conven-

tional devices (see Section 3.3.2).

This chapter provides a description of the experimental set up and the principles behind the use of the HTMFB. Moreover, the reader will find here mention of the materials and the procedures with which the interactions of interest took place and the analytical tools used to collect, analyse and interpret the outcome from experiments. However, due to the diverse experimental approach employed in the case studies investigated, the descriptions of the experimental method and materials have been included, together with results and conclusions, in each relevant section of **Chapters 6** and **7**.

5.1 Experimental setup

In order to develop a new design, the limiting features of the old model (the MFB) and the project requirements of the new model (the HTMFB) were identified. Essentially, the features that the novel device needed to meet have been listed in the following points:

- Ability to carry out force measurements at ambient and high temperatures.
- Capability to take force measurements of different magnitudes (from liquid up to solid bridges).
- Capability to take these measurements during the same experiment (i.e. measurement of the strength exerted by a liquid bridge that undergoes physical change to become solid).
- Force measurement assembly positioned outside of the environment where the particle-particle interactions take place.
- Provision of accurate control and extensive motion to set particle interactions.
- Being a modular setup, flexible and adaptable to different configurations, according to experimental needs.

On the basis of these requirements the new apparatus was designed[1] and a schematic representation of the award-winning[2] experimental setup is illustrated in figure 5.1.

[1] In collaboration with Dr L.R. Fisher of the Physics Department at University of Bristol.

[2] The Worshipful Company of Scientific Instrument Makers (London, UK) awarded Paolo Pagliai with a scholarship award in January of 2002.

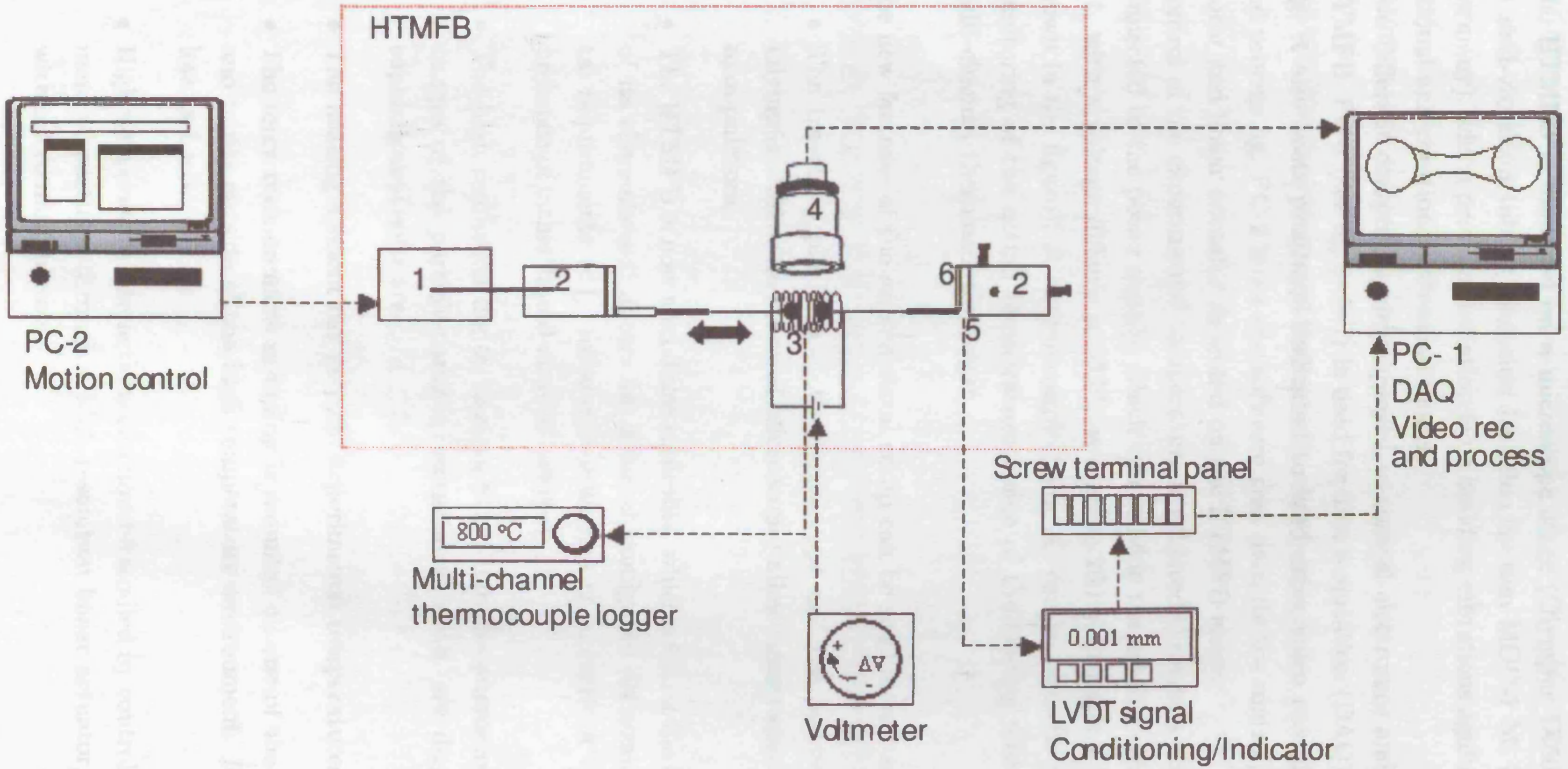

Fig. 5.1: Schematic representation of the experimental setup. The main elements of the HTMFB are sketched in the red box: (1) DC motor + linear actuator; (2) micropositioners; (3) heating element (mounted on a third micropositioner, not shown in the figure) + thermocouple (not shown in the figure); (4) microscope objective + digital camera; (5) LVDT displacement sensor (mounted on the force measurement assembly); (6) force measurement assembly (FMA).

At the centre of the apparatus (within the bounding red box in figure 5.1) is the high temperature micro-force balance (HTMFB), where the particle interactions take place. The HTMFB is mounted on a microscope stage (Olympus IX50) and placed on top of an anti-vibration table (Vibration Isolation System MOD-1 M, Halcyonics, Göettingen, Germany), which provides isolation from building vibrations against all six possible translational and rotational vibration modes.
Two different computers are employed to control electronics and retrieve data from the HTMFB. PC-1 (see figure 5.1) is used for data acquisition (DAQ) and data post processing; it also hosts programs dedicated to hard drive video recording and image analysis and processing. PC-2 hosts the software that permits the control/motion of both the DC motor and linear actuator mounted on the HTMFB stage.
Control of the experimental temperature is achieved through a potentiometer (voltmeter) connected to the power supply, which can provide the heating element, sketched in figure 5.1, with a voltage difference (ΔV) as high as 260 V through a 50 VA transformer (not shown in the figure). A thermocouple (type K) can be used for pre-calibration or direct monitoring of the actual temperature inside of the heating element by the means of a multi-channel thermocouple logger.

The new features of the experimental setup can be summarised as follow:

- The travelling platform of the microscope and the position of its objective (the Olympus IX50 is an inverted microscope) allow clearer space for operation with the manipulators.
- The HTMFB is now a modular assembly, which permits the customisation and setup of its elements and allows for different configurations according to the experimental requirements (e.g. force measurements at ambient or high temperature in the presence of either liquid or solid bridges).
- The high resolution digital camera fitted into the microscope provides sequence of images of the particle-particle interactions, which are digitally analysed through sophisticated software.
- The heating element can provide experimental temperatures as high as 1000 °C.
- The force measurement assembly is mounted on one of the two micromanipulators and it sits outside of the high temperature environment. It can measure forces as low as 1 μN.
- High temperature interactions can now be studied by control of the relative displacement of particles through a high resolution linear actuator, or by direct operation with micromanipulators.

5.1.1 The HTMFB assembly

The High Temperature Micro-Force Balance, shown in figure 5.2, consists of an Olympus IX50 optical inverted microscope fitted with an adapted stage (20x15x1.2 cm Femto-Bench^{TM} MDE 802, Elliot Scientific Ltd, Herts, UK); the Femto-Bench is customised with a 50 mm square hole at its centre to allow the microscope objective to reach the working distance from the particle interaction environment.
Because the bench is a matrix of holes, it is possible to fit the assemblies needed for the handling of particulates (marked as A and B in figure 5.2), the motion mechanism for setting the particle-particle interactions (the linear actuator fitted with the element tagged with A in figure 5.2), the heating element (a heating coil fitted with the micropositioner indicated with C) that provides the necessary temperature for the interactions to happen and the force measurement assembly (mounted on the micropositioner B), in accordance to the specific design.

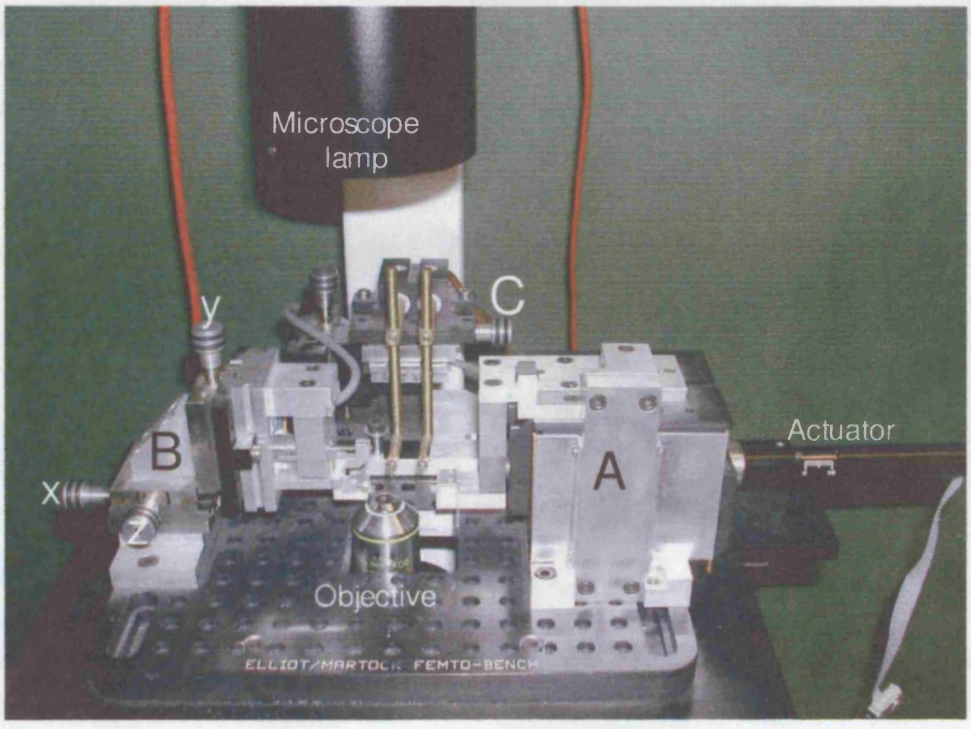

Fig. 5.2: Photograph of the HTMFB

With reference to figures 5.1 and 5.2, the procedure to measuring particle-particle interactions with the HTMFB can be summarised in the following manner. Particles, which can be of diameters as low as 30 μm, are attached to the tips of two micropipettes and mounted, via a micropipette holder, on the elements A and B (see Section 5.1.2). Alignment and initial separation distance of particles is obtained under the focus of the microscope lens by causing the pipette displacement along the x,y and z axes with the micropositioner B

(MDE850 fitted with MDE851 accessory platform, Elliot Scientific Ltd, Herts, UK): this micropositioner provided the coarse adjustment through its micrometres (indicated with x,y and z, respectively in figure 5.2), whilst fine-approach along the x axis was ensured by the linear actuator fitted with the element A (see Section 5.1.4).

A liquid bridge can be formed either by the addition of a liquid onto the particles or by melting the particle surfaces (i.e. as occurs during sintering). In the former case, a third micropipette, which can be fitted on a dedicated accessory (ferrule holder MDE701, Elliot Scientific Ltd, Herts, UK, shown in figure 5.13 in Section 5.1.5) and mounted on the micromanipulator tagged with C in figure 5.2, is used to add liquid onto one of the particles. The particles are then positioned within the coils of the heating element (see Section 5.1.5) and brought together using the micropositioners A and B until the liquid forms a bridge between them, as illustrated by the 3D computer drawing shown in figure 5.3. If particle sintering is being studied, then the particles are simply positioned and put in contact within the heating coil. The environment where the interactions take place (i.e., inside a predefined zone of the heating element) is previously calibrated with a thermocouple in order to reach temperatures up to 1000 °C (Section 5.1.5).

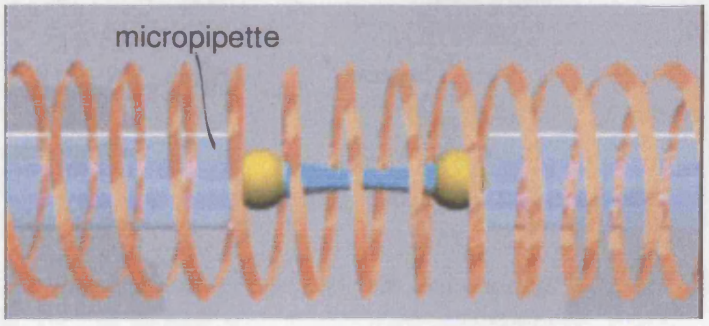

Fig. 5.3: HTMFB assembly: particles held by a liquid bridge inside the heating coil.

Of the two micropositioners, B is held static whilst A causes the axial separation of the particles via a linear actuator driven by a DC motor. The linear actuator (see Section 5.1.4) can be programmed via a software interface installed on PC-2 (figure 5.1), to ensure high resolution of displacement (up to 0.05 μm) and, if required, to perform cycles of particle contact and separation at different velocities (in order to study the effects due to particle motion). A digital camera, plugged into a personal computer (PC-1 in figure 5.1) and fitted in the observation tube of the microscope, grabs image sequences for each run of experiments for later analysis of, for example, the surface effects (Section 5.1.6).

The separation, or compression, of the particles causes any force to be transferred to the

micropipette holder and then to the force measuring device through movement in the direction of the applied force of a two parallel sheets assembly mounted onto micromanipulator B (see Section 5.1.3). The movement of the lower block of the flexure strips (whose spring constant, K, has been previously calibrated as explained in Section 5.1.3.1) is measured by a displacement sensor (LVDT), which provides the position (X_b in figure 5.4) of the strips with a resolution as low as 20 nm, with the data collected by a data logger in the PC-1.

According to Hooke's law, once a material bridge has been formed between the two particles, it is possible to measure the adhesion force F by pulling the particles apart until rupture occurs (figure 5.4(1)). Alternatively, after placing the pair of particles in contact, sintering can be studied by applying a known initial load L (figure 5.4(2)) and producing typical Elongation/Contraction vs Temperature diagrams. The magnitude of the force enhanced by sinter neck formation is then measured as in figure 5.4(1).

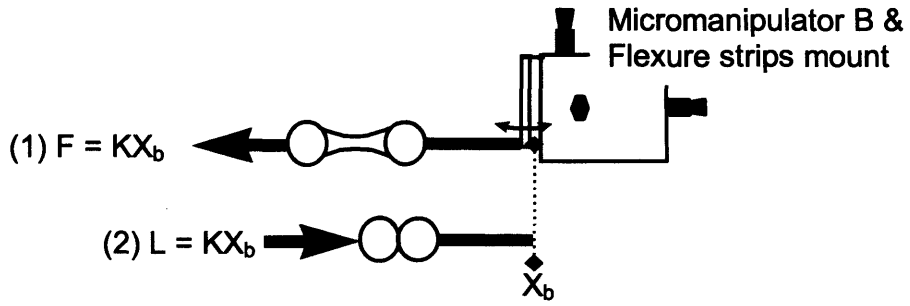

Fig. 5.4: HTMFB assembly: force measurement detail

5.1.2 *Preparation of micropipettes and handling of particulates*

In the experimental work described in **Chapters 6** and **7**, borosilicate glass micropipettes were employed to hold particles inside the heating element, as well as for carrying them throughout the interactions. Glass micropipettes have the advantage that they can acquire the desired shape for making them suitable for use in the HTMFB up to temperatures as high as 500 °C, depending on the interaction of interest.

In order to accommodate the glass pipettes inside the heating element, as well as to favour the gluing of microsized particulate on their tips, the micropipettes were produced from 650 mm length of 0.97 mm O.D., 0.7 mm I.D. borosilicate glass tubing (Cole & Parmer, Saffron Walden, Essex, UK). The preparation and shaping procedure of the pipettes, which is described in the following section, was routinely adopted for all the experimental works reported in this thesis.

5.1.2.1 The pipette puller

The pipette puller shown in figure 5.5 is used to thin and stretch the micropipettes by means of two nichrome wire heating elements. The relative position of these elements to the borosilicate tubing allows micropipettes of varying size (length and diameter) and stiffness to be produced.

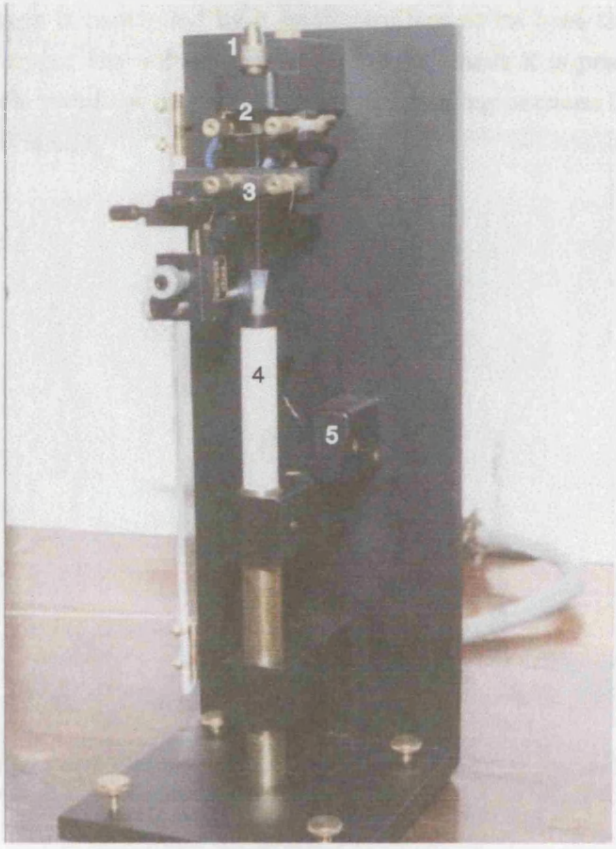

Fig. 5.5: Photograph of the pipette puller: 1-Jeweller's chuck; 2-Melting element; 3-Cutting element; 4-Weighted plunger; 5-Microswitch.

The borosilicate capillary tubing is passed through the jeweller's four-jaw chuck at the top of the puller, down through the top melting element and the bottom cutting element. The chuck is then tightened around the tubing. The bottom of the capillary tubing is then attached to the weighted plunger by placing a small piece of either silicone capillary tubing or a small amount of Blue Tack (Bostik) around the glass and pushing the top of the plunger onto the tubing. The frictional force between the two keeps them attached.

A voltage is then applied across the top heating element (indicated with 2 in figure 5.5). This element consists of a 0.5 mm diameter nichrome wire wound 11 or 12 times to produce a cylinder of around 4 mm O.D. and 11 mm in length. To achieve an homogeneous

temperature distribution along the glass tubing, ideally the turns should not be separated by more than the thickness of the wire. The amount of current flowing through, and thus the temperature of the element, can be varied by a potentiometer on the power supply. The temperature of the element, should be adjusted so the tubing starts moving, at a constant rate, after around 15 seconds. Through extensive production of pipettes, the time of 15 seconds seems to provide the correct rate of melting in the glass. The rate of descent of the plunger is controlled by a small capillary at its base that provides for the egress of air. By varying the voltage on the melting element it is possible to control the rate of descent. Scale readings of the potentiometer ranging between 6 and 6.5 have been found suitable for this aim.

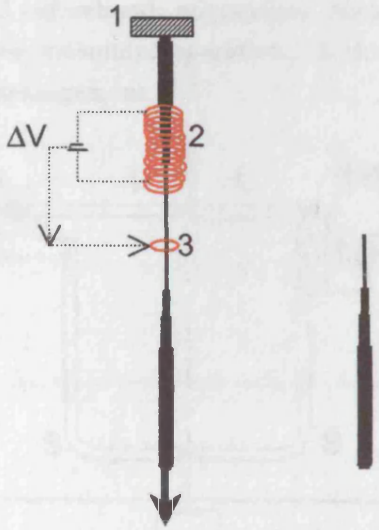

Fig. 5.6: Schematic of procedure for micropipette formation and cutting. As in figure 5.5: 1- Jeweller's chuck; 2-Melting element; 3-Cutting element.

Towards the end of the plunger's descent a microswitch on the plunger vertical stand (figure 5.5) is used to redirect the current flow from the melting element to the cutting element and to make a plain straight edge on the pipette tip (see figure 5.6).
This fact is very important for the feeding pipette in order to have a regular flow of liquid binder on to the particles when the liquid bridge is formed. The cutting element consists of a one turn coil of 0.25 mm O.D. located as close to the pipette as possible. Again the current to the element is varied via a potentiometer on the power supply. The temperature should be adjusted so that the cut takes around 10 seconds. Of the two halves thus obtained, only the lower half pipette (figure 5.6 right) is used for particle attachment. Such a pipette consists of a variable size tubing whose thick end is clamped to the micromanipulator by means of a pipette holder, as shown in figure 5.7, whilst the thin end (between 20 and 30 μm radius and length of 3.5 cm) is used to attach the particle, as described in the following section.

5.1.2.2 Attachment of particles to micropipettes

In the early design of the HTMFB, micropipettes were thought to be S-shaped, figure 5.7, in order to permit the microscope objective to reach the working distance necessary to focus the particles attached on to the pipettes tip. Such a configuration had some disadvantages since it required precise bending of the micropipette by means of a mini-gas torch and changes in the set up were also necessary; in fact, whenever particle attachment was needed, the force assembly had to be dismounted from micromanipulator B to allow the clamping of a dedicated element (MDE701, Elliot Scientific Ltd, Herts, UK), used to pick up particles resting on a glass plate on the stage.
Hence, in order to ease the experimental procedure, a certain number of ready-to-use pipettes was usually prepared beforehand; nonetheless, sticking particles on to pipettes with such a procedure is a time consuming operation, which has been avoided by using a different, and more suitable, arrangement.

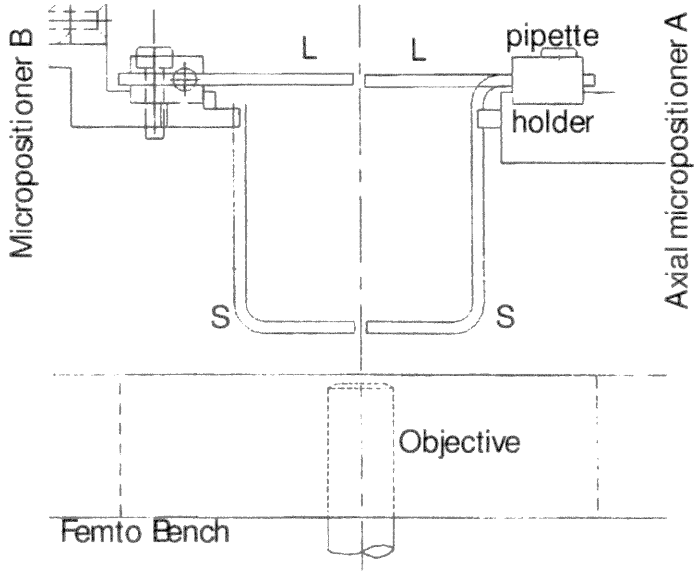

Fig. 5.7: Shape of micropipettes as indicated in the original drawings of the HTMFB (S) and as employed in the actual set up (L). The micropipettes are clamped to both micromanipulators (A and B in figure 5.2) by means of pipette holders.

In the actual set up, the travel distance of the microscope objective has been extended by using dedicated spacers (depending on the objective magnification, usually 2 or 3 connected RMS spacers of 10 mm each, Microscope-Service and Sales, Surrey, UK), which are screwed between the objective and the revolving nosepiece of the microscope (the rotating plate where the objective is usually mounted on). Such arrangement allows the use of straight pipettes (L in figure 5.7), such as those illustrated in figure 5.6, and permitted faster operation of particle attachment and pipette positioning.

After producing a suitable number of micropipettes, it is necessary to attach the particles and achieve a stable bond that will survive even at high temperatures. This is obtained manually with the aid of the microscope. On the Femto-Bench, a clean microscope slide is placed onto which a few particles have been placed alongside a drop of cyanoacrylate glue (Bondloc B499, Bewdley, UK). Before depositing the glue the slide should be gently tapped on the bench to achieve uniform spreading of particles on its surface. The thin end of the pipette is first dipped in the glue and then put under the objective focus in order to attach a particle from those previously targeted. When a suitable particle has been located, a gentle touch with the pipette tip secures a strong bond, as shown in figure 5.8. The small amount of Bondloc B499 (left on the pipette after dipping it into the glue drop) allows ≈30-40 seconds for dry curing, which is enough for selecting and attaching the particle.

By using the Bondloc B499 glue, the pipettes can be employed in an experiment immediately after the particle has been attached. However, its relatively low service temperature allows for experiments to be carried at temperatures not greater than 200 °C. Other types of glue (mostly commercialized in the form of pastes rather than gels), which show higher resistance to temperature, have been found of poor application because of the weak bond generated between the small contact areas that are developed.

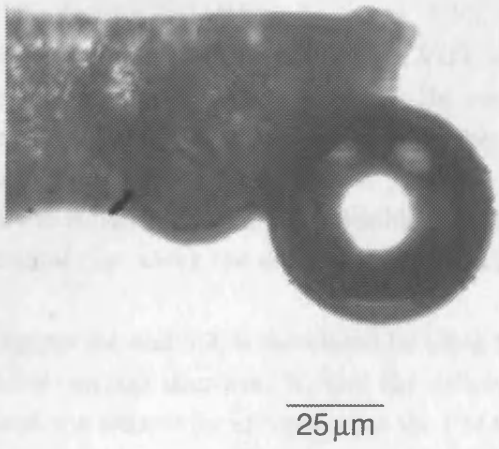

Fig. 5.8: Photograph of a glass sphere attached to the tip of a micropipette.

Alternative materials and gluing techniques are therefore required for carrying out experimental investigations at higher temperatures; in fact, difficulties can arise from melting of the glass pipette (above 500 °C) or by detachment of the particles from the tip of the

pipettes.
In this regard, **Chapter 7** describes a new technique, which has been invented in order to avoid particle detachment at temperatures as high as 350 °C.

5.1.3 Force measuring assembly (FMA)

The bonding force exerted by a liquid/solid bridge formed between two particles can be assimilated to the force needed to disrupt such a bond. This can be measured by means of the force measuring assembly (FMA, KFH Design Ltd, 2000), shown in figure 5.9, which has been mounted on one of the two micropositioners (B).

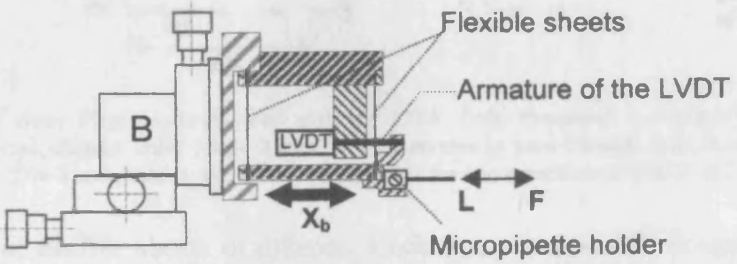

Fig. 5.9: Schematic representation of the force measuring assembly (FMA).

As indicated in Section 5.1.1, any type of force (Load or rupture Force) applied along either axial direction is transferred to the micropipette holder and makes two flexible sheets bend accordingly to a distance X_b.
At the centre of the FMA there is the -fixed- body of an LVDT displacement sensor (D5/25K-L25, RDP Electronics Ltd, Wolverhampton, UK), which measures the deflection (X_b) of the flexible sheets. The armature of the LVDT is free to move inside within the fixed body whenever the sheets deflect, changing the output signal (voltage) of the LVDT sensor. The motion is practically frictionless, since there is no contact between the armature and the body of the LVDT.
Due to the weight of the blocks supporting the flexible sheets, forces could only be measured along the horizontal (i.e. along the deflection axis) direction.

The force, F or L in figures 5.4 and 5.9, is calculated by using Hooke's law, which requires both values of the force (spring) constant, K, and the deflection distance of the sheets, X_b. The magnitude and the sensitivity of forces that the FMA can detect depend on two factors, namely, the flexibility of the sheets, expressed as the force constant K and the range and sensitivity of the displacement transducer.

The flexibility of the sheets depends on their shape, material and thickness. The sheets are thin (typically 50-150 μm) and rectangular in shape, as shown in figure 5.10. The

window design (figure 5.10 right) is the same as the *standard* design (figure 5.10 left) but with a rectangular hole at its centre, which increased further the flexibility of the sheet[3].

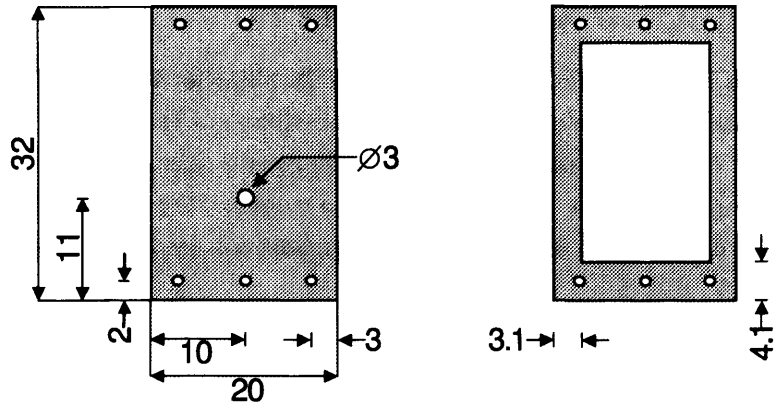

Fig. 5.10: (Front view) Flexible sheets used with the FMA. (left) Standard, and (right) window design. The top and bottom aligned holes (circa 2 mm) are for screws to pass through and secure the sheets on the FMA blocks. The 3 mm hole in the standard design is for the armature of the LVDT to pass through.

Several types of flexible sheets of different thickness, material and design, as shown in Table 5.1, have been tested. However, in the studies presented in **Chapters 6** and **7** the need to measure a wide range of force magnitudes during the same experiment required the use of relatively low force constant sheets (in order to measure the adhesion of drying liquid bridges), which were also flexible enough to provide rupture data of solid bridges within the range of measurement of the LVDT (i.e., within the maximum displacement, X_b, detected by the LVDT). The window design and the acetate transparency material (see Table 5.1) had suitable characteristics for this purpose.

Material	Thickness [μm]	Design
Stainless steel	100	Standard
Stainless steel	50	Standard
Copper	75	Standard
Copper	50	Window
Acetate transparency	130	Window

Tab. 5.1: Types of flexible sheets tested with the FMA.

Since the two spring-like sheets ($K_{sh,1}$ and $K_{sh,2}$) act in series, the flexibility of the FMA, which is determined by the force (spring) constant K, is given by the following expression:

$$\frac{1}{K} = \frac{1}{K_{sh,1}} + \frac{1}{K_{sh,2}} \tag{5.1}$$

[3] The sheets are very sensitive and any mishandling will seriously affect their flexibility. Moreover, when fitting them to the FMA, fitting screws should make no contact at all.

A description of the method followed for the calibration of the FMA is provided in the following section.

5.1.3.1 FMA calibration

A simple method for spring calibration, K, involves the use of known weights. From the same physical principle of the pulley, the force applied along the vertical direction by a known weight hung on a thin thread of negligible mass (see figure 5.11), is transformed, as to a pulley system, in a pulling force operating along the x-axis, which makes the flexible sheets of the force measurement assembly move a distance X_b proportional to the mass of the weight.

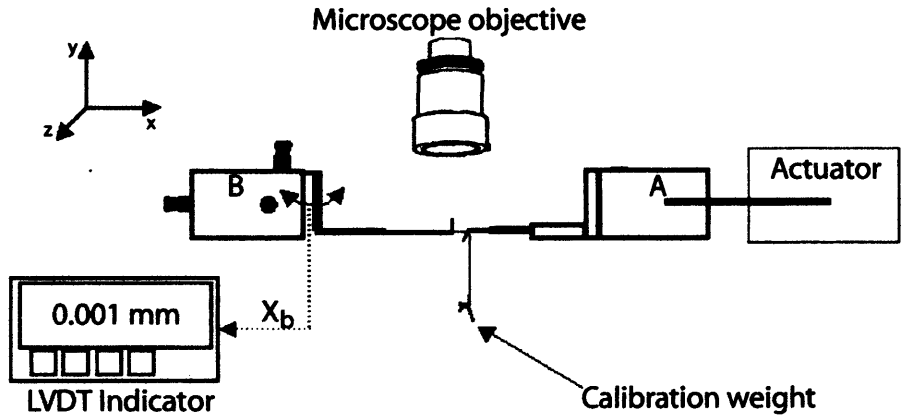

Fig. 5.11: Set up for the calibration of the flexible sheets of the FMA.

The heavier the hung weight the greater the displacement, X_b, which is read by means of the LVDT indicator (see Section 5.1.7.1) and recorded, along with the relevant weight, in a calibration table (such as Table B.1 in Appendix B). As indicated by Hooke's law, the overall force constant of the FMA, K, is obtained from linear fitting of the force (calibration weight) versus displacement (X_b) data, as shown in figure B.2.

5.1.4 Motion mechanism

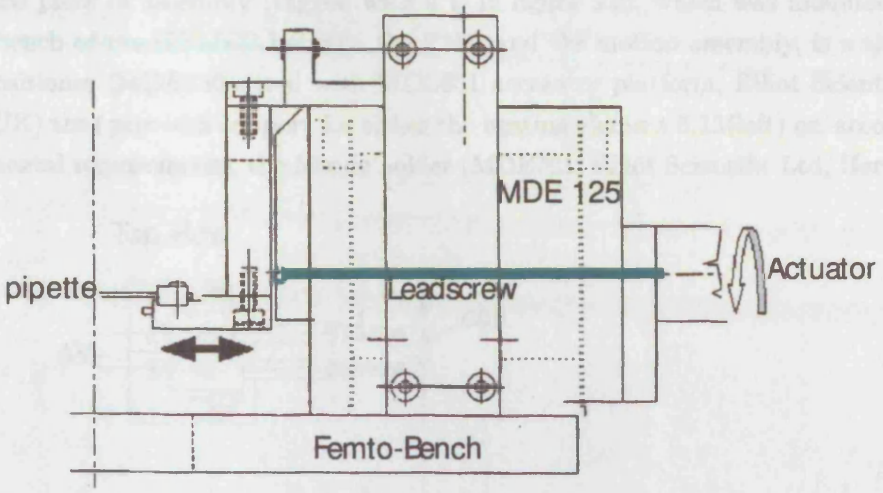

Fig. 5.12: HTMFB detail: the motion assembly.

Different from micropositioner B shown in figure 5.2, the fine motion that enables particulates to interact is provided by the motion mechanism shown in figure 5.12. This is composed of a single axis flexure stage (MDE125, Elliot Scientific Ltd, Herts, UK) whose original design has been modified (KFH Design Ltd, 2000) in order to fit a linear actuator (EncoderDriver^{TM} Linear Actuator, Coherent, Herts, UK), which ensures the axial motion of the micropipette.

The linear actuator package is a combination of integral DC motor (which provides rotational movement), gearhead and micrometer precision leadscrew (drawn in green colour in figure 5.12, the leadscrew shifts the motion mechanism from rotational to axial movement) whose terminal spherical tip is placed into contact with the flexure element. The motion of the EncoderDriver is programmed by means of a dedicated device driver software through the EncoderDriver^{TM} Control Card (see Section 5.1.7.2); a maximum travel distance of 10 mm can be reached with a resolution as high as 50 nm at constant velocities ranging between 0.8 up to 470 $\mu m/s$.
The choice of using a DC motor driven motion mechanism, instead of the commonly employed piezo-actuators, arises from the need to achieve greater separation distances, which may be required to obtain the rupture of solid/highly viscous bonds; moreover, the absence of hysteresis effects and the high resolution of the linear actuator allow precise investigation of the velocity effect on the strength exerted by liquid bridges.

5.1.5 The heating element

The third piece of assembly (tagged with a C in figure 5.2), which was mounted on the Femto-bench of the HTMFB between the FMA and the motion assembly, is a three axis micropositioner (MDE850 fitted with MDE851 accessory platform, Elliot Scientific Ltd, Herts, UK) that provides support for either the heating element 5.13(left) or, according to experimental requirements, the ferrule holder (MDE701, Elliot Scientific Ltd, Herts, UK).

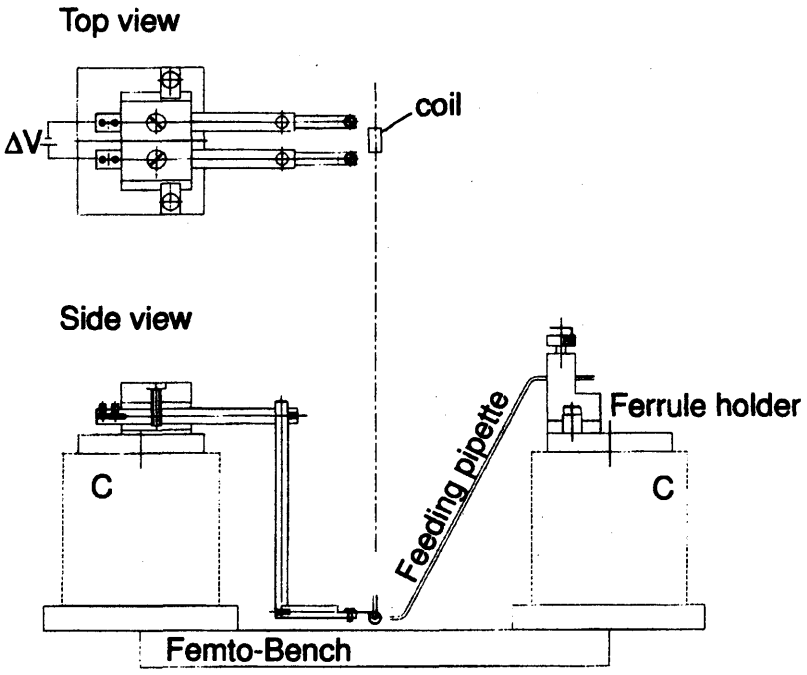

Fig. 5.13: HTMFB detail: the micropositioner C provides support for either the heating element (left) or the feeding pipette set up (right).

In the heating element set up, a specific accessory has been designed (KFH Design Ltd, 2000), which permits a known voltage, ΔV, to be applied between the ends of two separate electrodes, as shown in figure 5.13(left). A platinum wire with the shape of a coil, see figure 5.14, was screwed at the other end of the electrode mount. Such electrical scheme permits heat generation through the platinum coil via electrical energy dissipation.
After positioning the particles within the heating coil, the micropositioner C is typically employed to adjust the position of the coil in such a manner that the particles and pipettes lie on its axis of symmetry. Alternatively, the same micropositioner can be used, in the feeding pipette arrangement, figure 5.13(right), in order to place a certain amount of liquid on to the particle surfaces.

The heating coil is a 0.4 mm diameter platinum wire wound 8 times to produce a cylinder of around 1.5 mm O.D. and 8 mm in length, as shown in figure 5.14.

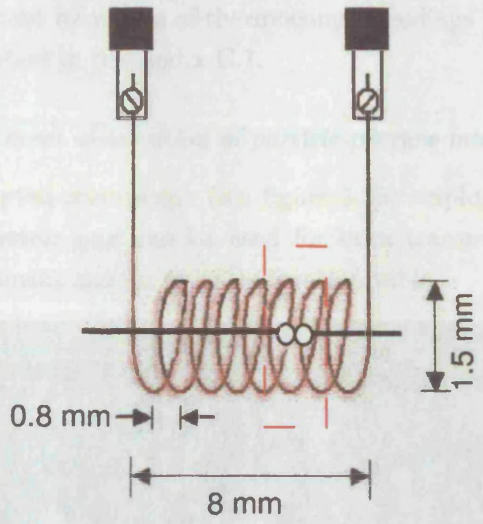

Fig. 5.14: The heating coil is a platinum wire screwed on the arms of a two electrodes mount. The red dashed line indicates the environment where the interactions will take place during experiment.

In a typical experimental set up, the environment where the high temperature interactions take place is bounded by two consecutive turns of the coil, as shown in figure 5.14. Heat transfer is mainly achieved by gas conduction (and radiation at temperatures higher than 400-500 °C) and, due to the geometry of the configuration, each time a desired voltage is applied, a new equilibrium temperature is fast approached (see Appendix C). The distance between consecutive turns and their outer diameter affect the isothermal condition within the interaction environment. As a general rule, the higher the value of the radius of the coil the lower the maximum temperature which can be achieved and the higher the time spent to reach such temperature. Moreover, the closer the winds of the wire (the distance between each consecutive turn of the coil) the more homogeneous the temperature along the axial coordinate; on the other hand, sufficient space has to be allowed between consecutive turns in order to permit adequate field of view for observation (see Section 5.1.6).

In light of these considerations and depending on the experimental requirements, such as the size and physical properties of the material employed (i.e., particle diameter, volume of the liquid/solid bridge between particles, material melting temperature, etc.), and the operative temperature needed for investigation, several heating coils can be produced of different characteristic lengths. Nonetheless, it should be emphasized that, once a suitable coil is mounted on the heating element, the spatial uniformity of temperature within the interaction environment has to be determined. Moreover, thermal stresses, which can be generated during operation at high temperatures, may be the cause of bending and axial distortion of the coil geometry, and, in fact, they represent a source of axial and radial temperature gradients. It is therefore advisable to carry out accurate calibration of

the interaction environment by means of thermocouple readings before each experimental campaign. This is described in Appendix C.1.

5.1.6 Direct observation of particle-particle interactions

The Olympus IX50 inverted microscope (see figure 5.15) employs the UIS (universal infinite system) optical system and can be used for both transmitted and reflected light illumination. The instrument sits on an anti-vibration table.

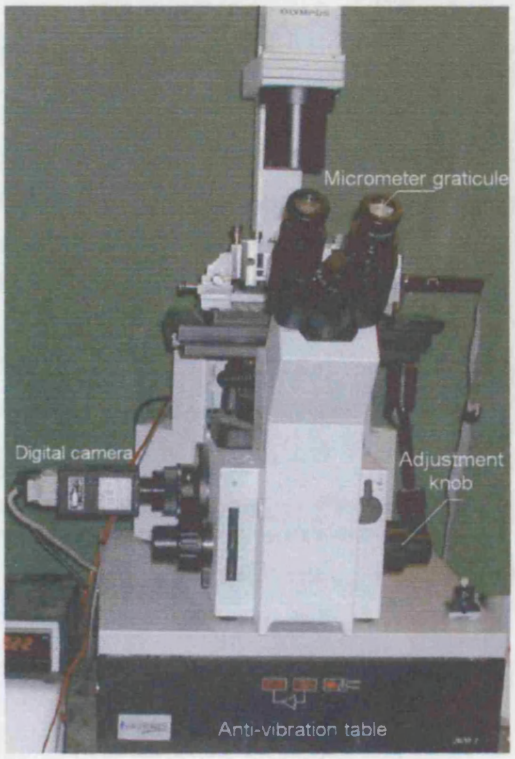

Fig. 5.15: The IX50 Olympus inverted optical microscope.

Coarse and fine adjustment of the optical focus is facilitated by the adjustment knob, which is calibrated in microns. Four objective lenses (5x, 10x, 20x and 50x) allow liquid/solid bridges between particles down to 3 μm (limit of optical microscopy) in diameter to be viewed. The maximum size of particle is limited by the field of view. The field of view with the 5x objective is 4.4 mm. The working distance required to reach the optical focus within the field of view is 3 mm if a 20x objective is used. Information about the characteristics of each objective is printed on the casing.

The observation tube of the microscope allows the image to be viewed directly or via a digital camera. Usually the light path is split, 20% for the binocular eyepieces and 80% for the camera, although if brighter observation is required 100% can be directed to either.

One eyepiece (right) also contains a micrometer graticule divided into one hundred units. Table 5.2 provides the calibration for the eyepiece:

Objective lens	1 eyepiece graticule unit equals
5x	20 μm
10x	10 μm
20x	5 μm
50x	2 μm

Tab. 5.2: Eyepiece graticule calibration.

The digital camera (Jai CV-M4 Digital Double Speed Megapixel Progressive Scan camera, Firstsight Vision Ltd, Surrey, UK) is attached to the observation tube via an U-TV1X video attachment and an U-CMAD C-mount adapter. The camera provides both single shots and sequences of images at a resolution of 1280 (H) x 1024 (V) effective pixels and a frame rate of 24 fps. Higher frame rates (up to 120 fps) can be reached by lowering the resolution (up to 1280 (H) x 130 (V) pixels). The digital output of the camera is connected to a frame grabber (PC-DIG-L, Firstsight Vision Ltd, Surrey, UK) fitted into PC-1 (see figure 5.1).

The images/sequences obtained from the camera are hard-disk recorded through a 36 Gb (10 krpm) U160/M SCSI hard drive mounted on PC-1. A description of the recording/playing back and image analysis software used in this work can be found in the following section.

5.1.6.1 Processing the images

Sequences of images and single shots are recorded during experiments with the Sequence tool (see the screenshot shown in figure 5.16), which is a real time monitoring and recording software tool included in the Common Vision Blox software package (CVB by Stemmer Imaging, Firstsight Vision Ltd, Surrey, UK). The Common Vision Blox is a development environment and function library for imaging applications, which executes on PCs under Microsoft Windows OS. It contains an extensive operator library for filtering, segmentation, edge detection, grouping, morphology, analysis, geometry, classification and image recording. It has powerful tools for data visualisation and chart graphics and its functions are accessible either from the graphical user interface, or from a stand-alone program written in Visual Basic, C++, Java, or Delphi.

The software tool Sequence, licensed with the CVB software package, is used for recording image sequences. The DLL Sequence library provides functions for recording, playing back and storing 8-bit image sequences. The recorded sequences are cached in the main

memory of the image processing computer and can be stored onto the hard drive as **.seq* files. The maximum length of an image sequence depends on the amount of main memory installed in the computer (512 Mb on PC-1). To save memory space and improve performance, it is possible to define an image region for recording sequences. In this case, only the corresponding part of the image is recorded.

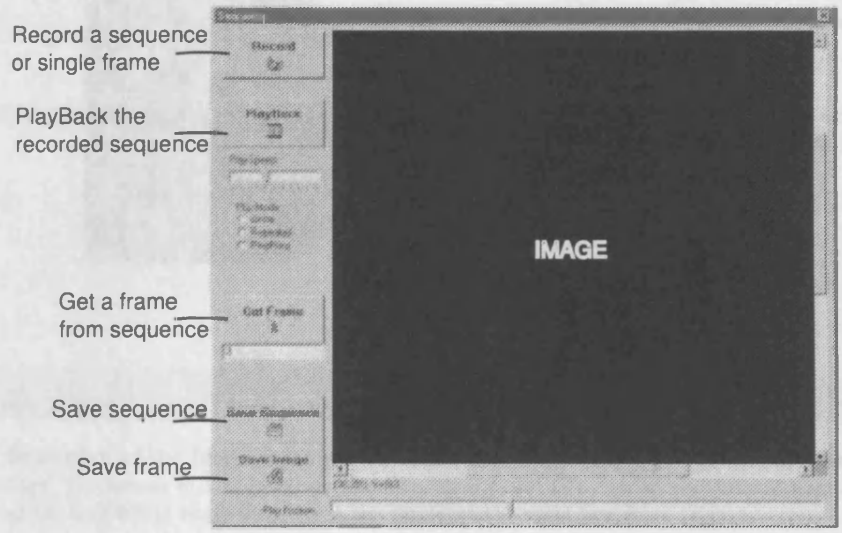

Fig. 5.16: Screenshot of the Sequence software tool.

Unfortunately, the Sequence tool lacks Loading functions, which would allow loading and extraction of frames from a specific sequence previously stored onto the hard drive. A dedicated Visual Basic code was therefore written and integrated with the Sequence tool (see Appendix D). The executable program (**Sequoia.exe**) can be launched as a stand-alone application or run together with the Sequence environment.

Typically, the processing and analysing procedures are aimed at measuring the values of various geometrical properties of the objects shown in the images. These include the diameter of particles, the contact angle formed between liquid and solid interfaces, the half-filling angle, the separation distance between two particles throughout the interactions and the relative coordinates of liquid bridge profiles that permit back-calculation of the liquid volume between particles, etc. All these measurements are achieved through a user friendly application, namely the Morphometrics Tool Box (**mtb2.exe**) application, which has been successfully tested by other researchers at UCL.

The graphic user interface of the Morphometrics tool is shown in figure 5.17. A new image (saved in TIFF format) is imported by choosing its file name on the Image menu on the menu bar (Image $\succ$ New image $\succ$ Load). The desired measurements are then carried out by choosing the Mode menu. As shown in figure 5.17, the application provides instructions

for every action required.

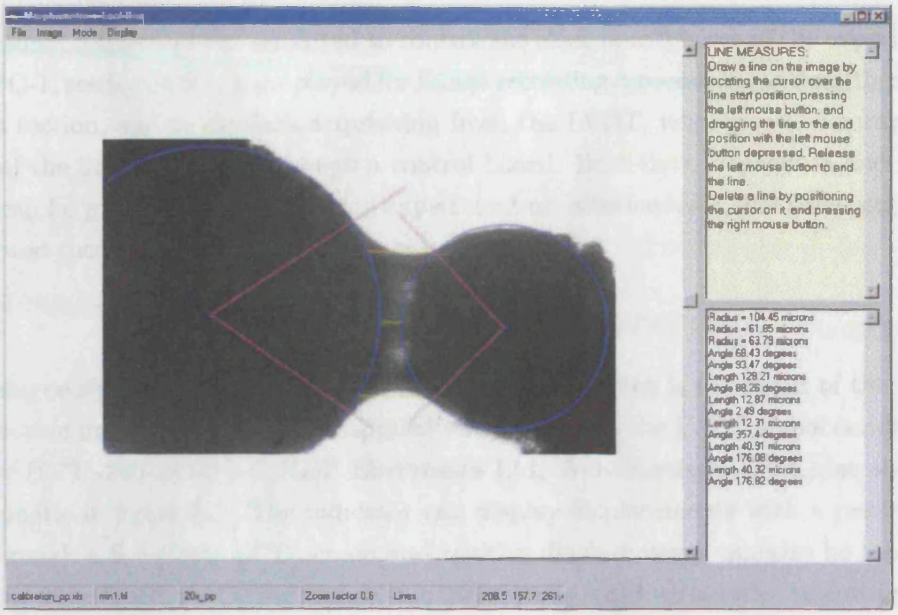

Fig. 5.17: Screenshot of the Morphometrics Tool Box. The image shows two E-cat particles bonded by a liquid bridge. By means of the Mtb2 application, it is possible to ascertain their radius, interparticle distance and the half-filling angle formed by the liquid at the solid interface.

Indeed, the application needs pre-calibration, in order to convert the measured values to the metric system from the display units (pixels). This is achieved by recording the image of a reticle (i.e. a micrometer scale), shown in figure 5.18, using the same microscope lens as in the experiments.

Fig. 5.18: Image of a micrometer scale taken with a 10x objective lens.

The image of the reticle is used in the Morphometrics Tool Box application to find the conversion ratio, which enables measurements of the reticle from pixel units to microns. The measured distances (obtained by operating the MTB in the Line mode) have a different scale value according to both the lens used and the conversion table shown in Table 5.2. The calibration sheet is then saved in an Excel file (Calibration_ pp.xls). Hence, prior to opening any image for analysis, the calibration file needs to be loaded in the application and a suitable conversion ratio (i.e. 10x or 20x) being selected. Using the Olympus IX50 microscope with 10x and 20x objective lenses, the conversion ratio is 1.477 and 2.98 μm/pixel, respectively.

5.1.7 DAQ and motion control

Two personal computers are employed to control the electronic devices of the experimental setup. PC-1, see figure 5.1, is employed for image recording/processing, as described in the previous section, and to do data acquisition from the LVDT, whereas PC-2 controls the motion of the linear actuator through a control board. Both data acquisition and motion control can be programmed before each experiment or, alternatively, real time control can be operated through the relevant software interfaces.

5.1.7.1 DAQ

The analogue signal produced by the LVDT transducer, which is the result of the flexible sheets motion under the action of an applied force, is sent to the LVDT signal conditioning indicator (E725-230-AC-0-0-0, RDP Electronics Ltd, Wolverhampton, UK), as shown by the schematic in figure 5.1. The indicator can display displacements with a resolution of 1 μm through a five digits LCD screen and relative displacements can also be monitored by a set-to-zero function. Calibration of the indicator is required in order to convert input voltages into displacement units and the calibration procedure can be found on the product manual. Data are digitally re-directed from the LVDT indicator to a screw terminal panel (STP68, Amplicon Liveline Ltd, Brighton, UK) with a resolution of 20 nm.

Data acquisition is accomplished by installing a 16 bit PCI board (DT321, Data Acquisition Board, Amplicon Liveline Ltd, Brighton, UK) to the motherboard of PC-1. The DT321 has a 10 digital input channels, which are connected through a 68 pin shielded cable (EP305, 68 Pin Shielded Cable, Amplicon Liveline Ltd, Brighton, UK) to the screw terminal panel. The acquisition board scans the channel list continuously and acquires data until either the operation is stopped or a specific number of samples is acquired.

The software interface between PC-1 and the DT321 acquisition board is composed of two distinct packages:

- The Omni CD application, bundle shipped free software that provides all the drivers and libraries necessary for the DT321 installation.
- The HP VEE-Pro, graphical programming environment (Agilent Technologies Inc., USA). This is a visual programming language which works connecting easy-to-understand block diagrams, instead of writing lines of code. It automatically handles the interfacing details so it is no longer necessary to manage I/O session handles.

A block diagram was built within the HP VEE-Pro environment, see Appendix E, to produce an application program (**DAQ.exe**) that controls the data acquisition during experiment, see figure 5.19.

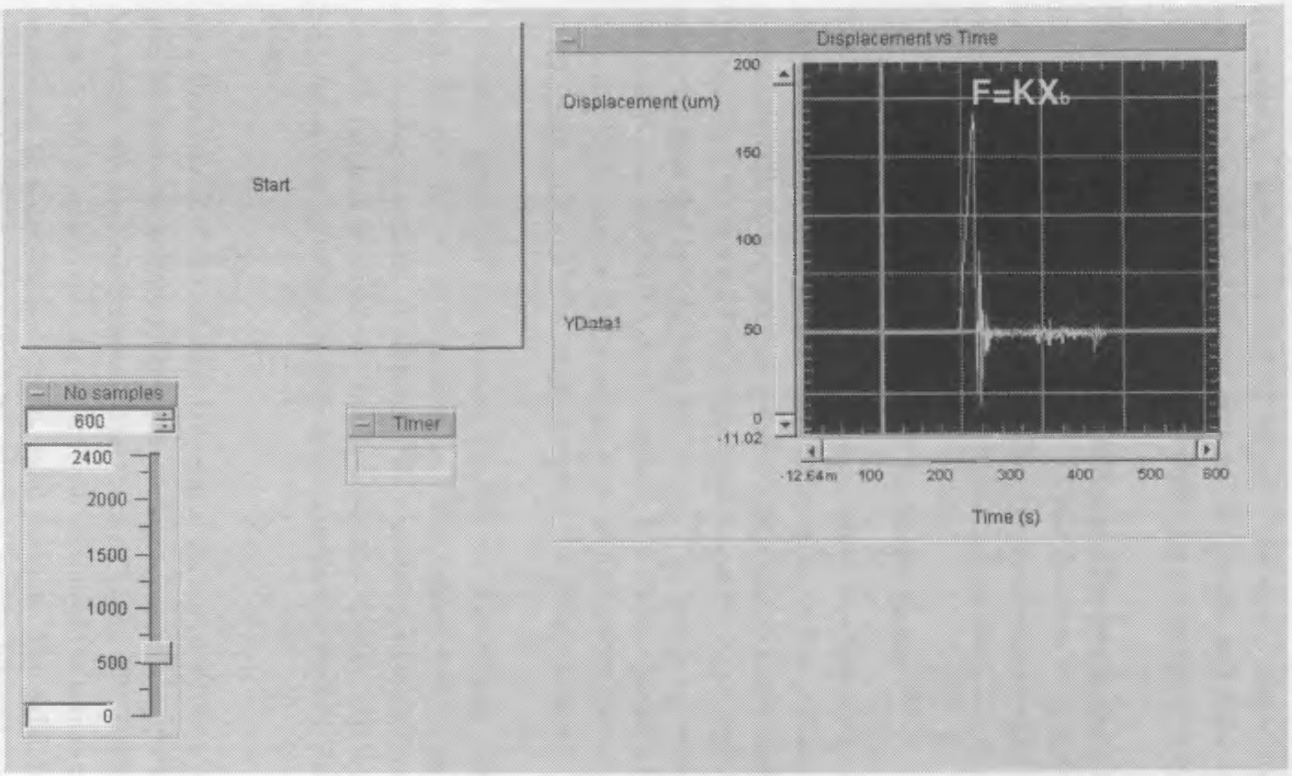

Fig. 5.19: Screenshot of the DAQ application, DAQ.exe, built within the HP VEE environment. In this example, the graph shows the time step rupture sequence of a sinter bridge formed between two PE particles. The XY tracer shows the relative displacement, X_b, of the LVDT armature mounted on the Force Measurement Assembly (FMA). The rupture force, F, is obtained afterwards by using the Hooke's law.

A user-defined number of samples can be collected according to the duration of the experiment. The DAQ application was built in order to grab one sample of data every second; however, faster frequencies can be set up and customisation of the application can be obtained by changing specific variables within the program environment. The application is started by clicking the START button. The actual displacement of the LVDT armature, which is displayed in real time on the screen, and collection of data stops after a user-defined number of samples is reached. A warning sound is played by the application.

The output of the acquisition program is a text file (saved as *1.txt*) where all the sampled data are aligned along a single column. These data can be imported afterwards for further analysis within the working environment of a common spreadsheet program. With such a procedure, force versus time or force versus temperature diagrams can be plotted.

5.1.7.2 Motion control

The magnetic encoder inside the linear actuator (see Section 5.1.4) is linked to the motor shaft and detects rotation, providing feedback to the EncoderDriver^{TM} Control Card (Coherent, Herts, UK) to track position and tightly control motor speed. The EncoderDriver^{TM} Control Card fits in a 8 bit ISA expansion slot of PC-2 (see figure 5.1). The Control Card can drive from one to eight EncoderDriver^{TM} Actuators by means of a fully proportional integral/derivative (PID) control interface. It features a position mode of operation, where accurate displacements of the actuator are achieved with a resolution of 50 nm, and a velocity mode, where velocity of the actuator is tightly controlled.

Communications with the Control Card is via the PC bus, using a straightforward instruction set. An extensive number of motor control commands is available to fine-tune the actuator operation. A software disk containing a comprehensive installation and diagnostic program is supplied with the hardware. Control and motion of the actuator can be programmed by writing specific command lines in BASIC, Pascal, C, or assembly language.

Real time control of the actuator is operated through a software interface (MC API, available for download at http://www.pmccorp.com/support/support.php), which runs under Microsoft Windows environment. The Motion Control API interface (see the screenshot in figure 5.20), provides real time control and motion of the actuator in terms of its absolute, or relative to a user-defined *origin*, axial position. The axial displacement is expressed in non-dimensional arbitrary units, *pts*, and can be inserted manually by means of the input *Distance* window. In the *absolute* and *relative* operation modes, see figure 5.20, the user can drive the actuator (the axial direction is assigned by pushing the buttons *Move +* or *Move -*) along both directions up to a defined distance; once the target is reached,

the actuator stops and waits for further instructions. Alternatively, in the *cycle* operation mode the actuator moves along cyclic trajectories (i.e. forward and backward) between the origin and a target distance until the *Stop* button is pushed.

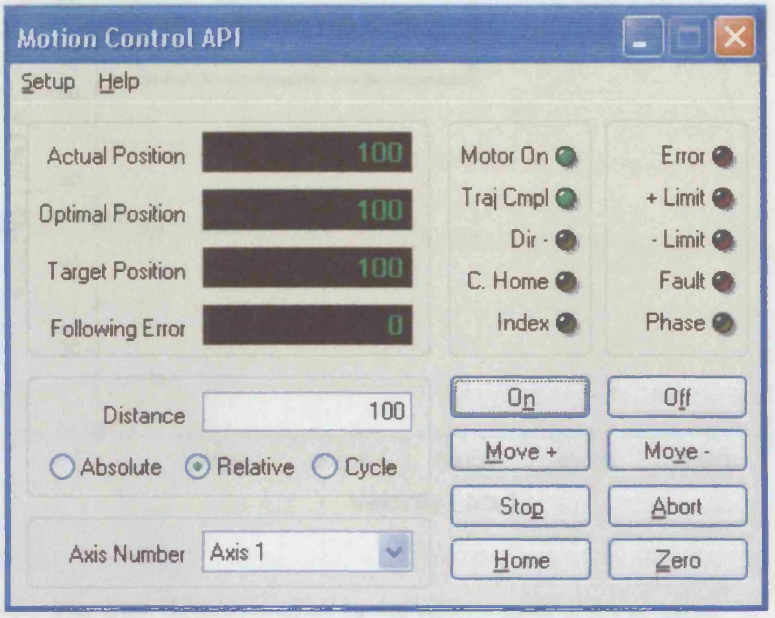

Fig. 5.20: Screenshot of the motion control interface MC API.

The actuator velocity, the acceleration needed to reach constant velocity and the deceleration required to stop when approaching a target distance, are all parameters, expressed in *pts*, which require assignment prior to experiment through the Set Up menu of the MC API interface. The number of *pts* required to cover a known distance, measured in microns, depends on the values of these parameters[4], see figure 5.22. Hence a conversion factor for the *velocity mode* was necessary to achieve the instrument calibration in the *position mode* of operation. Calibration of the velocity mode is explained in Appendix F and a calibration chart is shown in figure 5.21. The linear fit of the average velocity values provides a simple formula for velocity conversions from *pts* units to microns/s. Thus, a conversion factor can be obtained for the position mode by linear fitting the displacement values (see Table F.2 in Appendix F and figure 5.22) according to each relevant calibration velocity.

[4] After carrying out several tests, the values of acceleration and deceleration were set at 250 pts by default for all the experiments described in this thesis.

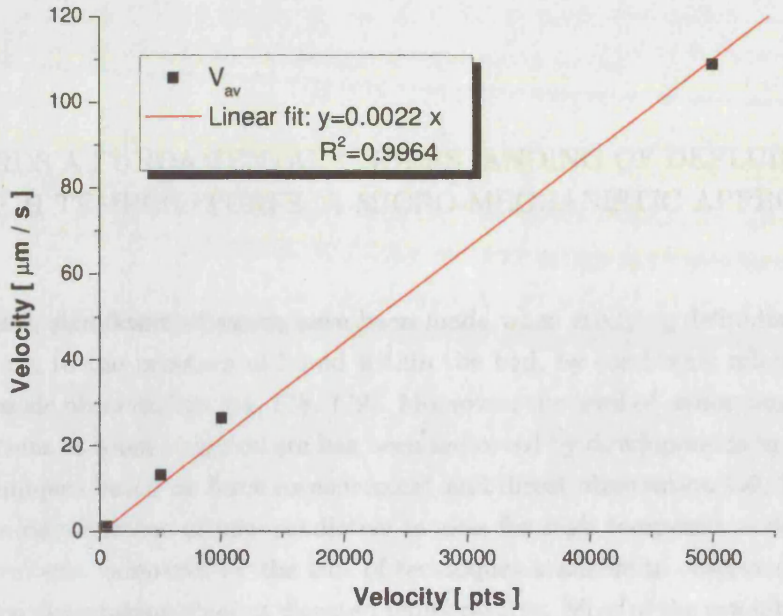

Fig. 5.21: Calibration chart for the velocity mode of the actuator.

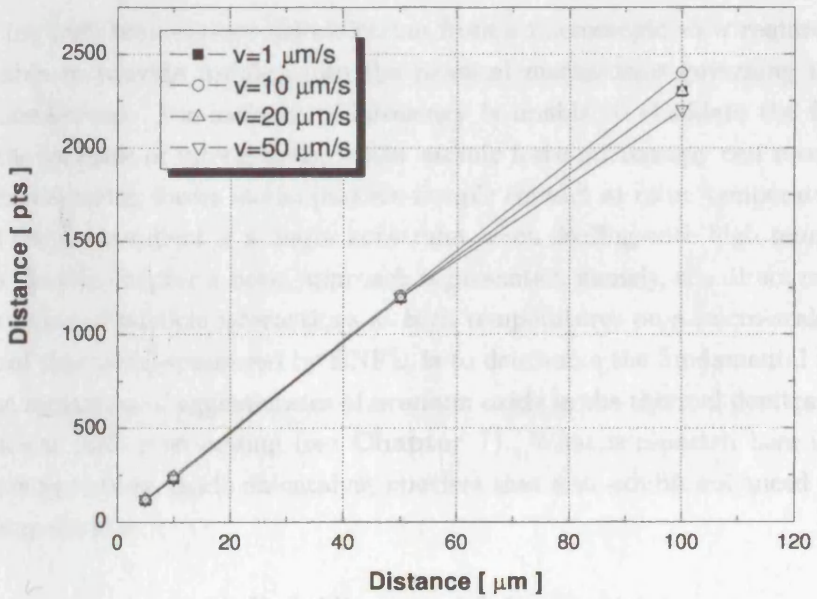

Fig. 5.22: Calibration chart for the position mode of the actuator.

6. TOWARDS A FUNDAMENTAL UNDERSTANDING OF DEFLUIDISATION AT HIGH TEMPERATURES: A MICRO-MECHANISTIC APPROACH

In recent years, significant advances have been made when studying defluidisation of fluidised beds due to the presence of liquid within the bed, by combining micro-scale data with macro-scale observations [54, 178, 179]. Moreover, the level of understanding of particle interactions at room temperature has been improved by developments in microscopic analysis techniques based on force measurement and direct observation [50, 121]. Unfortunately, the development of new predictive models for high temperature defluidisation seems to have been hampered by the lack of techniques available to observe and measure particle interactions taking place at elevated temperatures. Most of the available literature concerns studies of defluidisation due to thermally induced surface cohesiveness: previous works by Compo et al. [10], Tardos et al. [95] and Seville et al. [110] have shown that, by combining the results obtained from dilatometry and fluidisation tests, it is possible to model the limiting conditions of the process when fluidising pure material at high temperatures.

Investigating high temperature defluidisation from a microscopic view requires new tools that are able to provide insights into the physical mechanisms governing the particle-particle interactions. For instance, dilatometry is unable to elucidate the fundamental cause of the increase of interactions, whilst atomic force microscopy can return good results when measuring forces at the particle-sample contact at room temperature, but the control of the environment is a major constraint when dealing with high temperature interactions. In this chapter a novel approach is presented, namely, the direct measurement and observation of particle interactions at high temperatures on a micro-scale. The ultimate aim of this work, sponsored by BNFL, is to determine the fundamental mechanisms behind the formation of agglomerates of uranium oxide in the thermal denitration process during nuclear fuels reprocessing (see **Chapter 7**). What is reported here is the initial proof-of-concept study, made on catalyst powders that also exhibit enhanced interactions at high temperatures.

6.1 Defluidisation of E-Cat particles

In a recent investigation on high temperature fluidisation, Lettieri et al. [111, 180] have reported observations of the flow behaviour of different materials belonging to Geldart's

Group A as the temperature of the fluidised bed was increased up to 650 °C. In order to elucidate the factors responsible for the observed changes, the authors combined the results of both thermomechanical (TMA) and thermogravimetric (TGA) analysis for each sample of powder with the experimental observations obtained using an X-ray imaging technique. Among the materials employed in their work, the equilibrium (E-cat) FCC catalyst received particular attention because of its physical properties and flow behaviour. As explained by the authors, this powder, provided by BP Chemicals, had been employed in several cracking and regeneration cycles in an FCC unit and thus contained process residues such as oil and coke and deposit of metals such as Iron, Nickel and Vanadium. Ni and V are usually the most problematic: vanadium can cause destruction of the FCC catalyst, nickel can catalyse unwanted side reactions to form coke and H_2. Typical levels of impurities present on an E-cat catalyst are indicated by the ranges below:

- Fe: 0.2-0.5% wt
- Ni: 200-500 ppm
- V: 1500-10000 ppm
- C: 1-6% wt
- Oil: 2-3% wt

The physical properties of the E-cat FCC, which are shown in figure 6.1, classify it as a Geldart Group A powder, but in the light of its chemical characteristics it may not show the fluidisation behaviour of a typical Group A material.

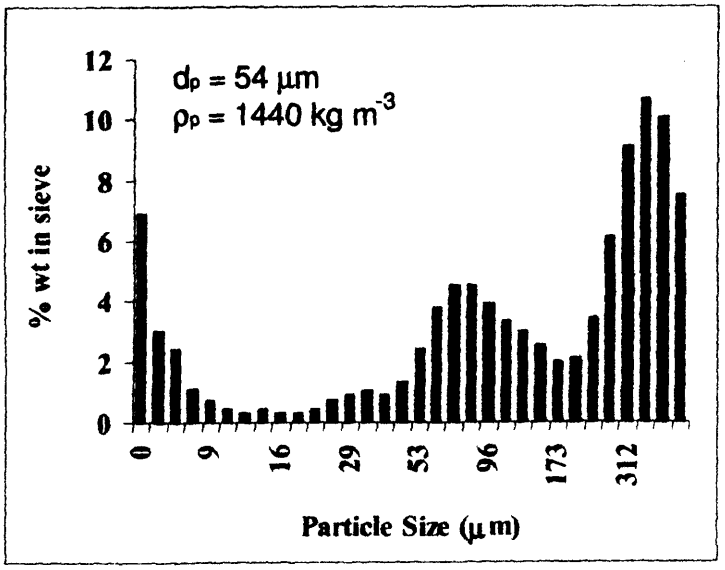

Fig. 6.1: E-cat: Particle size distribution (PSD), mean diameter (d_p) and density (ρ_p). Adapted from [6].

Figure 6.1 presents the particle size distribution (PSD) obtained by Lettieri [6] from analysis of a sample of E-cat FCC prior to fluidisation. The E-cat FCC is characterised by an extremely wide PSD and the balance between large (i.e. particles with diameter larger than 300 μm) and small particles (i.e. percentage of fines with diameter below 10 μm) sets the mean diameter, d_p, of this powder around a value of 50 μm.

Fluidisation tests conducted without pre-treatment of the powder showed poor fluidisation behaviour when compared to other fresh FCC catalysts. Drastic changes in the fluidisation behaviour of the E-cat particles, such as the formation of channels and rat holes within the bed, were observed as the temperature was increased to 150 °C, with complete loss of fluidisation experienced at 200°C. The internal flow patterns of the gas and solids were studied using an X-ray technique. A schematic of the types of behaviour depicted in the X-ray images is shown in figure 6.3. On increasing temperature, the curves describing the $\Delta P_m/\Delta P_c$ ratio (i.e., the ratio of the measured and calculated pressure drop values) versus gas velocity deviate progressively according to whether the gas flow rate was increased or decreased, see figure 6.2, thus indicating the presence of enhanced interparticle forces within the bed.

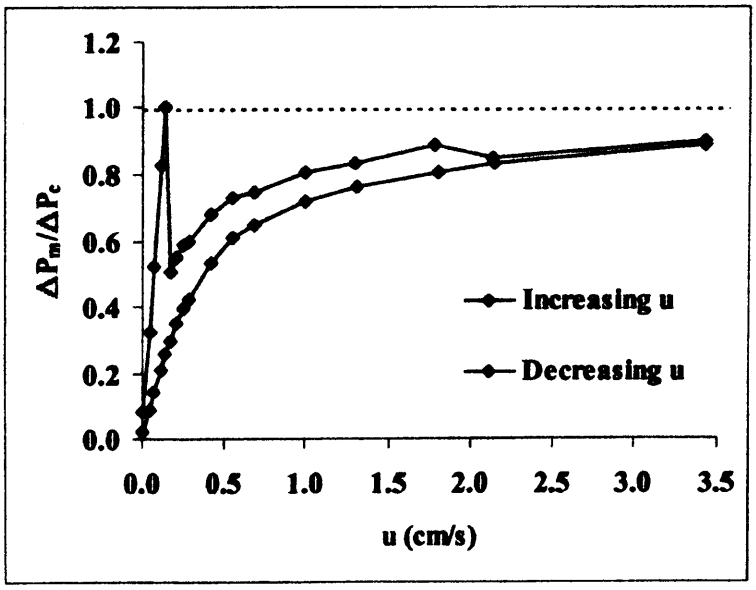

Fig. 6.2: $\Delta P_m/\Delta P_c$ versus superficial gas velocity, E-cat at 100 °C. From [6].

Moreover, increasingly higher gas velocities were needed to break down the channels and rat holes, in order to bring the powder close to the fluidised state.

Further analysis on the changes of the bed material physical properties with temperature [6] led the authors to state, as a possible explanation, that heavy hydrocarbons, which were solid at ambient conditions, may have melted with increasing temperature causing

liquid to be expelled from within the pores of the catalyst and the particles to agglomerate and defluidise. Furthermore, the catalyst could not be re-fluidised after the system had been cooled back down to ambient temperature due to the formation of large agglomerates at the distributor plate of the vessel.

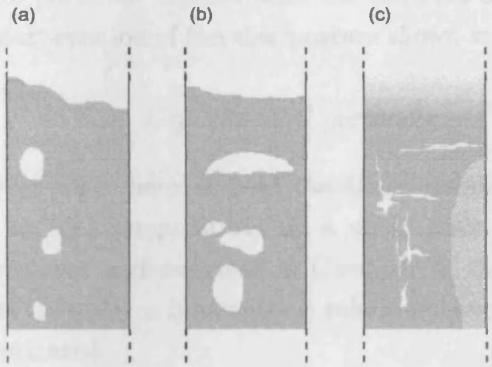

Fig. 6.3: (a) Bubbling, (b) Slugging, (c) Channelling flow behaviours when fluidising the E-cat catalyst at different temperatures.

During TMA, the E-cat sample being analysed was heated up to 1000°C at a rate of 10 °C per minute and subjected to a static force of 0.2 N. The thermogram, obtained by dilatometry, figure 6.4, shows an initial expansion up to 134 °C, after which a sharp decrease in size occurs up to around 200 °C.

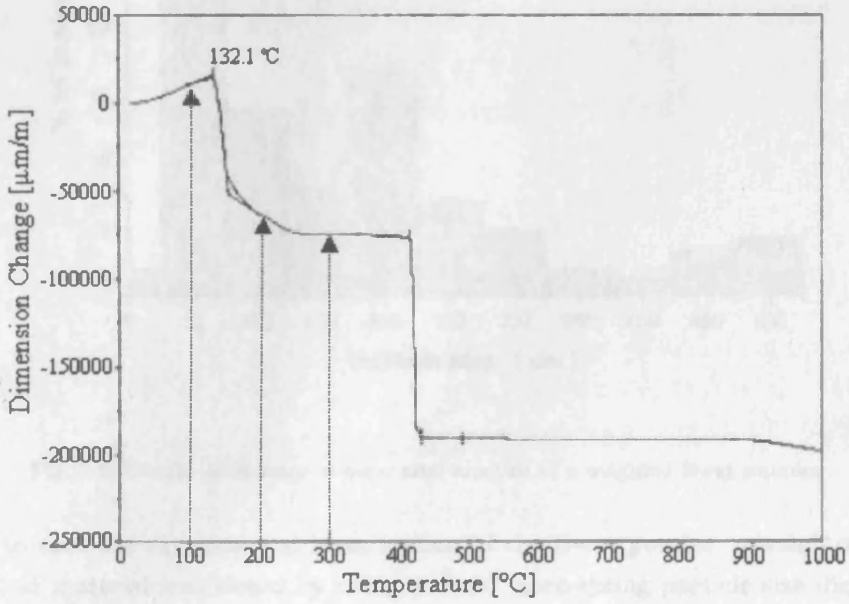

Fig. 6.4: Thermogram of E-cat, adapted from [111].

In the work reported here, a campaign of three different experimental studies, using the novel, purpose built, high temperature micro-force balance (HTMFB), was carried out on E-cat particles in order to investigate the physical changes of the particle surfaces with increasing temperature and to evaluate the magnitude of the force of a drying liquid bridge formed between a pair of particles. Results from the third set of experiments were used to provide a different interpretation of the thermogram shown in figure 6.4.

6.2 Experimental methods

A novel approach has been taken here, namely, the direct measurement and observations of particle interactions at high temperatures on a micro scale. To this end, a unique instrument has been developed and described in **Chapter 5**, the HTMFB, which allows for the main parameters that play a fundamental role in enhancing particulate adhesion and cohesion to be investigated.

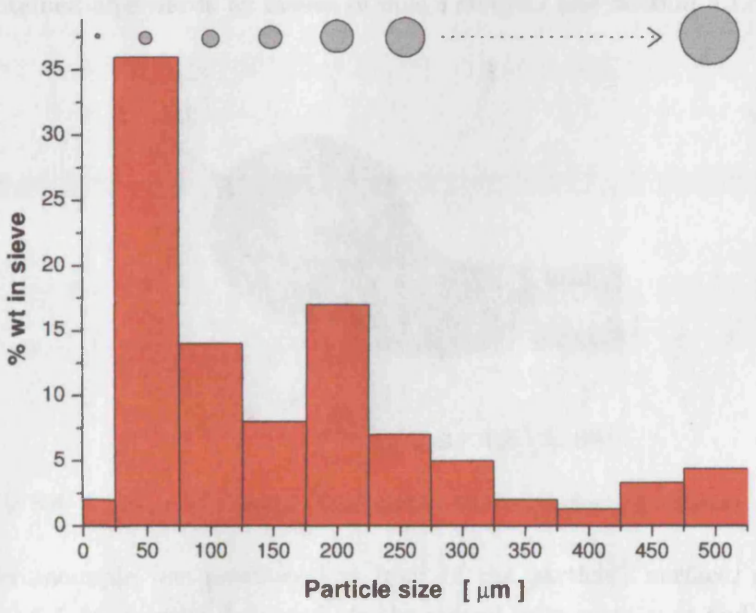

Fig. 6.5: Weight percentage in sieve after analysis of a weighted E-cat sample.

In order to ease the experimental investigation of the E-cat powder, a weighted sample (i.e. 3 g) of material was sieved by using a novel vibro-spring particle size distribution analyser[1], which has been invented by the instrumentation team at UCL and is capable of sizing particles in the range of 20 to 3000 μm. By means of the vibro-spring PSD analyser

[1] The author wishes to thank his colleague Richard Kamugasha for his technical support.

it was possible to evaluate the PSD of the sample analysed, see figure 6.5, and to sieve and collect eleven different batches of powder according to its size distrubution (i.e., the first batch of powder was filled with particles with diameter ranging from 0 to 50 μm and so on, up to the last batch, which contained powder of diameter greater than 500 μm). Having the powder finely sized helped to accelerate both the procedures of particle selection via microscopy and particle attachment to the glass micro-pipette.

6.2.1 Direct observation

E-cat particles of diameters ranging between 60 and 500 microns were investigated using the following procedure. For each run a single particle was attached to the tip of a glass pipette, as described in Section 5.1.2.2, and aligned inside the heating element under the lens of the microscope by means of the micromanipulator, figure 6.6. The size of each particle is initially estimated by means of a micrometer graticule, which is contained in one of the eyepieces of the microscope, whereas a more precise measurement of the particle diameter is obtained afterwards by means of image analysis (see Section 5.1.6.1).

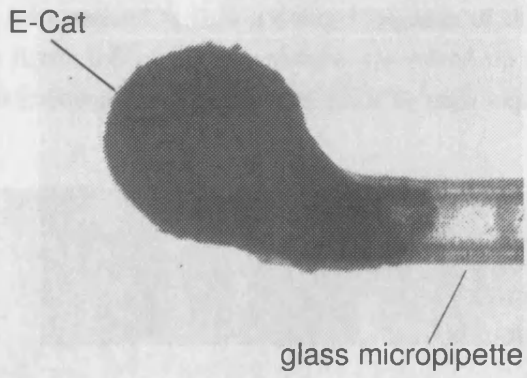

Fig. 6.6: A 100 μm in diameter E-cat particle glued to a glass micropipette.

A type K thermocouple was positioned in front of the particle's surface, as shown in figures C.1 and 6.7, its position adjusted via the second micropositioner and the focus of the microscope's objective.

Temperature was then increased by means of the potentiometer from room values up to 200 °C, in steps of 10 °C/min. The digital camera provided images of the particle's surface at each experimental temperature, monitoring the physical changes that occurred.

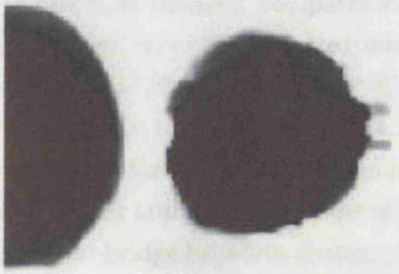

Fig. 6.7: A typical image representing the E-cat particle (right) and the edge of the thermocouple (left).

6.2.2 Force measurement

A 250 μm E-cat particle and a 100 μm diameter particle of the same material were attached on the tip of two micropipettes and mounted onto the micromanipulators by means of the pipette holders. Alignment inside the heating element was achieved by operating the micropositioners and adjusting the focus of the microscope objective. The pair of particles was brought into contact within a defined location of the heating element (i.e., the dashed red line in figure 6.8) and temperature was raised up to 90 °C. A calibration of the experimental temperature was performed prior to each experiment (see Appendix C).

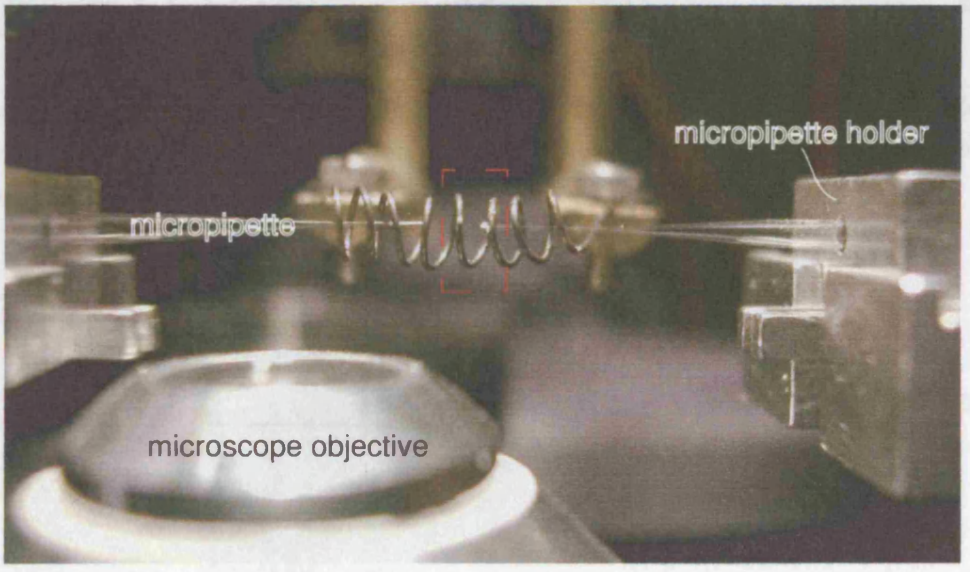

Fig. 6.8: Photograph of the experimental set-up employed for the measurement of the pulling force exerted by a drying liquid bridge. The dashed red line represents the location of the heating element where the interactions take place.

A liquid bridge was formed (figure 6.9) between the particles by pulling apart the pair by means of the linear actuator fitted on one of the two micromanipulators. The temperature was then increased further to 100, 150 and 200 °C, respectively, by means of the potentiometer (voltmeter) coupled to the heating element.A type K thermocouple was positioned in front of the particle's surface, as shown in figures C.1 and 6.7, its position adjusted via the second micropositioner and the focus of the microscope's objective. When kept at such temperatures, the liquid bridge began to change phase and become solid. The cause of this change could be due to crystallization or thermal decomposition followed by crystallization of certain compounds and evaporation of low molecular weight compounds. It will be referred to here as a "drying" process. As a result, the bridge volume shrinks, until complete solidification has occurred.

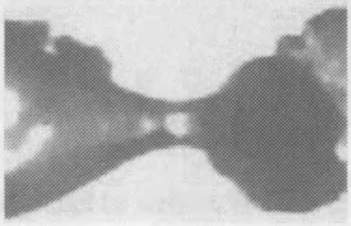

Fig. 6.9: Typical experimental set-up during the measurement of the pulling force exerted by a drying liquid bridge initially formed at 90 °C between a 250 μm diameter E-cat "particle" (left) and a 100 μm diameter E-cat particle.

According to figure 6.10, during the drying process the pulling force exerted by the bridge, F_b, was evaluated using Hooke's law (see Section 5.1.3) and physical changes, such as the initial and final separation distance, were monitored by means of image analysis.

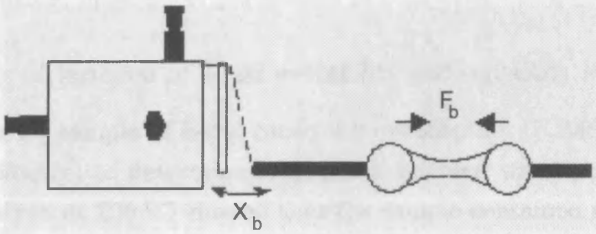

Fig. 6.10: Force measurement. The magnitude of the force exerted by the bridged particles, F_b, can be easily calculated once the displacement of the force measurement assembly, X_b, is known.

As depicted in figure 6.11, the difference between X_f, the final bridge length, and X_i, the initial bridge length, is a function of the three variables characterizing the drying process,

namely, the drying time, the temperature and the initial volume of liquid and thus it was used to describe the development of the bond. The magnitude of the maximum force for a given initial bridge configuration will depend on the same three variables and can therefore be related to X_i. If we assume that the maximum force exerted by the bridge without rupture occurs when the bridge shrinks a distance equal to X_i (i.e. X_f is zero), then at this point the drying process is complete.

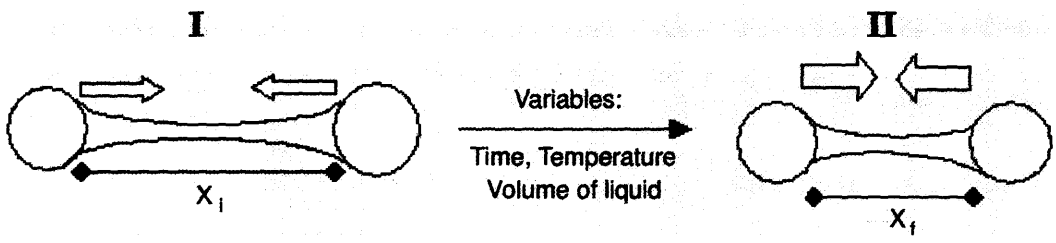

Fig. 6.11: Shrinkage of the liquid bridge is dependent on time, temperature and volume of liquid.

Thus X_p is defined as

$$X_p = \frac{X_i - X_f}{X_i} \tag{6.1}$$

Hence, the strength of the bridge can be written as

$$F_b = F_{max} X_p \tag{6.2}$$

where F_{max}= KX_i, with K being the spring constant of the force measurement assembly.

Experimental graphs obtained with this method will represent changes in the force exerted by the drying liquid bridge and can thus be used as indicators of relative phase composition at a given temperature, in terms of percentage of completion of the drying process.

6.2.3 *Study of variation of liquid wettability and spreading with temperture*

Lettieri [6] analysed a sample of E-cat catalyst by desorption GCMS (Gas Chromatography Mass Spectrometry) to determine compounds released with increasing temperature. Results of the analysis at 200 °C showed that the sample contained a complex mixture of alkanes and alkenes from C_4 to C_{16}. Some chlorinated compounds, which might be impurities, at a very low level. The chromatogram obtained at 250 °C indicated desorption of a larger amount of material, especially for the highest molecular weight compounds (C_9 to C_{20}). A detailed study of the chromatogram obtained at 250 °C highlighted also the presence of aromatic compounds such as alkylbenzenes and alkylnaphtalenes. Hence, the wetting properties of the liquid during fluidisation may be affected by changes in the chemical composition of both the liquid and the solid when increasing the operative tem-

perature.

In order to study contact angle hysteresis with increasing temperature, a small droplet of liquid was obtained by stretching a liquid bridge, initially formed between E-cat particles of 150 μm and a 250 μm in diameter, until rupture of the bond occurred (see figure 6.12). Photographs of the droplet, resting on the surface of a 150 μm-diameter E-cat particle, were taken, while the temperature was raised from 90 °C up to 200 °C in steps of 10 °C/min. Measurements of the variation of the contact angle formed by the liquid with the particle surface were subsequently calculated through image analysis.

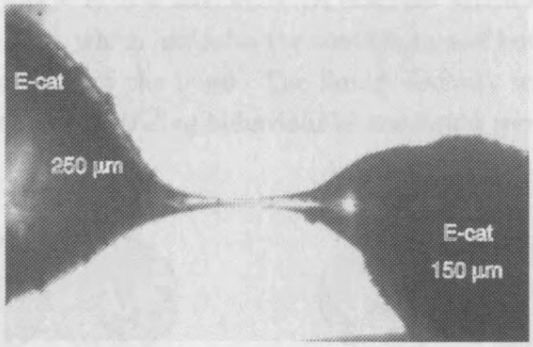

Fig. 6.12: A small droplet of liquid is obtained by stretching a liquid bridge, initially formed between two E-cat particles, until rupture occurs.

Further experimental study was conducted on a pair of 150 μm-diameter E-cat particles when bonded by a liquid bridge. By following the procedure explained above, after a small droplet had been formed on one particle surface, the 250-μm-particle was carefully removed from the heating element to be replaced by another 150 μm E-cat particle, as shown in figure 6.13(a).

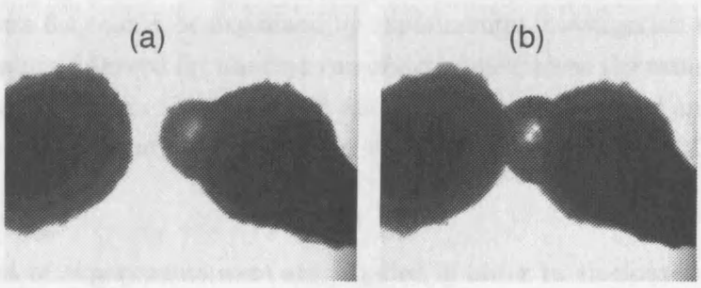

Fig. 6.13: Sequence showing particle approaching (a) and liquid bridge formation (b) between two E-cat particles of 150 μm diameter.

The separation distance between the pair of particles was further reduced by operating their relative displacement through the linear actuator, figure 6.13(b). The operation was conducted at a relatively low velocity ($\approx 3\mu$m/s) that permitted the liquid to be gently squeezed between the two surfaces. Particles contact was determined by means of

visual observation and the LVDT indicator. The linear actuator was then stopped and programmed to execute dynamic cycles at a velocity of 10 μm/s, figure 6.14. Particles were separated to a distance, a, equal to 25 μm and re-approached until zero separation while temperature was increased at a rate of 10 °C/min. Separation between particles was small enough and the liquid volume sufficiently high to guarantee elongation of the liquid bridge without rupture. The maximum force, F_{max}, measured during elongation of the bridge was recorded together with the operative temperature. Upon complete solidification of the bond, the entire system, which is composed by the pair of particles rigidly connected by the solid bridge, will displace of a distance equal to 25 μm, hence the maximum theoretical force is calculated as $F_{solid} = K \cdot a = 227.38 \mu N$. A diagram where F_{max} was normalised in respect to F_{solid} was plotted, which indicates the contribution of both capillary and viscous terms to the overall strength of the bond. The liquid viscosity was therefore calculated and some conclusions on the spreading behaviour of the liquid were therefore drawn.

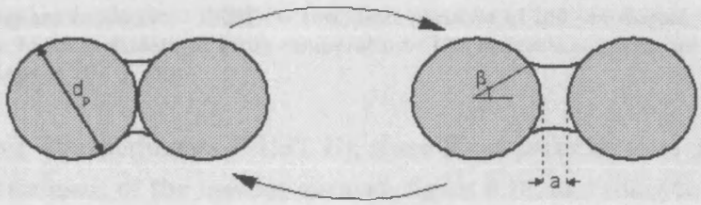

Fig. 6.14: Sequence showing liquid bridge stretching and squeezing between two 150 μm-E-cat particles. The separation velocity, da/dt, was set at 10 μm/s. The maximum separation distance, a, was set at 25 μm.

6.2.4 Thermogram validation

The physical changes reported during the thermo-mechanical analysis (TMA) between 100 and 300 °C (figure 6.4) could be explained by experimental investigation at a microscopic level. The procedure followed for the first run of experiments was the same as described in the force measurement tests (Section 6.2.2) and the nature of the bond and its magnitude were recorded as the operative temperature was increased up to 300 °C in steps of 10 °C/min. [2]

Two different set of experiments were also studied in order to elucidate how the particle size distribution of the E-cat sample analysed by TMA may affect the final interpretation of the thermogram. In the first run of experiments (TEST A), two E-cat particles of 100

[2] During the experiment a small reservoir of liquid would flow from the large E-cat particle onto the smaller particle's surface to collect at the pipette-particle junction (see Appendix G). At 200 °C such a small amount of liquid was already dry and, in fact, the solid bond, which had been formed between particle and micro-pipette, allowed the two particles to be firmly held at temperatures much higher than the maximum working temperature (up to 200 °C) allowed by the high temperature glue.

μm diameter were brought into contact within the heating element, figure 6.15.
A small load, L (circa 20μN), was applied in order to avoid slipping or detachment of particles at the point of contact due to external vibrations. Temperature was then increased up to 200 °C in steps of 10 °C/min. Changes in the initial length ($\ell_0 = 200\mu m$) of the sample, which may have been caused by expansion or contraction of the solids with temperature, were monitored and recorded.

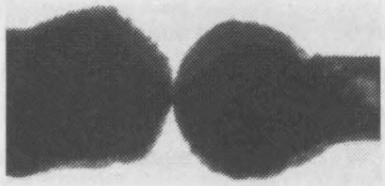

Fig. 6.15: Thermogram validation - TEST A: two E-cat particles of 100 μm diameter were brought into contact within the heating element at room temperature. The interaction environment was then heated up to 200 °C in steps of 10 °C/min.

In the second run of experiments (TEST B), three E-cat particles were placed within the interaction environment of the heating element, figure 6.16, according to the same set-up employed for the calibration of the heating element along the z axis (see figure C.4 in Appendix C.1).

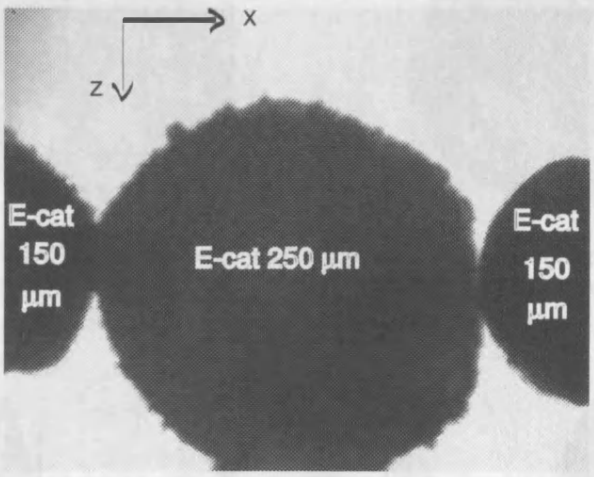

Fig. 6.16: Thermogram validation - TEST B: a 250 μm-diameter E-cat particle was placed between two equal sized (150 μm in diameter) particles of the same material. The interaction environment was then heated up to 200 °C in steps of 10 °C/min.

A pair of E-cat particles (150 μm in diameter) were attached to the micro-pipettes and mounted onto the micromanipulators. Alignment within the heating element was achieved by means of the micropositioners. Some space was allowed between the two particles

in order to introduce a third E-cat particle of larger diameter (250 μm). Particle and micropipette were introduced between the two consecutive turns of the heating coil along the z direction until the three particles centres were aligned along the x direction. A small load was then applied in order to reach a stable configuration. Changes in the initial length of the sample ($\ell_0 = 550\mu m$) were monitored and recorded while temperature was increased up to 200 °C in steps of 10 °C/min.

6.3 Results and discussion

Image analysis of E-Cat particles with diameters up to 190 μm revealed that no expansion or shrinkage took place in the range of temperatures investigated. In figure 6.17 the sequence of two images of a 100 μm particle shows that the surface of the particle did not experience any physical macroscopic change.

Particles above 190 μm in diameter showed behaviour more similar to that explained by Lettieri et al. [111]; at temperatures ranging between 90 °C and 130°C, a small increase in size was observed. A typical observation is shown in figure 6.18, where the sequence of images for a 250 μm E-Cat particle shows different physical stages as temperature is varied from room temperature up to 180 °C (the photographs shown in figure 6.17 and 6.18 were taken with objectives of different magnitude).

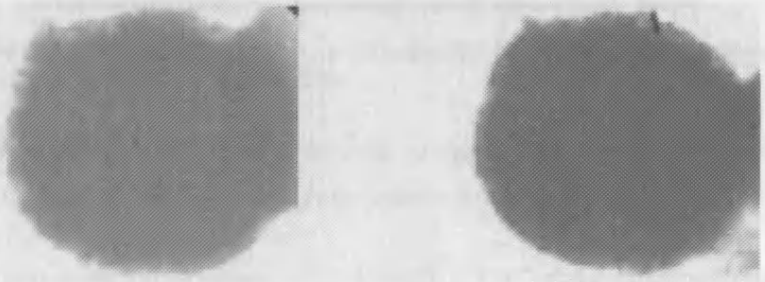

Fig. 6.17: The 100 μm E-cat particle at room temperature (left) and 200 °C (right). No physical change in the particle is observed.

Fig. 6.18: The 250 μm E-cat particle at room temperature (left), 90 °C (center) and 180 °C (right). The apparent "particle" is, in fact, an agglomerate of catalyst powder and hydrocarbons, some of which start to melt at 90 °C.

It appears that low boiling compounds start to melt at 90 °C, thus forming a thin liquid layer around the surface of the particle. A slight increase of the size is caused by the liquid, which flows and fills the gaps present on the irregular profile of the particle. As temperature is increased to 180 °C, the whole particle is found to be in a semi-solid state, comparable to a highly viscous bubble of liquid. Because of the evaporation of the low boiling compounds at these higher temperatures, shrinkage of the drop then takes place and at 200 °C some solid material is eventually found on the tip of the pipette. It can be concluded, therefore, that particles that appeared to be of large diameter were actually semi-solidified agglomerates composed of fines and hydrocarbons, which underwent a phase change to become liquid droplets as the temperature reached a critical value. In contrast, particles below 190 μm in diameter were the original catalyst particles. This can be clearly seen in the SEM images shown in figure 6.19.

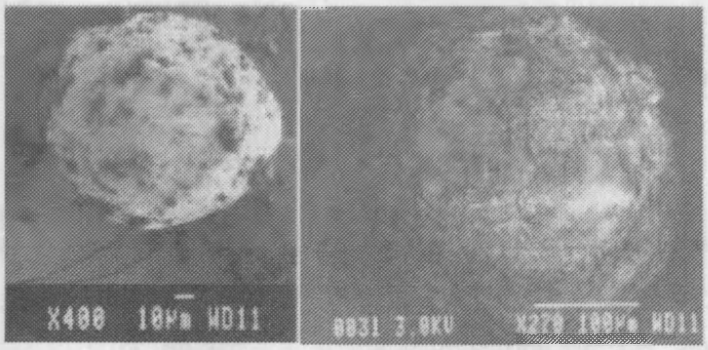

Fig. 6.19: SEM images of E-cat particles (left) a 100-μm-diameter catalyst particle, (right) a 250-μm-diameter agglomerate of catalyst and hydrocarbons

Results obtained from the force measurements of the drying liquid bridge are shown in figure 6.20 as the average values of five experiments for each temperature.

During drying, two main forces enhance the strength of the bond according to the operative temperature; the surface tension and the resultant force caused by the formation of a solid bridge. The solidification process was considered to be at an end when a steady value was reached within 90-100% of the maximum limit of shrinkage.

The surface tension, which is the dominant force at 100 °C, can be considered negligible as compared to the force arising during the solidification process at higher temperatures. At 100 °C, no increase in the force is observed and the bridge remains largely in the liquid phase (a thin crust does eventually form on the outer surface of the bridge, but this has no detectable effect on the force measurement).

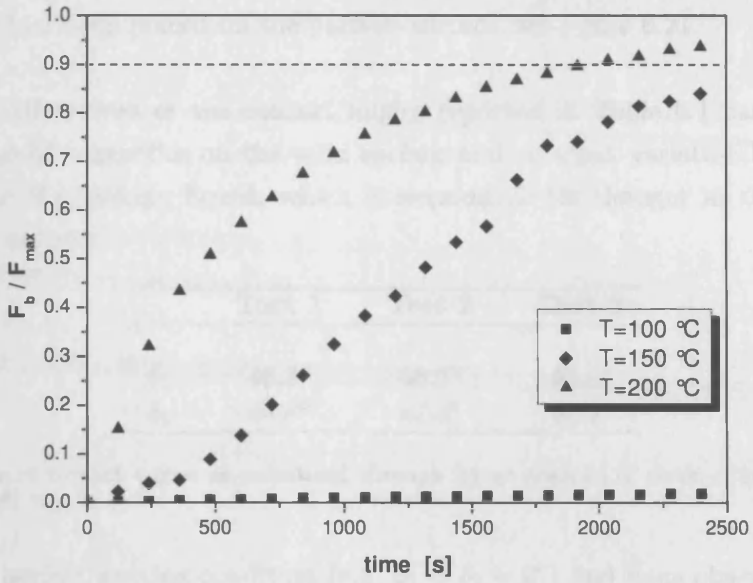

Fig. 6.20: Experimental drying curves of liquid bridges beween E-cat particles. At 100 °C, the bridge remains in the liquid phase. At 150 and 200 °C, the bridge dries to a solid, at rates that increase with temperature.

Temperature is the driving mechanism in the solidification process, since by increasing this parameter the evaporation rate and therefore the solidification rate increase to the maximum limit in a shorter time. The force due to surface tension is negligible at 200 °C, thus permitting the solidifying force to dominate almost instantaneously.

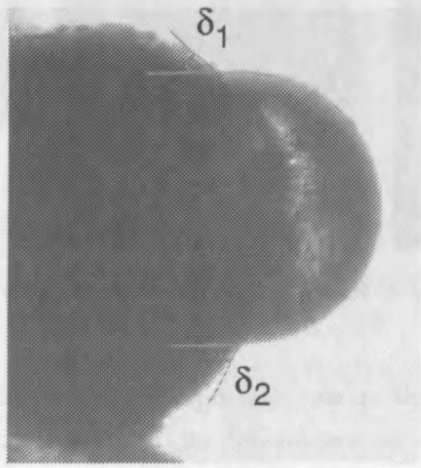

Fig. 6.21: Typical image used for direct observation and measurement of the contact angles, δ_1 and δ_2, formed by deposition of a liquid droplet on a 150 μm-diameter E-cat particle at 90 °C.

Results obtained from three different observations, see Table 6.1, and measurements of

the liquid/solid contact angles, δ_1 and δ_2, which are formed by a liquid droplet resting on a 150 μm E-cat particle, show poor tendency of the liquid to wet the solid as soon as a liquid droplet had been placed on the particle surface, see figure 6.21.

Differences in the values of the contact angles reported in Table 6.1 can be addressed to the presence of impurities on the solid surface and/or small variation in the chemical composition of the wetting liquid, which is responsible for changes in the value of the liquid surface energy.

	Test 1	Test 2	Test 3
δ_1	46.3°	48.5°	43.8°
δ_2	44.8°	47.4°	45.6°

Tab. 6.1: Values of contact angles as calculated through image analysis of three different experimental observations at 90 °C.

However, the perfect wetting condition (e.g. $\delta_1 = \delta_2 = 0°$) had been observed as temperature was increased up to 120 °C; in fact, at such temperature, the droplet collapsed to form a thin liquid film around the particle surface, as illustrated by the sequence of images in figure 6.22. It can be assumed that wettability was enhanced by both the lowering of the surface tension of the liquid with temperature and the complete dissolution of solid impurities into the liquid mixture, thus enhancing the chemical affinity between the solid and the liquid.

Fig. 6.22: Sequence showing the variation of the contact angle at 90 °C (left), 110 °C (centre) and 120 °C (right), respectively.

Indeed, viscosity of the liquid played an important role on the spreading dynamics of the droplet over the particle surface. Hence, its dependence on temperature was studied by measuring the overall force exerted by a liquid bridge when routinely stretched to a known distance while temperature was raised up to 200 °C. Five experiments were conducted for different liquid bridge volumes, V_b, as shown in Table 6.2.

The volume of the liquid bridge, which is a non-controlled variable, was obtained at the perfect wetting condition[3]: in fact, as shown by the previous results, during experiment the contact angle initially formed by the liquid and the particles surface was observed to reduce to zero degrees as soon as the experimental temperature reaches 120 °C. Images of the bridge were taken at its maximum elongation (e.g. $a = 25\mu$m) in order to calculate, by image analysis, the half-filling angle, β. In this regard, a large amount of liquid was always necessary in order to reach the end of the experiment by avoiding complete evaporation of the liquid at high temperatures.
In order to calculate the bridge volume, V_b, a suitable expression, among those listed in Table 2.4 of Section 2.2.4.1, was chosen, which provides a better approximation with the theoretical values (see figure 2.13). According to both the measured values of the half-filling angle and the normalised separation distance between particles ($a/d_p = 0.16 \approx 0.2$), the Tomas equation, (2.19), was employed for this calculation, since, at these conditions, it provides sufficiently high accuracy when compared with numerical results.

	Half-filling angle, β [°]	**V_b (Eq. 2.19) [μm^3]**	$\varphi = V_b/2V_p$
Test 1	41	133406.437	0.037
Test 2	47	211226.300	0.059
Test 3	43	157042.406	0.044
Test 4	45	182993.946	0.051
Test 5	48	226177.094	0.063

Tab. 6.2: Values of the half-filling angles and liquid bridge volumes calculated through image analysis and Tomas equation, respectively. The non-dimensional parameter, φ, was also calculated for each liquid volume.

Results from the measurement of the overall force exerted by the liquid bridge when stretched at constant velocity show a typical trend, which is indicated in figure 6.23.

The "shaded" region drawn in figure 6.23 between 90 and 150 °C is indicating that the bond formed between the two particles exists in liquid phase, whereas solidification, and, therefore, the net increase of the maximum overall force, occurs when the temperature is raised above 150 °C. Hence, within the "shaded" region the strength of the liquid bridge is determined by the sum of the surface tension and viscous terms (see Equation 2.33 in Section 2.2.7). However, it is assumed here that the solid-liquid phase change that occurs at 90 °C can be described similarly to the viscous sintering mechanism (Section 2.3.1.3). Thus, changes in the surface tension can be neglected at such temperature and only the viscosity of the particles surface changes during the phase transition.

[3] The variation of the liquid volume between 90 and 120 °C (i.e., the temperature at which the perfect wetting condition occurs) is negligible. This was confirmed by visual observation and measurement of the half-filling angle operated at both experimental temperatures. Hence it was assumed that significant loss of mass due to evaporation occurs at higher temperatures ($\succ$ 120°C), whilst only small liquid volume variations happen in the lower range of temperatures.

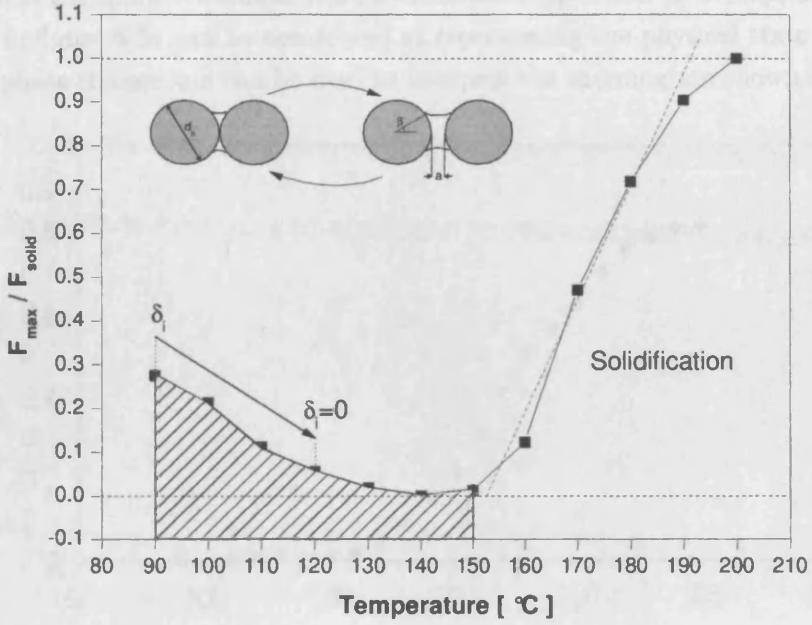

Fig. 6.23: Typical diagram obtained by plotting the variation of the maximum overall force exerted by a liquid bridge when stretched of a known distance, a, at temperatures ranging between 90 and 200 °C. The "shaded" region indicates the liquid phase composition of the bond. The slope of the red dashed line represents the solidification rate.

It can be seen from figure 6.23 that the overall force, F_{max} exerted by the bridge at 90 °C is about 30 % of the maximum limit, F_{solid}, thus a theoretical value of the viscosity of the liquid, η, was calculated by substituting the values of the relative velocity, separation distance as well as the measured force, respectively in Equation 2.30. η was found to be in the order of $5 \cdot 10^3 Pa \cdot s$. Such a high value can explain why, although wettability of the liquid is enhanced by temperature, its spreadability onto the solid particles is hampered between 90 and 120 °C. As temperature is increased up to 150 °C, the maximum force exerted by the pendular liquid bridge decreases due to the lowering of both surface tension and viscous terms. In this range of temperatures, viscosity could not be calculated through Equation 2.30, since the liquid surface tension, which is unknown, can be an important variable in the computation of the overall force exerted by the liquid bridge. Both wettability and spreading of the liquid, in this range of temperature, are highly enhanced. Above 150 °C, the solidification process takes place at a solidification rate (i.e., the slope of the red dashed line, which approximates the experimental curve that is lying within the solidification region, see figure 6.23) that depends on both the drying temperature and initial liquid volume.

The behaviour of a liquid bridge that goes on to change phase and become solid was investigated as the operative temperature was increased up to 300 °C in steps of 10 °C/min. The graph in figure 6.24 can be considered as representing the physical state of the bond during the phase change and can be used to interpret the thermogram shown in figure 6.4.

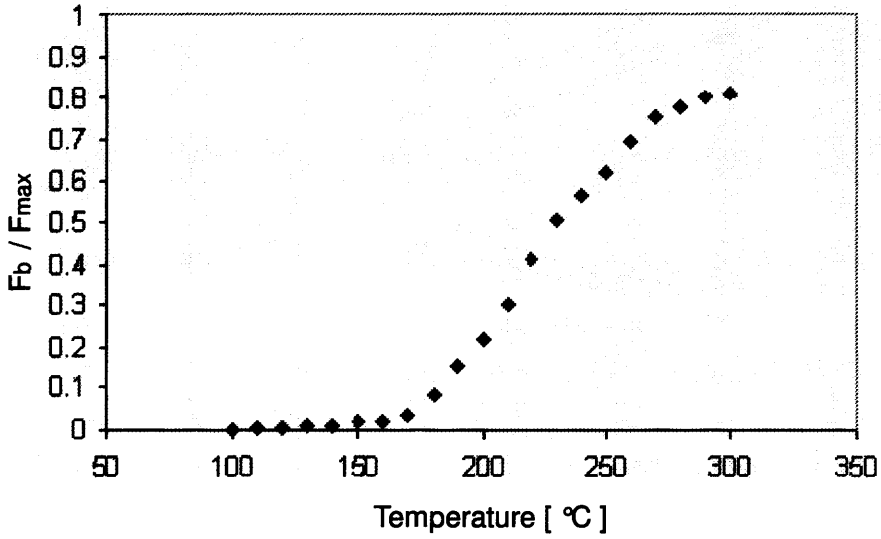

Fig. 6.24: Force/temperature profile for a drying liquid bridge between E-cat particles. The temperature is increased in steps of 10 °C/min, from 100 °C, where the bridge forms initially, to 300 °C, where the bridge has completely solidified.

Results obtained from the thermogram validation campaign were plotted in a diagram, such as the one in figure 6.25, which shows different characteristic elongation/contraction curves according to the initial particle size employed in the experiment.

A typical elongation curve was observed (see results from TEST A in figure 6.25) for two E-cat particles of small size (100 μm), which were initially placed in contact. In fact, changes in the initial length of the sample analysed, $\Delta\ell/\ell_0$, followed an almost linear trend when increasing temperature up to 200 °C. On the other hand, results from two different runs of TEST B showed that, by introducing a larger E-cat particle (250 μm) between two 150 μm particles, shrinkage of the sample occurs at the critical phase-change temperature (i.e., between 80 and 90 °C) and the contraction proceeds until completion of the experiment.

Results from both "TEST B" runs showed that, although only a small load, L, was exerted during the experiments, such a compressive force was high enough to ensure contraction of the sample in the range of temperature between 80 and 140-150 °C. Engulfment of the two solid particles in the large liquid droplet as the large particle melted was, in fact, aided by the action of the operative load (20 μN) and by the lowering of the surface tension and viscosity of the liquid. Evaporation and solidification processes also contributed to further

shrinking of the sample size because of the compressive drying force developed at higher temperatures.

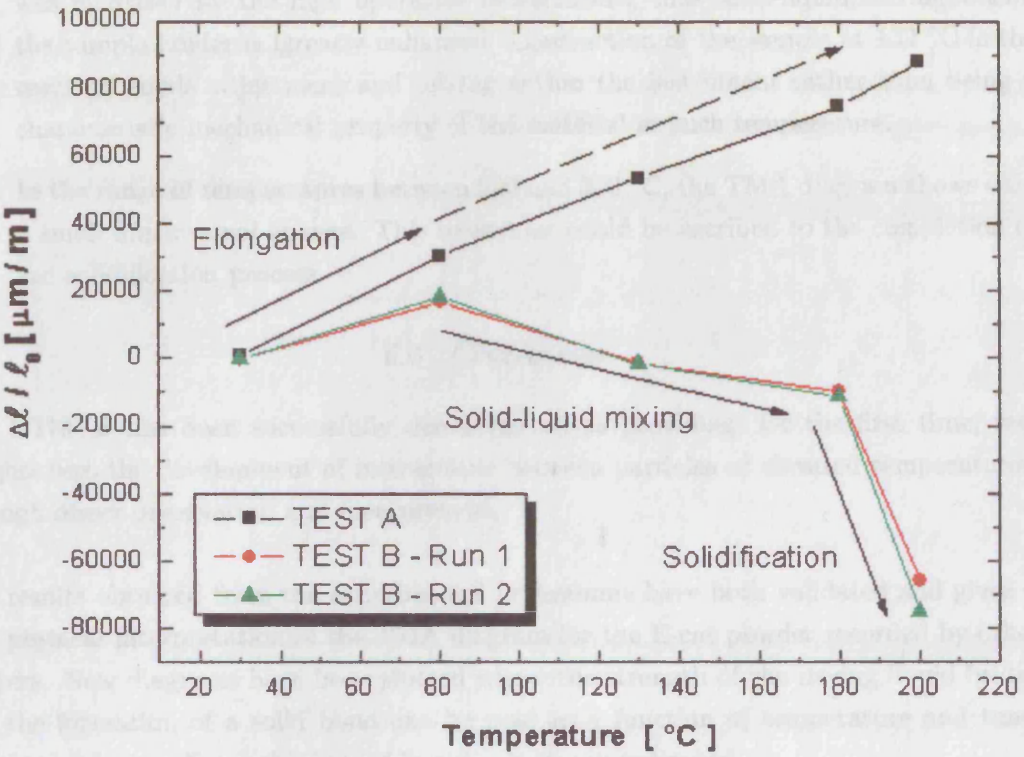

Fig. 6.25: Thermogram validation - Results from TEST A and TEST B: E-cat particles of diameters up to 200 μm show linear expansion when increasing temperature up to 200 °C. Results from TEST B, show that, when the E-cat particles of larger diameter change phase, they become a sort of liquid reservoir between the two, smaller, particles. Shrinkage occurs, in fact, as the resulting action of three phenomena: the engulfment of solids into the large liquid droplet, the evaporation of liquid with increasing temperature and the shrinking force exerted during the solidification process.

In light of these results, a different interpretation of the thermogram in figure 6.4 can be given as follow:

1. The positive dimensional change in the range of temperature between 100 and 132 °C has to be ascribed to the presence of the melting liquid that expands and shifts the solids surrounding each melting particle. The maximum positive elongation recorded during dilatometry depends on the liquid content of the analysed sample and therefore from its particle size distribution. Moreover, the way particles are aligned within the sample holder during dilatometry can bring to a misleading interpretation of the results.
2. The rapid shrinkage in the range of temperature between 132 and 200 °C is the result of both the operative pushing force (0.2 N) exerted during the TMA and the evaporation of low boiling compounds. Bonds between particles are shown to be

still in a semi-solid state and, in fact, the sample being analysed is a mixture of solids and liquid. The capability of liquid to spread and wet the surrounding solids was increased by the high operative temperature, thus solid-liquid mixing within the sample holder is lgreatly enhanced. Contraction of the sample at 132 °C is the result of solids adjustment and mixing within the instrument rather than being a characteristic mechanical property of the material at such temperature.

3. In the range of temperatures between 200 and 300 °C, the TMA diagram shows only a small dimensional change. This behaviour could be ascribed to the completion of the solidification process.

6.4 Conclusions

The HTMFB has been successfully demonstrated as providing, for the first time, real insights into the development of interactions between particles at elevated temperatures, through direct observation and measurement.

The results obtained from the experimental programme have both validated and given a new physical interpretation of the TMA diagram for the E-cat powder recorded by other workers. New diagrams have been plotted where the strength of the drying liquid bridge and the formation of a solid bond can be read as a function of temperature and time. Wetting and spreading behaviour of liquid was also investigated.

Some considerations on the relevant behaviour of the E-cat fluidised bed can be drawn as follows:

- At 100 °C, the fluidised bed is a mixture of solids and liquid that is going to evaporate and solidify. Hence, classical equations, which describe the state and quality of fluidisation of the bed, should be used carefully, since substantial changes in the bed material density (i.e., the bed weight) have to be taken into account.

  Spreading of liquid over the solids is hindered by the relatively high liquid viscosity, whilst the formation of liquid bridges between particles is hampered by the poor wetting behavior exhibited by the liquid at this temperature. Moreover, the induction time taken to form the solid bonds is extremely long and temperature and liquid volume sensitive, the latter being dependent, at each fluidisation run, on the initial particle size distribution of the bed material. This explains the sluggish bed behaviour as well as the formation of channels and rat holes within the bed.

- By increasing the temperature from 100 up to 200 °C, spreading of liquid among the bed contents is enhanced by its lower viscosity and formation of liquid bonds between particles is helped by the perfect wetting condition. Hence slugging and

channelling of the bed become more evident and higher gas flow rates are required to break the bonds formed between particles.

However, at 200 °C, the rate of solidification is extremely high. Liquid bridges may thus be able to generate solid bonds before rupture, causing agglomerate formation and subsequent defluidisation. Furthermore, during process, coalescence of liquid droplets may occur, thus enhancing the presence of large liquid volumes among the bed material. In such case, the solidification process proceeds at a relatively slow rate until complete evaporation of low melting compounds; hence, large liquid droplets can behave as a very viscous liquid before solidification, thus enhancing the formation of large lumps within the fluidised bed. In this work, every attempt to break the solid bond formed at the end of each experiment failed. This result explains the inability to re-fluidise the catalyst after the bed has been allowed to cool down.

7. MICRO-SCALE OBSERVATIONS AND MEASUREMENTS OF HIGH TEMPERATURE PARTICLE-PARTICLE INTERACTIONS

This chapter presents a novel approach that allows the direct measurement and observation of particle-particle interactions at high temperatures on a micro-scale. The aim of this experimental investigation is to determine the fundamental mechanisms behind the formation of agglomerates of uranium oxide in the thermal denitration process of Uranyl Nitrate Hexahydrate. Due to the radioactive nature of uranyl, suitable simulants have had to be found for laboratory studies. What is reported here is the initial proof-of-concept study, made on magnesium nitrate hexahydrate, which decomposes in a similar way and at similar temperature to uranyl.

7.1 Defluidisation of TDN fluidised bed reactors

Fluidised bed re-processing[1] has been successfully applied to the production of uranium trioxide by calcination of uranyl nitrate solutions through the following thermal decomposition reaction (i.e. TDN process):

$$2UO_2(NO_3)_2 \cdot 6H_2O = 2UO_3 + 4NO_2 + 12H_2O + O_2 \tag{7.1}$$

The feed to the TDN reactor is a purified and concentrated (1000 gU/l) Uranyl Nitrate Hexahydrate solution. During operation the fluidised bed consists of three phases - the solid oxide, the liquid uranyl feed, the fluidising gas (air) and reaction gas products (water, oxygen and nitrogen oxides), as shown by figure 7.1.

For 5 teU/day throughput (208 kgU/hr), 454.5 kg/hr of Uranyl Nitrate Hexahydrate will produce the following at 100% conversion[2]:

- 250.5 kg/hr Uranium trioxide
- 80.5 kg/hr Nitrogen dioxide
- 109.5 kg/hr water (steam)
- 14.0 kg/hr Oxygen

[1] Re-processing: the mechanical and chemical processing of spent nuclear fuel to separate usable products (Uranium and Plutonium) from waste material (fission products).

[2] Actual conversion is 99.4% at 300 °C with a residence time of 10 hours in the TDN reactor.

The initiating heat for the exothermic reaction is supplied by electrically heated elements, applied externally to the walls and also inserted in a single vertical tube, centrally positioned in the reactor. The heaters maintain the fluidised bed at circa 300-350 °C. The fluidising air is electrically preheated by heaters to 500 °C and leaves the reactor along with the reaction off-gases through sintered stainless steel filters in the lid of the reactor (not shown in figure 7.1).

UO_3 particles with diameter ranging between 50 and 350 μm (approx. 60-70% of the entire powder bed) are coated by the feed at temperatures ranging between 300 and 350 °C and continuously withdrawn as product through an overflow tube, thus maintaining a constant volume in the reactor. Moreover, the bed can be described as a mixture of solid particles and liquid drops that go on to change phase to become solid particles, see figure 7.2 (left). At 280 °C, when the water is driven off the reaction products, the particle surfaces become sticky. Moreover, there will also be liquid layers present on the solid particles each time they pass through the spray cone. When these particles come together and depending on process conditions, agglomerates will form, as shown in figure 7.2 (right).

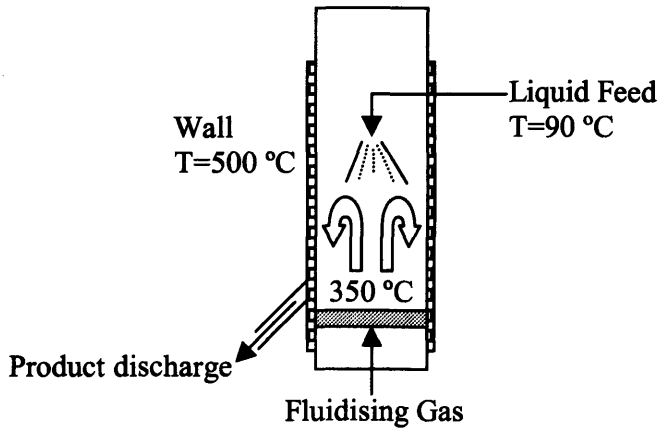

Fig. 7.1: Schematic and process temperatures for the TDN process.

These agglomerates, being heavier than the individual constituent particles, are less easy to keep fluidised and eventually the entire bed will defluidise unless the agglomerates are kept below a certain size limit via breakage processes.

The finite bed life is a particular problem in nuclear fuel re-processing, which is thought to be caused by over-spraying of the liquid fuel material. Once large areas of defluidised bed material are formed inside the reactor, the solid bed can only be removed by sending operators physically into the process chamber to literally dig the material out. The conditions under which this process takes place are very unpleasant and hazardous, not only because of the heat and dust but also due to the risk posed by radiation. Hence, there is

a significant environmental impact associated with this operation.

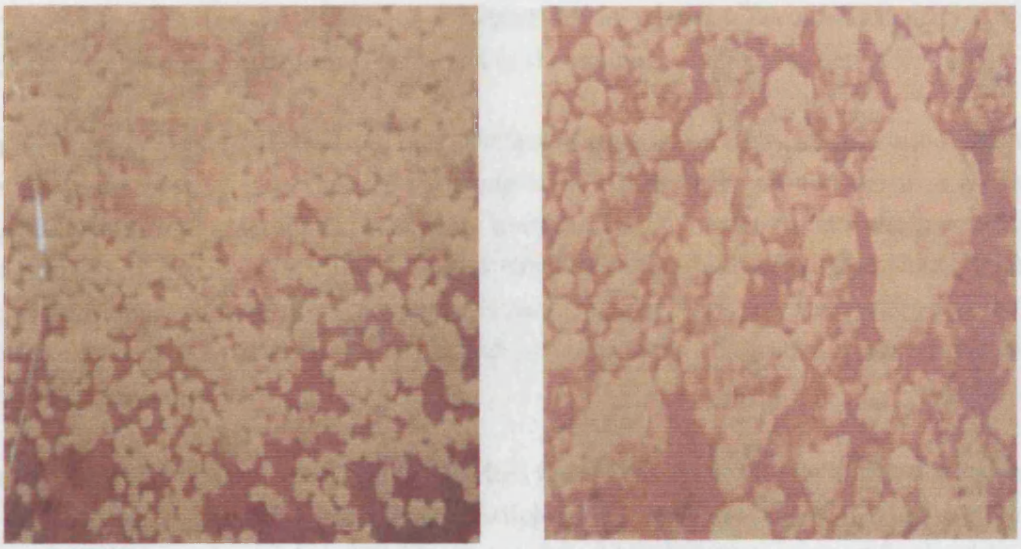

Fig. 7.2: Photographs of a bed of UO_3 particles at normal process conditions (left) and during agglomeration (right).

The effect of the operative variables over the particle size evolution of the bed material, during coating and drying processes using fluidised bed reactors, has been the subject of several studies. Gonzalez and Otero [181] reported in their work the size evolution of UO_3 particles inside a fluidised bed during the calcination process (i.e. Equation 7.1); they showed that whether an equilibrium particle size is obtained is the result of two independent mechanisms:

1. growth, which takes place by deposition of the feed on a particle each time it goes through the spray zone.

2. production of fine material caused by attrition, i.e. collision between particles or between particle and reactor walls.

However, the authors stated that the problem in the continuous reactor starts when the particles in the bed become too large, since as they grow continuously, fluidisation becomes poor and heat transfer rates decrease to the point where partially reacted/decomposed bonds, formed for instance by liquid bridge formation between particles, can sustain the disruptive forces generated by fluidisation and, eventually, bed caking occurs.

From the experimental results Gonzalez and Otero [181] concluded that attrition, and therefore breakage of particles as well as of small agglomerates, occurs during the early stage of the formation and calcination of the particles as they pass through the spray cone (which geometrically defines that part of the reactor where particles are wet by the liquid

feed): UO_3 particles are coated by the feed, which is almost instantaneously decomposed. But the more time the particles remain wetted by the partially decomposed uranyl, the higher the probability of rupture, thus raising the amount of fines content in the bed.

Liu and Litster [158] in their study on the effect of process variables of a spouted bed on the maximum coating rate, defined the spray zone, which forms around the feed nozzle. The spray zone is characterised by a higher humidity and a lower temperature in comparison to the rest of the bed, thus leading to changes in the fluidisation behaviour. If the spray zone is particularly moist, individual particles may stick together and eventually, the formation of large lumps may even lead to the collapse of the bed material and the shut down of the process.

A relatively large body of literature has studied the high temperature defluidisation caused by a change in the magnitude of particle-particle interactions. Seville et al. [110] (see also Section 4.2.3) have shown that defluidisation induced by sintering occurs in fluidised beds when the particles are allowed to remain in quiescent contact for long enough for a critical size of sinter neck to grow. Here, the employment of dilatometry tests on pure material samples (i.e. polyethylene) was necessary in order to develop a simple predictive theory, which predicts the limiting fluidising velocity below which the bed will defluidise due to sintering. On the other hand, it was shown in the previous chapter, that poor interpretation of results, as obtained through constant heating rate dilatometry, may occur in certain cases (for instance when the powder is composed of a mixture of low and high melting compounds) and possible explanations on the micro-mechanisms of agglomeration have to be searched through alternative experimental techniques.

Compo et al. [109] went on to investigate the minimum sintering temperatures for different types of fluidisable powder materials by producing accurate analysis of the results for the relevant thermograms obtained by dilatometry. However, Compo et al. [10] reported difficulties of interpretation for the contraction-dilation behaviour shown by different inorganic hydrated salts ($Al_2SO_4 \cdot 14H_2O$ and $CaCl_2 \cdot 2H_2O$); in fact, three major issues were pointed out in relation to the validity of the experimental technique employed (see also Section 4.2.2):

1. the virgin sample could not be used in the dilatometer because otherwise the release of surface water dissolved the sample and formed a solution. Hence drying of the sample was required prior to analysis.

2. because of the release of intercrystalline water from the material, the dried sample expanded upon heating and formed an agglomerate. The non-sintering mechanism of this type of agglomeration could not be further investigated (i.e. evaluation of the magnitude of the bond formed between particles) since rupture of the agglomerated

sample occurred whenever it was removed from the dilatometer.

3. none of the experiments were conducted under the same conditions. Intergranular force, particle diameter and shape factor, heating rate and sample load (see also Section 2.3.1.2) all varied from run to run, making a quantitative numerical comparison impossible.

Hence, the investigation of the mechanisms involved in the cohesion of particles when coated by a reactive liquid requires new tools and experimental techniques, which lead to a better explanation of defluidisation in function of process key-parameters: for instance, studying the magnitude of the force exerted by a material bridge formed between a pair of particles during its decomposition (i.e. at different temperatures), would help the understanding of agglomerates formation within the fluidised bed as a consequence of changes in the heat transfer in the reactor. Moreover, the amount of feed deposited on each primary particle (i.e. "green" granule) can be an important process parameter (which is related to the size of droplets sprayed over the bed contents) that enhances strong particle-particle interactions.

7.2 Dehydration of crystalline hydrates and choice of a simulant

Although crystalline hydrates cannot be distinguished from other solid reactants on chemical or structural criteria, the considerable interest which has been directed towards investigation of the dehydrations of this group of substances makes it convenient to discuss them as a single class.

Dehydration reactions are typically both endothermic and reversible. Reported kinetic characteristics for water release show various α_r-time relationships (see Section 3.3.1) and rate control has been ascribed to either interface reactions or to diffusion processes. Where water elimination occurs at an interface, this may be characterised by:

1. rapid, and perhaps complete, initial nucleation[3] on some or all surfaces, followed by advance of the coherent interface thus generated,

2. nucleation at specific surface sites, perhaps maintained during reaction, followed by growth or

3. (exceptionally) water elimination at existing crystal surfaces without growth [133].

A most important feature of dehydration reactions is the influence of the product phase on the ease of water escape, since such residual material invariably tends, to a greater or

[3] The *nucleation* process involves conversion of a small volume of reactant into a stable "particle" of product and continued reaction (*growth*) relationships, such as those shown in Table 3.3, which have found greatest application in kinetic analyses.

lesser extent, to diminish the rate of diffusion of water from the reaction interface, an effect that is often referred to as *impedance* [133]. In these reversible reactions, the adsorption of evolved water by adjacent dehydrated solid may significantly influence the measured overall reaction rate. Thus, in the formulation of a reaction mechanism, it is necessary to characterise all participating phases, particularly those in the immediate vicinity of the interface. In fact, $UO_2(NO_3)_2 \cdot 6H_2O$ shows an unusual behaviour in that there is no induction period to dehydration, the generation of specialized nuclei is apparently unnecessary since water evolution occurs by desorption at the existing crystal surfaces and no migratory interface is developed. Moreover, water elimination from a number of reactants proceeds through the intermediate formation of one or more lower hydrates. Both stepwise dehydration and reaction products delayed-recrystallization may be interrelated and vary with prevailing conditions, particularly the water vapour pressure (P_{H_2O}). From a kinetic point of view, the strength of adsorption of water on the product solid, which is in equilibrium both with water at the interface and water vapour in the surrounding atmosphere, is expected to vary with surface coverage, since surface bonding forces will probably be perturbed when adsorbed molecules occupy adjoining sites. It is believed that the energy barriers to water movement are influenced by the configuration of water molecules, but a quantitative treatment is not possible due to the absence of the necessary quantitative information concerning the sizes, spacings and dispositions of species at the interface [133].

Product phase recrystallization is facilitated by water vapour and is thus dependent on P_{H_2O} which exerts an influence over structural reorganization, leading to development of cracks, channels and pores through which water may escape from the reaction interface. With the possibility that behaviour is sensitive to P_{H_2O} and that intermediate phases of variable crystallite sizes may be formed, it is necessary to exercise great care in propounding mechanisms from rate measurements for the overall change [133]. In fact, during dehydration in high vacuum, the water molecules leave the interface without hindrance, passing easily through the product, which may be unstable, amorphous or pseudo-morphous. At low P_{H_2O}, water may be adsorbed on the walls of narrow capillaries and the escape of further water through these channels of molecular dimensions is impeded. The availability of water is sufficient to promote the formation of a crystalline product by a nucleation and growth process, schematically represented in figure 7.3.

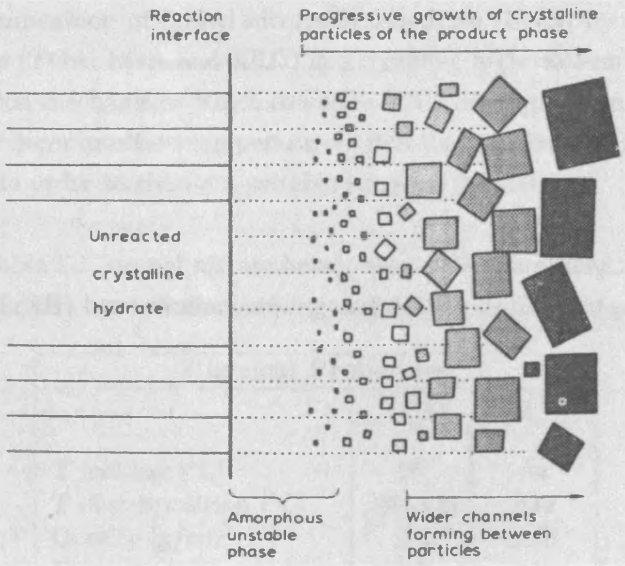

Fig. 7.3: Schematic representation of dehydration followed by recrystallization of the product phase behind the advancing interface. After [133].

At higher values of P_{H_2O}, the increased rate of the reverse reaction results in a progressive diminution in the net rate of water loss, becoming zero at equilibrium.

Early (ca. 1930) dehydration studies used gravimetric methods, often combined with photo-micrography. Allowance for self-cooling of these endothermic reactions was usually made and the influence of water vapour pressure in controlling reaction rates was appreciated. These techniques have since been supplemented by X-ray diffraction, thermal analysis, infrared spectroscopy, etc. Results have been interpreted with due regard to phase stability diagrams (P_{H_2O}, T), although there are difficulties of interpretation, concerned, for instance, with the effect of heating rate on the detection and characterisation of intermediate hydrates and the thermal consequences of melting and/or condensation of water, followed by its subsequent evaporation.

Franklin and Flanagan [182] have studied dehydration kinetics of uranyl nitrate hexahydrate (abbr. UNH) single crystals under vacuum. They observed a typical sequential transformation of UNH into $UO_2(NO_3)_2$, which occurred following dehydration steps. The authors also noted linear dependence of dehydration on water vapour pressure. Other studies have been addressed to the investigation of UNH decomposition, which are reported elsewhere [183], but the results have been unable to explain the complex multistep weight loss profiles observed during TGA as well as provide the thermo-kinetic investigation on decomposition of UNH at temperatures beyond 1000 K.

Recently, Dash et al. [183] accomplished an extensive investigation on the temperature

programmed decomposition of uranyl nitrate hexahydrate (UNH) by carrying out accurate measurements (TGA, EGA and XRD) in a dynamic high vacuum environment. The complex dehydration mechanisms which drive the UNH decomposition were identified, as well as the critical decomposition temperatures. Results from Dash et al. [183] have been used in this work in order to choose a suitable simulant for UNH.

As indicated by Table 7.1, uranyl nitrate hexahyrate (UNH) and magnesium nitrate hexahydrate (abbr. MgNH) have similar melting and decomposition temperatures.

Physical Properties		
	UNH	**MgNH**
T melting [°C]	90	89
T decomposition [°C]	280-300	330
Density [g/cm^3]	2.3	1.46
Viscosity [cp]	2-3	-

Tab. 7.1: Characteristic physical properties of UNH and MgNH.

In order to qualitatively define the critical temperatures and the relevant stages at which decomposition of MgNH take place, thermogravimetric analysis (TGA) has been carried out over two samples of material. The temperature was raised up to 350 °C at a rate of 4 and 10 °C/min respectively, see figure 7.4, using air as the carrier gas at atmospheric pressure.

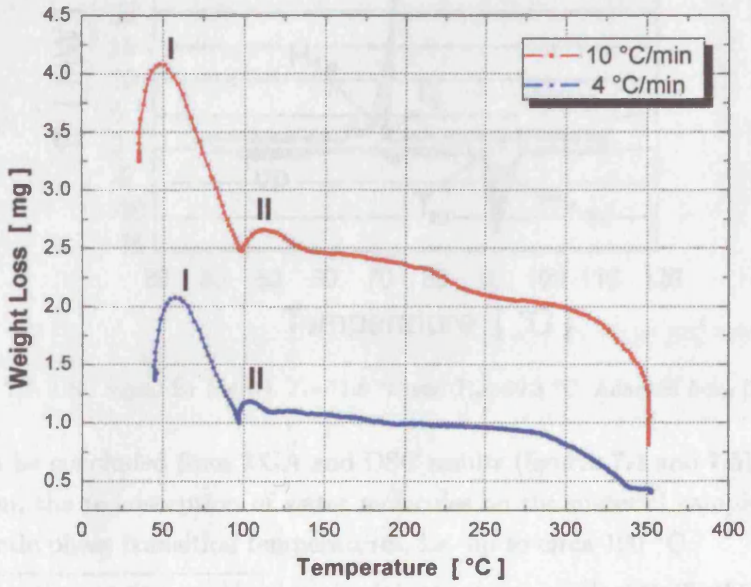

Fig. 7.4: Results from temperature programmed gravimetric analysis (TGA) carried out at different increasing rates for two MgNH samples of different initial weight.

The curves obtained from TGA, figure 7.4, exhibited similar trends and thus it was concluded that the decomposition reaction for both samples of MgNH occurs, at these experimental conditions, through the same multistep mechanisms, regardless of the temperature program (i.e. the rate at which temperature is raised during analysis)[4].
Both results showed two characteristic peaks (indicated with **I** and **II** in figure 7.4), which represent the physical re-adsorption of water molecules from the surrounding environment over the reacting material. Moreover, such a phenomenon was observed in a specific range of temperatures, i.e. between 60 and 70 °C for peak **I** and between 90 and 100 °C for peak **II**. Nagano et al. [184] have studied the melting temperature, T_m, heat of fusion, H_{f-m}, solidification temperature, T_s and heat of solidification, H_{f-s}, of magnesium nitrate hexahydrate by differential scanning calorimetry (DSC). Their results, see figure 7.5, showed two characteristic phase transitions:

1. between 60 and 70 °C the fused crystals of MgNH change phase to become solid and the heat of solidification is $H_{f-s} = 150mJ/mg$,
2. between 90 and 100 °C the solid solution changes phase to become liquid again. The melting heat is $H_{f-m} = 150mJ/mg$

At temperatures higher than 100 °C decomposition of MgNH proceeds as a dry solid phase.

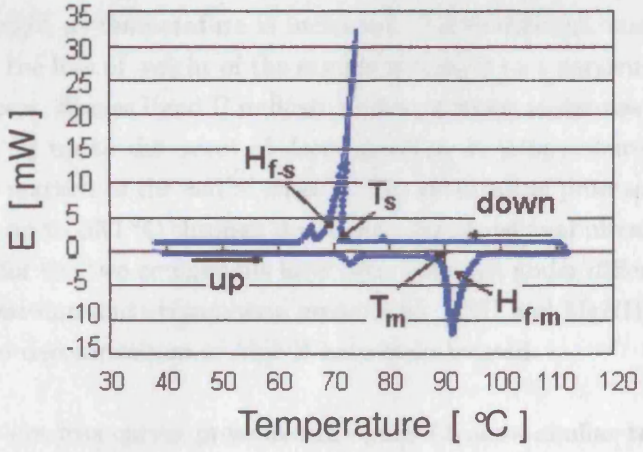

Fig. 7.5: DSC signal for MgNH. T_s=71.8 °C and T_m=89.3 °C. Adapted from [184].

Hence, it can be concluded from TGA and DSC results (figures 7.4 and 7.5) that, during decomposition, the re-adsorption of water molecules on the material sample occurs only at characteristic phase transition temperatures, i.e. up to circa 100 °C.

[4] A third TG analysis (not reported here) was carried out over one sample of MgNH (1.95 mg in weight) by increasing temperature at a rate of 30 °C/min. Results showed a steep weight loss profile characterised by the absence of the two peaks exhibited by previous thermograms. It was impossible to ascertain any critical decomposition temperature and, in fact, it was concluded that operating TGA at heating rates greater than 10 °C/min can produce useless results for the scope of this investigation.

Results obtained from TGA carried out at 10 °C/min over a MgNH sample were adjusted by eliminating the water re-adsorption contribution and compared with weight loss data for UNH available from literature [183], as shown in figure 7.6.

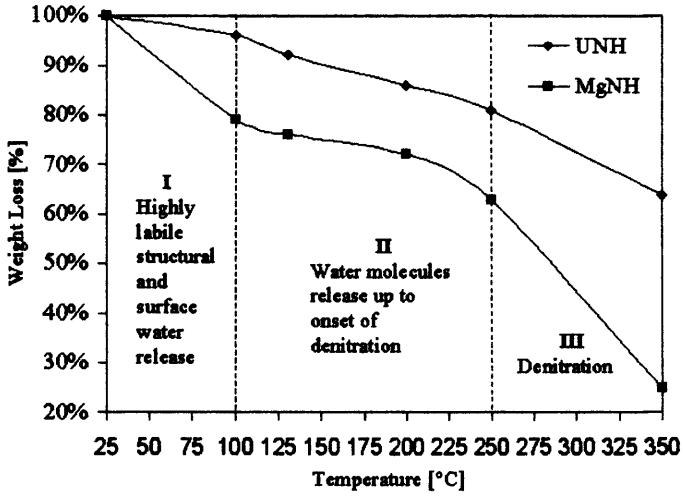

Fig. 7.6: Loss of weight for MgNH and UNH during decomposition

The curves illustrated in figure 7.6 represent the actual loss of weight in respect to the initial sample weight as temperature is increased. Three different zones can be roughly identified, where the loss of weight of the sample is related to a particular stage of the decomposition process. Stages I and II indicate release of water molecules, from highly labile structural water (I) up to the onset of decomposition at temperatures ranging between 220-250 °C, thus marked as the end of stage II. The denitration process takes place at 250 °C and develops up to 350 °C through decomposition of residual nitrate (III). Hence, although the data for the two compounds have been obtained under different environmental conditions (i.e. vacuum and atmospheric pressure for UNH and MgNH, respectively), the different stages of decomposition of MgNH have been located.

Although the weight loss curves presented in figure 7.6 show similar trends, it should be observed that the loss of weight of the MgNH, which occurs at all stages of decomposition, is somewhat higher than the behaviour shown by UNH. This can be explained as follows:

- Despite UNH and MgNH having similar physical properties, they differ in what is the type of chemical structure:

UNH $2UO_2(NO_3)_2 \cdot 6H_2O \rightarrow 2UO_3 + 4NO_2 + 12H_2O + O_2$

MgNH $Mg(NO_3)_2 \cdot 6H_2O \rightarrow$?

In the UNH formula, Uranium is bonded to the nitrate term, NO_3, through its oxide, UO_2, whilst, at the end of decomposition, solid Uranium trioxide, UO_3, is formed; on the other hand, in the MgNH compound, Magnesium forms a direct bond with NO_3. Hence, it might be possible that during reaction the release of the nitrate term is somewhat facilitated by a "weaker" bond exhibited with magnesium. Thus, decomposition of MgNH, and therefore the loss of weight of the analysed sample, can straightforwardly proceed with absence of intermediate compounds, as occurs in the multistep decomposition of UNH. In addition, due to the lack of experimental studies on the decomposition of MgNH at high temperatures, it is not clear whether the final reaction product at 350 °C would be magnesium oxide (MgO), or a metastable compound of magnesium. Unfortunately, after carrying out an extensive literature survey, no final conclusions were reached, thus leaving this topic for future investigation. It will be assumed in this work that complete denitrification occurs at 350 °C and, therefore, MgO will be addressed as the final product of reaction.

7.3 Materials and experimental method

The HTMFB was employed in this investigation to measure the force required to rupture a material bridge/neck formed between a pair of particles and to study the thermal and mechanical properties of the particles after coating their surfaces with different volumes of liquid MgNH. The force measurement detail was shown in figure 5.4, Section 5.1.1 of this thesis.

7.3.1 Thermo-mechanical tests of coated primary particles

Single glass ballottini particles of 150 μm diameter were glued onto the tip of pre-shaped micro-pipettes. The particles were subsequently coated with MgNH using the technique shown in figure 7.7. One particle-micro-pipette was chosen, among those prepared, as the "feeding" set-up: a small amount of MgNH crystals was placed onto a microscope glass slide and heated up to nearly 50 °C by means of an electrical heater, stage **I** in figure 7.7. At such a temperature, the MgNH crystals were found to be in a semi-solid phase and deposition onto the particle was assisted by gently touching and withdrawing the material with the micro-pipette tip. As soon as the MgNH 'solution' cooled a few degrees, the material was perfectly adhered, by re-solidification, onto the particle surface.

The "feeding" pipette thus obtained was placed inside the heating element of the HTMFB (not shown in the figure) and approached, until contact distance was reached, to a pre-mounted virgin glass particle by means of micromanipulation, stage **II** in figure 7.7.

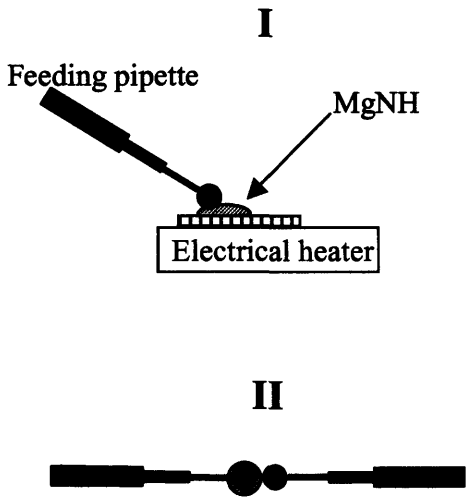

Fig. 7.7: Experimental technique used for coating a 150 μm diameter glass particle. In stage **I** a small amount of MgNH was adhered on to the surface of a glass particle. The feeding particle (left) was then aligned inside the heating element of the HTMFB (not shown) with a virgin glass sphere (right), stage **II**.

By operating with the potentiometer, voltage was provided to the heating element and, therefore, temperature raised until the solid MgNH, which was deposited on the feeding particle, became liquid and slipped onto the facing glass particle according to the mechanism explained in Appendix G. If enough feeding material had been collected by the feeding pipette-particle system during stage **I** then the virgin particle would be entirely covered by liquid MgNH and liquid reservoirs would form at the particle-pipette junctions. The whole operation and the coating conditions of the virgin particles were monitored under the microscope objective.

After optimal coating was achieved, the feeding pipette was removed from the heating element while the coated particle was kept at a constant temperature of 70-75 °C (i.e. the temperature at which the liquid MgNH changes phase to become solid). The temperature was subsequently raised up to 350 °C in order to obtain thin (less than 5 μm thickness) layers of magnesium oxide on its surface, figure 7.8. Moreover, deposition and formation of solid magnesium oxide at the particle-pipette junctions, see figure 7.8, had the advantage of creating an adhesive bond between the pipette and the particle that did not melt at the interaction temperatures used (up to 350 °C).

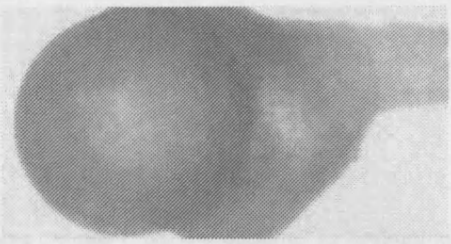

Fig. 7.8: Primary particle ($d_p \approx 150\mu$m diameter) attached to the tip of the micro-pipette.

This procedure was carried out to simulate the wetting of the decomposed oxide solid primary particle by the fresh nitrate liquid feed in the spray zone of the fluidised bed reactor (see next section), as well as allowing for the growth of the particles by further addition of the nitrate. In fact, such a procedure proved to be of great convenience to this investigation: first the porosity of the particle was kept low, which was useful, as explained here after, when simulating over-wetting conditions; this also allowed further study on changes of the particle surface properties upon addition of coating material. Second, by following the same experimental technique explained above, the thin porous layer allowed small droplets of MgNH (which is a liquid at 90 °C) to be added onto the coated primary particles without dripping, as occurred with the glass surfaces. Once the liquid covered the particle's surface, temperature was raised by means of the potentiometer up to the solidification point of the coating salt solution (i.e. 100 °C). Hence, size enlargement of the primary particle was both achieved and controlled by routinely adding liquid followed by partial drying, see figure 7.9.

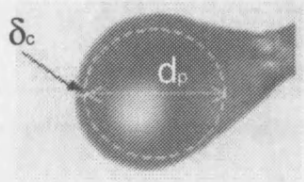

Fig. 7.9: Primary particle as it appears after coating with MgNH. d_p is the primary particle diameter and δ_c is the coating thickness.

The thickness δ_c of the coating layer was calculated at the point of particle contact, see figure 7.10, through images superimposition, obtained with a dedicated image analysis software (see Section 5.1.6.1) prior to and after coating.The reason for following this procedure lies in the fact that the thermo-mechanical properties being investigated depend on the local thickness of coating material; it has therefore been assumed that such properties extend to the whole particle surface, whose theoretical coating thickness is δ_c.

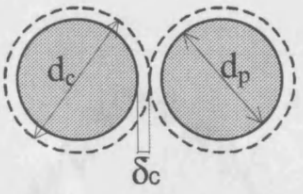

Fig. 7.10: The equivalent coating diameter, d_c, was obtained by evaluation of the coating thickness, δ_c, at the point of particle contact.

Prior to each test, the pair of particles was held apart within the heating element and further dried at 150 °C in order to allow any excess surface water to be released; moreover, "touch and separate" cycles were performed in order to confirm the absence of free superficial liquid (i.e. stable liquid solution), which could lead to the development of a material bridge upon contact. Since the dimensional changes in d_c $(= d_p + \delta_c)$ were negligible between 90 and 150 °C, the volume of coating material, V_c, was considered equal to the volume of the coating liquid; hence, the non-dimensional parameter φ, defined as the ratio between the volume of coating liquid (calculated from evaluation of d_c) to twice the volume of the primary particle (V_p obtained from measurement of d_p), could be evaluated for each experimental test, see Table 7.2.

Test	d_c [μm]	$\varphi = V_c/2V_p$
1	180	0.36
2	182	0.39
3	250	1.81
4	300	3.5
5	375	7.31
6	450	13

Tab. 7.2: Thermo-mechanical properties were investigated for increasing coating layers.

By operating the micromanipulators, the two coated particles were brought together until zero separation distance was obtained, as shown schematically in figures 7.10 and 5.4. In order to simulate the physical conditions in a fluidised bed, an initial constant load L as low as 200 μN was applied for all runs. This also ensured good reproducibility of the results as shown in figure 7.11.

Calibration of the experimental temperature, within a defined location of the heating element, was performed prior to each experiment (see Appendix C). Temperature was raised from 150 °C in steps of 3 °C/min, while elongation or contraction ($d\ell$) of the sample was recorded and monitored simultaneously.

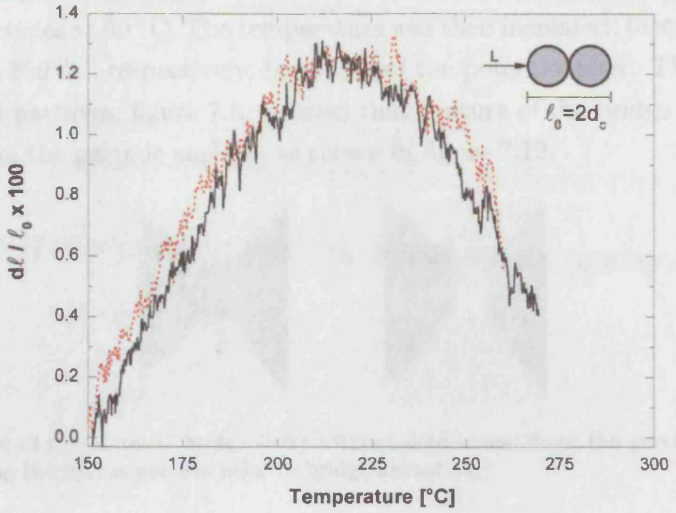

Fig. 7.11: Dilation vs Temperature thermogram: $\varphi = 0.36$ and 0.39 (red dotted line).

By controlling the gradual increase of the experimental temperature and considering the relatively low reactant volumes involved in the tests, it was assumed here that isothermal conditions were respected for all the particle systems investigated. Clearly, the thermal expansion of the glass core contributes to the dilatation of the sample to some extent, especially for those systems characterized by low values of δ_c. However, by re-arranging the dilatometry results obtained by Compo et al. [109] for a sample of glass particles of 190 μm diameter, it was found that, for Tests 1 and 2, the glass contribution to total expansion was less than 10%.

7.3.2 *Direct observation and force measurement*

By monitoring the contraction-expansion curves and observing the particle-particle interface, it was possible to record the temperature at which softening or collapse of the particle surfaces takes place. In the former case, the stickiness developed by neck formation was measured by rupture tests (see Section 5.1.1).

The other possible cause of agglomeration, which is enhanced by over-wetting, is the generation of liquid bridges between particles. Here, the force resulting from partial and complete decomposition of a pendular liquid bridge of MgNH, which has been initially formed between the particles, has been measured using the following experimental procedure.

After placing a small amount of MgNH onto a primary particle surface by using the tech-

nique shown in figure 7.7, a liquid bridge was formed within the heating element between two primary particles at 90 °C. The temperature was then increased, in steps of 10 °C/min, to 100, 250 and 350 °C, respectively, by means of the potentiometer. The employment of the coated glass particles, figure 7.8, ensured that rupture of the bridge occurred without detachment from the particle surface, as shown in figure 7.12.

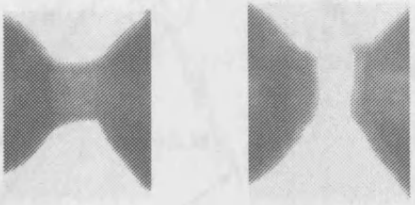

Fig. 7.12: Rupture of the material bridge (left) without detachment from the particle surface (right) is achieved by coating the parent particle prior to bridge formation.

Particles were held at a distance not greater than 30% of their diameter. The amount of initial liquid bridge was back-calculated at the end of each experiment by means of dedicated image analysis software, which helped to approximate the bridge profile with a polynomial curve; the liquid bridge volume was then evaluated by integration carried out using the Mathematica software package. The liquid bridge was then compared to the particle volume by defining:

$$\varphi' = 2\varphi = \frac{V}{V_p} \tag{7.2}$$

where V and V_p are the initial bridge and particle volume respectively.

During each experiment, changes in the geometry of the bridge were monitored and a few minutes after reaching the programmed temperature, rupture of the bridge was obtained by axial displacement via the linear actuator and the relevant rupture force, F, was measured and calculated through the equation shown in figure 5.4.

7.4 Results and discussion

The thermogram illustrated in figure 7.13 reports the Dilation vs Temperature curves obtained for the different wetting conditions. The initial considerable expansion recorded for all the tested samples is indicating, as explained by Galwey [185], a reactant structure in which H_2O vacancies are highly mobile and water molecules rapidly reoccupy surface sites vacated by desorption. In fact, water desorption appears to be a fundamental stage of decomposition, which affects the mechanical and surface properties of the coated particle.

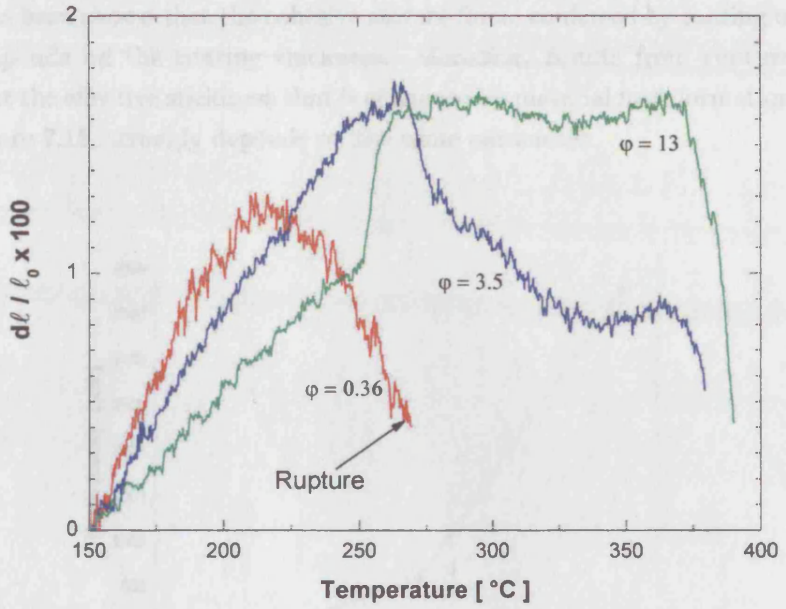

Fig. 7.13: Dilation curves obtained from Tests 1, 4 and 6 (see Table 7.2).

In the case of low amounts of coating material (i.e. $\varphi = 0.36$), a global weakening of the surface cohesion force was observed during water desorption (in both Tests 1 and 2 collapse/rupture of the thin coating layer occurred). This can be explained by the following mechanism: according to the amount of coating material, a superficial crust is formed upon drying, which is strengthened by both the diffusion of crystalline water from the bulk of the particle and the subsequent rearrangement of the crystalline structure.

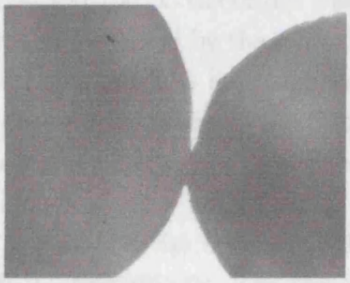

Fig. 7.14: Test 6: neck formation between coated primary particles.

Structural weakening is also experienced for moderate values of φ in the completion stage of denitrification. This is associated with the high loss of weight that occurs at temperatures from 250 up to 350 °C, as shown in figure 7.6. In the case of a large amount of coating material (i.e. $\varphi = 13$ in figure 7.13), the structural re-organization of the particle surface results, at the point of contact between the particles, with the formation of a material neck, as shown in figure 7.14. This is typically associated with *swelling*, followed by a *plateau* region in the dilation curve.

So far, it has been shown that the cohesive surface force, conferred by coating of a primary particle, depends on the coating thickness. Moreover, results from rupture tests also indicate that the effective stickiness that is enhanced by material neck formation at particle contact, figure 7.15, strongly depends on the same parameter.

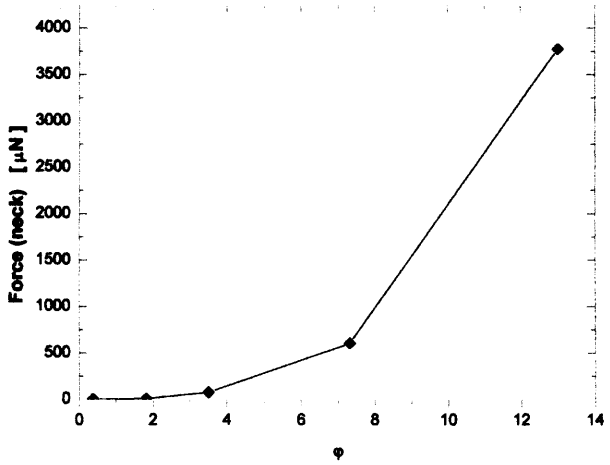

Fig. 7.15: Experimental force measured from rupture tests in the case of neck formation.

These conclusions were also confirmed by the results obtained from rupture tests illustrated in Section 7.3.2. Direct observation of the decomposition of MgNH, by monitoring the shape of a pendular material bridge formed between two particles, revealed three main physical-state stages: between 90 and 100 °C the bridge was found to exist as a semi-solid state. At 100 °C, its geometry was preserved by the formation of a thin superficial crust, figure 7.12 (left). When the temperature was approximately 250 °C, the denitrification process could be monitored by rapid brightening of the bridge: depending on each experiment, it was possible to observe some crater-like vacancies on its surface.

The chart, shown in figure 7.16, reports the experimental values for the rupture force measured at 100, 250 and 350 °C, respectively. The trend lines plotted in the diagram indicate a rise of the adhesive force with the volume of the solid bridge. At any of the experimental temperatures, increasing $\varphi\prime$ of one order of magnitude enhanced forces by nearly one order of magnitude.

The effect of temperature over the rupture force seems to maintain the same proportionality when comparing the experimental values at 100 and 350 °C respectively. The adhesiveness resulting from the denitration stage rupture tests, which takes place at 250 °C, is comparable to the values measured at 350 °C.

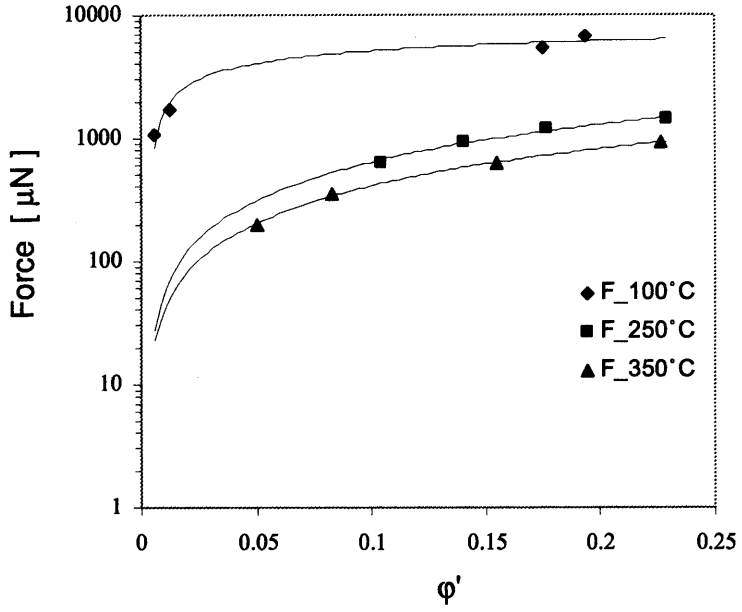

Fig. 7.16: Experimental force measured from rupture tests in the case of material bridge formation.

In light of these results, some considerations can be drawn here:

1. In the early stages of the decomposition of MgNH, the adhesive force, developed between particles by the formation of material bridges, is one order of magnitude stronger in respect to the values obtained at the end of the reaction. Dehydration of water is then assumed the first controlling step in enhancing the formation of small agglomerates. In fact, partially reacted material bridges could have enough strength to withstand the disruptive forces developed during fluidisation.

2. Although the adhesiveness developed by completely decomposed material bridges is much weaker in respect to those just partially reacted, the amount of initial liquid volume is still playing an important role in the agglomerate formation in two ways. Stickiness of the particle surfaces is enhanced by the operative temperature, or the possible thermal gradients within the bed, and largely depends on the volume of unreacted deposited material. The ratio between the average droplet size sprayed over the bed contents and the average primary particle diameter is an important operative parameter; in fact, changes in its value can lead the particle size evolution of the process towards the formation of larger agglomerates and, eventually, defluidisation and shut down of the reactor.

8. CONCLUSIONS AND FUTURE WORK

This thesis has focused on improving the understanding of the relationship between particle surface properties and liquid/solid bridges characteristics and has discussed the consequences these phenomena may have on agglomeration and defluidisation processes at high temperatures.

Prediction of the fluidisation behaviour at high temperature is of major importance given that most of the industrial processes which use fluidised beds are operated at temperatures well above ambient. The aim of this work, which was sponsored by British Nuclear Fuels, was to develop a novel device based on a micro-manipulation technique, the HTMFB, capable of investigating the types of particle-particle interactions that can occur during fluidisation at high temperature.

In particular, this work deals with those interactions enhanced by the presence of a material bridge. In fact, the formation of a liquid/solid bond can be a desired feature of the fluidisation process (e.g. size enlargement, granulation, etc.), usually obtained by spraying a liquid binder over the bed contents, or a non-desired phenomenon, which mainly occurs by temperature induced surface modification (e.g. sintering).

In the former case, models to predict agglomerate growth have been developed in the literature at ambient conditions by looking both at the properties of the liquid binder, such as its viscosity and surface tension, and the strength as well as the energy required to rupture large agglomerates in order to avoid defluidisation. In addition, model fluid-beds have been employed to study the effect of process variables, such as the liquid content and viscosity, on fluidisation by scaling up the micro-scale interactions that occur between particles to multi-body systems. However, in many industrial processes, which involve the spraying of a liquid binder over the bed contents either at ambient or elevated temperature, particles of different surface properties can exhibit and develop different wetting behaviour and interparticle forces, which, ultimately, can cause problems in the final composition of the product, since some species can be agglomerated at the expense of others. Despite the fact that the wetting behaviour of a species can be throughly investigated and many studies have concentrated on the geometry and adhesiveness of liquid bridges formed between well-wetted particles, similar studies regarding either particles exhibiting differences in wetting behaviour or the force of adhesion exerted by reactive materials have

not received the same attention in the literature.

8.1 Conclusions

The experimental work described in this thesis starts, in fact, from the investigation of the wetting behaviour of real particles by means of a micro-manipulation technique. The case study presented in Chapter 3 has given some useful indications for liquid binder selection in a real process performed in a gaseous bulk medium. Liquid bridge forces, wettability and post-rupture binder distribution were tested between paracetamol crystals and different liquid binders commonly used in the pharmaceutical industry (PVP, HPMC) using a Micro Force Balance (MFB). Both the binders have high wettability towards paracetamol, with PVP exhibiting the highest liquid bridge forces, whilst HPMC produced a better binder distribution. Data presented in literature [81] on the final strength of paracetamol crystals either granulated with PVP or HPMC showed better mechanical properties in favour of HPMC. In light of the observations using the Micro-Force Balance (MFB), it seems that the liquid binder distribution inside a granule is a much more important parameter than the particle-particle adhesion. It can be concluded that the better distribution of the HPMC liquid binder confers, at the moment of drying, a more homogeneously distributed matrix of solid bridges, which ultimately increases the mechanical properties of the agglomerate.

During a high temperature fluidisation process, the properties that characterise both the liquid-particle and particle-particle interactions (i.e. spreadability, wetting, adhesion, cohesion, etc.) can change according to the operative temperature, thus affecting not only the performance of the process but also the quality of fluidisation itself. Hence, despite the MFB being a very promising tool to study such changes, it has the main limitation that all the measurements and observations are carried out at ambient conditions. Thus, in light of the experience in micro-manipulation, which was gained by the author through using the MFB, a novel apparatus was designed and developed at UCL, which is termed a High Temperature Micro-Force Balance.

The work carried out using the HTMFB has shown that fundamental investigations of particle-binder and particle-particle interactions are a very powerful tool to understanding agglomeration during fluidisation. Direct observations of the mechanisms responsible for particle interactions (obtained at the same size scale of a technological process) help in the understanding of the phenomena behind defluidisation without introducing side effects, such as gravity. Among the mechanisms that can be investigated using the HTMFB, the measurements, which can be carried out at temperatures as high as 1000 °C, of the liquid/solid bridge strength (either axial or of shear), the advancing and receding contact angles (liquid-to-particle), the liquid bridge drying rate, the adhesion/cohesion exerted by

a reactive liquid over a pair of particles, the particle shape and porosity as well as the coating thickness, all have an impact on the high temperature fluidisation process.

The conventional analytical techniques (e.g. dilatometry, thermogravimetric analysis, etc) employed by other researchers in order to characterise the fluid bed material at high temperatures can integrate data obtained using the HTMFB to obtain a clear picture of the phenomena behind agglomeration both at a macro (physical and mechanical properties) and micro (particle interactions) scale. This was clearly shown by the results obtained from the experimental investigation described in Chapter 6.

With regard to the fluidisation quality shown by the E-cat catalyst at high temperatures, Lettieri [6] concluded that high temperature conditions can cause sudden changes in the physical properties of the particles, enhancing the role of the interparticle forces (IPFs) over the hydrodynamic forces (HDFs). It was also added that a quantification of the magnitude of the IPFs remains to be accomplished, since quantifying the relative importance of the HDFs and IPFs is crucial in order to model/simulate the realistic fluid-bed behaviour. Moreover, Lettieri [6] stated, in the thesis conclusions, that within the context of a quantification of the interparticle forces at elevated temperature, the results obtained from thermomechanical analysis should be exploited further, given that a clear correspondence was found between temperatures at which modifications in the particles physical properties occurred and changes in the fluidisation behaviour were observed.

In light of the conclusions drawn by Lettieri [6], some questions naturally arise, such as: Can the IPFs be identified and quantified with the conventional analytical tools? Is it only the magnitude of the IPFs that is responsible for the fluidisation quality? or, Should a realistic fluid-bed model take into account only the relative magnitude of IPFs over HDFs? Are the actual techniques of analysis (e.g. thermomechanical, thermogravimetric, SEM, etc.) of the fluid-bed material sufficiently explanatory to establish a correspondence between the quality of fluidisation and the particles physical properties?

The use of the HTMFB, employed as a tool of investigation for the physical properties of the E-cat material, allowed a precise answer to most of these questions from a micro-scale point of view. Findings from the experimental campaign, described in Chapter 6, have demonstrated the diverse nature of the material (E-cat) employed in the fluidisation tests carried out by Lettieri [6]. However, if on one hand Lettieri correctly found that the interparticle forces are enhanced by increasing the process temperature, as was also confirmed, in this work, by observation of the change of phase of large E-cat particles (i.e. $\succ 250\mu m$ in diameter), on the other hand, the crucial factors responsible for the different fluidisation behaviours between ambient and high temperature should be addressed to the spreading and the rate of drying of the liquid bonds formed within the solid bed, rather than to an

effective increase of the strength of such bonds with temperature. As confirmation of this, fluidisation tests have shown that a state of fluidisation of the E-cat bed could be achieved at temperatures as low as 100 °C, whereas measurements of the adhesion enhanced by a liquid bridge before drying indicate (see figure 6.23) a trend with a maximum overall force at 90-100 °C and a minimum at higher temperatures (circa 140-150 °C). Moreover, from the analysis of the contact angles formed by the liquid onto the solid particles it was concluded that, despite the high adhesion force that a liquid bond could exert at such temperature (i.e. 100 °C), spreading of the liquid is hampered and so is the development of large IPFs within the bed. Clearly, the dominant effect of the IPFs supposed by Lettieri [6] can be addressed to the effect of drying of wet agglomerates: in fact, the higher the operative temperature the higher the tendency of the liquid to spread among the solids (favoured by a decrease of its viscosity and an increase of its spreadability) and to form large wet agglomerates. Moreover, the higher the temperature the higher the drying rate and therefore the chance for these agglomerates to stick together before rupture and to form large lumps within the bed, which can lead to defluidisation. Hence, quantification of the IPFs, in this case, assumes minor importance in the description of the fluid bed model, since other parameters should be taken into account (i.e. spreadability and drying rate of the liquid) to describe the fluidisation behaviour of such a material at high temperatures.

The experimental campaign described in Chapter 6 has also shed some light on the effective capability of modern off-line particle characterisation techniques to define both the physical and chemical surface properties of the fluid-bed material, as well as to establish a direct correspondence between the changes in these properties with temperature and the relevant quality of fluidisation. Generally, at ambient conditions, investigations of wettability and spreadability can be successfully obtained on samples of larger dimensions in the cm scale. Contact angle measurements can be achieved by either using the Wilhelmy-plate technique or by direct observation of liquid binder deposited on large samples. Moreover, solid-particle adhesiveness can be measured using a process tensiometer. However, in this particular case study, none of these techniques could be employed, mainly because of the limited sizes of the sampled material and the occurrence of a high temperature phase-change. Furthermore, the thermogram validation of E-cat samples, obtained by using the HTMFB, has led the author to conclude that, despite the fact that dilatometry has proved to be a useful technique for the determination of a material's sintering temperature, it can offer a misleading interpretation when samples of non-pure materials are analysed. As a matter of fact, this can lead to non trivial consequences on the interpretation and "prediction" of the fluid-bed behaviour. Thus, by means of the HTMFB it has been possible to provide unique information, through direct observation and force measurement techniques, on the E-cat catalyst surface behaviour at high temperature; moreover, a complete explanation of the mechanisms of particle agglomeration was given at a micro-scale and the parameters responsible for the defluidisation of the process were discussed.

A different experimental approach was undertaken in Chapter 7: here, quantification of the particle-particle interactions in the presence of a solid bond was necessary in order to elucidate the mechanisms of agglomeration of Uranium trioxide powder, which is re-generated from spent nuclear fuel and processed by spray-drying through fluidised beds at high temperature.

The Nuclear industry, in fact, belongs to the large variety of industries dealing with both the processing and handling of bulk powders. Considering the specificity of the materials at stake, any problem with powder flow and packing can be difficult to address. Difficulties in the understanding the uranic powder reside in the characterisation of its flowing properties.

For instance, bulk powder testing (rotating drums, shear cells) have been used, together with non-intrusive on-line measurement techniques, to characterise the flowing properties; however, these tests are nevertheless time consuming, difficult to set up and are not sufficient to understand all powder flow mechanisms. Hence, an alternative approach consists of investigating both the role of individual particles in the bulk powder behaviour and their tendency to form agglomerates.

One type of experimental approach to study the uranic bulk powder flow (developed in order to optimize the silo and hopper designs) was conducted at NSTS Springfield in collaboration with work at the University of Leeds and NSTS Sellafield. Such an investigation has become possible thanks to the parallel invention of atomic force measurement devices and increase in computer calculation power. The project's ultimate goal was to inject, in a well-chosen distinct element model (DEM) of a particulate system, the experimental data on the particle-particle and particle surface interactions and to validate the results by comparison with shear test measurements. Experimental data was obtained by means of atomic force microscopy on both model systems (spherical glass particles and plane mica surface) and real uranic particles; the study provided useful information for the analysis of the flowing properties of a powder, by highlighting the role of key parameters, such as contact radius or relative humidity.

In light of such promising results, the HTMFB was employed at UCL to investigate, on a micro-scale, the adhesiveness developed between particles and its dependency on major key process variables (i.e. temperature, volume of liquid), which can cause the formation of large agglomerates of uranic powder within the TDN reactors. By using, as a model material, glass particles coated with Magnesium Nitrate Hexahydrate (MgNH, used as a simulant for the Uranyl Nitrate Hexahydrate, UNH) it has been possible to quantify the strength exerted by solid bridges formed between a pair of particles (also named "primary" particles) when these bonds undergo a sequential step-decomposition at incresing

temperatures.

The experimental technique and set-up considered and developed for this investigation (see Chapter 7) have allowed, for the first time, the study and quantification of the sintering mechanisms that can occur during decomposition of the inorganic salts. By means of the HTMFB, unique information on the sinter neck formation was provided by means of direct observation and rupture tests. Results have shown the likelihood for a pair of particles to form a solid bond at high temperatures by simply being in contact and according to the initial volume of unreacted coating material (i.e. the amount of liquid necessary to uniformly coat a "primary" particle of a measured thickness).

From rupture tests carried out over pairs of "primary" particles, adhesion of a solid bond was quantified in respect to its critical decomposition temperatures and volume; special diagrams have thus indicated a trend where the strength of adhesion decreases with increasing temperature, until completion of the decomposition reaction. It was therefore concluded that interparticle forces can be enhanced, within the fluidised bed, by formation of solid bridges made of partially reacted material, but, due to the decreasing adhesiveness exerted during its decomposition, only relatively large bridges can sustain the disruptive hydrodynamic forces developed by the fluidisation process. These results have clearly indicated that, if strong IPFs (and defluidisation) occur within the TDN reactor during operation, then the main causes are due to the average amount of the material sprayed over the bed contents (i.e. the average volume of a sprayed droplet of reacting material) or, in other words, to the over-wetting conditions of the fluid bed. The major outcome of this investigation has seen BNFL undertaking a new project that involves a new design and subsequent substitution of the actual spray nozzle mounted within the TDN reactor, which is capable of spraying droplets of UNH of smaller diameters over the fluidised uranic powder.

8.2 Future work

The different experimental campaigns that were carried out during this work have clearly demonstrated the important effect that temperature and wettability can have on the fluidisation behaviour of the various materials tested. It has also been shown that the development of a unique device, which is capable of investigating the effects of these parameters on the particle-particle interactions, was necessary in order to understand the powder flow behaviour on a micro-scale.

The HTMFB can be employed whenever data integration is required from other methods of analysis (TMA, TGA, etc.), since unique information can be obtained through the direct observation and force measurement at high temperature. The High Temperature

Micro-Force Balance can also be employed as a precise dilatometer to achieve measurements of the coefficient of expansion or sintering temperatures of a wide range of materials: it allows, in fact, these measurements to be taken using only a pair of particles, avoiding the typical experimental errors concerning the size and shape of the analysed sample of material. Furthermore, a new design is being developed that will permit particle-particle interactions to be investigated at high temperatures within an insulated environment. An environmental chamber, to be mounted on the microscope stage, will permit to study the effect of humidity on certain particle-particle set-ups.

The use of the HTMFB is not restricted only to investigation of agglomeration / defluidisation problems, but also to elucidate other types of interactions, such as the mechanisms associated with caking during storage of certain materials (i.e. polymeric powder) and in the development of composite materials. In particular, much interest has been shown over the last few years in the development of wood/hemp fibre reinforced polymers. In fact, the compatibility between natural fibres and polymer matrices is described by the wettability or surface tension of the polymer on the fibre. These characteristics will govern the impregnation of a fibre assembly by the (normally) liquid polymer during processing to composites (process temperatures up to 160 °C). In general, there is a poor surface wetting of plant fibres by most thermoplastic polymers commonly used in composites. This can lead to the formation of ineffective interfaces between the fibre and matrix phases, with consequent problems such as poor stress transfer, small void spaces and debonding in the resulting composite materials. There seems at present to be no well-defined measurements of relevant wettability parameters for natural fibres and polymer matrices at high temperatures. In this regard, some preliminary tests (not described in this thesis) have been carried out, using the HTMFB, to study the wetting behaviour shown by different types of hemp fibres when wetted by melted PE particles (circa 300 μm in diameter).

The design of the HTMFB has shown fully improved features in respect to the previous MFB model. However, there are some drawbacks. First of all, the glass micropipettes are inadequate for carrying out experiments at temperatures higher than the glass softening and melting transitions. Hence, other materials have to be researched, which should meet the following requirements:

- micropipettes should have a low coefficient of thermal expansion as not to affect the high temperature measurements of the investigated set-up (particularly in the dilatometry analysis)
- in order to ensure the isothermal condition for the attached particles during experiment, the micropipettes should have a low thermal conductivity
- the micropipettes should be cheap, readily available and suitable for use with the

pipette puller (see Section 5.1.2.1)

Secondly, in order to reach high temperature values (say greater than 800 °C) within the interaction environment of the heating element, the separation distance between two consecutive turns of the coil must be reduced as well as its diameter; by modifying the coil geometry in such a way, the non-isothermal conditions and distortion effects caused by the presence of thermal gradients will be minimised (see Section 5.1.5 and Appendix C.1); on the other hand, the field of view required to monitor any particle-particle interactions will be substantially reduced, thus permitting only partial experimental observation and image analysis of the investigated system. Moreover, the actual set-up allows the use of microscope objectives with magnitude not greater than 20X, since, after this limit, the working distance of the objective decreases below the physical limit posed by the geometry of the coil. This means that if smaller particle systems (say particles of diameters lower than 30 μm) are being studied, then reduction of the coil geometry is required, which can be a problem in relation to the limited field of view.

Other limits of the HTMFB used in this work are the selection of a high temperature resistant glue and the difficulty experienced in measuring small adhesive forces, such as those exerted by liquid bridges of low surface tension and viscosity. In fact, although force measurements rely, theoretically, only on the spring constant of the flexo-strip assembly, the vibrations produced by the surrounding environment are nonetheless a major issue, since the oscillations transmitted to the flexure strips make the force readings useless under a certain limit. This problem was partially solved by sitting the rig on an anti-vibration table.

Future works should be directed to laboratory-scale high temperature agglomeration and fluidisation units to verify the properties of agglomerates and to establish scale up correlations between micro and macro-scale measurements, which provide further information on the bulk flow behaviour. Furthermore, experimental work should be dedicated to the study of models of prediction and development of defluidisation due to sintering mechanism. In this regard, unique dilatometry measurements on model materials, such as polyethylene beads, should be carried out by using the HTMFB and validated with results available from literature.

Particle surface chemistry, shape and porosity and liquid/solid bridges shear forces seem to have an important role in the high temperature fluidisation behaviour, which have not been investigated in the work reported in this thesis. Therefore they represent an interesting matter of study for future work.

APPENDIX

A. CALCULATED VALUES OF THE LIQUID BRIDGE VOLUME

In this section, the values for the volume of the liquid bridge, $V^* = V/(0.5d_p)^3$, calculated through numerical resolution of the Young-Laplace equation, are reported in function of both the half-filling angle, β, and the dimensionless interparticle distance, a/d_p. The constant mean curvature, $h^* = \Delta p a/2\gamma$, is also provided in Table A.1.

$\frac{a}{d_p} = 0.01$		h^*	V^*
β [°]	5	30.964	0.000423
	10	17.014	0.002470
	15	9.225	0.007824
	20	5.335	0.018701
	25	3.248	0.037479
	30	2.033	0.066512
	35	1.274	0.108184
	40	0.775	0.164500
	45	0.430	0.238165
	50	0.184	0.331261

$\frac{a}{d_p} = 0.05$		h^*	V^*
β [°]	-	-	-
	10	4.374	0.005131
	15	3.789	0.015463
	20	2.800	0.032776
	25	1.968	0.059084
	30	1.335	0.096766
	35	0.872	0.147901
	40	0.531	0.214869
	45	0.277	0.300088
	50	0.085	0.406243

$\frac{a}{d_p} = 0.1$		h^*	V^*
β [°]	5	-	-
	10	-	-
	15	1.007	0.015033
	20	1.258	0.040195
	25	1.041	0.075247
	30	0.765	0.123000
	35	0.512	0.185645
	40	0.297	0.265827
	45	0.123	0.365471
	50	-0.018	0.487755

$\frac{a}{d_p} = 0.2$		h^*	V^*
β [°]	5	-	-
	10	-	-
	15	-	-
	20	-	-
	25	-	-
	30	-0.040	0.124394
	35	-0.004	0.214445
	40	-0.048	0.321936
	45	-0.117	0.452644
	50	-0.184	0.608947

Tab. A.1: Numerical values of the liquid bridge dimensionless volume, V^*, obtained from resolution of the Young-Laplace equation.

B. PROCEDURE FOR FMA CALIBRATION

This appendix explains the technique used to calculate the flexibility of the Force Measurement Assembly (FMA) by evaluation of the overall spring (force) constant, K, of the pair of flexible sheets.

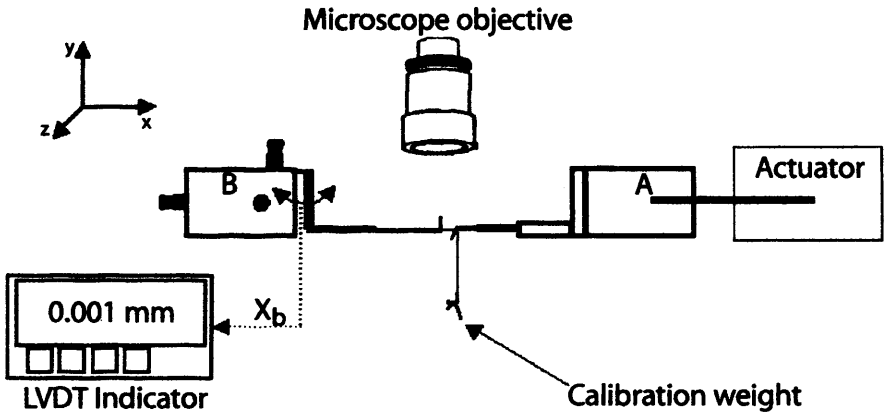

Fig. B.1: Set up for the calibration of the flexible sheets of the FMA.

To measure the spring constant of the acetate transparency sheets, two borosilicate glass tubes (Cole & Parmer, Saffron Walden, Essex, UK) were mounted onto micromanipulators B and A, respectively. As shown in figure B.1, the pipette mounted onto micromanipulator B has a 90° bend along the y direction, which was obtained by means of a mini gas torch; whereas the second pipette (i.e., the one fitted into micromanipulator A) has a 90° bend along the z direction.

A thin thread (drawn in red colour in figure B.1) was glued to the former pipette and passed over the bend of the second. A small reference weight (electrical nichrome wire, drawn in black colour in the figure), shaped as a hook, was glued to the other end of the thread; this ensured the orthogonal direction of the thread in respect to the pipette axis. The alignment of the pipettes along the x-axis and the microscope focus were adjusted until the pipettes and thread lay at the same height.

The small reference weight caused the two flexible sheets to shift a distance X_{b0}, which

was read on the LVDT indicator, see section 5.1.7.1. The indicator was then set to zero.[1]

Several calibration weights of small lengths of electrical nichrome wire were bent into horseshoe shapes and hung onto the hook. Their mass was measured to the nearest one thousandth of a gram using a balance and converted into a force, as shown in Table B.1. Their addition and removal was facilitated using long nosed tweezers. Each time a weight was hung in order to take the displacement measurement, some time was allowed to obtain a stable reading from the LVDT indicator. The same procedure was followed on removal of the calibration weight off the hook (i.e. time was allowed before taking further readings until the LVDT indicator displayed the reference zero). For each calibration weight, five consecutive readings were taken and the most recurrent deflection value was considered.

Calibration weight [g]	**F [μN]**	**Deflection, X_b [μm]**
0	0	0
0.004	39.240	5
0.007	68.670	7
0.0108	105.948	12
0.02	196.200	22
0.0312	306.072	30
0.0521	511.101	65
0.084	824.040	85

Tab. B.1: Deflection of the flexible sheets for each calibration weight.

According to Hooke's law, the slope calculated from linear fitting ($y = Kx$) of force data versus deflection, X_b, represents the overall spring constant of the flexible sheets, see figure B.2.

For the acetate transparency sheets used in this study, the value of the spring constant, K, was calculated as 9.0953 $\mu N/\mu m$. Such a value has been recently found to agree (K=5.7899 $\mu N/\mu m$), at least in the order of magnitude, with that obtained by alternative calibration measurements carried out at UCL for the same sheets geometry (but slightly different thickness) and material [186].

[1] The friction between the thread and the glass tubing was considered of negligible magnitude, thus the calibration set up can be assumed as an ideal pulley.

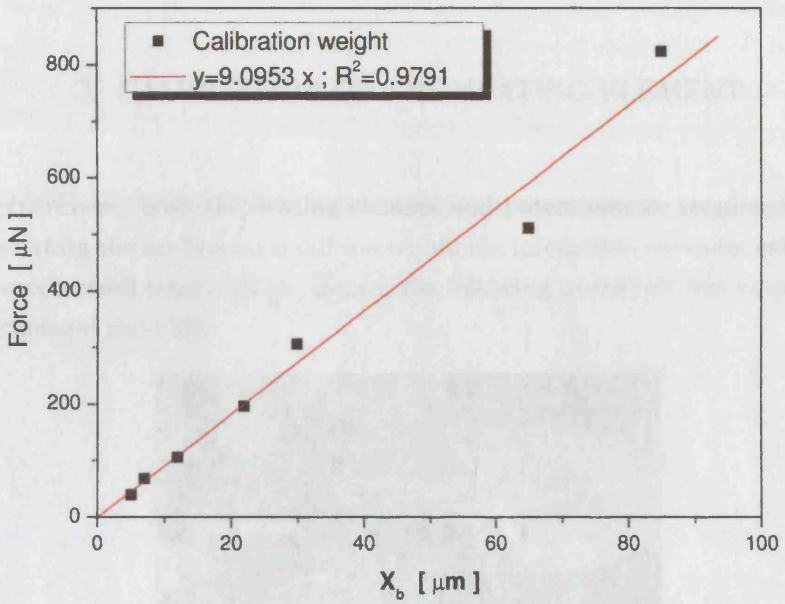

Fig. B.2: Calibration graph for the determination of the overall force constant of the acetate transparency flexible sheets.

C. CALIBRATION OF THE HEATING ELEMENT

Prior to experiment, both the heating element and potentiometer require calibration in order to ascertain the isothermal condition within the interaction environment and to control the experimental temperature. Hence, the following procedure was employed before each experimental campaign.

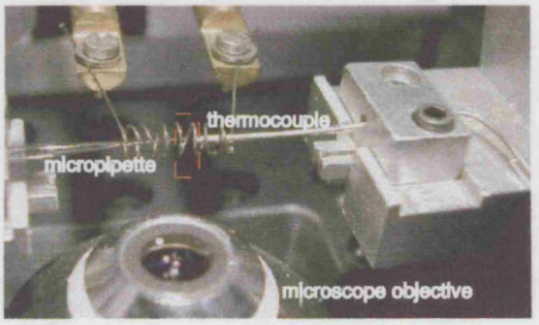

Fig. C.1: Set up for the calibration of the heating element and potentiometer (voltmeter).

As shown in figure C.1, a micropipette is mounted on the left hand micropositioner (indicated with B in figure 5.2) of the HTMFB and brought within the heating coil until the tip of the pipette is equi-distant from the centre of two consecutive turns of the platinum wire; in fact, this location represents the centre of the environment where the high temperature interactions will take place (red dashed box in figure C.1). Fine adjustment of its position (including the alignment along the central axis) is obtained by means of a micrometer graticule, which is contained in one of the eyepieces of the microscope (see section 5.1.6). A type K ($NiCr^{+}$-$NiAl^{-}$) cylindrical thermocouple of 15 cm length and 0.60 mm in diameter (the tip of the thermocouple is 0.5 mm in diameter) is bent to assume the L-shape and mounted on the right hand micropositioner by means of the pipette holder (figure C.1). The thermocouple is then connected to the thermocouple logger (Digitron Instrumentation 12-way selector unit. See figure 5.1), which displays temperature values with a resolution of 1°C.

By operating with the linear actuator and the microscope objective, the thermocouple is axially driven towards the tip of the micropipette and within the heating element; the final set up, necessary for calibration, is obtained when the tips of both the pipette and thermocouple are facing within a few microns distance. The pipette is then removed to

allow for calibration at temperatures higher than the glass melting point. A constant voltage difference, ΔV, of 10 volts was increasingly applied up to 260 volts by means of the potentiometer (see figure 5.1). At each value of V, the relevant temperature was read on the temperature logger and recorded. The same procedure was operated for decreasing voltages. Hence, a characteristic calibration chart can be plotted, as in figure C.2.

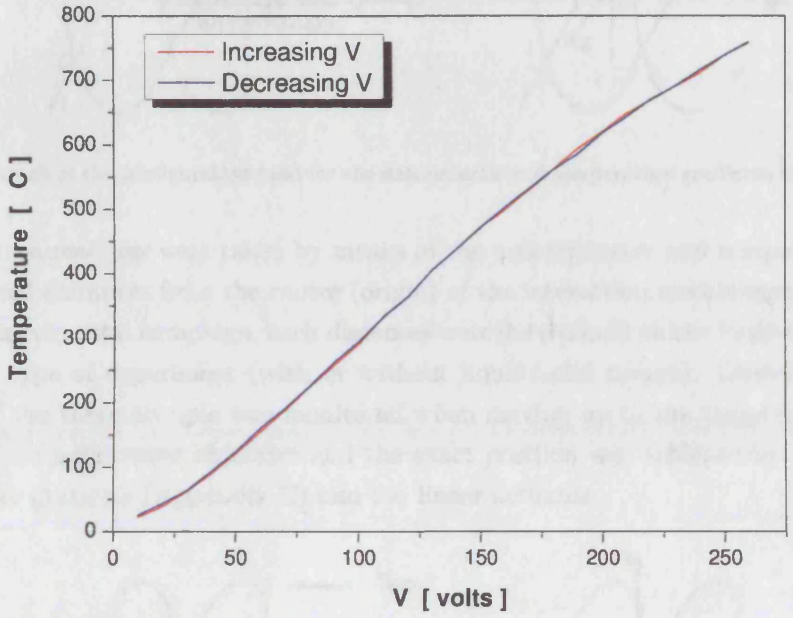

Fig. C.2: Typical chart obtained from calibration of the heating element and potentiometer.

C.1 Evaluation of thermal gradients within the heating coil

Non-uniformity of temperature can occur within the interaction environment (the red dashed box shown in figure C.1) because of the environment geometry itself and of either axial or radial bending of two adjacent turns of the coil. In fact, changes in the initial geometry are mainly due to thermal stresses, which arise within the material (i.e., the platinum wire) at high temperatures.

Hence, in order to ascertain the range of uniformity of temperature during experiment, it is necessary to evaluate any temperature gradients which may occur at different experimental temperatures.
This is achieved by operating the following procedure before each experimental campaign[1].

[1] The procedure hereafter described has been used for the experimental campaigns reported in **Chapters 6** and **7**. Hence, the determination of temperature gradients within the interaction environment was limited

In order to evaluate the temperature gradient along the x-axis of symmetry of the heating coil, see figure C.3, the thermocouple was placed within the interaction environment in the same manner explained in Appendix C.

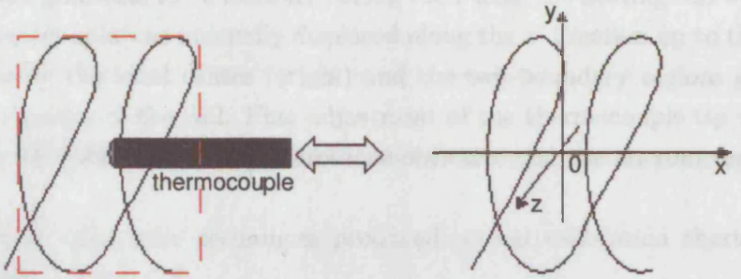

Fig. C.3: Sketch of the configuration used for the determination of temperature gradients along the x-axis.

Temperature readings were taken by means of the potentiometer and temperature logger at four fixed distances from the centre (origin) of the interaction environment. According to each experimental campaign, such distances were determined on the basis of the particle sizes and type of experiment (with or without liquid/solid bridge). During calibration, the tip of the thermocouple was monitored when moving up to the targeted distance by means of the microscope objective and the exact position was achieved by means of the micrometer graticule (Appendix C) and the linear actuator.

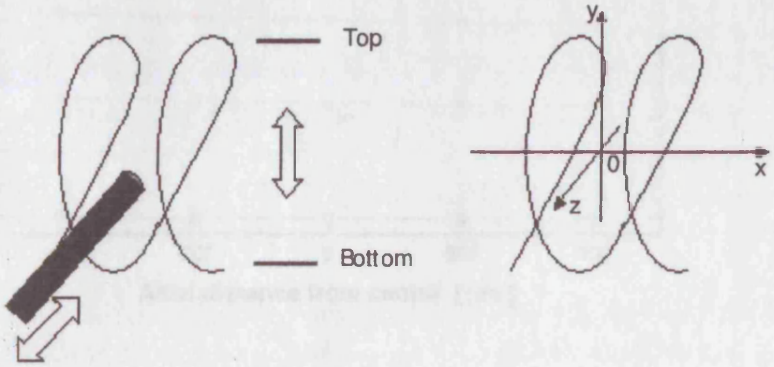

Fig. C.4: Sketch of the configuration used for the determination of temperature gradients along the z and y axis of symmetry.

A different configuration, shown in figure C.4, was used to evaluate the thermal gradients along the z and y axis of symmetry. Temperature readings were taken by placing the thermocouple tip between the two consecutive turns of the heating coil. This was achieved by mounting the thermocouple on the ferrule holder element, shown in figure 5.13(right), which was previously screwed onto the Femto-Bench in front of the heating

to the experimental temperatures investigated in these chapters.

coil. By operating with the micropositioner C (figure 5.13(left)), the centre of the interaction environment was held at the same height of the thermocouple tip.

For temperature gradients to be measured along the z-axis, the heating coil was held static while the thermocouple was manually displaced along the z direction up to three targeted distances, namely the axial centre (origin) and the two boundary regions geometrically defined by the radius of the coil. Fine adjustment of the thermocouple tip was operated by controlling its position with the microscope objective and the micrometer graticule.

Results obtained using such techniques produced typical calibration charts, which are shown in figures C.5 and C.6.

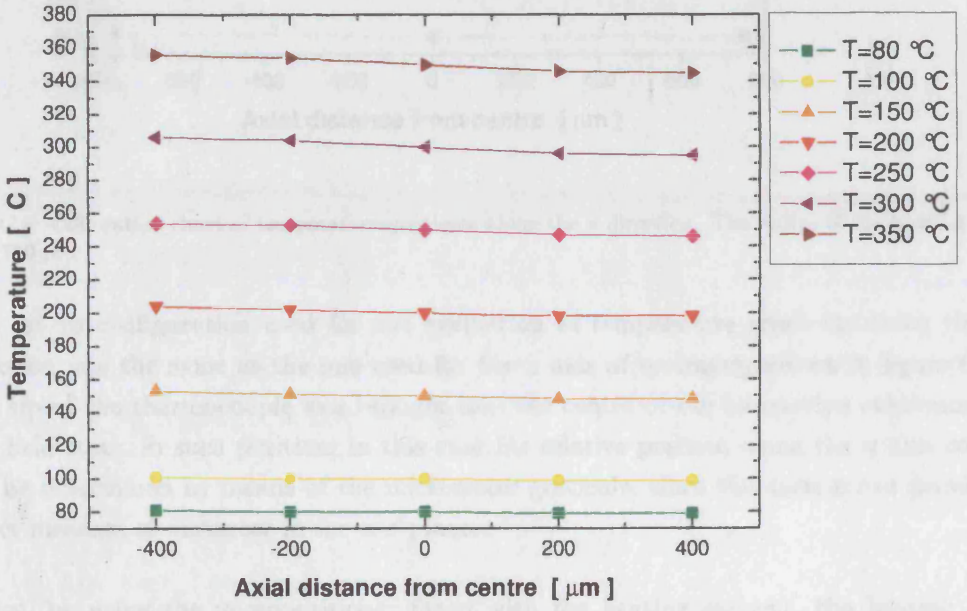

Fig. C.5: Calibration chart of temperature gradients along the x direction.

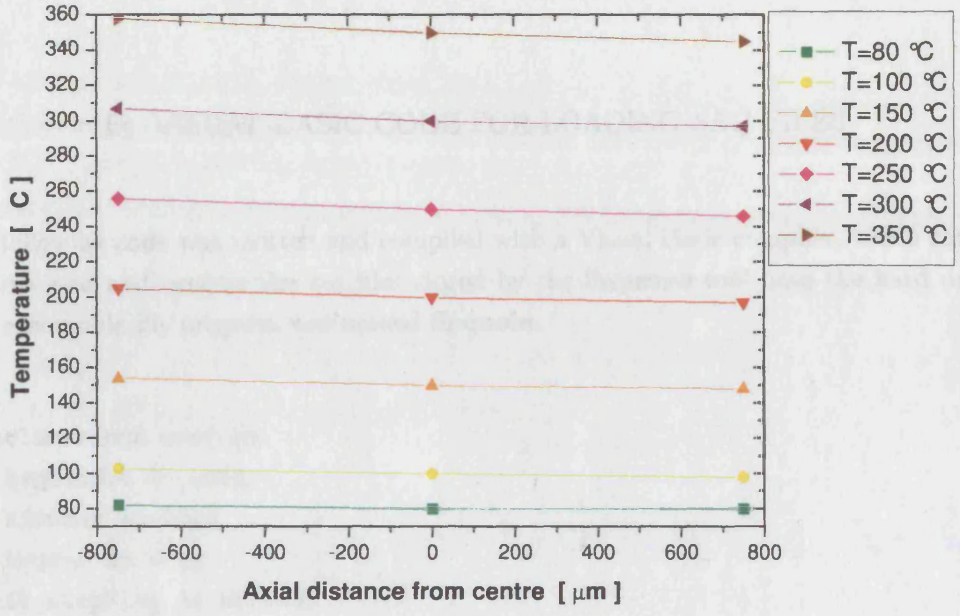

Fig. C.6: Calibration chart of temperature gradients along the z direction. The radius of the heating coil is of 750 μm.

The set-up configuration used for the evaluation of temperature gradients along the y direction was the same as the one used for the z axis of symmetry shown in figure C.4. The tip of the thermocouple was brought into the centre of the interaction environment and held static in such position; in this case, its relative position along the y axis could not be determined by means of the micrometer graticule, since this instrument provides direct measure of distances in the x-z plane.

Hence, by using the micropositioner fitted with the heating element, the heating coil was vertically shifted up to the top and bottom boundaries defined by the coil geometry (see figure C.4). Although such a calibration technique presented poor resolution of the top and bottom calibration distances (these were achieved by adjusting the microscope focus distance), results showed that, for all the tested temperatures up to 350 °C, the temperature gradient between the centre of the interaction environment and the top and bottom positions was not higher than 2-3 °C. Thus it could be considered negligible.

D. VISUAL BASIC CODE FOR LOADING *SEQ* FILES

The following code was written and compiled with a Visual Basic compiler, which can be used to load and process the *seq* files stored by the Sequence tool onto the hard drive. The executable file program was named **Sequoia.**

```
' declarations section
Dim Seqhandle As Long
Dim xframes As Long
Dim seqerr As Long
Public StopFlag As Boolean
Option Explicit

Private Sub Command2_Click()

End Sub

Private Sub CVdisplay1_ImageUpdated()

End Sub

Private Sub Form_Load()
    ' load image into the image control
    CVimage1.FileName="C:\CVCPCDIG.vin"
    ' setup user interface
    SetupUI

    ' TODO: add your program initialization here

    ' setup display control
    CVdispDst.LeftButtonMode = LB_AreaMode
    CVdispDst.RightButtonMode = RB_MENU
    CVdispDst.DirectDrawEnabled = True
```

```
End Sub

Sub SetupUI()
    ' TODO: add your UI setup code here
    ' set display image
    CVdispDst.Image = CVimage1.Image

    ' set grabber image
    CVgrabber1.Image = CVimage1.Image

    ' enable/disable grab checkbox
    Check1.Enabled = CVimage1.IsGrabber

End Sub

Private Sub CVimage1_ImageSnaped()
    ' refresh display
    CVdispDst.Refresh

    ' TODO: add your processing here

End Sub

Private Sub CVgrabber1_ImageUpdated()
    ' reset display
    CVdispDst.Image = 0
    CVdispDst.Image = CVimage1.Image
End Sub

Private Sub Command1_Click()
    ' load image using dialog
    CVimage1.LoadImageByDialog
    ' refresh UI
    SetupUI
End Sub

Private Sub Check1_Click()
    ' toggle grab
    CVimage1.Grab = Check1.Value
End Sub
```

```
Private Sub Get_frame_Click()
Dim FrameImage As Long
Dim RetVal As Long
If SEQPlayIsSequence(Seqhandle) = 1 Then
RetVal = SEQPlayGetFrame(Seqhandle, E_Get.text, FrameImage)
CVdispDst.StatusUserText = "Frame # " + Format$(RetVal)
CVdispDst.Image = FrameImage
ReleaseObject (FrameImage)
Else
MsgBox "Sequence not initialized"
End If
End Sub

' Load a sequence file *.seq stored in C:
Private Sub LoadSeq_Click()
If SEQPlayIsSequence(Seqhandle) <> 1 Then
Seqhandle = SEQPlayInit("C:\*.seq", xframes, seqerr)
    If seqerr <> -1 Then
    MsgBox "The sequence contains" + Format$(xframes) + "frames"
    Else
    MsgBox "not enough memory available"
    SEQPlayFree (Seqhandle)
    End If
Else
MsgBox "No sequence loaded"
End If
End Sub
' Start Playback
Private Sub Playback_Click()
Dim procPlayCb As Long
Dim Playfps As Double
StopFlag = False
If SEQPlayIsSequence(Seqhandle) = 1 Then
Form1.Refresh
Dim ProcPlayCBfps As Long
procPlayCb = GetProc(AddressOf PlayCB)
Playfps = SEQPlayPlay(Seqhandle, 0, procPlayCb, 0)
CVdispDst.StatusUserText = Format$(Playfps, "###0.00") + " fps"
Else
```

```
MsgBox "no sequence loaded"
End If
End Sub

Private Sub Save_Frame_Click()
CVdispDst.SaveImageByDialog
End Sub

Private Sub Stop_Click()
StopFlag = True
End Sub
```

E. BLOCK DIAGRAM OF THE DAQ APPLICATION

The DAQ application is composed of several blocks of different functionality, see figure E.1. Here are reported the functions of the main blocks of the program:

- **START** button: initialize the execution of the application.
- **A/D Config**: initialize the channel number of the acquisition board from which the program starts the data collection and the sample frequency of acquisition.
- **No Samples** and **For Range**: ask input for a user-defined number of samples to be collected and read the input step.
- **Timer**: shows the actual sample number and stops the program when the total amount of samples is reached.
- **Formula**: here the conversion (voltage to microns) formula is stored.
- **To file** and **File name selection**: displacement data are stored in a user allocated text file beforehand data collection.
- **XY Tracer**: the displacement data are presented through the XY Trace box.
- **Beep**: makes a sound to signal the end of the program.

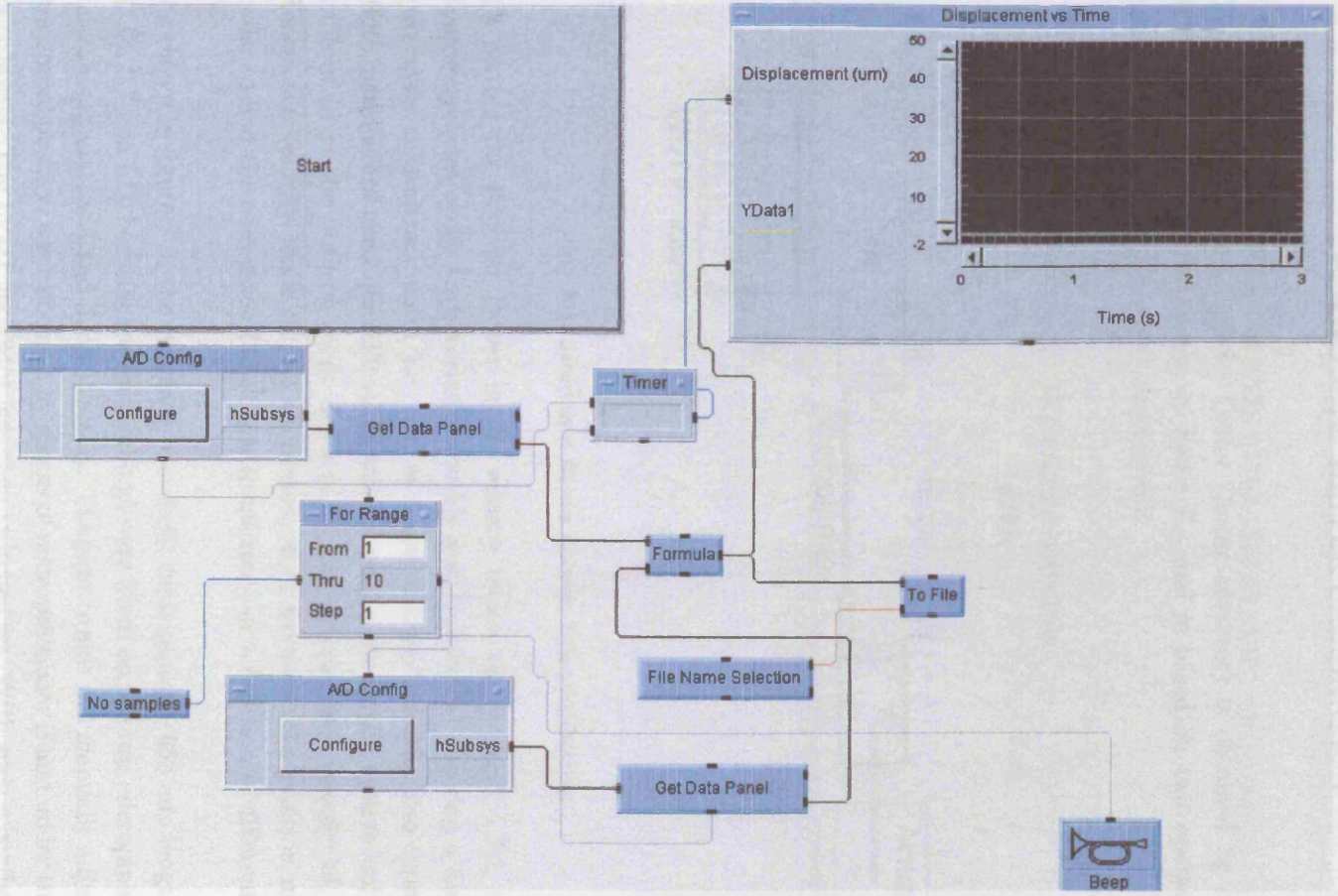

Fig. E.1: Screenshot of the DAQ block diagram.

F. ENCODER DRIVER CALIBRATION

The calibration of the Encoder Driver (linear actuator) is obtained by operating the HTMFB with the setup shown in figure F.1 and is based on two operational modes: the velocity and position mode, respectively.

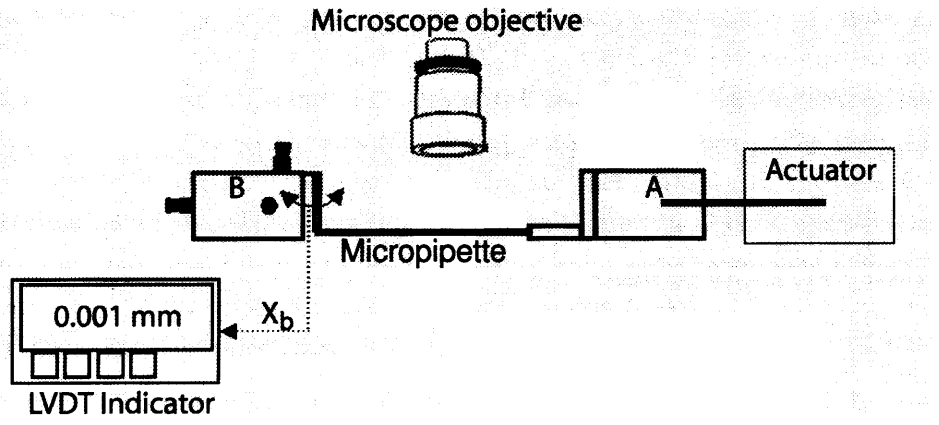

Fig. F.1: Setup used for the Encoder Driver calibration.

By setting the Encoder Driver in the velocity mode, see section 5.1.7.2, the linear actuator operates cyclic trajectories (forwards and backwards) covering a known distance (expressed in arbitrary units, i.e. *pts*) at a user defined velocity (also expressed in *pts*). Both parameters need quantification and conversion to metric system units; moreover, calibration of the position mode depends on the experimental velocity of the actuator; hence, the velocity mode is first calibrated, and, secondly, the position mode is set in order to find the conversion factor (*pts* to microns) as a function of different velocities[1].

As shown in figure F.1, the two ends of a single micropipette (650 mm length of 0.97 mm O.D., 0.7 mm I.D. borosilicate glass tubing) were fitted on the two micropipette holders of micromanipulators A and B, respectively. The pipette axis was manually adjusted until the horizontal position was obtained, by means of micropositioner B and under the focus of the microscope. The LVDT indicator was then switched on. With such a configuration, each

[1] Other parameters, which were necessary for fine tuning of the PID control interface of the actuator, were left at their default values, except for the Proportional gain control. This was set to 200 pts.

motion step executed by the actuator was rigidly transmitted, through the micropipette and the pipette holder, to the flexible sheets, and therefore to the LVDT. Displacement of the LVDT, X_b, was recorded through the DAQ application on PC-1, as described in section 5.1.7.1. Displacement data were collected with a frequency of 5 Hz (5 samples/sec).

- *Velocity mode*: the MC API software interface was launched on PC-2. The travel distance was set to 1000 pts and the operation mode set to *cycle*. Four different calibration tests were operated at velocity values respectively of 500, 5000, 10000, 50000 pts. The DAQ program was started on PC-1 and, after a few seconds, the Encoder Driver was actuated. By importing the text file, *1.txt*, which contains all the saved displacement data, into a spreadsheet program, it was possible to draw a graph (see figure F.2), where the displacement X_b (e.g., the displacement of the actuator) is plotted against time. In fact, five consecutive readings represent the travel distance, in microns, covered by the actuator during one second interval. The instantaneous velocity, v, is therefore calculated by dividing such distance in one second. The calculation was repeated three times at different positions of the trajectory (at half distance and close to the end of the path) for each cycle: three measurements were taken during the forward motion and three during backward motion. An average velocity was then calculated, as shown in Table F.1.

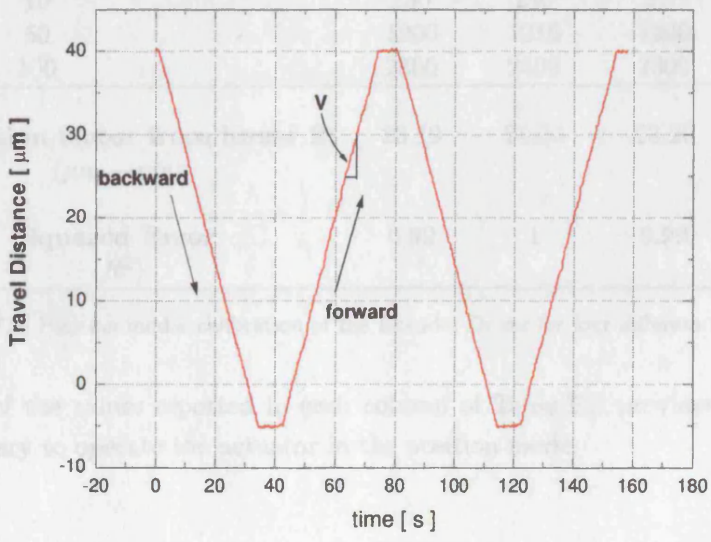

Fig. F.2: Velocity calibration chart.

Table F.1 shows the average velocity values thus obtained:

Experimental velocity [pts]	**Calculated average velocity [μm/s]**
500	1.13
5000	13.15
10000	26.49
50000	109

Tab. F.1: Velocity mode: experimental and calculated velocity values of the actuator.

- *Position mode*: the MC API software interface was launched on PC-2. The required *pts* units necessary to cover a target distance of respectively 1, 10, 20 and 50 μm, was recorded at four different velocities, as shown in Table F.2. Monitoring and control of the target distance is achieved by readings from the LVDT indicator. The optimal travel distance, expressed in *pts*, was found by trial and error attempts (position units are routinely inserted in the Distance input window on the MC API application until the exact position is displayed). The velocity values are obtained from the calibration chart shown in figure 5.21, and inserted in the velocity input window under the Set Up menu of the MC API software.

Target distance [μm]	$\rightarrow$ v =	[pts] **1μm/s**	[pts] **10μm/s**	[pts] **20μm/s**	[pts] **50μm/s**
5		115	120	120	120
10		230	240	240	230
50		1200	1210	1200	1200
100		2300	2400	2300	2200
Conversion factor from linear fit (μm $\rightarrow$pts)		23.19	24.04	23.20	22.40
Squared Error (R^2)		0.99	1	0.99	0.99

Tab. F.2: Position mode: calibration of the Encoder Driver for four different velocities.

A linear fit of the values reported in each column of Table F.2 provides the conversion factor necessary to operate the actuator in the position mode.

G. PRESSURE DIFFERENCE DRIVEN LIQUID DISTRIBUTION ONTO PARTICLE - MICRO-PIPETTE JUNCTIONS

What is reported here is a description, taken from a recent publication of Pepin et al. [43], of the mechanism behind the formation of liquid necks at the particle - micro-pipette junction during liquid bridge formation between a pair of particles. This mechanism has been exploited in the experimental work described in this thesis in order to obtain high temperature resistant solid bonds formed between the particle and micro-pipette.

Consider two spheres of different size, R_i, both of which are covered with the same liquid film of surface tension equal to γ_{LV} and brought into contact. For each sphere, the pressure difference, ΔP_i, between the film and the atmosphere is given by the Young-Laplace relationship (Equation G.1), neglecting the film thickness:

$$\Delta P_i = \frac{2\gamma_{LV}}{R_i} \tag{G.1}$$

Through the interparticle contact, liquid would move from the small particle to the large one, as the film pressure on the small particle is superior to the pressure on the large particle. However, if the liquid perfectly wets the particles as well as the micro-pipettes to which they are attached, then the experimental situation is more complicated; micro-pipettes are much smaller than particles, figure G.1.

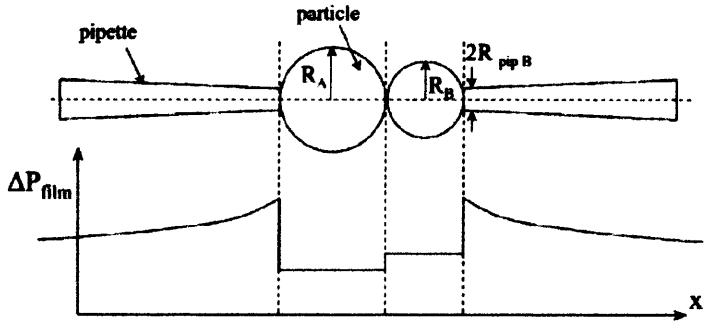

Fig. G.1: Liquid film pressure for the "dry" system in particle contact. After[43]

Micro-pipettes are obtained by larger glass tubes locally melted with a heating coil and

typically have a terminal radius ranging between 20 and 30 μm (see section 5.1.2.1). This radius increases further away from the tip. After the liquid has spread on the sphere surface and reaches the tip of the pipette, there is a high Laplace pressure, which then diminishes with distance according to the inverse of the pipette radius. The liquid is therefore pushed onto the pipette, figure G.1 by capillary forces and this is the reason why, at the beginning of liquid addition, no observable liquid is found at interparticle contact. A minimum liquid reservoir saturation is necessary before liquid can move to the interparticle contact. The liquid collects at the micro-pipette - particle junctions and forms liquid necks, which reduce the Laplace pressure to that of the particle-free surface, figure G.2.

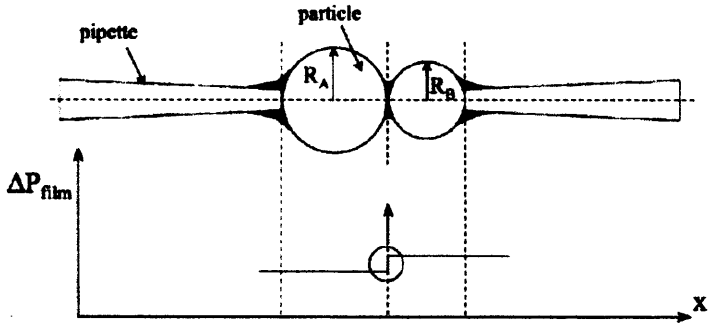

Fig. G.2: Pressure of liquid films in low saturation liquid reservoirs. After[43]

H. PUBLICATIONS, CONFERENCES AND COMPANY REPORTS

H.1 Publications referred in this thesis

S.J.R. Simons, D. Rossetti, P. Pagliai, R. Ward and S. Fitzpatrick. Predicting the performance of granulation binders through micro-mechanistic observations. *Part. Part. Syst. Char.* 21(4): page 284, 2004.

S.J.R. Simons, D. Rossetti, P. Pagliai, R. Ward and S. Fitzpatrick. Predicting the performance of granulation binders through micro-mechanistic observations. *Powder Technology* 140: page 280, 2004.

P. Pagliai, S.J.R. Simons and D. Rhodes. Towards a fundamental understanding of defluidisation at high temperature: a micro-mechanistic approach. *Powder Technology* 148: page 106, 2004.

P. Pagliai and S.J.R. Simons. High temperature particle interactions. Chapter 4: page 108. In *Granular Materials.* RSC, Cambridge, 2004.

H.2 Conference proceedings

P. Pagliai. High temperature investigation of particle-particle interactions. *UK Particle Technology Forum IV*, Leeds, UK, 11-12 April 2002.

P. Pagliai, S.J.R. Simons and D. Rhodes. Defluidisation at high temperatures: direct measurement of interparticle forces. *Proc. World Congress on Particle Technology 4*, Sydney, Australia, 21-25 July 2002.

P. Pagliai, S.J.R. Simons and D. Rhodes. High temperature defluidisation: a micro-mechanistic approach. *Proc.* 15^{th} *Int. Congr. Chem. Eng., CHISA*, Prague, Czech Republic, 25-29 August 2002.

P. Pagliai, S.J.R. Simons and D. Rhodes. Towards a fundamental understanding of high temperature defluidisation: a micro-mechanistic approach. *Proc.* 4^{th} *European Congr. Chem. Eng.*, Granada, Spain, 21-25 September 2003.

P. Pagliai, S.J.R. Simons and D. Rhodes. Micro-scale observations and measurements of particle sintering and drying at high temperatures. *Proc. AIChE Annual Meeting*, San Francisco, USA, 16-21 November 2003.

P. Pagliai, S.J.R. Simons and D. Rhodes. A novel experimental approach to high temperature particle-particle interactions. *UK Particle Technology Forum VI*, London, UK, 15-16 June 2004.

P. Pagliai, S.J.R. Simons and D. Rhodes. A novel experimental study of temperature enhanced cohesive interparticle forces. *PSA 2005*, Stratford upon Avon, UK, 21-23 September 2005.

S.J.R. Simons, P. Pagliai and D. Rhodes. Towards a fundamental understanding of defluidisation at high temperatures: microscopic measurement of interparticle forces. *Proc. AIChE Annual Meeting*, Indianapolis, USA, 3-8 November 2002.

S.J.R. Simons, P. Pagliai and D. Rhodes. Micro-scale observations and measurements of high temperature particle-particle interactions. *Proc. 7^{th} World Congress Chem. Eng.*, Glasgow, UK, 10-14 July 2005.

H.3 Company reports

S.J.R. Simons, D. Rossetti and P. Pagliai. Assessing the performance of different binders in relation to the agglomeration of paracetamol: a feasibility study using a novel micro-force balance. Report presented to Merck, Sharp and Dhome.

P. Pagliai. Towards a fundamental understanding of high temperature defluidisation: a micro-mechanistic approach. 2^{nd} *TDN Workshop*, Sellafield, UK, 10-12 September 2002.

REFERENCES

[1] S. Berbner and F. Loffler. Influence of high-temperatures on particle adhesion. *Powder Technology*, **78**:page 273, 1994.

[2] W. Pietsch. *Size enlargement by agglomeration.* Wiley and Sons, 1991.

[3] A.J. Forsyth, S. Hutton, and M.J. Rhodes. Effect of cohesive interparticle force on the flow characteristics of granular material. *Powder Technology*, **126**:page 150, 2002.

[4] P.N. Rowe, L. Santoro, and J.G. Yates. Division of gas between bubble and interstitial phases in fluidized-beds of fine powders. *Chem. Eng. Sci.*, **33**:page 133, 1978.

[5] R. Clift. Powder technology and particle science. *Powder Technology*, **88**:page 335, 1996.

[6] P. Lettieri. *A study of the influence of temperature on the flow behaviour of solid materials in a gas fluidized bed.* PhD thesis, University College London, 1999.

[7] H. Rumpf. The strength of granules and agglomerates. In *Agglomeration*, pages 379–418. Wiley and Sons, 1962.

[8] G.C. Kuczynski. Physics and chemistry of sintering. *Adv. Colloid Interface Sci.*, **3**:page 275, 1972.

[9] W. Klose and M. Lent. Agglomeration kinetics of coking coal particles during the softening phase. *Fuel*, **64**:page 193, 1985.

[10] P. Compo, R. Pfeffer, and G.I. Tardos. Minimum sintering temperatures and defluidization characteristics of fluidizable particles. *Powder Technology*, **51**:page 85, 1987.

[11] P.C. Wright and J.A. Raper. Examination of dispersed liquid-phase three-phase fluidized beds Part 1.Non-porous,uniform particle systems. *Powder Technology*, **97**:page 208, 1998.

[12] L.J. McLaughlin and M.J. Rhodes. Prediction of fluidized bed behaviour in the presence of liquid bridges. *Powder Technology*, **114**:page 213, 2001.

[13] S.H. Schaafsma. *Down-scaling of a fluidised bed agglomeration process.* PhD thesis, Rijksuniversiteit Groningen, 2000.

[14] G. Lian, C. Thornton, and M.J. Adams. Discrete particle simulation of agglomerate impact coalescence. *Chem. Eng. Sci.*, **53**(19):page 3381, 1998.

[15] R.A. Fisher. On the capillary forces in an ideal soil; correction of formulae given by W.B. Hines. *J. Agric. Sci.*, **16**:page 492, 1926.

[16] J.N. Israelachvili. *Intermolecular & surface forces.* Academic Press, S.Diego, 2nd ed. edition, 1992.

[17] H. Schubert. Principles of agglomeration. *Int. Chem. Eng.*, **21**(3):page 363, 1981.

[18] G. Lian, C. Thornton, and M.J. Adams. A theoretical study of the liquid bridge forces between two rigid spherical bodies. *J. Coll. Int. Sci.*, **161**:page 138, 1993.

[19] K.S. Hwang, R.M. German, and F.V. Lenel. Capillary forces between spheres during agglomeration and liquid-phase sintering. *Metall. Trans. A*, **18A**:page 11, 1987.

[20] D.N. Mazzone, G.I. Tardos, and R. Pfeffer. The effect of gravity on the shape and strength of a liquid bridge between two spheres. *J. Coll. Int. Sci.*, **113**(2):page 544, 1986.

[21] F.R.E. De Bisschop and W.J.L. Rigole. A Physical model for liquid capillary bridges between adsorptive solid spheres - The nodoid of Plateau. *J. Coll. Int. Sci.*, **88**:page 117, 1982.

[22] X. Pepin, D. Rossetti, S.M. Iveson, and S.J.R. Simons. Modelling the evolution and rupture of pendular liquid bridges in the presence of large wetting hysteresis. *J. Coll. Int. Sci.*, **232**(2):page 289, 2000.

[23] J. Götz, H. Lankes, H. Weisser, and K. Sommer. Characterization of products consisting of synthetic, amorphous silica and water with different moistures by means of nmr. *Chem. Eng. Technol.*, **25**(10):page 989, 2002.

[24] H. Rumpf. Particle adhesion. In *Agglomeration 1977*, AIME p.97, 1977. K.V.S. Sastry (Ed.).

[25] C.L. Feng and A.B. Yu. Effect of liquid addition on the packing of mono-sized coarse spheres. *Powder Technology*, **99**:page 22, 1998.

[26] S.M. Iveson, J.D. Litster, and B.J. Ennis. Fundamental studies of granule consolidation. Part 1: Effects of binder content and binder viscosity. *Powder Technology*, **88**:page 15, 1996.

[27] S.M. Iveson and J.D. Litster. Fundamental studies of granule consolidation. Part 2: Quantifying the effects of particle and binder properties. *Powder Technology*, **99**:page 243, 1998.

[28] H. Schubert. Tensile strength and capillary pressure of moist agglomerates. In *Agglomeration 1977*, AIME p.144, 1977. K.V.S. Sastry (Ed.).

[29] H. Schubert. Tensile strength of agglomerates. *Powder Technology*, **11**:page 107, 1975.

[30] S.J.R. Simons, J.P.K. Seville, and M.J. Adams. An analysis of the rupture energy of pendular liquid bridges. *Chem. Eng. Sci.*, **49**(14):page 2331, 1994.

[31] Y. Muguruma, T. Tanaka, and Y. Tsuji. Numerical simulation of particulate flow with liquid bridge between particles (simulation of centrifugal tumbling granulator). *Powder Technology*, **109**:page 49, 2000.

[32] C.L. Feng and A.B. Yu. Quantification of the relationship between porosity and interparticle forces for the packing of wet uniform spheres. *J. Coll. Int. Sci.*, **231**:page 136, 2000.

[33] R.Y. Yang and A.B. Yu. Numerical study of the packing of wet coarse uniform spheres. *AIChE Journal*, **49**(7):page 1656, 2003.

[34] T. Weigert and S. Ripperger. Calculation of the liquid bridge volume and bulk saturation from the half filling angle. *Part. Part. Syst. Charact.*, **16**:page 238, 1999.

[35] R.W. Coughlin, B. Elbirli, and L. Vergaraedwards. Interparticle force conferred by capillary-condensed liquid at contact points. 1. Theoretical considerations. *J. Coll. Int. Sci.*, **87**(1):page 18, 1982.

[36] M.T. Jacques, A.D. Horarongkura, and J.D. Henry. Feasibility of separation processes in liquid-liquid solid systems: free energy and stability analysis. *AIChE Journal*, **25**(1):page 160, 1979.

[37] W. Pietsch and H. Rumpf. Adhesion capillary pressure liquid volume and angle of contact of a liquid bridge between 2 spheres. *Chemie Ingenieur Technik*, **39**(15):page 885, 1967.

[38] J. Tomas. Untersuchungen zum fließverhalten von feuchten und leichtlöslichen schüttgütern. *Freiberger Forschungsheft*, **A**, 1983.

[39] O. Pitois, P. Moucheront, and X. Chateau. Liquid bridge between two moving spheres: an experimental study of viscosity effects. *J. Coll. Int. Sci.*, **231**:page 26, 2000.

[40] M.J. Matthewson. Adhesion of spheres by thin liquid films. *Phil. Mag. A*, **5**(2):page 207, 1987.

[41] D.N. Mazzone, G.I. Tardos, and R. Pfeffer. The behaviour of liquid bridges between two relatively moving particles. *Powder Technology*, **51**:page 71, 1987.

[42] X. Pepin, D. Rossetti, and S.J.R. Simons. Modeling pendular liquid bridges with a reducing solid-liquid interface. *J. Coll. Int. Sci.*, **232**(2):page 298, 2000.

[43] X. Pepin, S.J.R. Simons, S. Blanchon, D. Rossetti, and G. Couarraze. Hardness of moist agglomerates in relation to interparticle friction, granule liquid content and nature. *Powder Technology*, **117**:page 123, 2001.

[44] H.M. Princen. Comments on the effects of capillary liquid on the force of adhesion between spherical solid particles. *J. Coll. Int. Sci.*, **26**:page 249, 1968.

[45] K. Hotta, K. Takeda, and K. Iinoya. The capillary binding force of a liquid bridge. *Powder Technology*, **10**:page 231, 1974.

[46] F.M. Orr, L.E. Scriven, and P. Rivas. Pendular rings between solids:meniscus properties and capillary forces. *J. Fluid. Mech.*, **67**(4):page 723, 1975.

[47] M.J. Adams and V. Perchard. The cohesive forces between particles with interstitial liquid. *I.Chem.E. Symp. Ser.*, **91**:page 147, 1985.

[48] H. Schubert. *Kapillaritat in porosen feststoffsystemen.* Heidelberg, Springer-Verlag Berlin, 1982.

[49] G. Mason and C.G. Clark. Liquid bridges betwen spheres. *Chem. Eng. Sci.*, **20**:page 859, 1965.

[50] S.J.R. Simons and R.J. Fairbrother. Direct observations of liquid binder-particle interactions: the role of wetting behaviour in agglomerate growth. *Powder Technology*, **110**(1-2):page 44, 2000.

[51] C.D. Willett, M.J. Adams, S.A. Johnson, and J.P.K. Seville. Capillary bridges between two spherical bodies. *Langmuir*, **16**(24):page 9396, 2000.

[52] A. Cameron. *Basic lubrication theory.* John Wiley, Chichester, 2nd edition, 1976.

[53] B.J. Ennis, J.L. Li, G.I. Tardos, and R. Pfeffer. The influence of viscosity on the strength of an axially strained pendular liquid bridge. *Chem. Eng. Sci.*, **45**:page 3071, 1990.

[54] B.J. Ennis, G.I. Tardos, and R. Pfeffer. A microlevel-based characterization of granulation phenomena. *Powder Technology*, **65**:page 257, 1991.

[55] H.G. Kristensen, P. Holm, and T. Schaefer. Mechanical properties of moist agglomerates in relation to granulation mechanisms, Part 2: Effects of particle size distribution. *Powder Technology*, **44**:page 239, 1985.

[56] G.I. Tardos, M.I. Khan, and P.R. Mort. Critical parameters and limiting conditions in binder granulation of fine powders. *Powder Technology*, **94**:page 245, 1997.

[57] X. Pepin, S. Blanchon, and G. Couarraze. Power consumption profiles in high-shear wet granulation. II: Predicting the overwetting point from a spreading energy. *J. Pharm. Sci.*, **90**(3):page 332, 2001.

[58] M.J. Adams, D. Williams, and J.G. Williams. The use of linear elastic fracture-mechanics for particulate solids. *J. Mat. Sci.*, **24**(5):page 1772, 1989.

[59] M. Abdel-Ghani, J.G. Petrie, J.P.K. Seville, R. Clift, and M.J. Adams. Mechanical properties of cohesive particulate solids. *Powder Technology*, **65**(1-3):page 113, 1991.

[60] S.J.R. Simons, J.P.K. Seville, and M.J. Adams. In *Sixth International Symposium on Agglomeration*, page 117, Nagoya, Japan, 1993.

[61] M.J. Gluckman, J. Yerushalmi, and A.M. Squires. *Defluidization characteristics of sticky materials on agglomerating bed*, volume II, Fluidization Technology, page 395. Hemisphere, New York, 1976.

[62] W.A. Zisman. *Relation of equilibrium contact angle to liquid and solid constitution. Advances in chemistry series*, volume 43. Chapter 1. American Chemical Society, Washington, 1964.

[63] L. Boruvka and A.W. Neumann. Generalization of classical theory of capillarity. *J. Chem. Phys.*, **66**(12):page 5464, 1977.

[64] A.W. Neumann. *Applied surface thermodynamics.* Dekker, New York, 1996.

[65] A.D. Scheludko. Condensation of vapors on spherical nuclei and the line tension effect. *J. Coll. Int. Sci.*, **104**(2):page 471, 1985.

[66] D. Li. Drop size dependence of contact angles and line tensions of solid-liquid systems. *Colloids and Surfaces*, **A 116**:page 1, 1996.

[67] J. Drelich. The significance and magnitude of the line tension in three-phase (solid-liquid-fluid) systems. *Colloids and Surfaces*, **A 116**:page 43, 1996.

[68] Y. Liu and R.M. German. Contact angle and solid-liquid-vapor equilibrium. *Acta Mater.*, **44**(4):page 1657, 1996.

[69] J.P. Garandet, B. Drevet, and N. Eustathopoulos. On the validity of Young's equation in the presence of gravitational and other external force fields. *Scripta Mater.*, **38**(9):page 1391, 1998.

[70] G.R. Wickham and S.D.R Wilson. Deformation of an elastic solid by a sessile drop. *J. Coll. Int. Sci.*, **51**(1):page 189, 1975.

[71] M.A. Fortes. Deformation of solid surfaces due to capillary forces. *J. Coll. Int. Sci.*, **100**(1):page 17, 1984.

[72] A.W. Neumann and R.J. Good. *Surface and colloid science*, volume II. Plenum Press, New York, 1979.

[73] R.N. Wenzel. Resistance of solid surfaces to wetting by water. *Ind. Eng. Chem.*, **28**:page 988, 1936.

[74] C. Rado, C. Senillou, and N. Eustathopoulos. In *High temperature capillarity - 97*, page 133, Krakow, Poland, 1998. Foundry Research Institute.

[75] P. Neogi and C.A. Miller. Spreading kinetics of a drop on a rough solid-surface. *J. Coll. Int. Sci.*, **92**(2):page 338, 1983.

[76] J.F. Joanny and P.G. De Gennes. A model for contact angle hysteresis. *J. Chem. Phys.*, **81**(1):page 553, 1984.

[77] A. Murmur. The actual contact angle on a heterogeneous rough surface in three dimensions. *Langmuir*, **14**(18):page 5292, 1998.

[78] A.W. Adamson. *Physical chemistry of surfaces.* New York, 6th edition, 1997.

[79] R.C. Rowe. Interactions in colored powders and tablet formulations. A theoretical approach based on solubility parameters. *Int. J. Pharm.*, **53**:page 75, 1989.

[80] R.C. Rowe. Polar non-polar interactions in the granulation of organic substrates with polymer binding-agents. *Int. J. Pharm.*, **56**(2):page 117, 1989.

[81] R.C. Rowe. Correlation between predicted binder spreading coefficients and measured granule and tablet properties in the granulation of paracetamol. *Int. J. Pharm.*, **58**(3):page 209, 1990.

[82] O. Planinsek, R. Pisek, A. Trojak, and S. Srcic. The utilization of surface free-energy parameters for the selection of a suitable binder in fluidized bed granulation. *Int. J. Pharm.*, **207**:page 77, 2000.

[83] G. Buckton. Contact angle, adsorption and wettability- A review with respect to powders. *Powder Technology*, **61**:page 237, 1990.

[84] D. Zhang, J.H. Flory, S. Panmai, U. Batra, and M.J. Kaufman. Wettability of pharmaceutical solids: its measurement and influence on wet granulation. *Colloids and Surfaces*, **A 206**:page 547, 2002.

[85] C.W. Extrand. A thermodynamic model for contact angle hysteresis. *J. Coll. Int. Sci.*, **207**:page 11, 1998.

[86] A.W. Neumann and R.J. Good. Thermodynamics of contact angles. 1.Heterogeneous solid surfaces. *J. Coll. Int. Sci.*, **38**(2):page 341, 1972.

[87] N. Eustathopoulos. Dynamics of wetting in reactive metal/ceramic systems. *Acta Materialia*, **46**(7):page 2319, 1998.

[88] J. Lahaye and P. Ehrburger. Pitch-coke interactions. *Fuel*, **64**:page 1187, 1985.

[89] P. Couderc, P. Hyvernat, and J.L. Lemarchand. Correlations between ability of pitch to penetrate coke and the physical characteristics of prebaked anodes for the aluminum-industry. *Fuel*, **65**(2):page 281, 1986.

[90] V.G. Rocha, M. Granda, R. Santamaria, E.I. Diestre, and R. Menendez. A study of the wettability of pitch on coke. In *Proc. 4th ECCE*, Granada, Spain, September 21-25 2003.

[91] L.H. Tanner. Spreading of silicone oil drops on horizontal surfaces. *J. Phys. D - Applied Physics*, **12**(9):page 1473, 1979.

[92] B.G. Langston and F.M. Stephens Jr. Self-agglomerating fluidized bed reduction. *J. Metals*, **12**:page 312, 1960.

[93] J.H. Siegell. High temperature defluidization. *Powder Technology*, **38**:page 13, 1984.

[94] B. Liss. In *87th AIChE meeting*, Boston, USA, 1979.

[95] G.I. Tardos, D. Mazzone, and R. Pfeffer. Destabilization of fluidized beds due to agglomeration. Part II: Experimental verification. *Can. J. Chem. Eng.*, **63**:page 384, 1985.

[96] B.J. Skrifvars, M. Hupa, and M. Hiltunen. Sintering of ash during fluidized bed combustion. *Ind. Eng. Chem. Res.*, **31**:page 1026, 1992.

[97] B.J. Skrifvars, M. Hupa, R. Backman, and M. Hiltunen. Sintering mechanisms of FBC ashes. *Fuel*, **73**(2):page 171, 1994.

[98] U. Arena and M.L. Mastellone. Defluidization phenomena during the pyrolisis of two plastic wastes. *Chem. Eng. Sci.*, **55**:page 2849, 2000.

[99] U. Arena, A. Cammarota, and M.L. Mastellone. The phenomenology of comminution in the fluidized bed combustion of packaging-derived fuels. *Fuel*, **77**:page 1185, 1998.

[100] W.D. Kingery, H.K. Bowen, and D.R. Uhlmann. *Introduction to ceramics.* Wiley and Sons, 2nd edition, 1976.

[101] J.P.K. Seville, C.D. Willett, and P.C. Knight. Interparticle forces in fluidisation: a review. *Powder Technology*, **113**(3):page 261, 2000.

[102] T. Mikami, H. Kamiya, and M. Horio. The mechanism of defluidization of iron particles in a fluidised bed. *Powder Technology*, **89**:page 231, 1996.

[103] J. Frenkel. Viscous flow of crystalline-bodies under the action of surface tension. *J. Phys. USSR*, **9**:page 385, 1945.

[104] C. Herring. Effect of change of scale on sintering phenomena. *J. Appl. Phys.*, **21**:page 301, 1950.

[105] G.C. Kuczynski. Study of the sintering of glass. *J. Appl. Phys.*, **20**:page 1160, 1949.

[106] J.H. Siegell. *Defluidization phenomena in fluidized beds of sticky particles at high temperature.* PhD thesis, City University of New York, 1976.

[107] P. Basu. A study of agglomeration of coal ash in fluidized beds. *Can. J. Chem. Eng.*, **60**:page 791, 1982.

[108] G.I. Tardos, D. Mazzone, and R. Pfeffer. Measurement of surface viscosities using a dilatometer. *Can. J. Chem. Eng.*, **62**:page 884, 1984.

[109] P. Compo, G.I. Tardos, Mazzone, and R. Pfeffer. Minimum sintering temperatures of fluidizable particles. *Part. Part. Syst. Charact.*, **1**:page 171, 1984.

[110] J.P.K. Seville, H. Silomon-Pflug, and P.C. Knight. Modelling of sintering in high temperature gas fluidisation. *Powder Technology*, **97**:page 160, 1998.

[111] P. Lettieri, J.G. Yates, and D. Newton. The influence of interparticle forces on the fluidization behaviour of some industrial materials at high temperature. *Powder Technology*, **110**:page 117, 2000.

[112] G.I. Tardos, D. Mazzone, and R. Pfeffer. Destabilization of fluidized beds due to agglomeration. Part I: Theoretical model. *Can. J. Chem. Eng.*, **63**:page 377, 1985.

[113] F.A.L. Dullien. *Porous media - Fluid transport and pore structure.* Academic Press, New York, 1979.

[114] B. Waldie. Growth-mechanism and the dependence of granule size on drop size in fluidized-bed granulation. *Chem. Eng. Sci.*, **46**(11):page 2781, 1991.

[115] S.H. Schaafsma, P. Vonk, P. Sagers, and N.W.F. Kossen. Description of agglomerate growth. *Powder Technology*, **97**(3):page 183, 1998.

[116] K. Hapgood, H.E. Hartman, C. Kaur, R. Plank, P. Harmon, and J.A. Zega. A case study of drug distribution in wet granulation. In *Proc. World Congress of Particle Technology 4*, Sydney, Australia, July 21-25 2002.

[117] Y. Zhang and K.C. Johnson. Effect of drug particle size on content uniformity of low-dose solid dosage forms. *Int. J. Pharm.*, **154**:page 179, 1997.

[118] H. Vromans, H.G.M. Poels-Jansseen, and H. Egermann. Effects of high-shear granulation on granulate homogeneity. *Pharm. Dev. Technol.*, **4**:page 297, 1999.

[119] Q.R. Huang and C.H. Wang. Surface laser light scattering studies of the air/poly(n-vinyl-2-pyrrolidone)-water solution interface. *J. Chem. Phys.*, **105**:page 6546, 1996.

[120] S.A. Chang and D.G. Gray. The surface tension of aqueous hydroxypropylcellulose. *J. Coll. Int. Sci.*, **67**:page 255, 1978.

[121] G.I. Tardos and R. Gupta. Forces generated in solidifying liquid bridges between two small particles. *Powder Technology*, **87**:page 175, 1996.

[122] D. Rossetti. *Direct investigation of liquid bridges in relation to the mechanisms of particle agglomeration in gaseous and liquid media.* PhD thesis, University College London, 2002.

[123] J. Schwedes. Testers for measuring flow properties of particulate solids. *Powder Handling Process.*, **12**(4):page 337, 2000.

[124] T. Groger, U. Tuzun, and D.M. Heyes. Modelling and measuring of cohesion in wet granular materials. *Powder Technology*, **133**:page 203, 2003.

[125] A. Schweiger and I. Zimmermann. A new approach for the measurement of tensile strength of powders. *Powder Technology*, **101**:page 7, 1999.

[126] K.L. Johnson, K. Kendall, and A.D. Roberts. Surface energy and the contact of elastic solids. *Proc R. Soc. Lond. A*, **324**:page 301, 1971.

[127] K. Kendall, B.J. Briscoe, and M.J. Adams. *Tribology in particle technology.* Adam Hilger, Bristol, 1987.

[128] C. Thornton. Interparticle sliding in the presence of adhesion. *J. Phys. D: Appl. Phys.*, **24**:page 1942, 1991.

[129] T. Schaefer and O. Worts. Control of fluidized bed granulation. IV Effects of binder solution ad atomization on granule size and size distribution. *Arch. Pharm. Chem. Sci. Ed.*, **6**:page 14, 1978.

[130] D. Bika, G.I. Tardos, S. Panmai, L. Farber, and J. Michaels. Strength and morphology of solid bridges in dry granules of pharmaceutical powders. *Powder Technology*, **150**:page 104, 2005.

[131] F. Pratola, S.J.R. Simons, and A.G. Jones. A novel experimental device for measurement of agglomerative crystallization forces. *Chem. Eng. Res. Des.*, **80**(A5):page 441, 2002.

[132] Z. Zhang, M.L. Sisk, H. Mashmoushy, and C.R. Thomas. Characterisation of the breaking force of latex particle aggregates by micromanipulation. *Part. Part. Syst. Charact.*, **16**:page 278, 1999.

[133] C.H. Bamford and C.F.H. Tipper. *Chemical Kinetics*, volume 22. Reactions in the solid state. Elsevier, Amsterdam-Oxford-New York, 1980.

[134] M. Avrami. Kinetics of phase change. I General theory. *J. Chem. Phys.*, **7**:page 1103, 1939.

[135] J.J.M. Órfão and F.G. Martins. Kinetic analysis of thermogravimetric data obtained under linear temperature programming - a method based on calculations of the temperature integral by interpolation. *Thermochimica Acta*, **390**:page 195, 2002.

[136] G. Binnig, C.F. Quate, and C. Gerber. Atomic force microscope. *Phys. Rev. Lett.*, **56**(9):page 930, 1986.

[137] L.O. Heim, M. Kappl, and H.J. Butt. Tilt of atomic force microscope cantilevers: effect on spring constant and adhesion measurements. *Langmuir*, **20**(7):page 2760, 2004.

[138] T.R. Albrecht, S. Akamine, T.E. Carver, and C.F. Quate. Microfabrication of cantilever styli for the atomic force microscope. *J. Vac. Sci. Technol. A*, **8**(4):page 3386, 1990.

[139] S. Biggs. *Granular materials: Fundamentals and applications*, chapter 7, page 185. RSC, Cambridge, 2004.

[140] J.W.G. Tyrrell and J.A.S. Cleaver. Development of an instrument for measuring inter-particle forces. *Advanced Powder Technol.*, **12**(1):page 1, 2001.

[141] J.P. Cleaveland, S. Manne, D. Bocek, and P.K. Hansma. A nondestructive method for determining the spring constant of cantilevers for scanning force microscopy. *Rev. Sci. Instr.*, **64**(2):page 403, 1993.

[142] A. Hammiche, D.J. Hourston, H.M. Pollock, M. Reading, and M. Song. Scanning thermal microscopy: subsurface imaging, thermal mapping of polymer blends, and localized calorimetry. *J. Vac. Sci. Technol. B*, **14**(2):page 1486, 1996.

[143] G. Toikka, G.M. Spinks, and H.R. Brown. Fine particle adhesion measured at elevated temperatures using a dedicated force rig. *Langmuir*, **17**:page 6207, 2001.

[144] M. Fuji, K. Machida, T. Takei, T. Watanabe, and M. Chikazawa. Effect of wettability on adhesion force between silica particles evaluated by atomic force microscopy measurement as a function of relative humidity. *Langmuir*, **15**:page 4584, 1999.

[145] M. Kappl, L. Helm, S. Ecke, and H.J. Butt. Adhesion and friction forces between single particles. In *Proc. Partec 2004*, Nuremberg, Germany, March 16-18 2004.

[146] M. Preuss and H.J. Butt. Direct measurement of forces between particles and bubbles. *Int. J. Min. Process.*, **56**:page 99, 1999.

[147] J.P.K. Seville and R. Clift. The effect of thin liquid layers on fluidisation characteristics. *Powder Technology*, **37**:page 117, 1984.

[148] J.P.K. Seville, U. Tuzun, and R. Clift. *Processing of particulate solids.* Blackie Academic & Professional, London, 1997.

[149] D. Geldart. Types of gas fluidization. *Powder Technology*, **7**:page 285, 1973.

[150] O. Molerus. Interpretation of Geldart's type A, B, C and D powders by taking into account interparticle cohesion forces. *Powder Technology*, **33**:page 81, 1982.

[151] S.M. Iveson, J.D. Litster, K. Hapgood, and B.J. Ennis. Nucleation, growth and breakage phenomena in agitated wet granulation processes: a review. *Powder Technology*, **117**(1-2):page 3, 2001.

[152] T. Schaefer and C. Mathiesen. Melt pelletization in a high shear mixer. 9.Effects of binder particle size. *Int. J. Pharm.*, **139**(1-2):page 139, 1996.

[153] P.G. Smith and A.W. Nienow. Particle growth mechanisms in fluidised bed granulation - I) The effect of process variables. *Chem. Eng. Sci.*, **38**(8):page 1223, 1983.

[154] S.M. Iveson and J.D. Litster. Growth regime map for liquid-bound granules. *AIChE Journal*, **44**(7):page 1510, 1998.

[155] P.A. Shamlou, Z. Liu, and J.G. Yates. Hydrodynamic influences on particle breakage in fluidized beds. *Chem. Eng. Sci.*, **45**(4):page 809, 1990.

[156] Y.C. Ray, T.S. Jiang, and C.Y. Wen. Particle attrition in a fluidized-bed. *Powder Technology*, **49**(3):page 193, 1987.

[157] U. Arena, M. D'Amore, and L. Massimilla. Carbon attrition during the fluidized combustion of a coal. *AIChE Journal*, **29**:page 40, 1983.

[158] L.X. Liu and J.D. Litster. Spouted bed seed coating: the effect of process variables on maximum coating rate and elutriation. *Powder Technology*, **74**:page 215, 1993.

[159] B. Formisani, R. Girimonte, and L. Mancuso. Analysis of the fluidisation process of particle beds at high temperature. *Chem. Eng. Sci.*, **53**(5):page 951, 1998.

[160] J.S.M. Botterill. *Fluid bed heat transfer.* Academic Press, London, 1975.

[161] D. Kunii and O. Levenspiel. *Fluidization Technology.* Wiley and Sons, 1969.

[162] J.S.M. Botterill. *Fluid bed heat transfer*, chapter 9, Fluidization Technology. Wiley, Chichester, 1986.

[163] J.G. Yates. Effects of temperature and pressure on gas-solid fluidization. *Chem. Eng. Sci.*, **51**(2):page 167, 1996.

[164] S. Ergun. Fluid flow through packed columns. *Chem. Eng. Prog.*, **48**:page 89, 1952.

[165] Y.Y. Livshits, A.I. Tamarin, and S.S. Zabrodsky. Maximum forces acting on a body immersed in a fluidized bed. *Fluid. Mech. Sov. Res.*, **7**:page 30, 1978.

[166] J.L. Moseley and T.J. O'Brien. A model for agglomeration in a fluidised bed. *Chem. Eng. Sci.*, **48**(17):page 3043, 1993.

[167] S.J.R. Simons. Imaging techniques for fluidized bed systems: a review. *Chem. Eng. J.*, **56**:page 83, 1995.

[168] J. Werther. Measurement techniques in fluidized beds. *Powder Technology*, **102**:page 15, 1999.

[169] P.N. Rowe and B.A. Partridge. An x-ray study of bubbles in fluidised beds. *Trans. Inst. Chem. Eng.*, **43**:page 157, 1965.

[170] J.G. Yates, D.J. Cheesman, and Y.A. Sergeev. Experimental observations of voidage distribution around bubbles in a fluidized bed. *Chem. Eng. Sci.*, **49**(12):page 1885, 1994.

[171] J.G. Yates and S.J.R. Simons. Experimental methods in fluidisation research. *Int. J. Mult. Flow*, **20** Suppl.:page 297, 1994.

[172] D. Newton, M. Fiorentino, and G.B. Smith. The application of x-ray imaging to the developments of fluidized bed processes. *Powder Technology*, **120**:page 70, 2001.

[173] E.J. Morton and S.J.R. Simons. *The physical basis of process tomography. In* ***Frontiers in Industrial Process Tomography***, page 11. Chapter 2. Engineering Foundation, New York, 1995.

[174] M. Stein, Y.L. Ding, J.P.K. Seville, and D.J. Parker. Solids motion in bubbling gas fluidised beds. *Chem. Eng. Sci.*, **55**:page 5291, 2000.

[175] Y.T. Makkawi and P.C. Wright. Fluidisation regimes in a conventional fluidized bed characterized by means of electrical capacitance tomography. *Chem. Eng. Sci.*, **57**:page 2411, 2002.

[176] M.J. Rhodes, X.S. Wang, M. Nguyen, P. Stewart, and K. Liffman. Use of discrete element method simulation in studying fluidization characteristics: influence of interparticle force. *Chem. Eng. Sci.*, **56**:page 69, 2001.

[177] X.S. Wang and M.J. Rhodes. Mechanistic study of defluidisation by numerical simulation. *Chem. Eng. Sci.*, **59**:page 215, 2004.

[178] P.C. Wright and J.A. Raper. Role of liquid bridge forces in cohesive fluidization. *Trans. Inst. Chem. Eng.*, **76**(Part A):page 753, 1998.

[179] G.I. Tardos and R. Pfeffer. Chemical-reaction induced agglomeration and defluidization of fluidized beds. *Powder Technology*, **85**:page 29, 1995.

[180] P. Lettieri, J.G. Yates, and D. Newton. High temperature effects on the dense phase properties of gas fluidized beds. *Powder Technology*, **120**(1-2):page 34, 2001.

[181] V. Gonzalez and A.R. Otero. Formation of UO_3 particles in a fluidized bed. *Powder Technology*, **7**:page 137, 1973.

[182] M.L. Franklin and T.B. Flanagan. Kinetics of dehydration of single-crystals of uranyl nitrate hexahydrate. *J. Chem. Soc. Dalton Transactions*, **1**:page 192, 1972.

[183] S. Dash, M. Kamruddin, S. Bera, P.K. Ajikumar, A.K. Tyagi, S.V. Narasimhan, and B. Raj. Temperature programmed decomposition of uranyl nitrate hexahydrate. *J. Nuclear Materials*, **264**:page 271, 1999.

[184] K. Nagano, K. Ogawa, T. Mochida, K. Hayashi, and H. Ogoshi. Thermal characteristics of magnesium nitrate hexahydrate and magnesium chloride hexahydrate mixture as a phase change material for effective utilization of urban waste heat. *Applied Thermal Eng.*, **24**(2-3):page 221, 2004.

[185] A.K. Galwey. Structure and order in thermal dehydrations of crystalline solids. *Thermochimica Acta*, **335**:page 181, 2000.

[186] M.T. Spyridopoulos and S.J.R. Simons. Direct measurement of bubble-particle adhesion forces on the effect of particle hydrophobicity and surfactants. *Chem. Eng. Res. Des.*, **82**(A4):page 490, 2004.